

University of Naples “Federico II”



School of Mathematics, Physics and Natural Sciences

PhD in Chemical Sciences
cycle XXIII
(2007-2010)

INTEGRATED
COMPUTATIONAL/EXPERIMENTAL
APPROACHES TO THE STUDY OF THE
OXIDATIVE CHEMISTRY OF PHENOLIC
SYSTEMS

Dr. Marianna Arzillo

Supervisor
Prof. Orlando Crescenzi

Assessor
Prof. Marco d'Ischia

PhD coordinator
Prof. Lucio Previtiera

Università degli studi di Napoli “Federico II”



Facoltà di Scienze Matematiche Fisiche e Naturali

Dottorato di Ricerca in Scienze Chimiche
XXIII ciclo
(2007-2010)

APPROCCI INTEGRATI
COMPUTAZIONALI/SPERIMENTALI PER
LO STUDIO DELLA CHIMICA
OSSIDATIVA DI SISTEMI FENOLICI

Dott.ssa Marianna Arzillo

Tutore
Prof. Orlando Crescenzi

Relatore
Prof. Marco d'Ischia

Coordinatore
Prof. Lucio Previtiera

INDEX

GENERAL INTRODUCTION	6
INTRODUCTION TO COMPUTATIONAL METHODS	15
CHAPTER I: "Oxidative chemistry of the 2,7'-biindolyl "	23
INTRODUCTION	23
RESULTS AND DISCUSSION	25
CONCLUSIONS	41
CHAPTER II: "Structural effect on the electronic absorption properties of oligomers of 5,6-dihydroxyindole "	42
INTRODUCTION	42
RESULTS AND DISCUSSION	45
CONCLUSIONS	58
CHAPTER III: "Reaction behavior of 5,6-dihydroxyindole in acidic medium"	61
INTRODUCTION	61
RESULTS AND DISCUSSION	62
CONCLUSIONS	83
CHAPTER IV: "Oxidative chemistry of 5,6-dihydroxy-1-methylindoles"	84
INTRODUCTION	84
RESULTS AND DISCUSSION	86
CONCLUSIONS	103
CHAPTER V: "Oxidative polymerization of 5,6-dihydroxyindole in phosphate buffer/polyvinyl alcohol (PVA)"	105
INTRODUCTION	105
RESULTS AND DISCUSSION	109
CONCLUSIONS	117
CHAPTER VI: "Study of oxidative polymerization of 5,6-dihydroxyindole by Dinamic Light Scattering (DLS) and Small-angle Neutron Scattering (SANS)"	118
INTRODUCTION	118
INTRODUCTION TO LIGHT SCATTERING	119
DYNAMIC LIGHT SCATTERING (DLS)	123
SMALL ANGLE NEUTRON SCATTERING (SANS)	125

RESULTS AND DISCUSSION	127
CONCLUSIONS	133
CHAPTER VII: “Computational investigation of the stability of DHI-related catechols, radicals, and quinonoid forms”	134
INTRODUCTION	134
RESULTS AND DISCUSSION	137
CONCLUSIONS	152
CHAPTER VIII: “ Other studies”	153
INTRODUCTION	153
RESULTS AND DISCUSSION	155
CONCLUSIONS	170
EXPERIMENTAL AND COMPUTATIONAL METHODS	171
1. Study of oxidative chemistry of the 2,7'-biindolyl (4)	171
1.1 Material and strumenttion	171
2.1 Oxidation of 4 : Isolation of tetramers 9-11	172
2. Structural effect on the electronic absorption properties of oligomers of 5,6-dihydroxyindole (1)	176
2.1 Material and strumentation	176
2.2 Absorption measurements	176
2.3 Computational methods	177
3. Reaction behavior of 5,6-dihydroxyindole (1) in acidic medium	178
3.1 Materials and strumentation	178
3.2 Reaction of 1 in acidic medium. General procedure	179
3.3 Isolation of pentaacetyl derivative of 5,6-dihydroxy-2-(5,6-dihydroxyindol-3-yl) indoline (12) and heptaacetyl derivative of 2-(2-amino-4,5-dihydroxyphenyl)-1,1-bis(5,6-dihydroxyindol-3-yl)ethane (13)	180
3.4 Isolation of 2-(2-Acetamido-4,5-diacetoxybenzyl)-6,7-diacetoxy-3-(5,6-diacetoxyindol-3-yl)quinoline (14b)	181
3.5 Reactions of 14b with anions	182
4. Oxidative chemistry of 5,6-dihydroxy-1-metyl-indoles	183
4.1 Materials and strumentation	183
4.2 Isolation of 19 and 20 acetylated	184
4.3 Isolation of 21 -acetylated	185

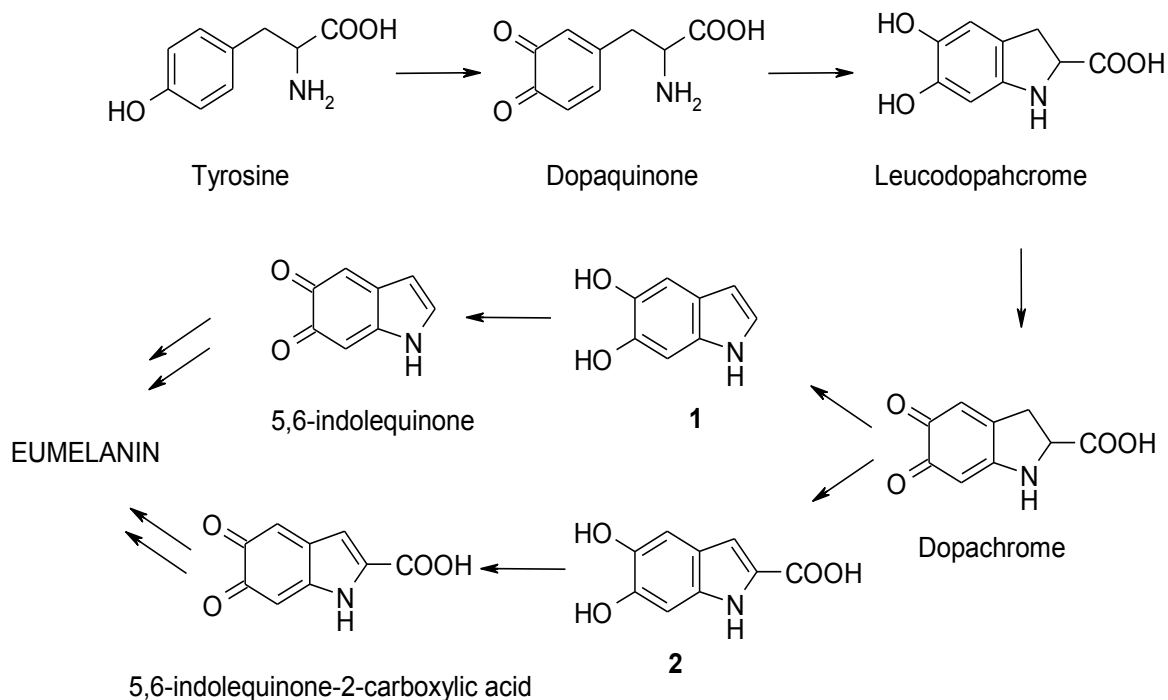
4.4 Computational methods	186
5. Oxidative polymerization of 5,6-dihydroxyindole (1) in phosphate buffer/polyvinyl alcohol (PVA)	187
5.1 Materials and instrumentation	187
5.2 Oxidation of 1 for recording absorption spectra	188
5.3 Oxidation of 1 for products analysis	188
6. Study of oxidative polymerization of 5,6-dihydroxyindole (1) by Dynamic Light Scattering (DLS) and Small-angle Neutron Scattering (SANS)	189
6.1 Materials and instrumentation	189
6.2 Preparation of the samples	190
7. Computational investigation of the stability of DHI-related catechols, radicals, and quinonoid forms	191
7.1 Computational methods	191
8. Other studies: Study of the chemistry of nitrated lipids	192
8.1 Experimental methods	192
8.2 Computational methods	192
REFERENCES	193
LIST OF PUBLICATIONS	202

GENERAL INTRODUCTION

Mono- and polyphenolic compounds represent a very large group of natural products with different structural and functional roles. Phenolic groups, and in particular catecholic groups, establish a strong tendency to autoxidation and enzymatic oxidation; these processes are accompanied by the formation of reactive radicals and quinones, which usually tend to evolve further with formation of complex polymeric materials.

5,6-Dihydroxyindoles are a unique group of catechol-containing heterocyclic compounds, which arise biogenetically by the oxidative cyclization of catecholamines and related tyrosine-derived metabolites. The parent member of the series, 5,6-dihydroxyindole (DHI, **1**), is of great biological interest because of its central role in the biosynthesis of eumelanins, the major determinants of human skin, hair, and eye pigmentation.^{1,2}

The biosynthesis of eumelanins takes place in specialized cells, the melanocytes, via the tyrosinase-catalyzed conversion of tyrosine to **1** and 5,6-dihydroxyindole-2-carboxylic acid (DHICA, **2**) through a sequence of spontaneous or enzymatically catalyzed reactions.³ Once formed, DHI and/or DHICA take part in a complex oxidative polymerization process that leads to the deposition of the black eumelanin pigments (**Scheme 1**).^{1,2}



Scheme 1. Scheme of the early stages of biosynthesis of eumelanins.

The unique status of eumelanins among natural pigments is due to their socio-economic and biomedical relevance, encompassing racial pigmentation, skin photoprotection, sun tanning and pigmentary disorders such as albinism, vitiligo and melanoma.⁴ Moreover, they display a quite unusual set of physico-chemical properties⁵ including insolubility in all solvents, broadband monotonic absorption in the UV-visible range,⁶ a persistent free radical character,⁷ metal and drug-binding properties,⁸⁻¹⁰ susceptibility to redox changes,¹¹ strong excited state-phonon coupling,¹² and amorphous electrical switch behavior.¹³ These properties have provided a basis to propose the potential application of eumelanin-related materials in the field of molecular electronics and photon harvesting systems¹⁴.

Despite many decades of work within the organic chemistry, biophysics and pigment cell communities, eumelanin structure remains virtually unknown, because of the marked chemical heterogeneity and the lack of well defined physico-chemical properties, preventing successful application of spectroscopic techniques.

While there is general agreement that at the primary level eumelanins are made up of 5,6-dihydroxyindole units at various degrees of oxidation and linked together in a covalent fashion, at the secondary level the situation is far less clear. According to an early view, eumelanins are highly heterogeneous linear polymers arising by random coupling of the monomer indole units.

According to a model proposed in the 90s^{15c} eumelanins are represented as a set of oligomers consisting of 5 to 7 units of 5,6-indolquinone arranged in a planar fashion to form 3-4 layers stacked with a distance of 3.4 Å (Figure 1).

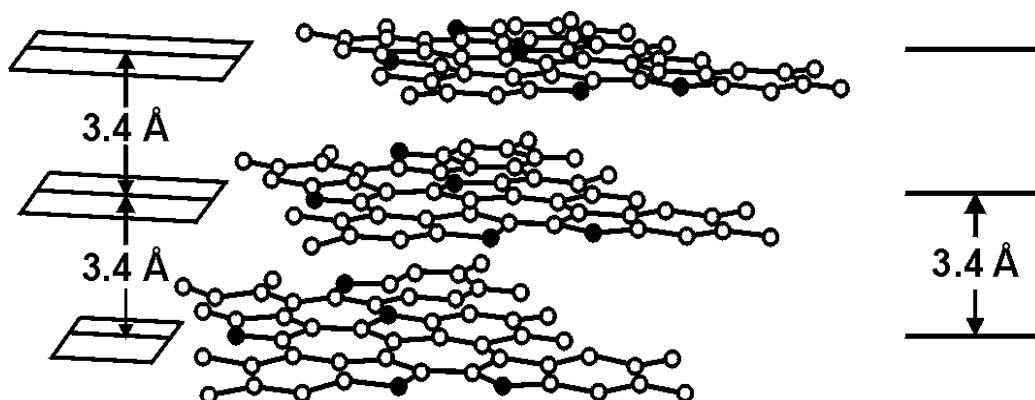


Figure 1. Eumelanins structural model proposed by Cheng et al.^{15c}

Subsequently, this model was extended on the basis of data obtained from X-ray scattering and scanning tunneling microscopy, suggesting that eumelanins consist of supramolecular aggregates of 4-6 oligomers stacked in the z-plane in a graphene-like fashion (Figure 2).¹⁶

In eumelanin from *Sepia* ink, a sequence of aggregation steps has been suggested to account for the apparent three levels of structural organization.^{16,17,18} To sum up numerous studies using atomic force microscopy (AFM),^{16,17,19} X-ray diffraction,²⁰ mass-spectrometry,²¹ NMR spectroscopy,²² and advanced quantum chemical calculations²³⁻²⁵ have addressed the eumelanin structure, and though most of them appear to support the stacked-aggregate picture (Figure 3), definitive proof this model remains however elusive.

In most cases, however, hypothetical structural models have been used as a working basis to fit experimental data, because of the lack of knowledge of the mechanisms of oxidative polymerization of **1** and its congeners.

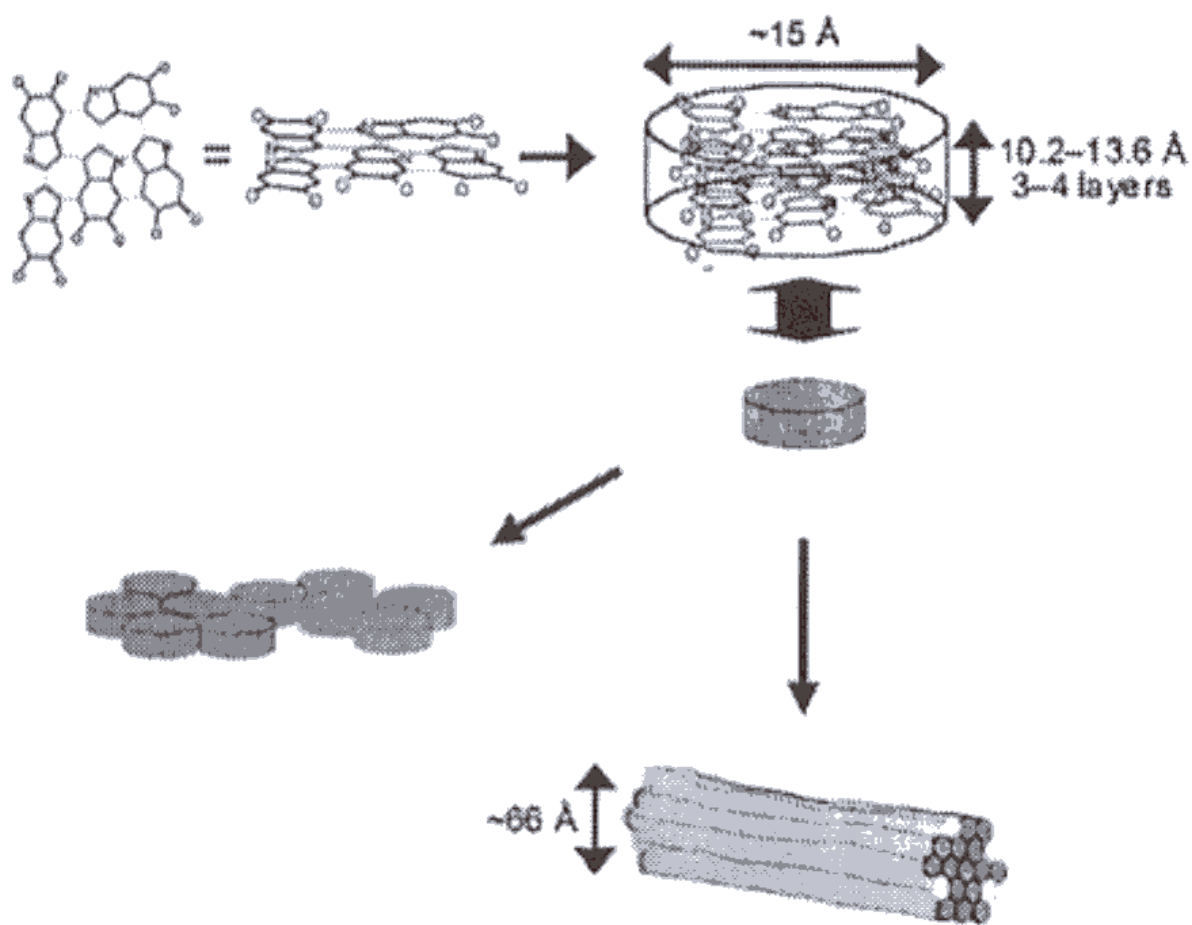


Figure 2. Structural model of eumelanins (Clancy and Simon, 2001).^{16b}

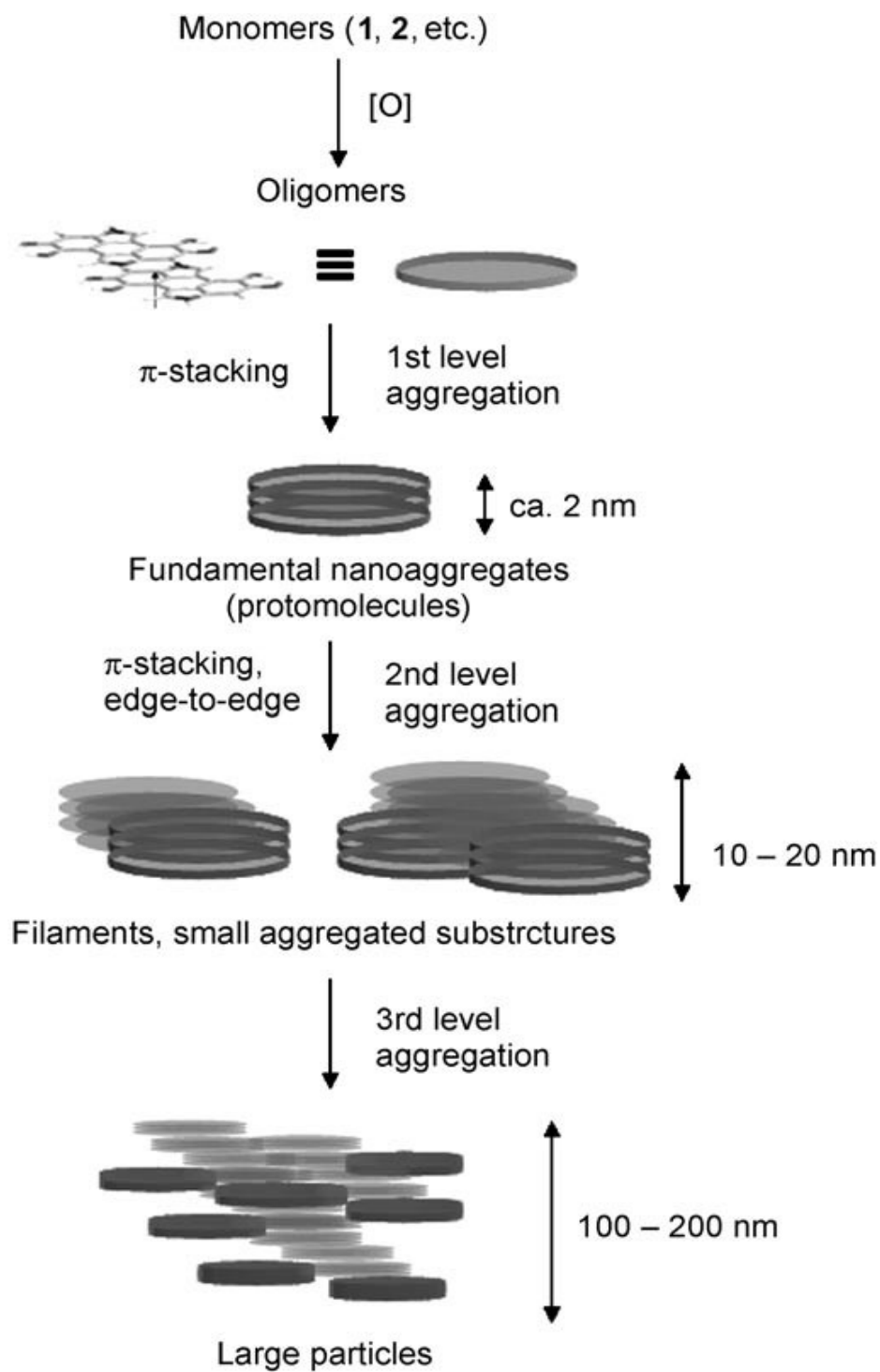
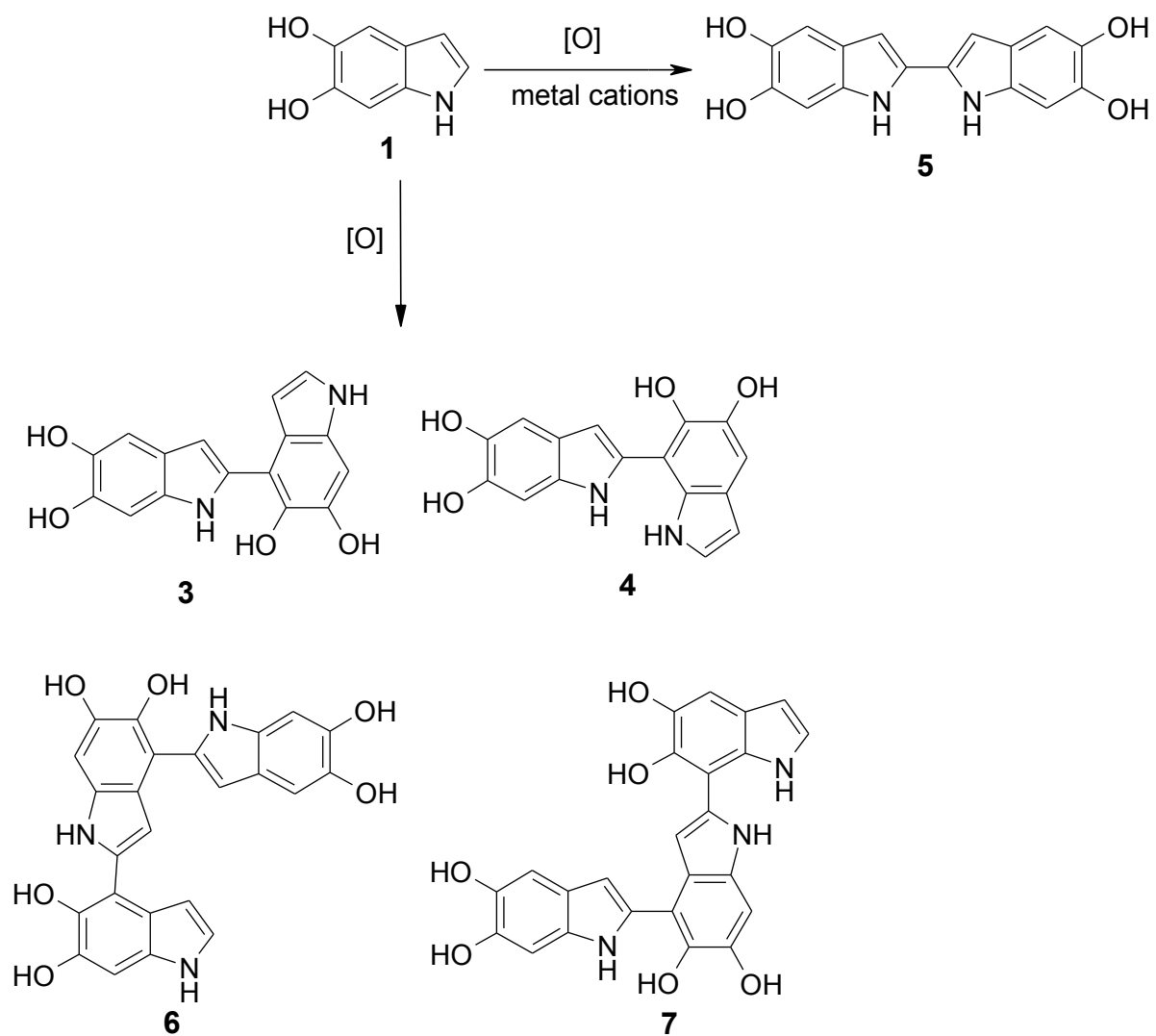


Figure 3. The hierarchical aggregate structure proposed for *Sepia* eumelanin.^{16,17,18}

Extensive studies carried out over the past two decades have elucidated the early stages of the oxidation of **1** leading to dimers **3-5** and trimers **6** and **7** as the main isolable oligomers.²⁶ These structures underscored a dominant mode of coupling of **1** involving nucleophilic attack through the 2-position to the 4- and 7-positions of a transient 5,6-indolequinone. Symmetric 2,2'-coupling leading to dimer **5**, on the other hand, prevails in the presence of transition metal ions, e.g. Zn^{2+} and Ni^{2+} , and is probably dictated by formation of chelate complexes affecting the positional reactivity of **1** or its quinone²⁷. The reactivity patterns of **1** exemplified by **3-7** (**Scheme 2**) have provided a convincing ground to postulate that the higher oligomer structures ultimately involved in the supramolecular aggregation processes are generated by sequential oxidative coupling of **1** through the 2-, 4- and 7-positions. This mechanism, however, has remained so far unverified because, as the size of the oligomers increases, their isolation becomes increasingly complex, due to the gradational range of species of increasing mass which typify the oxidation mixtures of **1**, and the consequent need to contend with very complex mixtures containing myriads of species.

In summary, while several aspects of the chemistry of 5,6-dihydroxyindoles have been reasonably well clarified, it is also clear that many more remain to be addressed.



Scheme 2. Oligomers obtained by oxidation of **1** in biomimetic conditions.

An important support to experimental studies in this field can be provided by computational techniques. A schematic and by no means exhaustive list of contexts in which modeling approaches may prove helpful includes:

- Providing structural confirmation for spectroscopically detected species (e.g. unstable reaction intermediates), based on the agreement between measured spectra and theoretically computed parameters;
- Evaluating the thermodynamic and kinetic plausibility of reaction mechanisms (typically postulated on the basis of experimental evidences);
- Inspiring the setup of new experimental measurements.

In the present thesis, the chemistry of 5,6-dihydroxyindole has been investigated by combining and integrating the information provided by computational and experimental methodologies. This approach has proved useful to address and settle many open issues concerning the mechanisms of oxidative polymerization of 5,6-dihydroxyindoles and the basic features of eumelanin building blocks.

Main topics described herein include:

1. Oxidative chemistry of the 2,7'-biindolyl (**4**); this study led *inter alia* to the isolation of three new tetramers of **1**
2. Structural effects on the electronic absorption properties of oligomers of **1**, analyzed by an integrated experimental-DFT approach
3. Reacation behavior of **1** in acidic medium; rather unexpectedly, this led to the isolation of a trimer with selective binding properties toward fluoride anion
4. Oxidative chemistry of 5,6-dihydroxy-1-metylindoles; this study led to the isolation of the first 5,6-dihydroxyindole macrocycle (alongside a tetramer)
5. Oxidative behavior of **1** in phosphate buffer/polyvinyl alcohol mixtures; the results obtained have led to the formulation of a new model for visible chromophore development in synthetic eumelanin polymers

6. Study of oxidative polymerization of **1** by Dynamic Light Scattering (DLS) and Small-angle Neutron Scattering (SANS) in collaboration with the group of Prof. Paduano of University of Naples “Federico II”
7. Computational investigation of the stability of DHI-related catechols, radicals, and quinonoid forms.

Moreover, during the course of my PhD, I collaborated in a project on the chemistry of nitrated lipids, performing the computational work.

These topics will be discussed individually in the following chapters.

INTRODUCTION TO COMPUTATIONAL METHODS

Computational chemistry approaches are categorized in terms of the underlying “model chemistries”. Each model chemistry consists in a specific combinations of a theoretical method with a basis set, and essentially represents a different approximation to the Schrödinger equation. Taking into account the Born-Oppenheimer approximation²⁸, this latter can be written as:

$$H_{el}\psi = E_{el}\psi \quad (1)$$

where ψ and E_{el} are wavefunction and energy of the electronic ground state, and H_{el} is the electronic Hamiltonian operator.

Basically all of the computational work presented in this thesis relies on methods rooted in the Density Functional Theory (DFT).

According to equation 1, the energy can be written as

$$E[\psi] = \langle \psi | H | \psi \rangle \quad (2)$$

The formula highlights the functional relation (correspondence between a function and a number) which connects ψ to E . In DFT, the multi-electronic wavefunction $\psi(\mathbf{r}_1, \mathbf{r}_2, \dots, \mathbf{r}_N)$ is replaced by the electronic density $\rho(x, y, z)$, a function of only three variables. The Hohenberg-Kohn theorem,^{29a} that forms the basis of DFT, demonstrates the existence of a unique functional which determines the ground state energy and density exactly; however, it does not provide the form of this functional. Afterwards Kohn e Sham^{29b} formalized the DFT in terms of mono-electronic Schrödinger equation:

$$\left(-\frac{1}{2} \nabla^2 + V_{KS} \right) \psi_i = \epsilon \psi_i \quad (3)$$

here, V_{KS} is a local mono-electronic potential, and the resulting orbitals are termed Kohn-Sham (KS) orbitals. The total density is linked to the KS orbitals by the relation:

$$\rho = \sum_i f_i |\psi_i|^2 \quad (4)$$

where f_i are the molecular orbital expansion coefficients.

Furthermore, V_{KS} can be decomposed into several terms:

$$V_{KS} = V_{ext} + V_C + V_{XC} \quad (5)$$

where V_{ext} is an external potential, V_C is a Coloumb term, and V_{XC} , the exchange-correlation term, includes whatever portion of the electron-electron interactions is not contained in the previous terms.

The energy of a interacting system is:

$$E = E_T + \int d^3r \rho V_{ext} + \frac{1}{2} \iint d^3r_1 d^3r_2 \frac{\rho(r_1)\rho(r_2)}{r_{12}} + E_{XC} \quad (6)$$

where E_T is the kinetic energy, and E_{XC} is related to corresponding potential as:

$$V_{XC} = \frac{\delta(E_{XC})}{\delta\rho} \quad (7)$$

The only system for which the density functional can be established exactly is the uniform electron gas. Starting from this functional form it is possible to develop the simplest approximation applied to real chemical systems, the Local Spin Density Approximation (LSDA): in essence, a term for the correlation between opposite spin densities ρ and ρ^* is added to the uniform electron gas functional.³⁰ Another group of functionals, dubbed Generalized Gradient Approximation (GGA) and capable of providing a higher level of accuracy, are obtained by introducing the electron density gradient in the functional form; this allows to explicitly account for density inhomogeneities within molecules or isolated atoms. The several GGA functionals differ for the presence of parameters; these can be provided by empirical optimizations relying on comparisons with selected experimental data; in alternative, they can be based on theoretical considerations.³¹ Among the most effective functionals are those that include a mixture of Hartree-Fock (HF) and DFT exchange along with DFT correlation; they are collectively termed hybrid functionals, representative members of the class being the well-known B3LYP and PBE0.³² In particular, most calculations performed in this thesis were based on the PBE0 functional, that has been shown to provide quite satisfactory energies and geometries for a wide range of organic and

biological systems,³³⁻³⁶ as well as a rather accurate description of low-lying excited states in the context of TD-TFD calculations (see below).³⁷⁻⁴²

DFT computations are very popular and highly successful, since in many cases they allow to obtain accurate data (that include electronic correlation) with computational costs quite comparable to those of a simple HF calculation. Therefore, DFT usually permits a quantum-mechanical study of large chemical system.⁴³

In order to investigate the effects of electric or magnetic fields on molecules and extract features like excitation energies, frequency-dependent response properties, and absorption spectra, time-dependent density functional theory (TD-DFT) can be used. The foundation of modern TD-DFT was laid by Runge & Gross,⁴⁴ who derived a Hohenberg-Kohn-like theorem for the time-dependent Schrödinger equation. The Runge-Gross theorem proves that there is a one-to-one correspondence between the external (time-dependent) potential, $V_{\text{ext}}(\mathbf{r}; t)$, and the electronic density, $\rho(\mathbf{r}; t)$, for many-body systems evolving from a fixed initial state. This is a nontrivial statement, and implies that, even if the information we have about a system is limited to its density, we can still obtain all of its properties.

Within rather general assumptions, spectroscopic interactions between radiation and matter can be modeled by an external perturbation (\mathbf{x}) that alters the unperturbed ground state energy of a molecular system, $E^{(0)}$:

$$E(\mathbf{x}) = E^{(0)} + \mathbf{E}^{(1)}\mathbf{x} + \frac{1}{2}\mathbf{x}^T\mathbf{E}^{(2)}\mathbf{x} + \dots \quad (8)$$

The coefficients of this expansion represent features of the molecular system and of its quantum state. The energy associated with a transition between electronic states of a molecular system typically falls in the UV-visible range of the electromagnetic spectrum. To describe the physical situation of spectroscopic transitions, time-independent perturbation theory⁴⁵ must be replaced by a time-dependent perturbation approach. The molecular Hamiltonian in the presence of a time-dependent perturbation can be written as⁴⁶

$$H = H^0 + H'(t) = H^0 + F(t)A \quad (9)$$

where H^0 is the unperturbed Hamiltonian, A is a Hermitian operator describing the type of perturbation, and F is a function determining its density. The problem is now to determine the response of some property (described by B) to the perturbation described by A . If the focus is initially placed on the first-order variation of B (linear response), application of time-dependent perturbation theory allows to demonstrate⁴⁶ that the variation $\langle \delta B \rangle = \langle B \rangle - \langle B_0 \rangle$ at the time t is given by:

$$\langle \delta B \rangle = \int_{-\infty}^t K(BA|t-t')F(t')dt' \quad (10)$$

where

$$K(BA|t-t') = -i \sum_{n \neq 0} \left\{ \langle 0|B|n \rangle \langle n|A|0 \rangle e^{-i\omega_{0n}(t-t')} - \langle 0|A|n \rangle \langle n|B|0 \rangle e^{i\omega_{0n}(t-t')} \right\} \quad (11)$$

is the time correlation function, and the summation runs over the eigenstates of the unperturbed Hamiltonian. This function can be transported into the frequency range by a Fourier transform, giving:

$$\Pi(BA_\omega|\omega) = \lim_{\varepsilon \rightarrow 0} \sum_{n \neq 0} \left\{ \frac{\langle 0|B|n \rangle \langle n|A_\omega|0 \rangle}{\omega - \omega_{0n} + i\varepsilon} - \frac{\langle 0|A_\omega|n \rangle \langle n|B|0 \rangle}{\omega + \omega_{0n} + i\varepsilon} \right\} \quad (12)$$

This amount is termed Frequency Dependent Polarizability (FDP) of B with respect to A_ω at the frequency ω . The FDP (eq. 12) presents real poles in correspondence to the natural frequencies of the system (the eigenstate energies); thus, computation of these poles allows to assign the energies of excited electronic states.

TD-DFT represents an application of the approach outlined above, casted in the frame of the electronic density functional. The DFT cannot be used directly in the form of eq. 12, since this would require knowledge of all the eigenstates of the system. A possible solution to this issue comes from an approximated variational expression of FDP,⁴⁶ that can be written as:

$$\Pi(AB|\omega) = (\nabla B \ B \nabla) \mathbf{P}(\omega) (\nabla A \ A \nabla)^\dagger \quad (13)$$

where $\mathbf{P}(\omega)$ is the response matrix that, for any frequency, describes the linear response to the temporal variation of the expectation value of B , following the perturbation associated to operator A . With good approximation, the poles of the response matrix correspond to the poles of the FDP. The response matrix of a molecular system can be expressed starting from a set of wavefunctions that approximate the eigenstates of the

system. In TD-DFT, the eigenstates chosen are obtained by allowing single excitations from an occupied orbital (in the ground state) to a virtual orbital.

In terms of a Kohn-Sham formulation for the ground state, the electronic density is represented by KS orbitals (eq. 4). From a phenomenological viewpoint, following a variation $\delta v(t)$ of the external potential, the electronic density undergoes a perturbation $\delta\rho(t)$ can be stated in terms of the eigenstates corresponding to single excitations.

In the frequency domain, the density change can be written as:

$$\delta\rho(\mathbf{r}, \omega) = \sum_{st} \delta P_{st}(\mathbf{r}, \omega) \psi_s(\mathbf{r}) \psi_t^*(\mathbf{r}) \quad (14)$$

where the subscripts s and t run over both occupied and virtual orbitals. It is possible demonstrate that the elements of the rotation matrix are:

$$\delta P_{st}(\mathbf{r}, \omega) = \frac{f_s - f_t}{(\varepsilon_s - \varepsilon_t) - \omega} [\delta v(\mathbf{r}, \omega) + \delta v^{SCF}(\mathbf{r}, \omega)] \quad (15)$$

where ε_s and ε_t are the eigenvalues associated to the eigenfunctions ψ_s e ψ_t , respectively (eq. 3); $\delta v^{SCF}(\mathbf{r}, \omega)$ indicates the first order variation of all terms of the *KS* operator that depend on electronic density:

$$\delta v^{SCF}(\mathbf{r}, \omega) = \int \frac{\delta\rho(\mathbf{r}', \omega)}{|\mathbf{r} - \mathbf{r}'|} d\mathbf{r}' + V_{xc}[\delta\rho](\mathbf{r}) \quad (16)$$

Therefore the general equations for forced oscillations can be written:⁴⁷

$$\left[\begin{pmatrix} \mathbf{A} & \mathbf{B} \\ \mathbf{B}^* & \mathbf{A}^* \end{pmatrix} - \omega \begin{pmatrix} \mathbf{1} & \mathbf{0} \\ \mathbf{0} & -\mathbf{1} \end{pmatrix} \right] \begin{pmatrix} \delta\mathbf{P} \\ \delta\mathbf{P}^* \end{pmatrix} = \begin{pmatrix} \delta\mathbf{v} \\ \delta\mathbf{v}^* \end{pmatrix} \quad (17)$$

where

$$\begin{aligned} A_{ai,bj} &= \delta_{ab} \delta_{ij} (\varepsilon_a - \varepsilon_i) + K_{ai,bj} \\ B_{ai,bj} &= K_{ai,jb} \\ K_{ai,bj} &= \iint \psi_a^*(\mathbf{r}) \psi_i^*(\mathbf{r}) \frac{1}{|\mathbf{r} - \mathbf{r}'|} \psi_b(\mathbf{r}') \psi_j(\mathbf{r}') d\mathbf{r} d\mathbf{r}' + \\ &+ \iint \psi_a^*(\mathbf{r}) \psi_i(\mathbf{r}) \frac{\delta^2 E_{xc}}{\delta\rho(\mathbf{r}) \delta\rho(\mathbf{r}')} \psi_b^*(\mathbf{r}') \psi_j(\mathbf{r}') d\mathbf{r} d\mathbf{r}' \end{aligned} \quad (18)$$

Subscripts i and j refer to occupied KS orbitals, whereas a and b refer to virtual orbitals; \mathbf{K} is the so-called coupling matrix. Based on this matrix equation it is possible to

compute electronic excitation energies: in practice, these correspond to those values of ω for which the matrix in square brackets in (eq. 17) has null eigenvalues.

One of the problems in computational work is the simulation of the reaction environment. Concerning solvation effects, approaches in which the solvent degrees of freedom are accounted for in an average way, e.g., in terms of a reaction field, have proven particularly effective. Extensive review of the continuum-based method of implicit solvation can be found in recent literature.^{48,49,50} Briefly, the most general approach to the problem of solvent effects is based on a system-bath decomposition. The solvation process can then be dissected into the creation of a cavity for the solute (spending energy E_{cav}), and the successive switching-on of dispersion-repulsion (with energy $E_{dis-rep}$) and electrostatic (with energy E_{el}) interactions with surrounding solvent molecules.

The polarizable continuum model (PCM),^{48,49,51} probably the best known example of continuum methods, has been adopted in the computational work presented in this thesis. The model consists of embedding the solute molecule within a cavity made by the envelope of spheres centred on the solute atoms. Inside the cavity, the relative dielectric constant has the same value as in a vacuum ($\epsilon = 1$), and it steeply goes to the solvent bulk value outside (e.g., $\epsilon = 78.4$ for water). The procedures to assign the atomic radii and to form the cavity have been described in detail together with effective classical approaches for evaluating E_{cav} and $E_{dis-rep}$.^{48,49,52}

The solvent is polarized by the presence of the solute molecule and undergoes a new equilibration, giving rise to a reaction field that acts back onto the solute molecule. Such phenomenon is described by the PCM in terms of a pattern of effective charges on the cavity surface. The simple introduction of the PCM often provides substantial improvements in energies, geometries and spectroscopic parameters computed for molecular systems in a variety of solvent media.

The cavity surface is finely subdivided into small tiles (*tesserae*), and the solvent reaction field determining the electrostatic contribution (E_{el}) is described in terms of a pattern of apparent point charges appearing in *tesserae* and self-consistently adjusted with the solute electron density. Within the framework of effective Hamiltonian schemes, it is possible to write the solute molecular Hamiltonian as perturbed by a reaction field operator:

$$\hat{H} = \hat{H}^0 + \hat{V}_{RF}$$

$$\hat{V}_{RF} = \frac{1}{2} \int_{surface} \varphi(r') D(r', r) \varphi(r) dr' dr$$

where H^0 is the Hamiltonian of the isolated molecule, $\varphi(r)$ is the electrostatic potential on the cavity surface, and $D(r', r)$ is a function depending on cavity geometry and solvent dielectric constant. Solvation charges (q) depend, in turn, on the electrostatic potential (V) on *tesserae* through a geometrical matrix Q ($q = QV$), related to the position and size of the surface *tesserae*, so that the free energy in solution G can be written:

$$G = E[\rho] + V_{NN} + 1/2 V^\dagger QV$$

here $E[\rho]$ is the free-solute energy, but with the electron density (ρ) polarized by the solvent, and V_{NN} is the repulsion between solute nuclei. The core of the model is then the definition of the Q matrix, which in the most recent formulations of PCM depends only on the electrostatic potentials, takes into the proper account the part of the solute electron density outside the molecular cavity, and allows the treatment of conventional, isotropic solutions, and anisotropic media like liquid crystals. Starting from these definitions, very effective linear-scaling algorithms⁵³ have been implemented for cavity construction and evaluation of energy and of its first and second derivatives with respect to geometric, electric and magnetic parameters, thus allowing for the inclusion of PCM contributions in the calculation of optical and magnetic spectroscopic parameters.^{33,54-56}

However, the PCM may also display limitations in some cases, e.g., when highly specific interactions, like hydrogen bonds, come into play.⁵⁷ Cluster approaches can provide a straightforward route to describe localized phenomena, including the spectroscopic transitions of molecules; once again, the PCM can be brought into play to account for the “bulk” solvent, and thus to reduce the number of solvent molecules to be described explicitly.³³ In other words, such a discrete-continuum scheme takes into account both the quantum mechanical nature of specific solute-solvent interaction, i.e. hydrogen bonds, and the classical Coulomb long-range effects tuned by the dielectric

properties of the solution. The resulting cluster-PCM description represents a very versatile tool that can be adapted to different structural and spectroscopic situations; of course, which and how many solvent molecules need to be explicitly described is a question that has to be defined case by case. Moreover, a single structure of the solute-solvent cluster or supra-molecular frame could not be representative of a very flexible situation.⁴⁰ This means that the structures of the solute and its closest solvent molecules must be statistically averaged among all the energetically accessible configurations.

Thus, the cluster-PCM approach is also attractive for the computation of averaging effects brought about by dynamics.

CHAPTER I

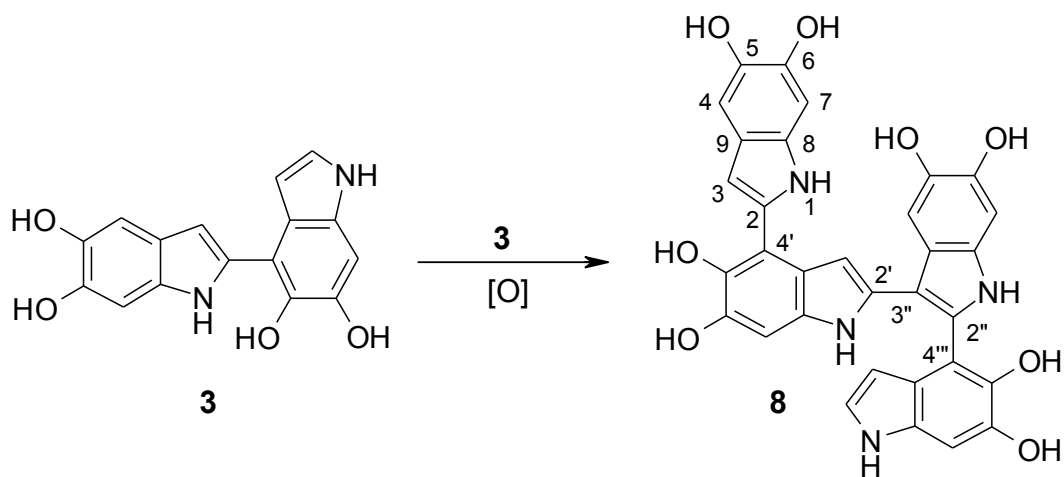
Oxidative chemistry of the 2,7'-biindolyl (**4**)

INTRODUCTION

Structural characterization of high oligomer derived from DHI (**1**) is essential for predicting their planarity and, hence, the efficiency of π -electron delocalization and the possible extent of the π -stacking in the final aggregation process.

Moreover, it would offer a valuable background for the purposeful design of eumelanin-like materials for potential practical applications.

A strategy to obtain higher oligomers of **1** is the oxidation of the oligomers previously isolated from the mixture. Thus, for example, a straightforward access route to tetramers is the oxidation of dimers. In a previous study the first tetramer of **1**, 5,5',5'',5''',6,6',6'',6'''-octahydroxy-2,4':2',3'':2'',4'''-tetraindolyl (**8**), was obtained as the acetyl derivative by oxidation of the 2,4'-biindolyl **3**⁵⁸ (**Scheme 3**). Structure **8** featured an “anomalous” 2,3'-biindolyl linkage which was unprecedented in 5,6-dihydroxyindole chemistry, and that was suggested to reflect nucleophilic attack of **3** to an extended quinone methide intermediate.⁵⁹ Whether this peculiar mode of coupling denoted a general modification of the 5,6-dihydroxyindole reactivity pattern in dimers and higher oligomers was an important issue raised by that study. It seemed therefore important to extend the study to the oxidation of another dimer, the 2,7'-biindolyl (**4**) in order to increase knowledge of the reaction behavior of dimer intermediates and gain further insights into higher oligomers. In this chapter, I report the structures of three new tetramers of **1** obtained by oxidation of the biindolyl **4** and a discussion of how the emerging pathways of dimer oxidation fit with currently accepted schemes of oxidative polymerization of **1**.



Scheme 3. Oxidative conversion of **3** to 5,5',5'',5''',6,6',6'',6'''-octahydroxy-2,4':2',3'':2'',4'''-tetraindole (**8**).

RESULTS AND DISCUSSION

The oxidation of **4** was carried out as described,⁵⁸ using the peroxidase/H₂O₂ system. The dimer, stored as the acetyl derivative, was deprotected by an established methodology involving treatment with 0.1 M phosphate buffer, pH 12 for 1-2 min under an Ar atmosphere, to prevent aerobic oxidation of the deacetylated dimer by air. Eventually, the pH was brought to 8, to ensure sufficient solubility of the dimer at 1 mM concentration.

A critical parameter affecting product composition and yields was the reaction time, with too short times resulting in much unreacted substrate and prolonged oxidation times leading to abundant eumelanin-like materials with little isolable oligomers. Accordingly, after several trials, a reaction time of 20s was adopted for all experiments. The purple-blue reaction mixture thus obtained was treated with excess sodium dithionite, and the clear ethyl acetate-extractable fraction was acetylated to ensure stability and improve chromatographic behavior of the products. TLC analysis (CHCl₃:CH₃OH=98:2) of the resulting mixture indicated little residual **4** and a number of chromatographically distinct fluorescent products, two of which could be isolated by repeated TLC and HPLC fractionation and were characterized by extensive spectral analysis, including ¹H, ¹H COSY, ¹H, ¹³C HSQC, ¹H, ¹³C HMBC and ROESY spectra.

The product at R_f = 0.42 gave a pseudomolecular ion peak in the ESI(+)-MS spectrum at *m/z* 949 [M+Na]⁺, indicating a tetramer of **1** and was formulated as the symmetric 5,5',5'',5'''-octahydroxy-7,2':3',3'':2'',7'''-tetraindole (**9**) acetylated in which the 2,7'-biindolyl units were linked through a 3,3'-bond.

The ¹H NMR spectrum of **9** acetylated (**Figure 4**) exhibited five signals in the aromatic region at δ 6.02, 6.94, 6.95, 7.34 and 7.49. Of the two NH protons, only that at δ 9.02 gave cross peaks in the ¹H, ¹H COSY spectrum with protons resonating at δ 6.95 (H-2) and 6.02 (H-3), while the N-H resonance at δ 10.54 did not show apparent correlation peaks (**Figure 5**).

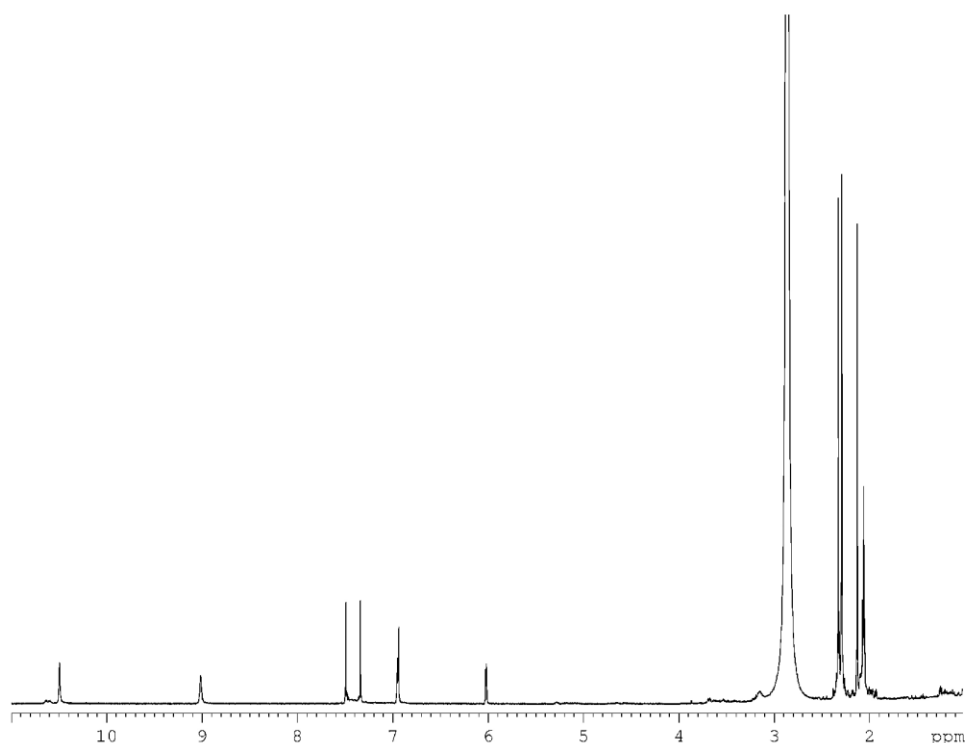


Figure 4. ^1H NMR spectrum of **9** acetylated.

The ROESY spectrum (**Figure 6**) revealed a distinct NOE contact between the H-7 proton at δ 7.34, and the N-H proton resonating at δ 10.54, allowing definitive assignment of this resonance to the disubstituted indole moiety, and between the two N-H protons, suggesting that they are in close proximity in the most populated conformations. It is also worth noting that a number of protons, i.e. H-3_a (δ 6.02), H-4_a (δ 6.94), H-2_a (δ 6.95) and N-H_a (δ 9.02) resonate significantly upfield relative to dimer 4, indicating that the outer ring a/a' falls in the shielding cone of the inner ring b/ b'. **Figure 7** shows the structure of **9** acetylated with assignment of the proton and carbon resonances.

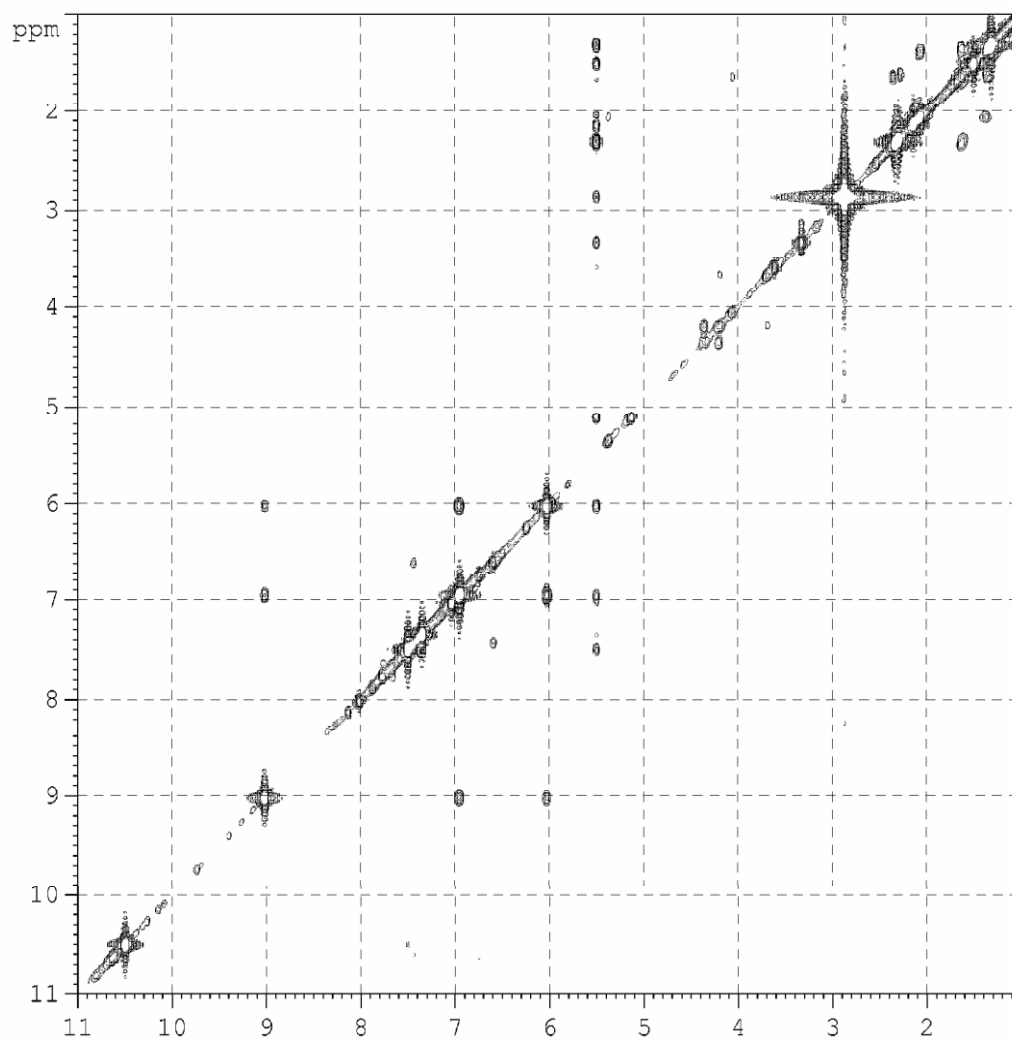


Figure 5. ^1H , ^1H COSY spectrum of **9** acetylated.

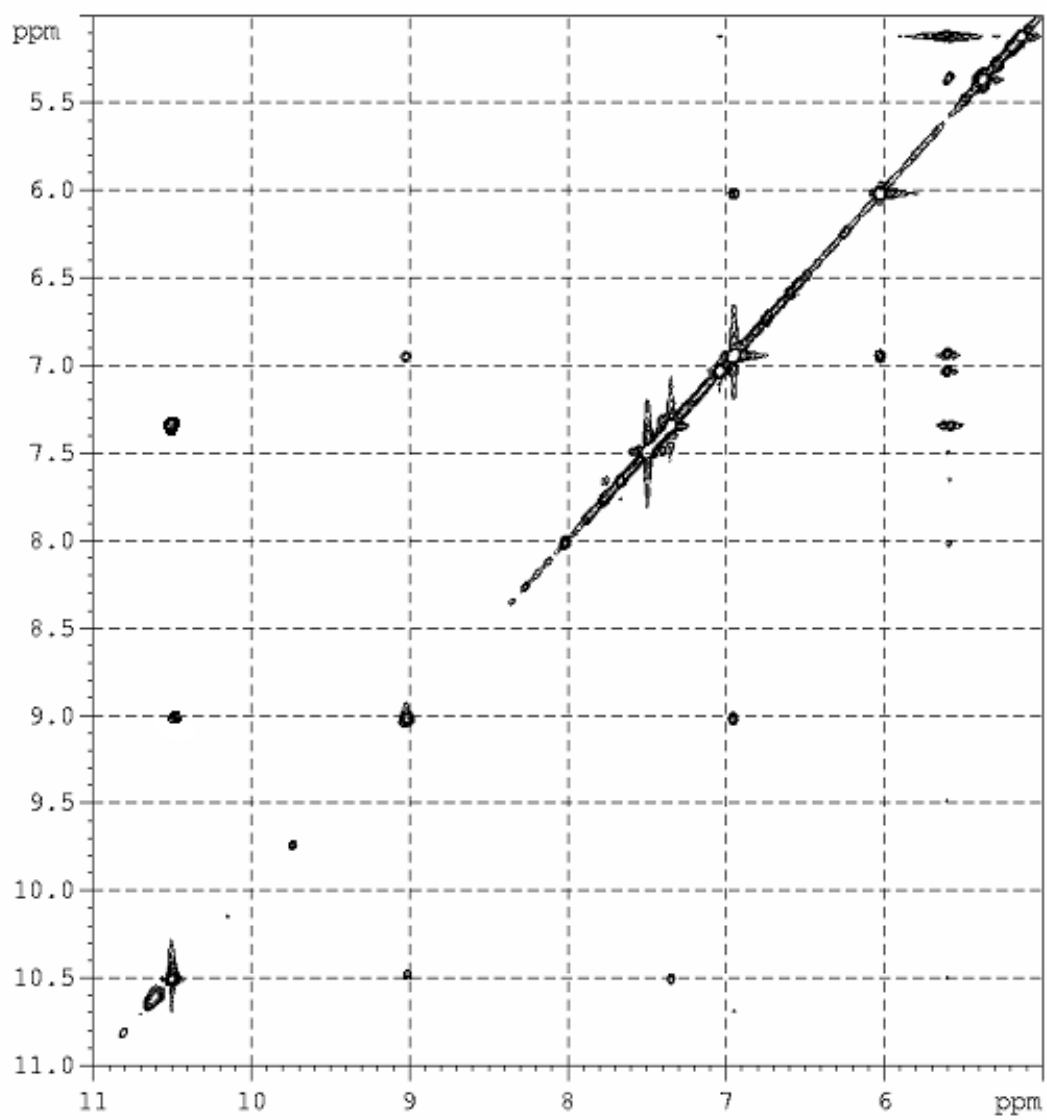


Figure 6. ROESY spectrum of **9** acetylated.

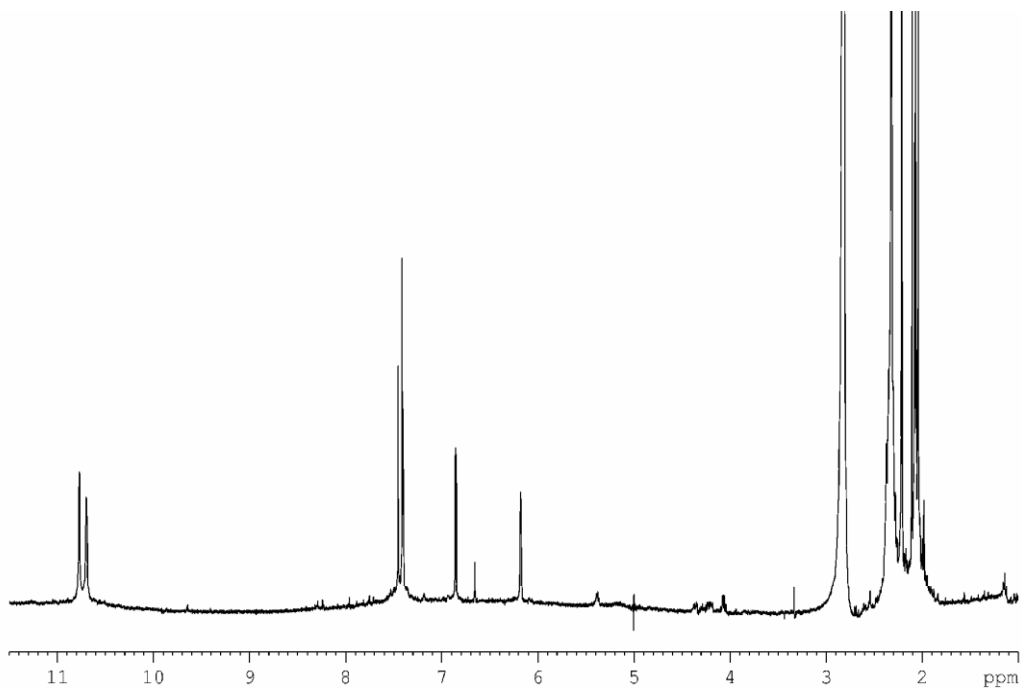


Figure 8. ^1H NMR spectrum of **10** acetylated.

The ROESY spectrum (**Figure 10**) showed moreover cross-peaks between H-3_a and H-4_a, H-7_a and NH_a, and H-3_a and NH_b allowing complete assignment of all resonances. The marked upfield shift of the H-3_b proton (δ 6.16) is attributable to the diamagnetic anisotropy of the adjacent indole ring. In **Figure 11** is represented the structure of **10** acetylated with assignment of proton and carbon resonances.

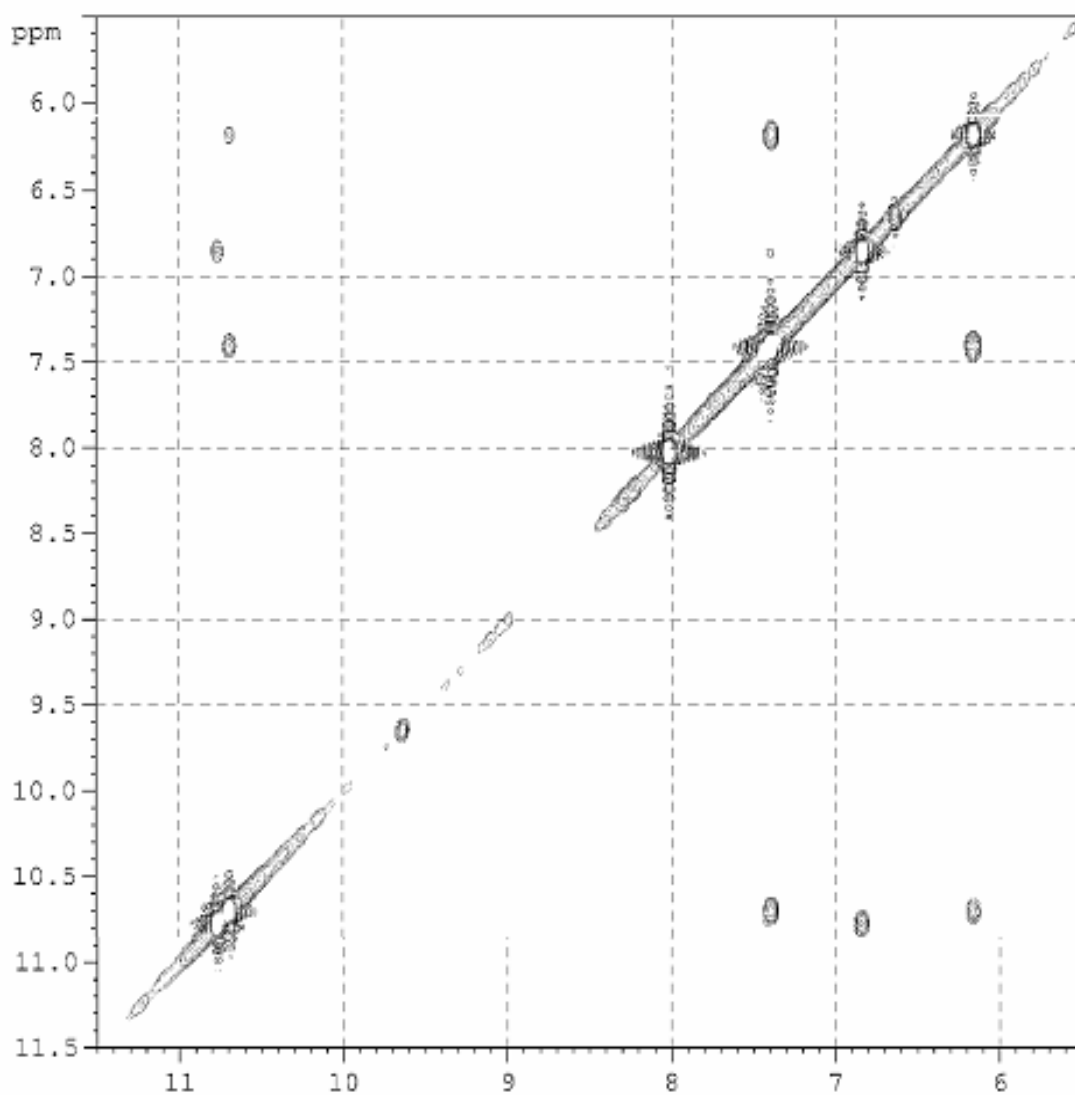


Figure 9. ^1H , ^1H COSY spectrum of **10** acetylated.

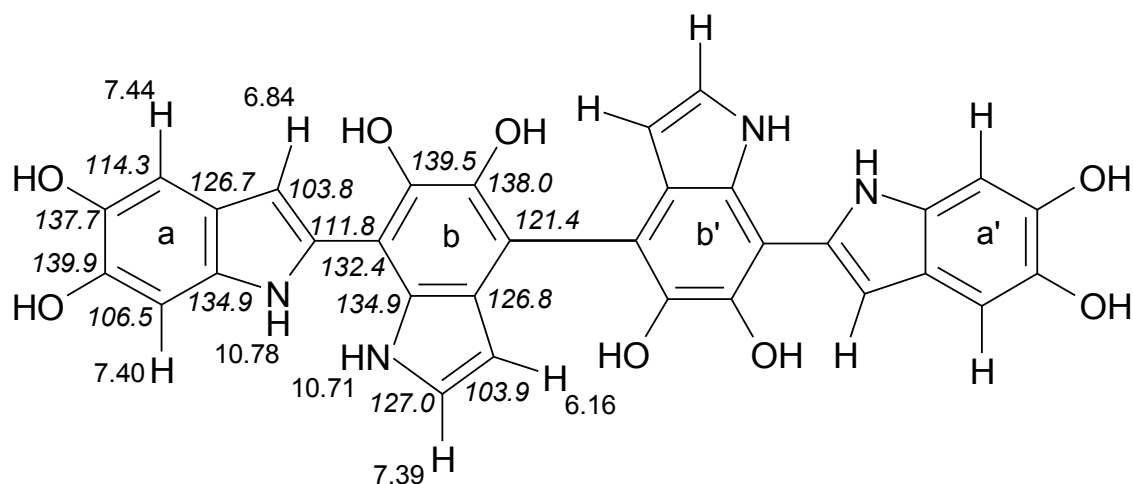


Figure 11. Structure of **10** acetylated with proton (regular style) and carbon (italic style) resonances.

The results so far described are a significant achievement when considered in the light of the notorious difficulties in isolating higher oligomers of **1**.

Unfortunately, attempts to isolate other oxidation products of **4** were unsuccessful due to the marked complexity of the reaction mixture and the very low formation yields of the products. During the recent investigation of the oxidation chemistry of **3**⁵⁸ it was found that transition metal cations, particularly Zn^{2+} and Ni^{2+} ions directed the reaction course towards the formation of a more defined pattern of products, allowing the isolation of tetramer **8** in sufficient yields for structural characterization. It seemed therefore of interest to extend the study of the role of transition metal cations to the oxidative coupling of **4**.

A preliminary screening of the effect of various divalent cations showed that Zn^{2+} ions could lead to a simpler reaction mixture. Accordingly, the oxidation of **4** (1 mM) was repeated in the presence of 3 mM Zn^{2+} in 0.5 M TRIS buffer, pH 8, using peroxidase/ H_2O_2 , the latter at 4.9 mM concentration.

TLC fractionation after the usual work up revealed two main products, one of which proved to be chromatographically and spectrally indistinguishable from **9** acetylated, while the other was a new tetramer which was present in much lesser amounts in the reaction mixture obtained under metal-free conditions, as evident from TLC and HPLC analysis.

On the basis of a pseudomolecular ion peak at m/z 949 $[M+Na]^+$ (ESI(+)-MS) and extensive 2D NMR analysis, the new product ($R_f=0.20$, $CHCl_3:CH_3OH=98:2$, isolated yield 5%) was eventually assigned the structure of the asymmetric tetramer 5,5',5'',5''',6,6',6'',6'''-octaaidroxy-2,7':2',3'':2'',7'''-tetraindole (**11**) acetylated.

The 1H -NMR spectrum (**Figure 12**) exhibited ten resonances in the aromatic proton region, with only one H-2-type proton (δ 7.18), showing coupling with the H-3 (δ 6.47) and NH (δ 10.39) protons on the same terminal unit, designated *d* in the structural formula.

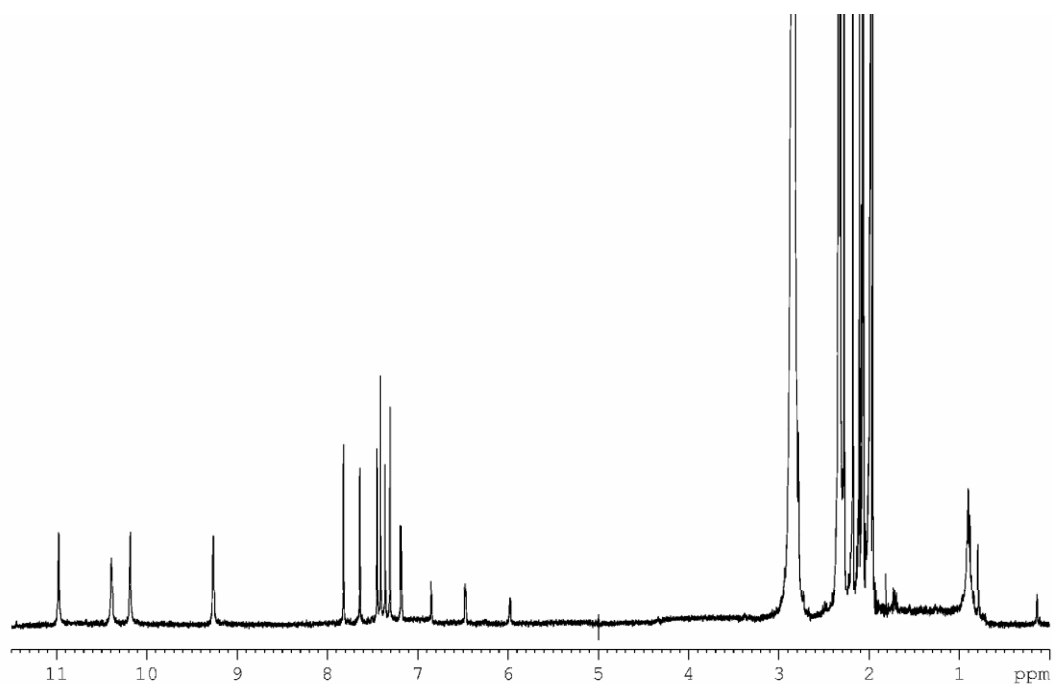


Figure 12. 1H NMR of **11** acetylated.

The ^1H , ^1H COSY spectrum (**Figure 13**) allowed unambiguous assignment of the four NH protons and the three H-3 protons to each of the remaining units, designated a, b and c.

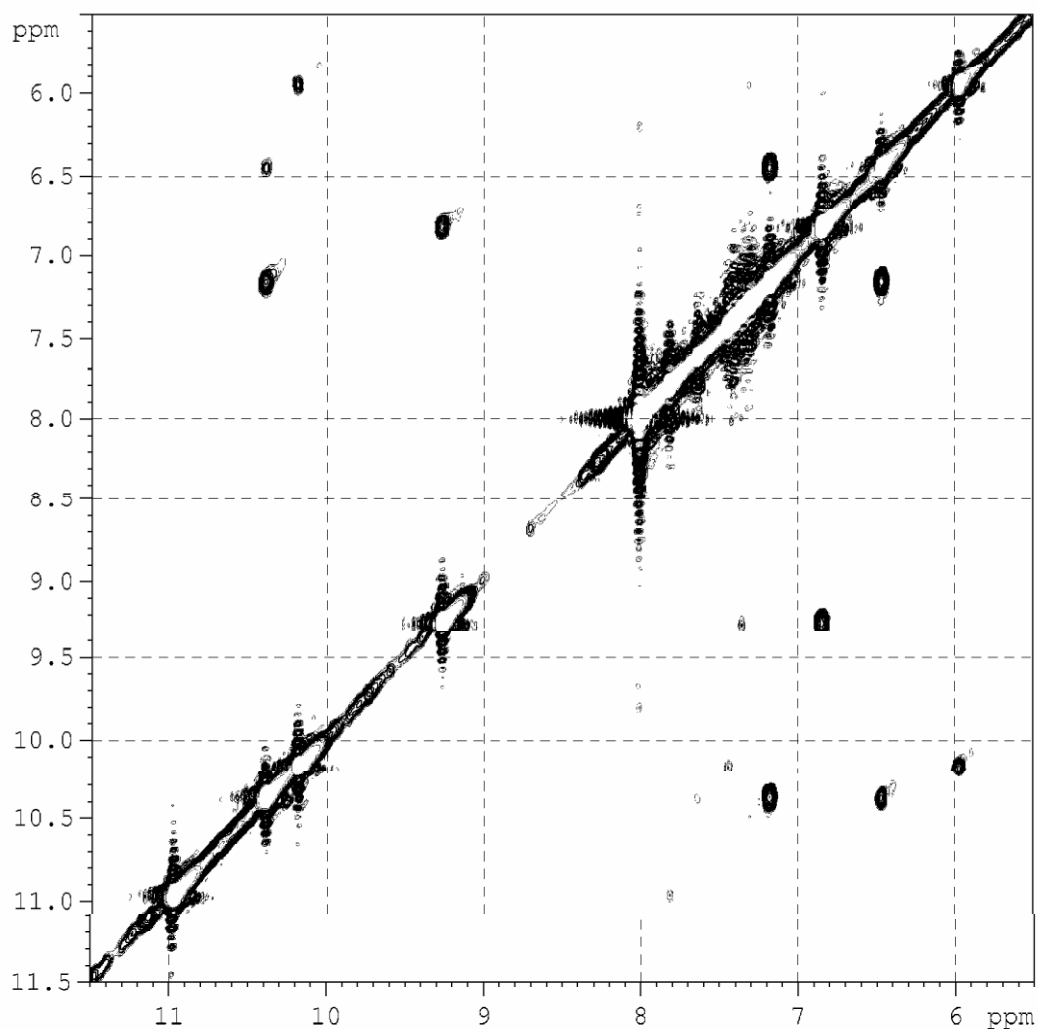


Figure 13. ^1H , ^1H COSY spectrum of **11** acetylated.

Distinct cross-peaks were observed in the ROESY spectrum (**Figure 14**) between the following resonances: H-3_b (δ 6.84) and H-4_b (δ 7.81); H-3_d (δ 6.47) and H-2_d (δ 7.18) and H-4_d (δ 7.64); H-7_a (δ 7.30) and NH_a (δ 10.18); H-7_c (δ 7.43) and NH_c (δ 10.97). This data, coupled with ¹H, ¹³C HMBC correlations, allowed straightforward assignment of all protons and carbons to the relevant units (**Figure 15**), and provided conclusive evidence for the 2,3'-mode of coupling of the dimer.

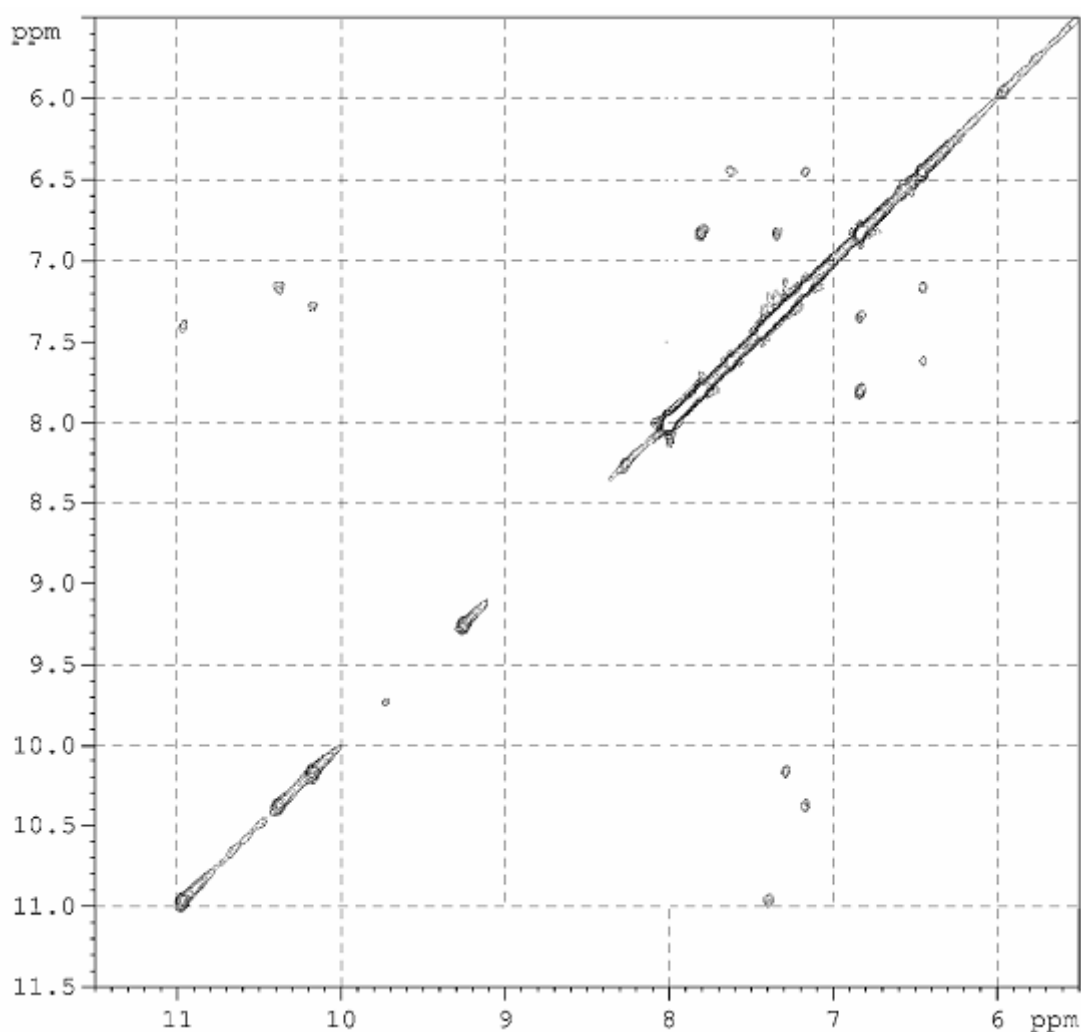


Figure 14. ROESY spectrum of **11** acetylated.

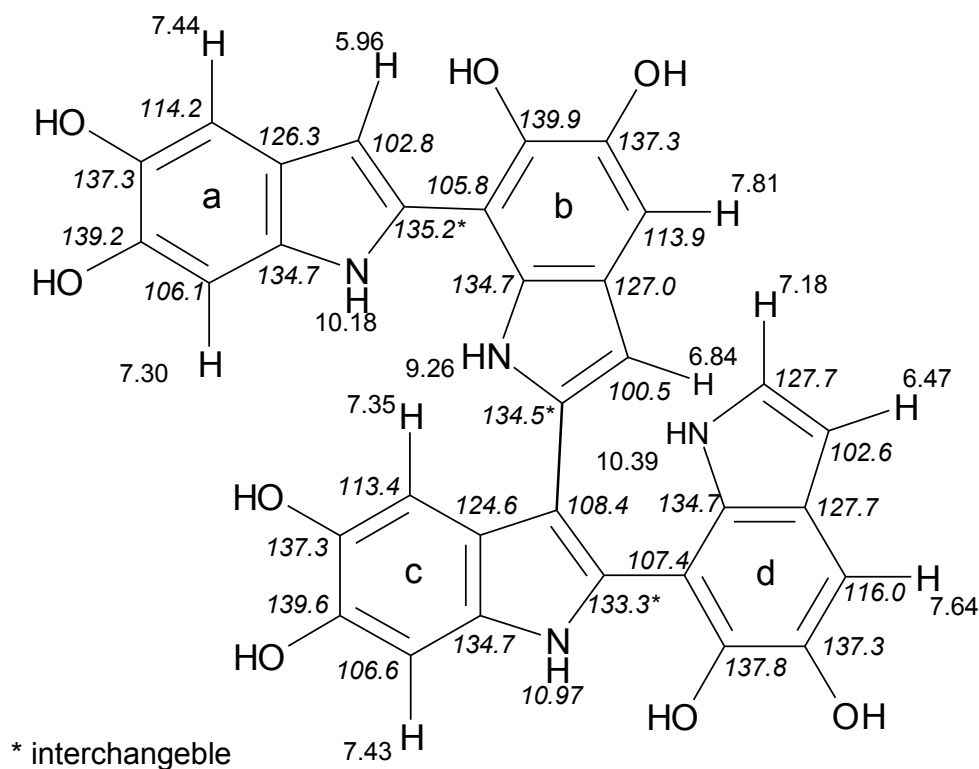


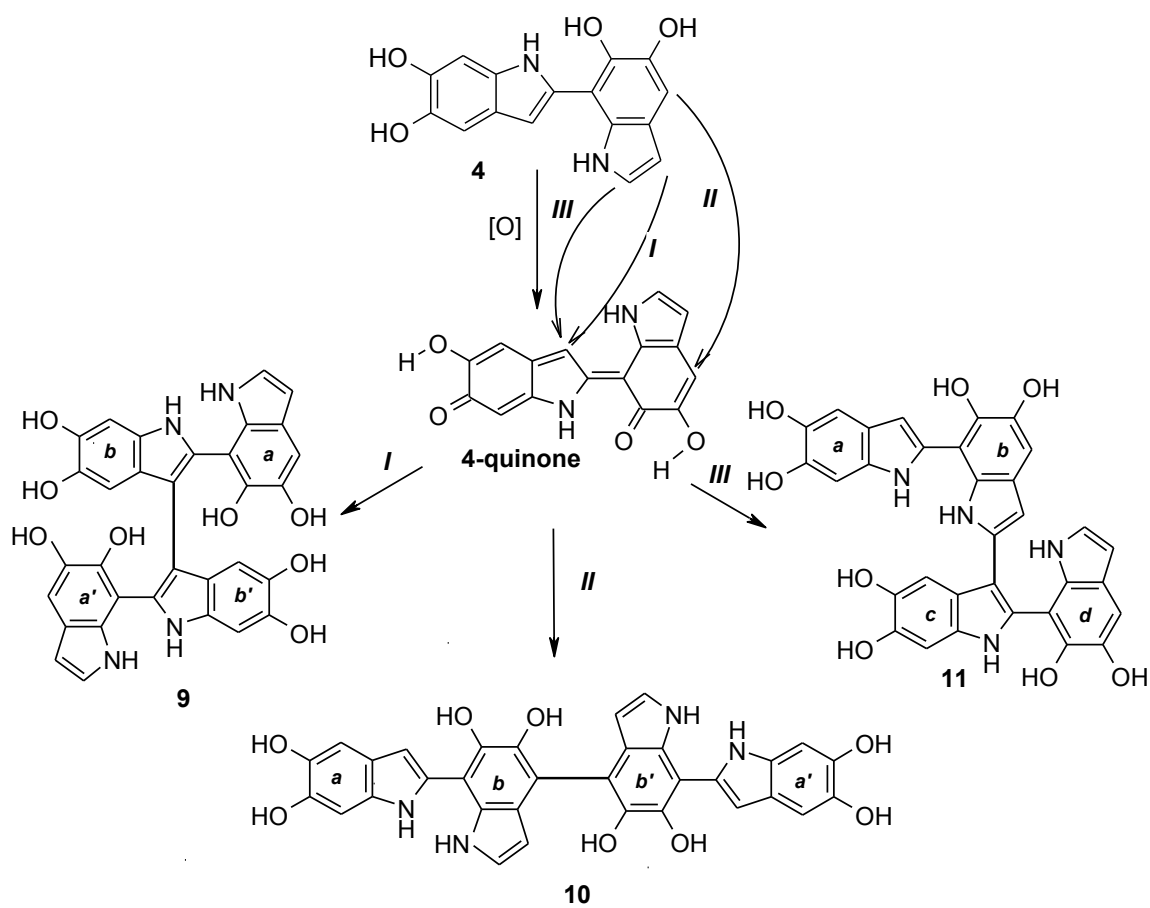
Figure 15. Structure of **11** acetylated with proton (regular style) and carbon (italic style) resonances.

Structures **9-11**, along with the previously isolated tetramer **8**, allowed an unprecedented insight into oligomers of **1** past the trimer stage. For all isolated tetramers markedly non planar structures would be anticipated, due to the presence of sterically congested 2,3'-disubstituted indole units in **9** and **11**, or the 4,4'-linkage with a high torsional barrier in **10**.⁶⁰ The novel bonding modes that derive from the dimer-dimer coupling pathways would accommodate a much greater degree of structural complexity and a broader variety of molecular shapes for higher oligomers than previously believed, supporting the chemical disorder model (but not a true statistical randomness) for the secondary level structures of eumelanins.⁶¹ Clearly, only a few tetramers have been isolated in small amounts; therefore, other oligomerization pathways and coupling mechanisms are possible.⁶² The workup procedure used, based on ethyl acetate extraction, ensured a virtually quantitative recovery of the low

molecular weight oligomers. This was checked in each experiment after ethyl acetate extraction by subjecting to acetylation the residual insoluble fraction of the mixture, with no further isolable species. Accordingly, it can confidently be argued that the workup procedure does not inherently favor linear oligomers over other possible species, e.g., extended aromatic oligomers or bi-coupled species. These latter, if present in sufficient amounts, should not have escaped isolation, as shown in previous studies demonstrating that planar diindolocarbazole cyclotrimers obtained from **1** are easily isolated by the same workup. Nonetheless, a note of caution about the actual significance of the isolated oligomers is in order until a more complete picture of the oligomerization process and product patterns is available.

Mechanistically, formation of tetramers **8-11** discloses different patterns of reactivity of the 5,6-dihydroxyindole system when framed into the dimeric scaffolds **3** and **4**. Oxidation of **3** has recently been shown to proceed via a quinone intermediate featuring a planar extended quinone methide structure with an interring double bond.⁵⁹ A similar intermediate, **4**-quinone, may be involved in the oxidative coupling of **4** leading to **9-11** (**Scheme 4**). DFT calculations on **4**-quinone indicated a planar structure with a high LUMO coefficient on the 3-position of the 2-substituted indole unit,⁵⁹ suggesting that such position may display electrophilic reactivity and may be attacked by **4** in a frontier orbital-controlled fashion leading to tetramers **9** and **11**. Whereas formation of **11** would thus resemble the previously described formation of **8**,⁵⁸ in the symmetric tetramer **9** the 3-position would serve both as electrophilic site in **4**-quinone and as nucleophilic site in the reduced counterpart **4**.

Tetramer **10** may arise by an alternate reaction mode of **4** and its quinone via the 4-positions, but the factors underlying this regiochemistry are less clear (**Scheme 4**). It may be worth noting that the LUMO of **4**-quinone bears a modest coefficient at the reactive 4-position,⁵⁹ but whether this has any role remains to be determined.



Scheme 4. Proposed mechanism of formation of tetramers **9-11**.

The ability of Zn^{2+} to favor formation of **11** (route *III*) over **10** probably reflects an enhanced nucleophilic reactivity at the 2-position of the 7-substituted unit of **4**. This effect is analogous to that observed in the case of dimer **3** and would be the consequence of the partial ionization of the OH group at C6 following chelate formation. It should be emphasized that the role of the metal is only to direct more dimer towards route *III*, since the same route is operative also under metal-free conditions, albeit to a lesser extent.

An alternative mechanism for **11** based on nucleophilic attack of **4** through the 3-position to the free 2-position of **4-quinone** would be ruled out on the basis of the negligible LUMO coefficient at the 2-position.⁵⁹

Tetramers **8-11** offer hints for an improved mechanistic view of the oxidative polymerization of **1**, in which the gradational sequence of oligomeric indole units would

be populated at the tetramer level both by species arising by attack of trimers to **1** quinone, likely *via* 2,4'-and 2,7'-linkages, and by species derived from oxidative coupling of **3** and **4** *via* 2,3'-, 3,3'- and 4,4'-linkages. The relative involvement of the oligomer-monomer versus the oligomer-oligomer coupling pathways would depend on several factors, including the rate of substrate oxidation and the extent of the reaction, since it is likely that the dimer coupling route becomes especially significant in the later phases of the process when most of the monomer has been consumed and sufficient amounts of dimers begin to accumulate. The tetramer construction process *via* dimer-dimer coupling offers significant opportunities to engineer the structures of 5,6-dihydroxyindole oligomers beyond the limits explored to-date and might allow the design and preparation of innovative bioinspired polyindole-based materials for various applications.¹⁴

An important point raised by this study concerns the relevance to eumelanin structure and properties. It is known that, in addition to **1**, 5,6-dihydroxyindole-2-carboxylic acid (**2**) also plays an important role in melanogenesis.²⁻⁵ The presence of the carboxylic group dramatically affects the reactivity and oxidative coupling patterns of the 5,6-dihydroxyindole system, hindering reactivity at the 3-position. Indeed, an array of tetramers of the 2-carboxylic acid have been described in a previous paper,⁶⁰ which exhibit only 4,4'-, 7,7'-, and 4,7'-inter-unit bonds, implying atropisomerism, at least in their reduced forms. It will be of interest, and an important goal for future studies, to investigate how the different coupling behaviors of the indole monomers and their oligomers affect the geometry/planarity of eumelanin building blocks, both in their reduced and oxidized states, and concur to determine the final properties of natural eumelanins also in terms of chemical disorder.

CONCLUSIONS

In this chapter I have reported the results of a study on the oxidative polymerization of the 2,7'-biindole **4** leading to the isolation and structural characterization of three new tetramers of **1**. This study represents an important step forward toward an improved model of eumelanin structure. One important outcome is the recognition of the potential role of dimer coupling as an alternative to the trimer-monomer reaction in the mechanisms of tetramer formation. This issue has been overlooked in traditional models of 5,6-dihydroxyindole polymerization and should now be taken into due consideration when attempting to draw consistent models of oligomer chain growth.

Another relevant outcome is the availability of structurally characterized tetramer structures to probe currently held models of supramolecular organization of oligomers in eumelanin related polymers.¹⁶ A variety of fully planar structures for 5,6-dihydroxyindole oligomers have been proposed^{24,63} which envisage either bicoupling (two bonds between adjacent monomer units) or cyclic scaffolds featuring an inner porphyrin ring. Though in principle attractive, these structures remain so far hypothetical and have never been supported by direct experimental evidence.

While waiting for additional oligomers to be isolated and characterized, to depict a more detailed scenario of the later stages of 5,6-dihydroxyindole polymerization, it is advisable that only the structures of tetramers **8** and **9-11** be used when elaborating predictive or interpretative models of supramolecular oligomer layer aggregation and particle buildup.

CHAPTER II

Structural effect on the electronic absorption properties of oligomers of 5,6-dihydroxyindole (1)

INTRODUCTION

As anticipated in the background section, eumelanins display a peculiar set of optical and photochemical properties, including a broad, monotonic and featureless absorbance profile extending from the UV to the near-IR, that are defined by the molecular, supramolecular and aggregate-level structures of the pigments.⁵ These properties, that still defy elucidation, are central to elucidating the actual role of eumelanins in skin photoprotection, one of the main supposed functions of the pigmentary system.^{5,64,65}

Therefore, dissecting the fundamental structural factors responsible for the broad-band absorption spectrum and black color remains a central goal of eumelanin research. In particular, it is actively debated whether the eumelanin “chromophore” is due to an extended conjugated polymeric backbone or rather reflects a highly disordered system made up of mixtures of π -stacked oligomers.^{5,15,16}

A viable approach toward settling this controversy relies on systematic studies of spectrophotometric properties in the oligomeric series, which have so far remained largely uncharted. Elucidation of the structural effects on the optical band gap may enable structure-property relationships to be derived to aid a fundamental understanding of the underlying photochemical and optical processes.

Recent advances in computational methods have provided basic information on the structural and photophysical properties of **1** and **2**.⁵ In addition to structural studies on the monomeric 5,6-dihydroxyindoles^{63(a),66-70} and a time dependent density functional theory (TD-DFT) investigation of the oscillator strengths of various tautomers of **1** and its quinone to predict absorption spectra⁷¹ a number of papers have focused on the HOMO-LUMO gap and the compression effects of oxidation states, tautomerism and π -stacking in oligomers of **1**. Besides semiempirical quantum mechanics calculations on small oligomeric units⁷², semiempirical spectroscopic simulations of five dimeric structures in a double-quinone form, comprising two

rotamers of the 2,2'-biindolyl (**5**), the 2,7'-biindolyl (**4**) and two rotamers of a hypothetical 3,7'-biindolyl, have been reported.^{63(a)}

Calculated absorption spectra showed for oxidized dimer **4** an absorption maximum at 320 nm and for the rotamers of oxidized dimer **5** bands around 300 nm. HOMO–LUMO gaps for a range of oligomers have also been calculated^{63(b)} using as structural models polyquinone layers up to a hexamer with the carbonyl residing along the perimeter of the nanometer-sized structures. The simulations have been extended²³ to include stacked aggregates of the oligomeric sheets as well as changes in their oxidation states.

The key findings from all these papers are that different oxidation states and tautomeric forms can have dramatically different gaps, and that increasing oligomer size can have the effect of red-shifting the absorption maxima as can π -stacking, to the point that the whole UV-vis absorption spectrum can be covered through proper structural combinations at the low oligomer level.

Notably, as few as 11 individual species have been calculated as being necessary to cover the UV, visible and near infrared with realistic inhomogeneous line broadening.^{14b,61}

More recently a structural model for eumelanin protomolecules, consisting of 4 or 5 of the basic molecular units (hydroquinone, indolequinone, and its tautomers), in arrangements that contain an inner porphyrin ring has been proposed. Interestingly, an average of the spectra of the 16 dominant tetramers produced a largely featureless spectrum, except for two weak and broad shoulders at around 350 nm and around 240 nm.²⁴

Although these calculations concur to delineate a model in which the broad, featureless eumelanin spectrum can indeed be constructed from a few chemically distinct building blocks with overlapping individual absorption spectra, they have a fundamental limitation in that they refer to hypothetical, chemically unverified oligomeric skeletons that bear little resemblance to the structures so far isolated.

Some insight into the relationship between oxidation level, π -electron delocalization and HOMO-LUMO gaps in DHI oligomers has derived from integrated pulse radiolysis and computational investigation of the transient species generated by oxidation of DHI and related oligomers^{59, 73}.

On this basis, a systematic investigation of the effects of structural parameters on the spectroscopic absorption properties of isolated oligomers of **1** appeared desirable as a necessary background on which to build an improved model to understand the optical properties of eumelanins.

In this chapter I report the first vis-à-vis comparison of the experimental spectra of the known oligomers of **1** with the corresponding ones simulated at the TD-DFT level.

RESULTS AND DISCUSSION

Dimers **3–5** were prepared as described⁵⁹ and were obtained as the acetyl derivatives. To determine their absorption spectra, a mild deacetylation procedure was used, which involves treatment with 0.1 M phosphate buffer, pH 12, under argon prior to acidification to pH 7.0 and registration of the spectrum. Under these conditions, deacetylation was complete, as checked by NMR analysis of samples obtained under the same conditions,⁵⁹ and no oxidation to melanin-like material occurred.

The experimental UV absorption spectra of **3–5** are reported in **Figure 16**.

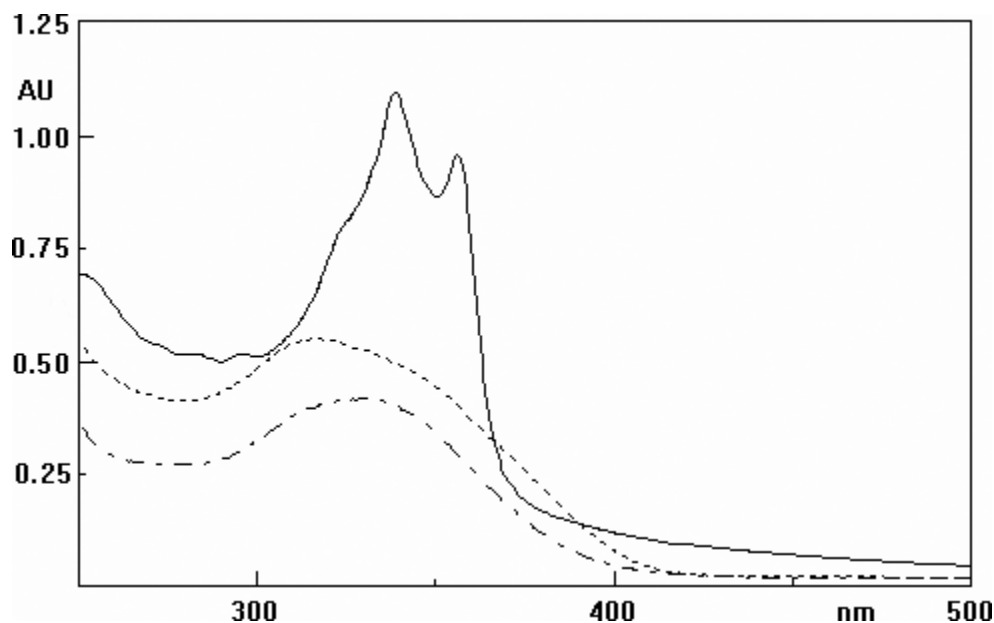


Figure 16. UV absorption spectra of dimers **3–5** (2.5×10^{-5} M) in aqueous phosphate buffer, pH 7.0. **3**, dotted line; **4**, dot-dashed line; **5**, full line.

Symmetric biindole **5** absorbs at relatively high wavelengths and its highest wavelength maximum (369 nm) is shifted as much as 60 nm relative to **4** (λ_{max} 308 nm), whereas a less pronounced shift is observed in the case of **3** (λ_{max} 328 nm). A similar trend can be observed for the acetylated derivatives: in methanol as solvent, acetylated **5** shows a complex absorption spectrum with maxima at 325 (sh), 342 and 361 nm, acetylated **3** displays a maximum at 322 nm and acetylated **4** exhibits bands at 297 and 307 (sh) nm.²⁶ Notably, recent studies of the transient species obtained by pulse radiolytic oxidation of dimers **3–5** at pH 7.0 also indicated a relatively long wavelength absorption for the extended quinone-methide like species obtained by oxidation of **5** (520 [sh], 570 nm), and similar absorption spectra for the quinonoid oxidation products of **3** and **4** (maxima around 530 nm).⁵⁹

To inquire into the structural factors underlying the different absorption properties of **3–5**, the structural and electronic absorption spectra of these dimers were investigated at the DFT level. Absorption spectra of all the energetically relevant species were computed using the TD-DFT approach,^{47,51,74,75} with a large basis set. The PCM^{52,53,76} was employed to account for the influence of the aqueous environment on molecular geometries and electronic transitions.⁷⁷ **Table 1** lists the conformers identified for the three dimers, along with relevant geometrical, energetic and spectroscopic features; UV spectra were computed for the most significant conformers of **3**, **4** and **5** and are displayed in **Figure 17** (a Lorentzian line-broadening of 20 nm was imposed). For **5**, two non-planar structures constrained to inter-ring dihedrals of 155° and 130° were also examined. For each dimer, a Boltzmann-weighted combination of the spectra of all individual conformer is also shown.

As confirmed by reference computations performed on **1**, in the absence of other constraints the phenolic hydroxyl groups tend to be coplanar to the ring they belong to, and to assume the same orientation, so as to form an intramolecular OH---O hydrogen bond. The preferred orientation places the OH groups *anti* with respect to the indole nitrogen. However, the opposite orientation, dubbed “OH *syn*,” is only slightly higher in energy (in the order of 0.3 kcal mol⁻¹), and can become predominant under the influence of a compensating favorable interaction: this is, for example, the case for the *syn* (OH *syn*) conformer of **3**, which features an inter-ring hydrogen bond between the

NH proton on the first indole moiety, and the oxygen atom at the 5 position of the second ring.

The most stable geometry of the symmetrical dimer **5** is planar, with an *anti* arrangement at the 2,2' ring junction, and a computed λ_{max} of 357 nm; by contrast, a *syn* inter-ring junction implies a non-planar minimum energy conformation, in which the reference dihedral (N-C2-C2'-N') takes on a value of 25°, and the absorption is blue-shifted by 6 nm; however, this conformer is higher in (PCM) energy by ca. 1.0 kcal mol⁻¹, and is expected to be significantly less populated at room temperature.

Table 1: Geometrical, energetic and spectroscopic features of the significant conformers of dimers **3**, **4** and **5**, computed at the PBE0 level in aqueous solution.

Conformer	Inter-ring dihedral, (degrees)	Relative energy, ^a (kcal mol ⁻¹)	Relative energy, ^b (kcal mol ⁻¹)	Oscillator strength (λ , nm)	Apparent λ_{\max} , ^c nm
3 ^d					
<i>anti</i>	180	0.0 ^e	0.0 ^f	357.0 (1.36)	357
<i>anti</i>	155 (restrained)	0.3	0.4	347.9 (1.28)	348
<i>anti</i>	130 (restrained)	1.9	2.2	327.8 (1.09)	328
<i>syn</i>	25	0.9	1.1	350.7 (1.26)	351
4 ^g					
<i>anti</i>	137	1.6	1.2	332.5 (0.70), 307.2 (0.12)	331
<i>anti</i> (OH <i>syn</i>) ^h	148	1.4	1.2	343.8 (0.79), 305.8 (0.11)	343
<i>syn</i>	41	2.4	-	-	-
<i>syn</i> (OH <i>syn</i>) ^h	24	0.0 ⁱ	0.0 ^j	349.9 (0.81), 308.3 (0.11)	350
5 ^k					
<i>anti</i>	143	1.3	1.2	332.2 (0.74), 303.7 (0.12)	331
<i>anti</i> (OH <i>syn</i>) ^h	133	1.9	1.6	322.4 (0.64), 303.9 (0.12)	320
<i>syn</i>	29	0.0 ^l	0.0 ^m	338.6 (0.80), 307.7 (0.10)	338
<i>syn</i> (OH <i>syn</i>) ^h	44	2.5	-	-	-

^aPBE0 / 6-31+G(d,p) / PCM. ^bPBE0 / 6-311+G(2d,2p) / PCM // PBE0 / 6-31+G(d,p) / PCM.

^cMaxima of a simulated spectrum with a Lorentzian line-broadening of 20 nm.

^dReference dihedral N-C2-C2'-N'. ^e-1026.303677 hartree. ^f-1026.543679 hartree.

^gReference dihedral N-C2-C4'-C5'. ^hOrientation of the phenolic hydroxyl groups on the second unit *syn* with respect to the indole nitrogen of the same ring.

ⁱ-1026.298457 hartree. ^j-1026.537480 hartree. ^kReference dihedral N-C2-C7'-C6'.

^l-1026.296921 hartree. ^m-1026.536278. Only maxima above 300 nm are recorded.

Accordingly, in the averaged spectrum the λ_{max} is close to that of the *anti* conformer, and compares quite well to the experimental value. If the *anti* conformation is forced out of coplanarity by the same extent as the *syn* conformer (inter-ring dihedral of 155°), the computed blueshift is similar (7 nm). Larger distortions can have much stronger effects (e.g. almost 30 nm for an inter-ring dihedral of 50°); this may be of interest in the comparison with other oligomers, for which strongly nonplanar conformers may occur.

As a matter of fact, both **3** and **4** feature nonplanar minima, with distortions from planarity that can exceed 45°; for the whole series of all conformers of **3**, **4** and **5**, a remarkable correlation is observed between the distortion from planarity and the computed transition wavelength. For each of the dimers **3** and **4**, a single main conformer contributes mostly to the spectra. The predicted λ_{max} of **3** is around 347 nm, in fair agreement with experiment. The agreement is worse in the case of **4** (~ 336 nm); however, the observed order of the absorption maxima wavelengths, $\lambda_5 > \lambda_3 > \lambda_4$, is well reproduced. For all three dimers, the long wavelength band is due to a HOMO → LUMO transition, both involved orbitals being strongly delocalized over the two rings.

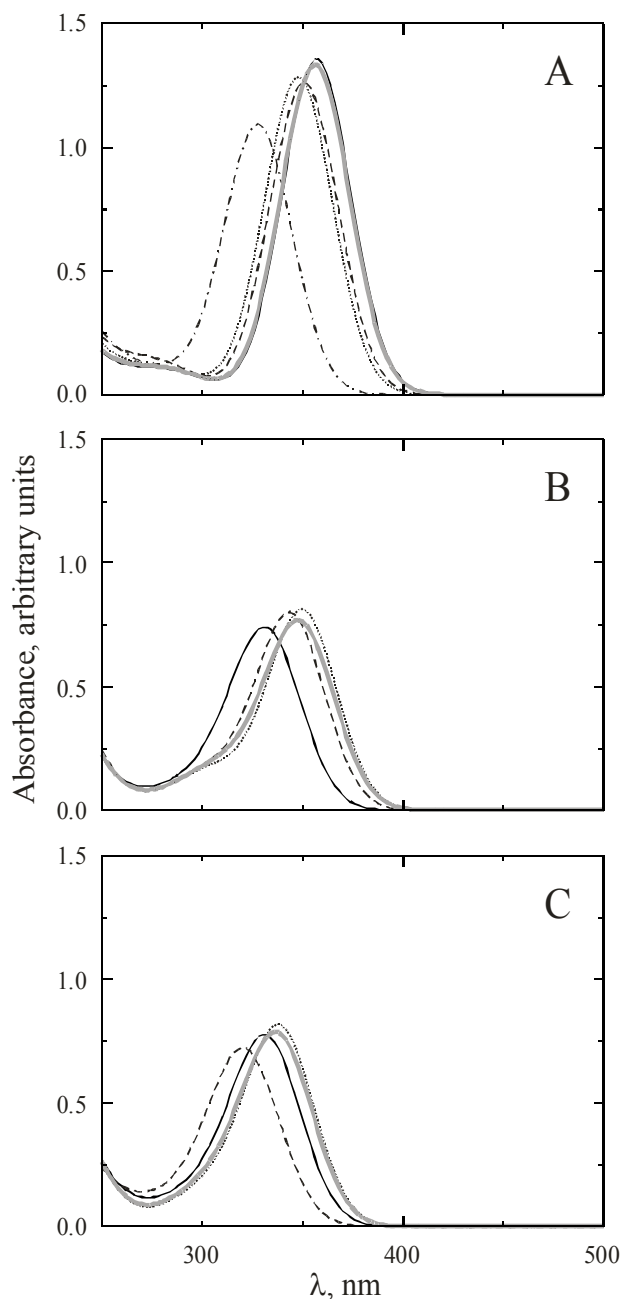


Figure 17. Computed [TD-DFT, PBE0 / 6-311++G(2d,2p) / PCM // PBE0 / 6-31+G(d,p) / PCM] UV-visible spectra of DHI dimers. Panel A, dimer **2**: full line, *anti*; dashed line, *syn*; dotted line, *anti* structure constrained to an inter-ring dihedral of 155°; dot-dashed line, *anti* structure constrained to an inter-ring dihedral of 130°; thick gray line, Boltzmann-weighted sum of *anti* and *syn* spectra. Panel B, dimer **3**: full line, *anti*; dashed line, *anti* (OH *syn*); dotted line, *syn* (OH *syn*); thick gray line, Boltzmann-weighted sum of the individual spectra. Panel C, dimer **4**: full line, *anti*; dashed line, *anti* (OH *syn*); dotted line, *syn*; thick gray line, Boltzmann-weighted sum of the individual spectra.

The trimers investigated in this study include **6** and **7**, which were obtained as the acetyl derivatives by oxidation of **1** according to a previous procedure²⁶ and were deprotected as above. From the structural viewpoint, **6** and **7** can be viewed as arising from dimer **3** via a 2,4'- or a 2,7'-linkage with an additional indole unit, so that they differ only by the mode of coupling of one terminal unit. Tetramer **8** was the sole tetramer available for this study. The UV spectra of the trimers **6** and **7** and of tetramer **8** are shown in **Figure 18**.

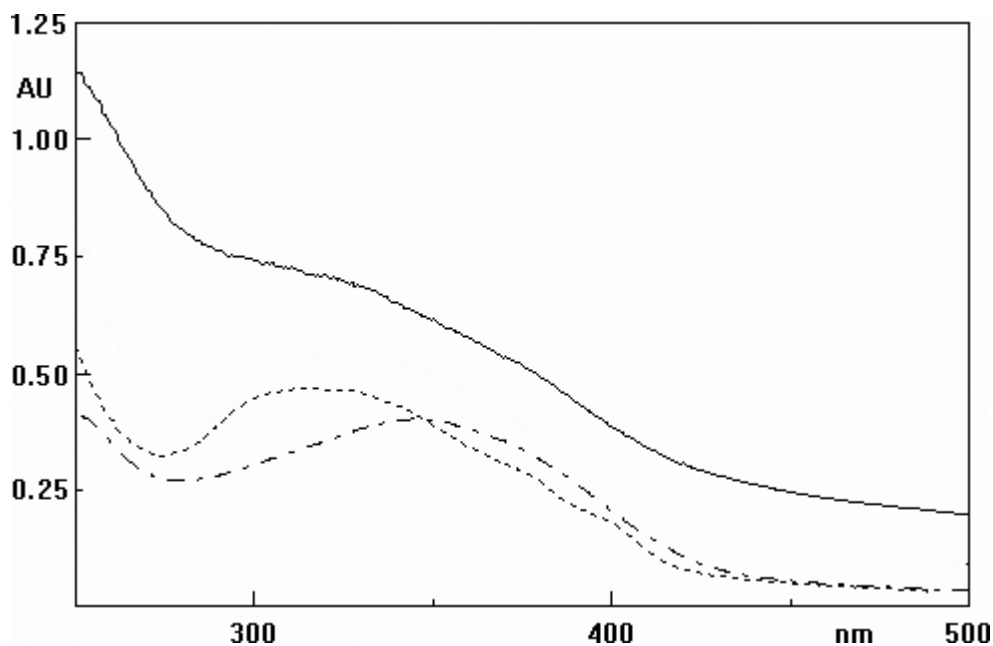


Figure 18. UV absorption spectra of 2.5×10^{-5} M trimers **6** and **7** and tetramer **8** in aqueous phosphate buffer, pH 7.0. **6**, dotted line; **7**, dot-dashed line; **8**, full line.

It is noted that the chromophores of the trimers differ appreciably despite rather similar structures with positional isomerism at one unit. Quite unexpectedly, **7** absorbed at longer wavelengths (maximum at 347 nm) relative to **6** (λ_{\max} 305 nm with shoulder

around 335 nm). Again, a similar trend can be observed for the acetylated derivatives: acetylated **7** displays a maximum at 342 nm whereas acetylated **6** shows a rather flat absorption band with broad maxima at 310 and 330 nm.

Interestingly, tetramer **8** exhibited an almost featureless chromophore extending over the entire UV range with a tail in the visible, while the spectrum of the acetylated derivative was characterized by a broad band centered around 315 nm with shoulder at 340 nm.⁵⁸ The absorption properties of trimers **6** and **7** were then investigated at the TD-DFT level. The large molecular size of the trimers, combined with the sizeable number of variable dihedrals, would make a systematic conformational search like that carried out for the dimers extremely demanding in terms of computational resources. Therefore, DFT optimizations were performed for a subset of starting structures which, based on a preliminary visual exploration, could be energetically favored, e.g. because of inter-ring hydrogen bonding. As a matter of fact, the first and the third indole units are always rather distant from each other, and their interaction is expected to be small: therefore, preliminary criteria to score the conformations of **6** can be deduced in a rather straightforward way from the results of the conformational analysis of dimer **3**, discussed above, while for trimer **7** the conformational preferences of both dimers **3** and **4** must be taken into account. **Table 2** lists the conformers identified for the two trimers, while UV spectra of the most significant conformers are displayed in **Figure 19** (as before, a Lorentzian line-broadening of 20 nm was imposed).

Table 2: Geometrical, energetic and spectroscopic features of the significant conformers of trimers **5** and **6**, computed at the PBE0 level in aqueous solution.

Conformer	Inter-ring dihedrals, degrees	Relative energy, ^a kcal mol ⁻¹	Relative energy, ^b kcal mol ⁻¹	λ ,nm (Oscillator strength)	Apparent λ_{max} , ^c nm
6^d					
+anti, -anti	136, -136	3.6	-	-	-
+anti, +anti	135, 136	3.0	-	-	-
+anti, -syn (OH syn) ^e	136, -24	1.6	1.2	376.0 (0.74), 340.6 (0.32), 316.8 (0.11), 311.6 (0.23)	374, 318
+anti,+syn (OH syn) ^e	136, 22	2.0	1.6	376.8 (0.73), 341.2 (0.32), 317.1 (0.11), 312.6 (0.23)	374, 317
-syn (OH syn), +anti ^f	-25, 136	1.5	1.1	372.4 (0.79), 341.2 (0.31), 319.5 (0.09), 309.5 (0.07), 306.3 (0.19)	370,320 (sh)
-syn (OH syn), -anti ^f	-24, -136	1.6	1.3	373.5 (0.79), 341.1 (0.30), 320.0 (0.09), 310.1 (0.09), 307.3 (0.18)	371, 316
-syn (OH syn), +syn (OH syn) ^{e,f}	-24, 24	0.2	0.2	390.3 (0.72), 350.6 (0.36), 319.5 (0.09), 315.5 (0.33), 311.0 (0.06)	389, 317
-syn (OH syn), -syn (OH syn) ^{e,f}	-25, -24	0.0 ^g	0.0 ^h	389.4 (0.72), 350.5 (0.36), 319.4 (0.11), 314.9 (0.31), 310.9 (0.06)	388, 316
7ⁱ					
+anti, -anti	136, -144	2.9	-	-	-
+anti, -syn	135,-27	1.5	1.1	365.7 (0.77), 337.4 (0.26), 316.0 (0.13), 305.0 (0.18)	362, 308
+anti, +syn	136, 27	2.3	1.9	366.3 (0.76), 337.9 (0.26), 316.1 (0.13), 305.9 (0.18)	363, 308
-syn (OH syn), +anti ^f	-24, 143	1.0	0.9	376.8 (0.78), 342.2 (0.32), 316.4 (0.09), 309.22 (0.13), 307.0	374, 311

- <i>syn</i> (OH <i>syn</i>), + <i>anti</i> (OH <i>syn</i>) ^{e,f}	-25, 133	1.7	1.3	(0.22) 367.6 (0.75), 336.5 (0.33), 317.3 (0.08), 309.1 (0.06), 303.2 (0.22)	364, 313 (sh)
- <i>syn</i> (OH <i>syn</i>), - <i>anti</i> ^f	-24, -142	1.2	1.1	375.9 (0.78), 341.0 (0.32), 315.9 (0.08), 309.4 (0.15), 307.0 (0.20)	374, 312
- <i>syn</i> (OH <i>syn</i>), + <i>syn</i> ^f	-24, 28	0.5	0.5	382.0 (0.75), 346.4 (0.32), 318.8 (0.11), 311.9 (0.17), 309.4 (0.16)	380, 312
- <i>syn</i> (OH <i>syn</i>), - <i>syn</i> ^f	-25, -28	0.0 ^j	0.0 ^k	380.9 (0.76), 346.5 (0.32), 318.7 (0.12), 311.3 (0.10), 308.6 (0.20)	378, 311

[a] PBE0 / 6-31+G(d,p) / PCM. [b] PBE0 / 6-311+G(2d,2p) / PCM // PBE0 / 6-31+G(d,p) / PCM.

[c] Maxima of a simulated spectrum with a Lorentzian line-broadening of 20 nm.
[d] Reference dihedrals N-C2-C4'-C5' and N'-C2'-C4''-C5''. [e] Orientation of the phenolic hydroxyl groups on the third unit *syn* with respect to the indole nitrogen of the same ring.
[f] Orientation of the phenolic hydroxyl groups on the second unit *syn* with respect to the indole nitrogen of the same ring. [g] -1538.854019 hartree. [h] -1539.211479 hartree.
[i] Reference dihedrals N-C2-C4'-C5' and N'-C2'-C7''-C6''. [j] -1538.852378 hartree. [k] -1539.210035 hartree.

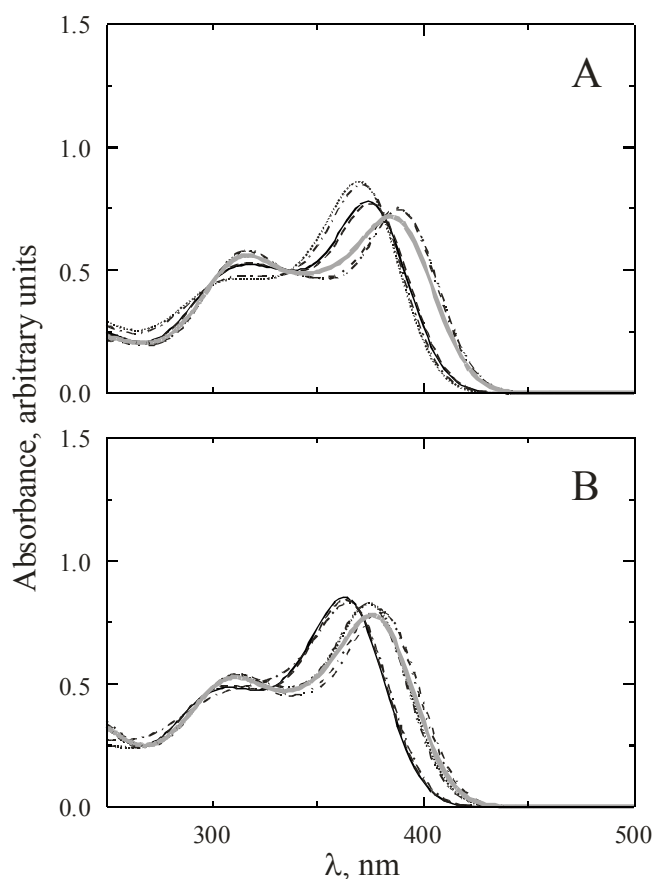


Figure 19. Computed [TD-DFT, PBE0 / 6-311++G(2d,2p) / PCM // PBE0 / 6-31+G(d,p) / PCM] UV-visible spectra of DHI trimers. Panel A, dimer **5**: full line, *+anti*, *-syn* (OH *syn*); dashed line, *+anti*, *+syn* (OH *syn*); dotted line, *-syn* (OH *syn*), *+anti*; dot-dashed line, *-syn* (OH *syn*), *-anti*; double-dot-dashed line, *-syn* (OH *syn*), *+syn* (OH *syn*); dot-double-dashed line, *-syn* (OH *syn*), *-syn* (OH *syn*); thick gray line, Boltzmann-weighted sum of the individual spectra. Panel B, trimer **6**: full line, *+anti*, *-syn*; dashed line, *+anti*, *+syn*; dotted line, *-syn* (OH *syn*), *+anti*; dot-dashed line, *-syn* (OH *syn*), *+anti* (OH *syn*); double-dot-dashed line, *-syn* (OH *syn*), *-anti*; dot-double-dashed line, *-syn* (OH *syn*), *+syn*; double-dot-double-dashed line, *-syn* (OH *syn*), *-syn*; thick gray line, Boltzmann-weighted sum of the individual spectra.

Inspection of simulated absorption spectra of **6** and **7** indicates in all cases two main bands around 310-320 and 360-390 nm. Depending on the specific conformation, the computed wavelengths display appreciable changes: in particular, the long wavelength band spans a range of about 20 nm. However, these conformational effects are comparable to those observed for some of the dimers. A significant difference with respect to the dimers is the presence of a large number of conformers with similar stabilities. Thus, the experimentally measured spectrum should reflect an overlap of all individual spectra, with comparable statistical weights. In other words, the conformational inhomogeneity of the sample is probably an important factor in determining the broader lineshapes of the experimental spectra of trimers with respect to those of the dimers.

A second factor which can play a role in this sense is represented by a more complex series of electronic transitions, which partly overlap to produce the overall bands. Thus, for all conformers of trimer **6** the long wavelength band is mostly due to a HOMO \rightarrow LUMO transition (ranging from 390 to 372 nm), but unresolved contributions from a HOMO-1 \rightarrow LUMO transition, at 351-341 nm, are also present, followed closely by other, essentially HOMO-2 \rightarrow LUMO and HOMO \rightarrow LUMO+1 transitions.

The situation is similar for **7**: the HOMO \rightarrow LUMO transition (ranging from 382 to 366 nm) is the main component of the long wavelength band, and overlaps to the HOMO-1 \rightarrow LUMO transition (346-336 nm); HOMO-2 \rightarrow LUMO and HOMO \rightarrow LUMO+1 excitations are also located above 300 nm.

In the case of the trimers, the comparison with experiment is less satisfactory than for the dimers, as it would appear that the computed maxima lie at significantly higher wavelengths with respect to the experimental spectra. However, it is also conceivable that the computed oscillator strengths may be slightly inaccurate: this would produce little change in the dimer spectra (**Figure 17**), but would impact significantly on the appearance of those of the trimers (**Figure 19**).

Moreover, some of the electronic transitions that underlie the trimer spectra feature a significant charge-transfer character, which may imply a distinctly less accurate description at the DFT level. For each trimer, the character of a given transition depends on the specific conformer: in particular, the HOMO-1 \rightarrow LUMO transition of

has strong charge-transfer character for the *+anti*, *-syn* (OH *syn*) and *+anti*, *+syn* (OH *syn*) conformers of **6**, and for the *+anti*, *-syn* and *+anti*, *+syn* conformers of **7**, i.e., for those structures where the junction between the first and the second indolic ring is *anti*. In these cases, the HOMO-1 is mostly located on the first and part of the second indolic ring, while HOMO and LUMO have little density on the first unit. Conversely, in those structures which adopt a *syn* orientation at this junction the predominant spatial localization of HOMO and HOMO-1 is inverted, and the charge-transfer transition becomes HOMO \rightarrow LUMO. Evidently, the overall effect of an hypothetical inaccuracy of oscillator strengths would be rather complex to predict. However, it is noteworthy that the ratio of computed oscillator strengths between the first and the second lowest energy transitions seems strongly affected by environmental effects: for example, for the *-syn* (OH *syn*), *+syn* (OH *syn*) conformer of **6** the ratio obtained with PCM is 2.0, but drops to 1.2 in a vacuum TD-DFT computation performed at the same molecular geometry.

Tetramer **8** was too demanding for DFT calculations and was not pursued further.

CONCLUSIONS

In this chapter I have reported the results of an integrated experimental and computational investigation on the absorption properties of dimers, trimers and a tetramer of **1** to gain some insight into the effects of bonding mode and increasing molecular size. Three key points emerged from this study.

1) No regular and predictable bathochromic shift occurs with increasing chain length. This is unusual in the field of aromatic π -conjugated oligomers, such as the phenyl oligomers⁷⁸ and is a consequence of the peculiar mode of coupling of the indole units connecting pyrrole-benzene moieties in a non-repetitive fashion incompatible with linear or rod-shaped oligomeric structures. In tetramer **8**, for example, the sterically congested 2,3-disubstituted moiety would force adjacent units out of coplanarity, thus limiting effective π -electron delocalization to lengths less than the molecular length.

2) A marked broadening of the absorption bands occurs when going from the monomer to the tetramer structure. This trend can be deduced from comparative inspection of the spectra in **Figures 17** and **19** and is even apparent in the more clearly shaped spectra of the acetylated derivatives. To better illustrate this trend, the acetylated monomer–dimer–trimer–tetramer series, which is characterized by a prevalent 2,4' mode of coupling, is shown in **Figure 20**.

This effect requires further investigation, especially when additional tetramer structures are available. The computational approach we adopted concentrates on the vertical excitation energy, and the vibrational structure of the absorption bands is neglected.^{79,80} Changes in the vibrational structure may in principle contribute to the observed dependence of bandwidth on oligomerization degree. However, as hinted before, it is probable that band broadening reflects mostly the presence of increasingly complex mixtures of conformers, whose chromophoric features are in turn modulated by the variable degree of conjugation; further, each conformation of the trimers (and presumably of the higher oligomers as well) displays an articulate array of low-energy transitions, which overlap to create broad absorption bands.

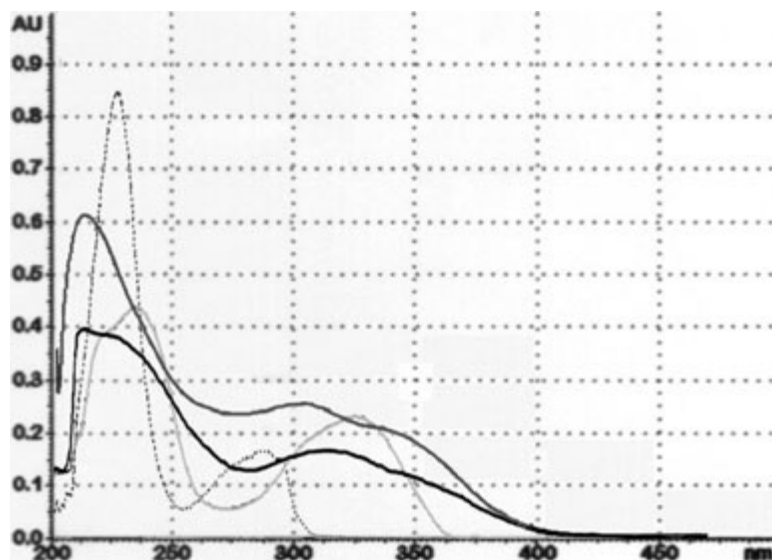


Figure 20. UV absorption spectra of acetylated **1** (dotted line), **3** (light grey line), **6** (dark grey line) and **8** (black line). Spectra were recorded in methanol as the solvent. Sample concentration was ca. 1×10^{-5} M.

3) The mode of coupling of the monomer units is a critical structural parameter governing the absorption properties of indole oligomers. This is perhaps the most significant and relevant result of this study which can be fully appreciated when considering the dramatic impact it may have on the degree of torsional freedom between the units and, hence, on the accessibility of fully planar conformations, efficient electron delocalization and, at the secondary level, π -stacking interactions. Based on the present and previous data, it appears that the indole bonding mode may affect the absorption properties of the oligomers both in the reduced and oxidized quinonoid forms.⁵⁹ The emerging implication is that, in addition to chain length and redox state, the mode of coupling may be another key contributor to the variety of chemically distinct chromophoric species supposedly responsible for the broad featureless spectrum of eumelanin. The effects caused by positional isomerism are complex, in some instances they may even exceed those due to chain length, and seem at present to escape rationalization.

In view of the foregoing, one could note that, apart from the pulse radiolysis results of transient species presented recently,⁵⁹ there does not appear to be any concrete

experimental verification of the existence of stable visible light-absorbing chromophores derived from oligomers of **1** in the reduced 5,6-dihydroxyindole form, however extended the oligomer size may be. In fact, the key question of why eumelanin is black can only be addressed in the context of the multi-chromophoric heterogeneous ensemble model by considering supramolecular aggregates in which oligomeric species at variable or mixed levels of oxidation are stabilized in the solid state. In other words, it is difficult to obtain a black chromophore by mixing oligomers of different chain lengths in their reduced form.

Visible light absorption and significantly redshifted HOMO-LUMO gaps can be achieved only by oxidizing oligomeric scaffolds. In this regard, the residual absorption tail of tetramer **8** in the visible region (**Figure 20**) is probably indicative of adventitious oxidation during rapid recording of the spectrum, reinforcing the notion that oligomer oxidation is a necessary requisite for visible absorption and significant narrowing of HOMO-LUMO gaps. Oxidized quinonoid oligomers, however, have never been identified as stable entities in solution as they tend to evolve through chemical coupling and/or supramolecular interactions leading to black insoluble materials which apparently owe their coloration to phenomena belonging to the realm of solid state physics.

In conclusion, despite some persisting uncertainties and the lack of a broad repertoire of oligomeric structures, the results of this study clearly show that a correct mode of coupling of monomer indole units derived from experimental evidence is a critical and essential prerequisite if feasible and reliable structural models are to be constructed for interpretative and predictive purposes, while arbitrary bonding may lead to misleading and unwarranted conclusions.

CHAPTER III

Reaction behavior of 5,6-dihydroxyindole (**1**) in acidic medium

The chemistry of indolic substrates in the presence of acids has been the subject of much interest since a long time, and is known to give rise to a variety of dimerization and trimerization products with partial oxidation and/or ring fission.^{81,82} Typically, dimers featuring a 2,3'-biindole mode of coupling and trimers with a 2-(2-aminophenyl)-1-bis(indol-3-yl)ethane ring system are obtained. Moreover, the unexpectedly facile cyclotrimerization of **1** and related hydroxyindole derivatives when oxidized with persulfate in acidic media has also been reported.⁶² In all these reactions, the starting event is protonation of the indole ring at the basic 3-position to produce an electrophilic imine-like species which then undergoes attack by the nucleophilic positions of the unprotonated indole. In the frame of a program aimed at designing novel DHI-based functional materials,^{14b} it was therefore of interest to explore in a systematic investigation the reaction behavior of **1** when left to stand in an aqueous medium under mildly acidic conditions. Main aims of the study were a detailed understanding of the chemistry of the 5,6-dihydroxyindole system when exposed to acids and an assessment of the scope of this reaction for preparative purposes.

In this chapter I report the unexpected results of this study leading to the isolation of a rearranged trimer featuring an unusual 2-benzyl-3-indolylquinoline skeleton. In addition, I describe the selective binding properties of the acetylated trimer toward fluoride anions, as revealed by the marked F⁻-induced changes in the absorption and fluorescence spectra.

RESULTS AND DISCUSSIONS

The reactivity of **1** in phosphate buffer at pH 2 was investigated. The course of the reaction was monitored by LC/MS (0.2% formic acid, solvent A; acetonitrile, solvent B; 5% B, 0–10 min; from 5 to 30% B, 10–25 min; from 30 to 70% B, 25–50 min); at a time of 3 h the mixture was characterized by the presence of two main products eluted at 11.1 and 16.7 min, with pseudomolecular peaks $[M+H]^+$ at m/z 299 and 448 respectively, indicative of the formation of a dimeric and a trimeric derivative of **1**.

After lyophilization of the residue and treatment with acetic anhydride/pyridine, TLC analysis showed the presence of two main products at R_f 0.39 and 0.15 (eluent $CHCl_3$: AcOet = 3:7).

The mass spectrum (ESI+) of the product at R_f 0.39 showed a pseudomolecular peak $[M+H]^+$ at m/z 509, indicative of a pentaacetylated dimeric structure.

The compound was therefore tentatively assigned the structure of the acetylated derivative of the dimer 5,6-dihydroxy-2-(5,6-dihydroxyindol-3-yl) indoline (**12**), previously obtained from **1** by oxidation with ammonium persulphate in 0.1 M phosphoric acid.⁶²

This structure was confirmed by a full one and two-dimensional NMR analysis (**Figure 21**). The 1H NMR spectrum showed only one signal typical of an NH proton (δ 8.39) and a doublet ($J = 9.6$ Hz) at δ 5.53, which correlated in the 1H , ^{13}C HSQC-DEPT spectrum with a signal at δ 57.8 and in the 1H , 1H COSY spectrum with a double doublet ($J = 16.0, 9.6$ Hz) at δ 3.53. The latter showed a correlation in the 1H , 1H COSY spectrum with a doublet ($J = 16.0$ Hz) at δ 2.58; also the protons at δ 3.53 and 2.58 correlated with the same signal at δ 36.9 in the 1H , ^{13}C HSQC -DEPT spectrum. These elements confirm the presence of a 5,6- dihydroxyindolic *N*-acetylated unit reduced at 2 and 3 positions and linked through the 2-position to the second indole unit.

The aromatic region of the 1H NMR spectrum was characterized by the presence of five signals, one at very low fields (δ 8.13), attributed to H-7 proton of the reduced indolic unit, probably deshielded because of a diamagnetic anisotropy effect exerted by the adjacent *N*-acetyl group. On the basis of the correlations observed in the 1H , ^{13}C HMBC spectrum, a signal at δ 6.78 was attributed to the H-4 proton of the reduced indolic unit, while the remaining 3 signals at δ 6.53, 7.15 and 7.18 were

assigned to the second indolic unit. Of these, the first correlated in ^1H , ^1H COSY spectrum with the signal of the NH proton at δ 8.39 and was therefore attributed to an H-2 type proton, while signals at δ 7.15 and 7.18, which showed a direct correlation with carbon signals at δ 111.9 and 106.1, were attributed to H-4 and H-7 type protons, respectively.

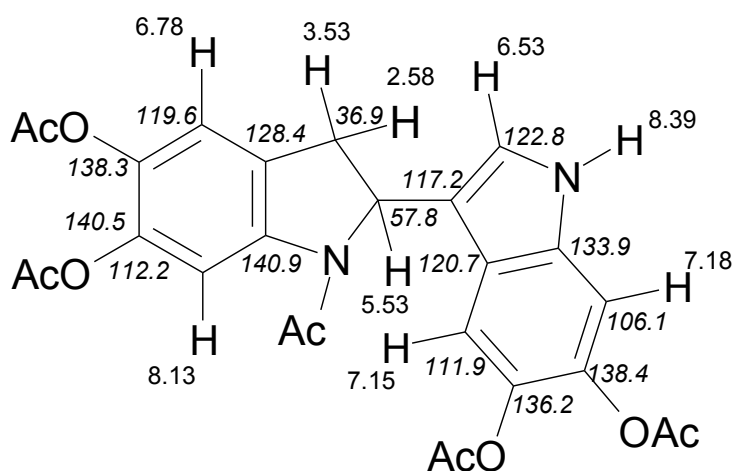
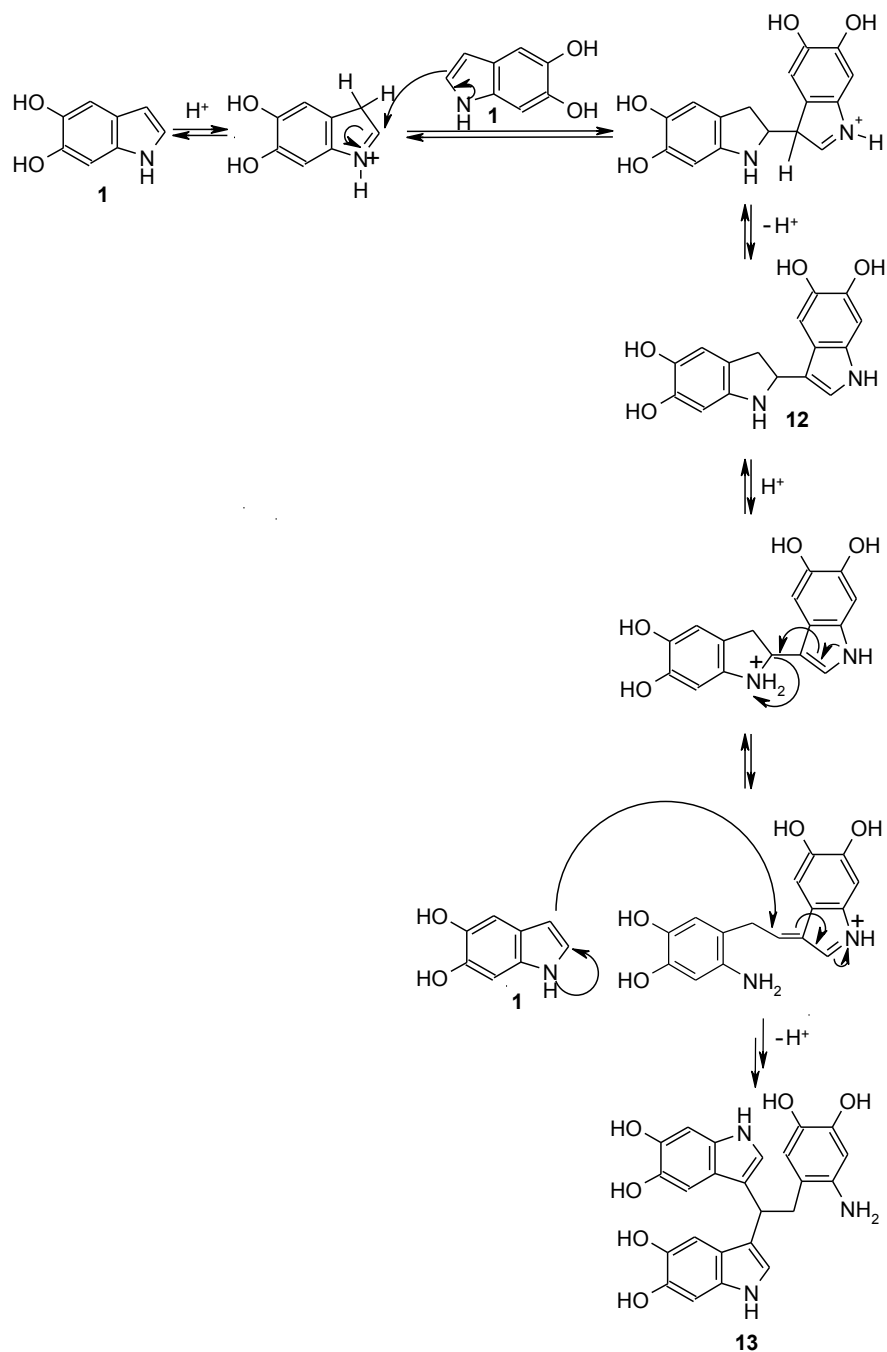


Figura 21. Structure of the acetylated derivative of **12** with proton (regular style) and carbon (italic style) resonances.

Product at R_f 0.15 presented in the ESI(+)-MS spectrum $[\text{M}+\text{H}]^+$ and $[\text{M}+\text{Na}]^+$ pseudomolecular peaks at m/z 742 and 764, respectively, indicative of a heptaacetylated trimeric structure, which is also characterized by the presence of a nitrogen functionality capable of acetylation. The ^1H NMR spectrum showed a triplet (1H) at δ 4.35 and a doublet (2H) at δ 3.15 in the aliphatic region, while in the aromatic region it was possible to distinguish two spin systems, one of which was characterized by signals integrating for 2H, and therefore hinted to a symmetrical structure. On this basis, and by comparison with data reported in the literature,⁶² the compound was assigned the structure of the acetylated derivative of 2-(2-amino-4,5-dihydroxyphenyl)-1,1-bis(5,6-dihydroxyindol-3-yl)ethane (**13**).

The formation of such products would proceed through the mechanism shown in **Scheme 5**, similar to that described above for the reaction of indolic systems at acid pH,⁶² which consists in the addition of an indolic unit through the 3 position to the 2 position of a second protonated indolic unit.



Scheme 5. Proposed formation mechanism of **12** and **13**.⁶²

In subsequent experiments further processes of conversion of compounds **12** and **13** in acidic conditions were examined. LC/MS analysis of the reaction mixture of **1** at pH 2 showed a progressive decrease of compounds with pseudomolecular peaks $[M+H]^+$ at m/z 299 and 448, accompanied by the formation of a product eluted at 23.6 min, characterized by a pseudomolecular peak $[M+H]^+$ at m/z 446, indicative of an oxidized trimeric derivative, which reached a maximum yield of formation at 24 h (**Figure 22**).

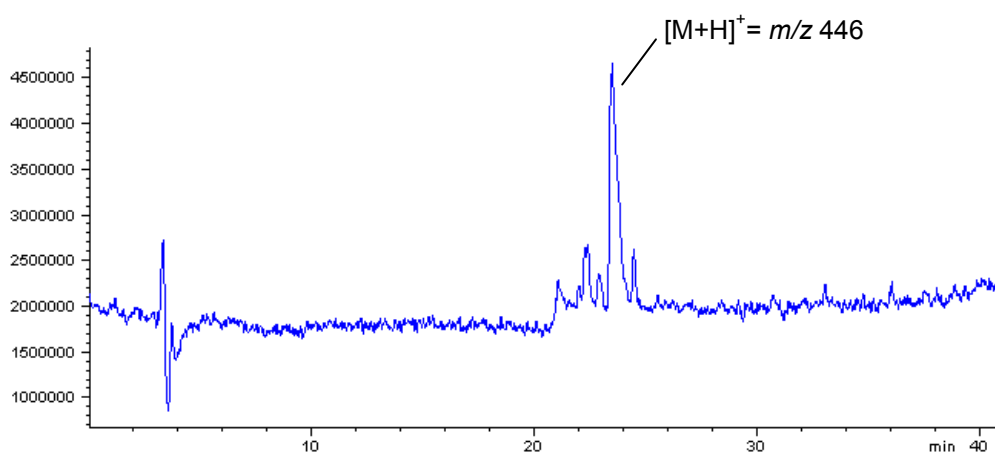


Figure 22. TIC of the reaction of **1** at pH 2 at 24 h.

This compound was obtained in 10% yield by a simple work-up procedure involving acetylation of the crude mixture followed by a chromatographic step, and was identified as 2-(2-acetamido-4,5-diacetoxybenzyl)-6,7-diacetoxy-3-(5,6-diacetoxyindol-3-yl)quinoline (**14b**) following complete spectral characterization.

The mass spectrum (ESI+) showed a pseudomolecular peak $[M+H]^+$ at m/z 740, indicative of a heptaacetylated trimer in an oxidation state higher than the acetylated derivative **13**. The compound showed absorption maxima in the UV-Vis spectrum at 276 and 330 nm in acetonitrile.

The ^1H NMR spectrum (**Figure 23**) was characterized by a singlet at δ 4.14 (2H), which correlated with a signal at δ 39.1 in the ^1H , ^{13}C HSQC-DEPT spectrum, indicating the probable presence of an open indolic unit.

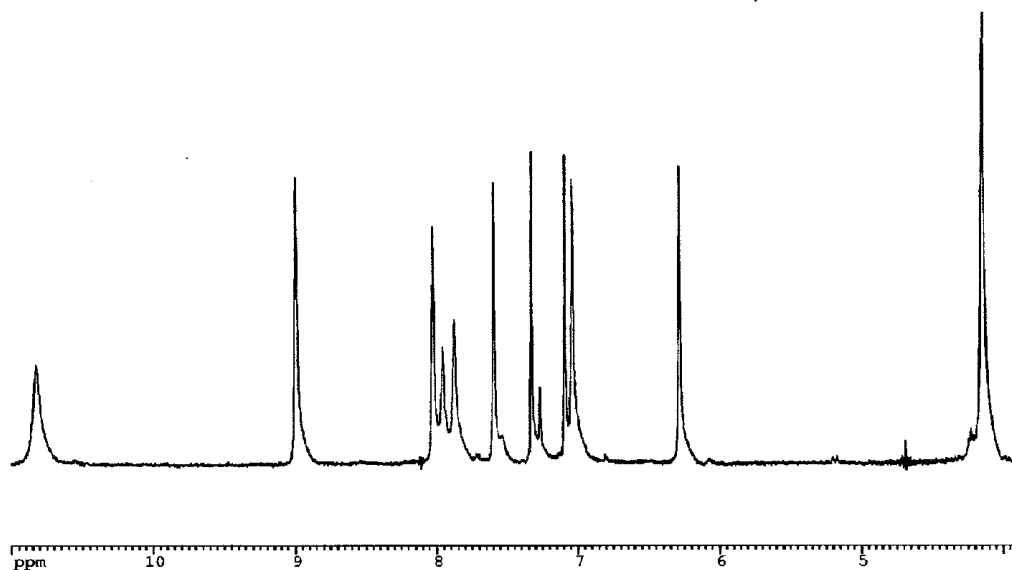


Figure 23. Selected region of ^1H NMR spectrum of **13b**.

The aromatic region of ^1H NMR spectrum showed eight signals; the singlets at δ 6.28 and 7.96, showing direct correlation with carbon signals at δ 124.8 and 117.3 respectively in the ^1H , ^{13}C HSQC-DEPT spectrum (**Figure 24**), were assigned to the 2-acetylamino-4,5-diacetoxybenzilyc unit deriving from opening of an indolic unit on the basis of correlations observed in the ^1H , ^{13}C HMBC spectrum (**Figure 25**). The signal at δ 7.04 was attributable to an indolic proton in 2-position, as correlated with a signal at δ 127.1 in the ^1H , ^{13}C HSQC-DEPT and with a signal at δ 8.99 assigned to the NH proton of the same indolic nucleus in ^1H , ^1H COSY spectrum (**Figure 26**).

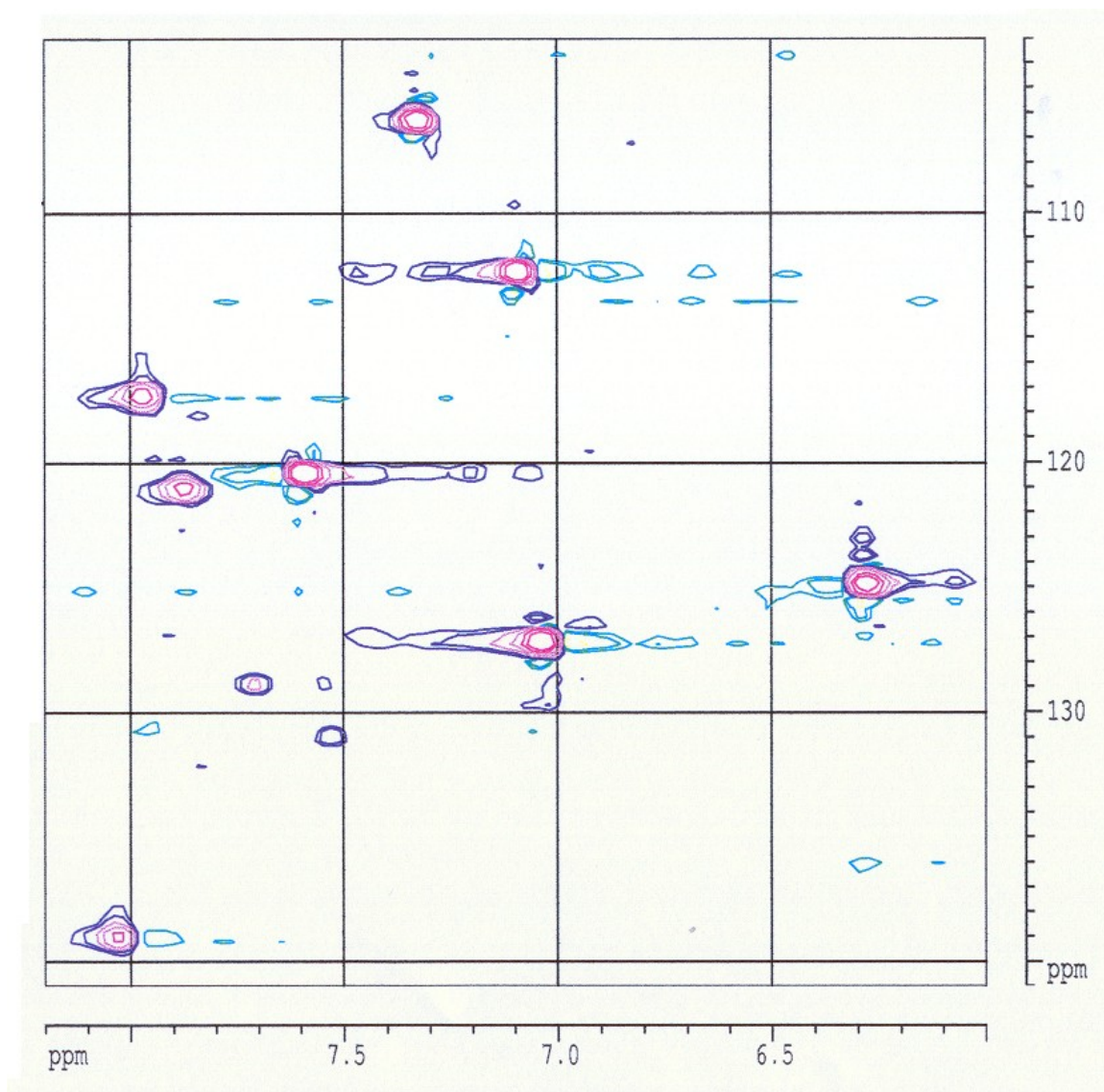


Figure 24: Selected region of ^1H , ^{13}C HSQC-DEPT of **14b**.

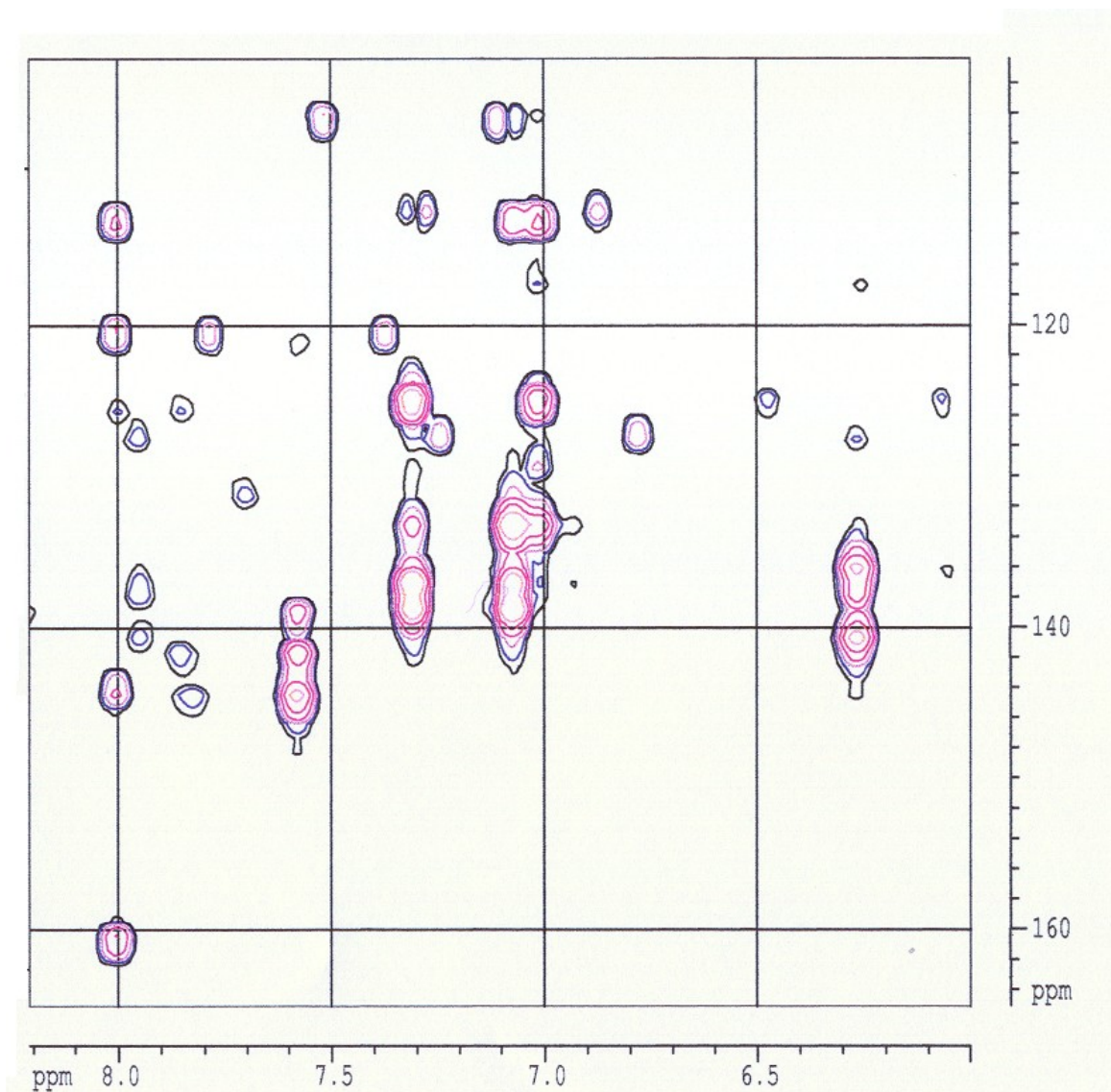


Figure 25. Selected region of ^1H , ^{13}C HMBC spectrum of **14b**.

The absence of other correlations in the ^1H , ^1H COSY spectrum for the signal at δ 7.04 suggested the lack of a proton in 2-position, indicating that the indolic unit in question had to be linked through 3 the position. Analysis of the ^1H , ^{13}C HSQC-DEPT, ^1H , ^{13}C HMBC and ROESY (**Figure 27**) spectra has allowed to assign to that unit also proton resonances at δ 7.09 (H-4 type proton, direct correlation with carbon signal at δ 112.3) and δ 7.32 (H-7 type proton, direct correlation with carbon signal at δ 106.2 and ROESY contact with the N-H proton at δ 8.99).

Signals attributable to the third unit were rather peculiar: a proton at δ 8.02, linked to a particularly deshielded carbon (δ 139.0) that correlates in the ^1H , ^{13}C HMBC spectrum with a quaternary carbon signal at δ 160.5, and two protons at δ 7.59 and 7.87 which showed a direct correlation with carbon signals at δ 120.4 and 120.9 respectively, values quite unusual for an indolic ring. Those factors, combined with the absence in the ^1H NMR spectrum of a signal attributable to a third NH proton, suggested the structure of the acetylated derivative of 2-(2-amino-4,5-dihydroxybenzyl)-6,7-dihydroxy-3-(5,6-dihydroxiindol-3-yl)quinoline (**14b**) for the compound at $R_f = 0.25$ (**Figure 28**). In agreement with the proposed structure, the signal at δ 2.8 attributed to the H-4 proton of the quinoline ring showed contacts in the ROESY spectrum with the H-5 proton at δ 7.59 and the H-4'' indolic ring proton at δ 7.09 while the signal of the benzylic protons at δ 4.14 correlated with the signal of the H-2 indolic ring proton at δ 7.04.

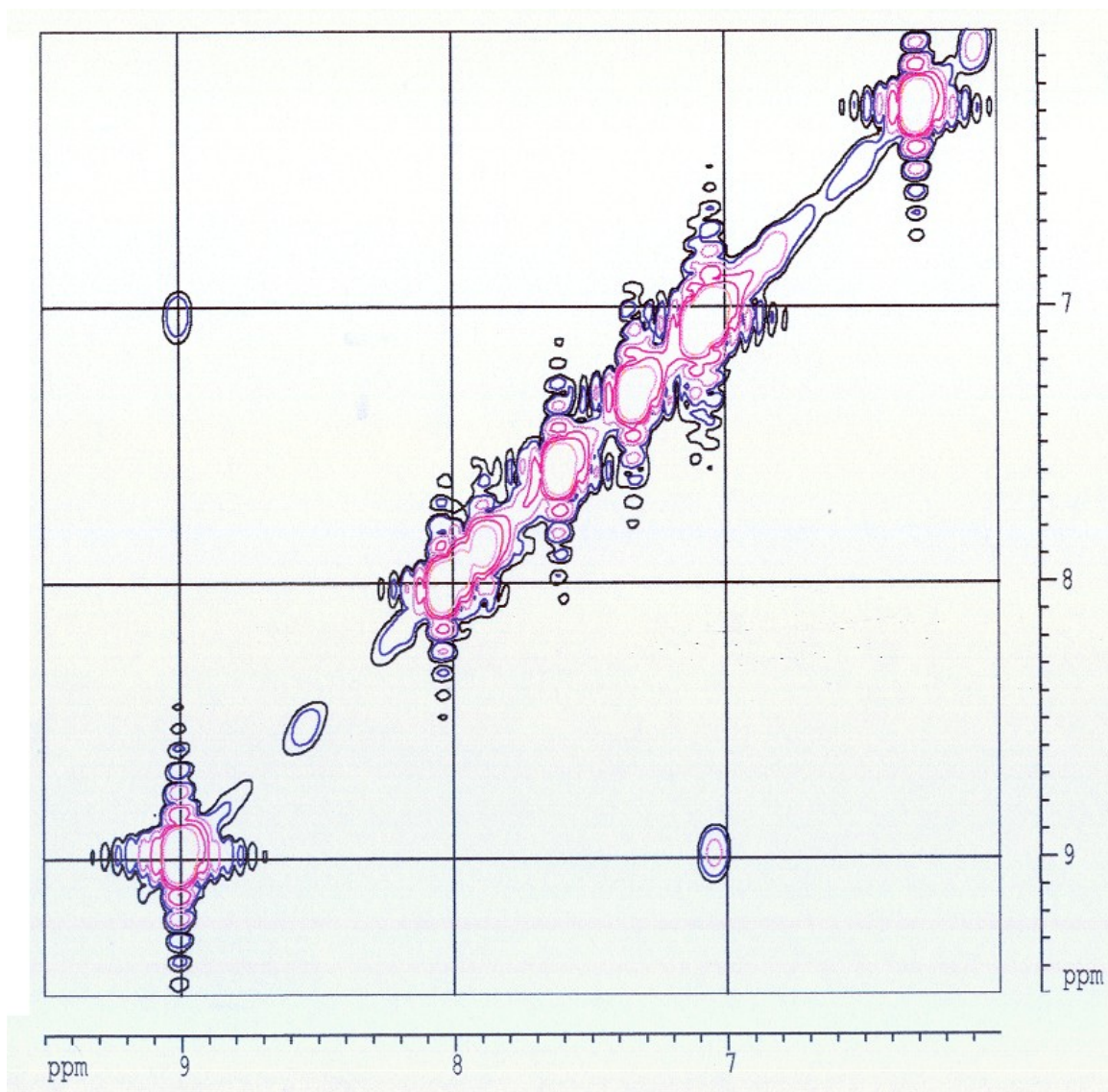


Figure 26. Selected region of ^1H , ^1H COSY spectrum of **14b**.

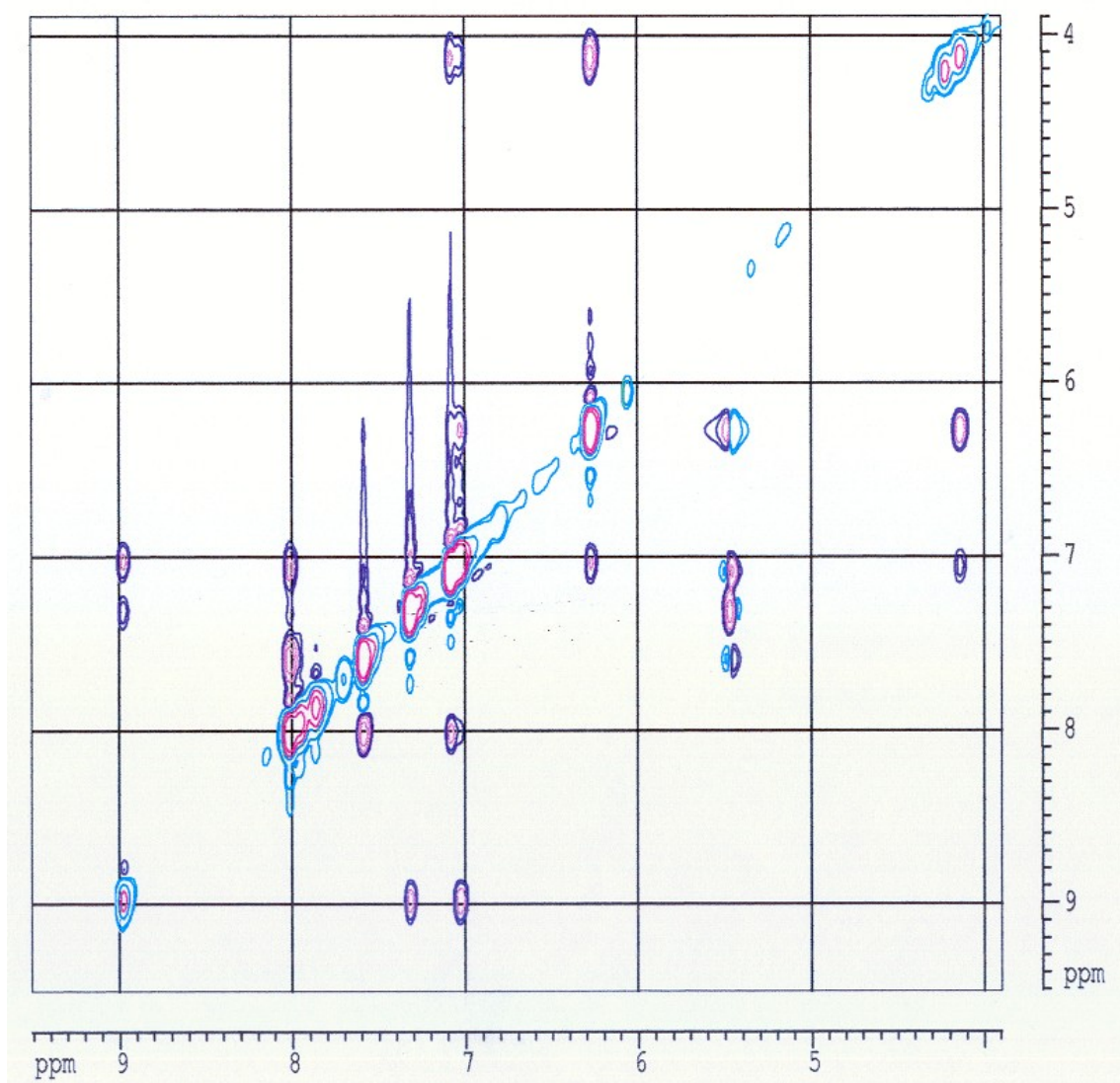


Figura 27. Selected region of ROESY spectrum of **14b**.

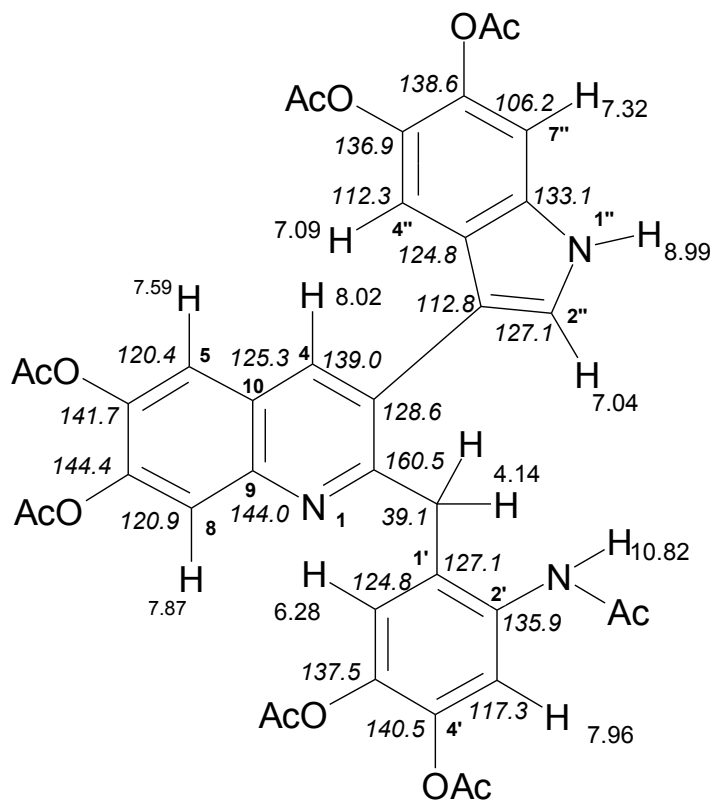
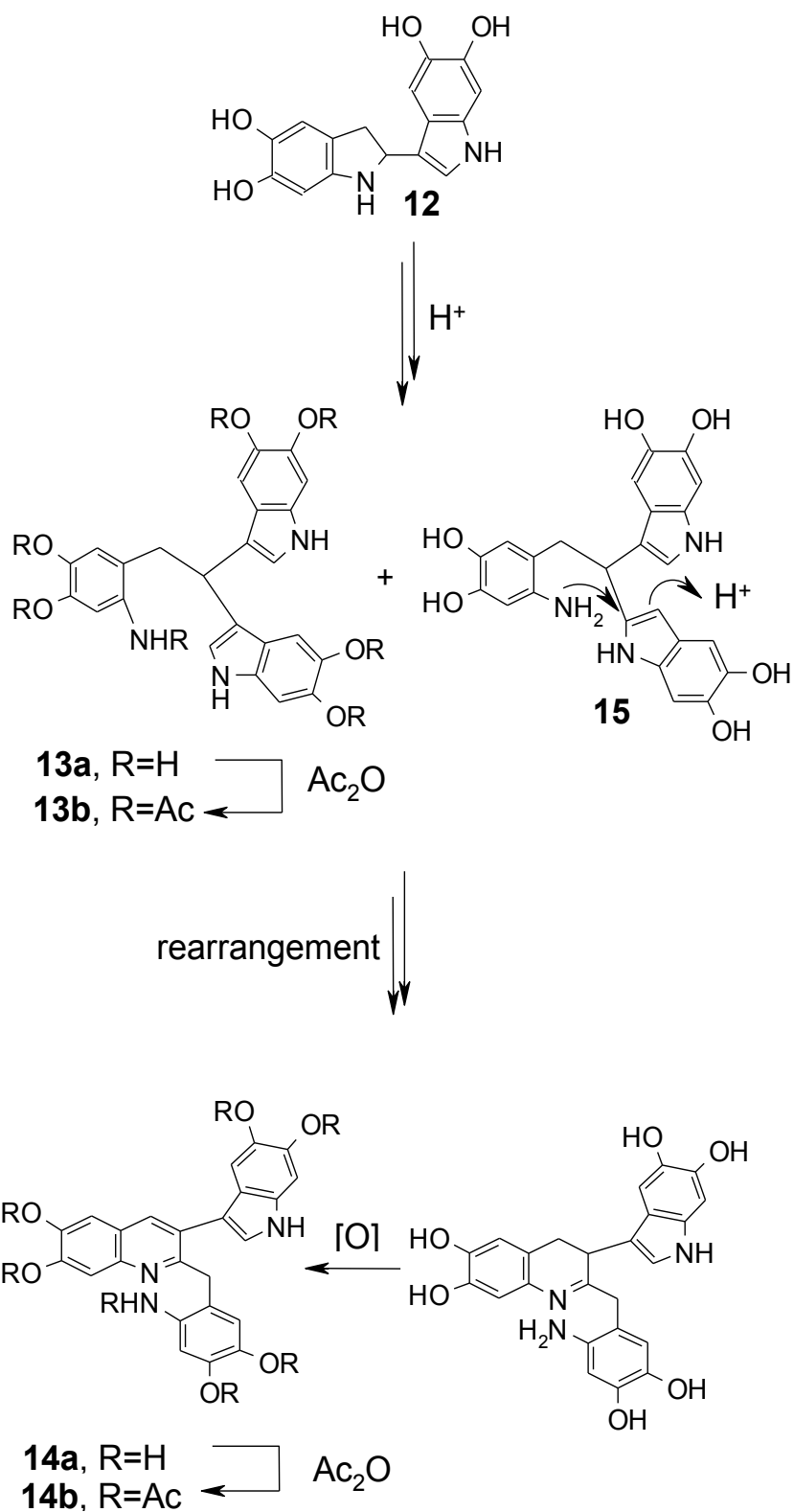


Figure 28. Structure of heptaacetyl derivative of 2-(2-amino-4,5-dihydroxybenzyl)-6,7-dihydroxy-3-(5,6-dihydroxyindol-3-yl)quinoline (**14b**) with proton (regular style) and carbon (italic style) resonances.

The facile formation of **14a** from **1** is therefore attributed to the specific reactivity of this indole via the 2-position,⁸³ steering in part the acid-promoted polymerization pathway through the usually less favorable 2-(2-amino-4,5-dihydroxyphenyl)-1-(5,6-dihydroxyindol-2-yl)-1-(5,6-dihydroxyindol-3-yl)ethane (**15**) (Scheme 6). Formation of the quinoline system of **14a** from **15** may proceed through a rearrangement step akin to that described for indole trimers in acidic media.⁸⁴



Scheme 6. Representative mechanism of formation of **14**.

A comparative study showed that none of the other indoles examined, i.e. indole, 5-hydroxyindole, 6-hydroxyindole, 5,6-dimethoxyindole, and 5,6-dihydroxy-*N*-methylindole, gives the corresponding 3-(indol-3-yl)quinoline trimer under the same conditions. Use of stronger acids, e.g., HCl, or organic acids, e.g., acetic acid, was not productive, furnishing invariably ill-defined mixtures.

The 2-(2-aminobenzyl)-3-(indol-3-yl)quinoline system featured by **14a** has previously been obtained only by harsh treatment of indole under Friedel–Crafts acylation conditions⁸⁵ or in the presence of *p*-toluenesulfonic acid followed by complex work-up, extraction, and chromatographic separation steps.⁸⁴

Given the structural characteristics of **14b** (an indolic unit linked to a quinoline unit), the properties of this compound as a sensor for the determination of F⁻ ions were evaluated.^{87c,90}

The absorption properties of **14b** are shown in **Figure 29**.

The compound exhibited a distinct maximum at 330 nm in CH₃CN. Upon the addition of increasing concentrations of F⁻ a yellow coloration developed, due to the formation of a chromophore absorbing at 414 nm. Examples of colorless-to-yellow color changes associated with F⁻ binding to an organic compound had already been reported in the literature.⁸⁶ No clear isosbestic point is apparent from data in **Figure 29**, which suggests that color development involves more complex equilibria than a simple 1:1 substrate–anion binding process.

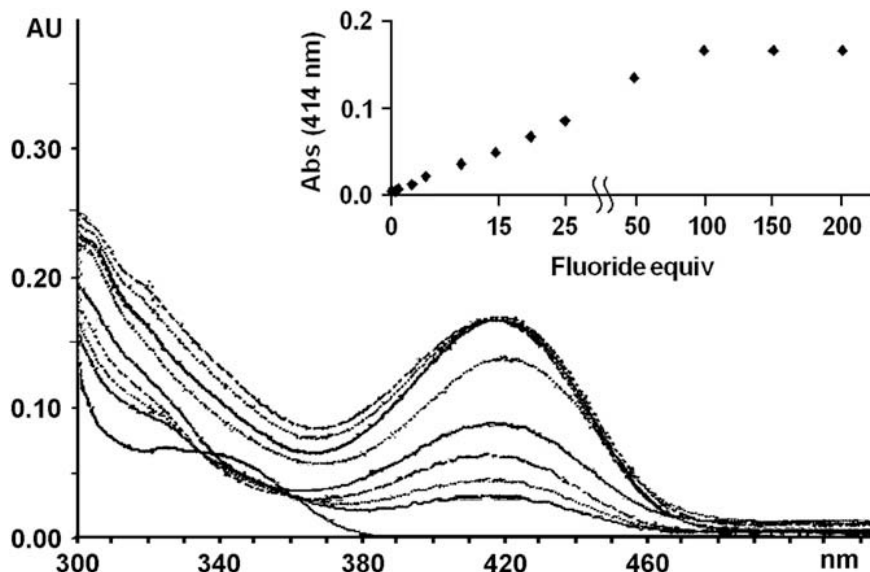


Figure 29. Changes in the UV-vis spectra of **14b** (1×10^{-5} M) in CH_3CN after addition of 0, 10, 15, 20, 25, 50, 100, 150, and 200 equiv of tetrabutylammonium fluoride (TBAF).

Inset: Absorbance at 414 nm versus equiv of F^- .

The acetylated derivative **14b** exhibited a remarkable fluorescence enhancement upon the addition of F^- (**Figure 30**). The fluorescence spectra of **14b** displayed important changes upon addition of up to 300 equiv F^- . In **Figure 31** the spectra of a 5×10^{-7} M solution of **14b** in acetonitrile are showed before and after the addition of 25 molar equivalents of F^- ions, for excitation wavelengths of 270 (plot A) or 414 nm (plot B), that is in correspondence with the absorption maxima developed following the addition of F^- . In both cases the development of a fluorophore at 489 nm is observed.

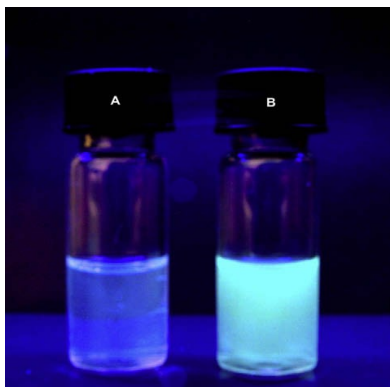


Figure 30. Fluorescence changes of **14b** (5×10^{-5} M) in CH_3CN upon addition of 25 equiv of TBAF. (A) no additive; (B) +TBAF (under a UV lamp at 366 nm).

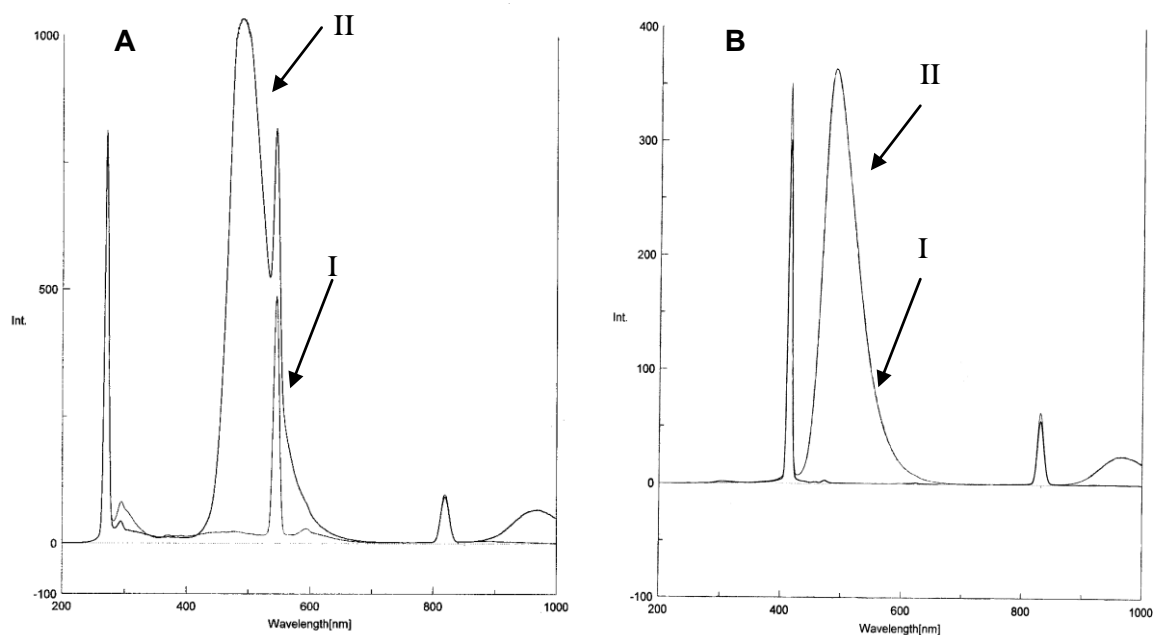


Figure 31. Fluorescence spectra of 5×10^{-5} M solution of **14b** in acetonitrile before (I) and after (II) addition of 25 molar equivalents of F^- ions: (A) excitation at 270 nm; (B) excitation at 414 nm. For recording the spectra the solutions were diluted 1:100.

The fluorescence response of **14b** (5×10^{-7} M) upon addition of up to 300 equiv F^- is shown in **Figure 32**. In the absence of F^- , fluorescence of the free compound was weak and barely detectable. Addition of the anion to the solution caused the emergence of a distinct emission band at 489 nm following excitation at either 270 or 414 nm.

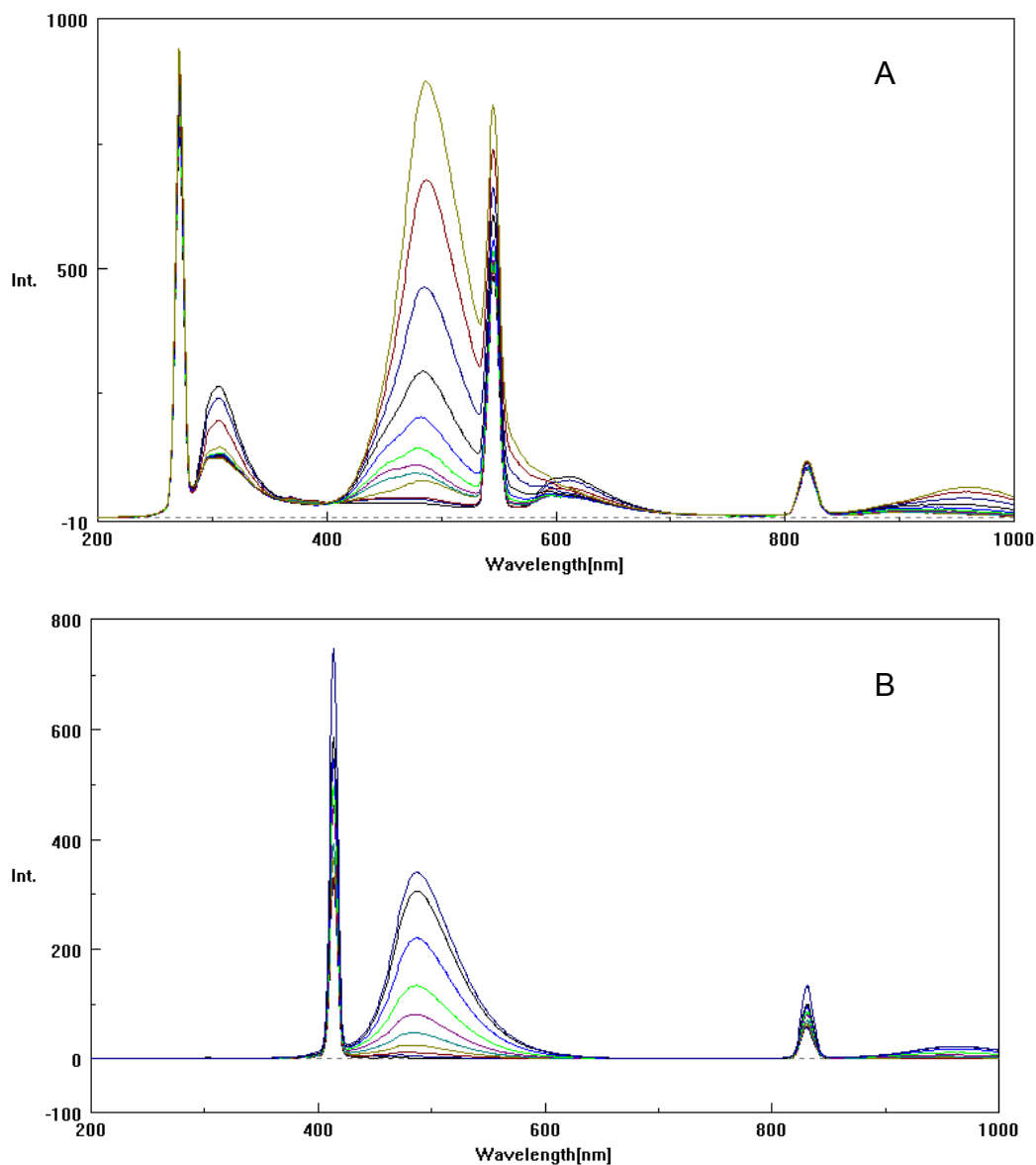


Figure 32. Changes in the fluorescence spectra of **14b** (5×10^{-7} M) in CH_3CN after addition of TBAF from 0 to 300 equiv.: (A) excitation wavelength 270 nm, (B) excitation wavelength 414 nm.

This effect is worthy of note since anion binding causes fluorescence quenching for most of the reported sensors,⁸⁷ with only a few exhibiting fluorescence enhancement.^{86c,88} The recognition process was selective for F⁻ since in the presence of other anions, including Cl⁻, Br⁻, I⁻, AcO⁻, NO₂⁻, HSO₄⁻, no significant changes in the fluorescence spectra were observed. Complete fluorescence quenching was noted however in the presence of water (>20%). The change of fluorescence intensity at 489 nm versus equivalents of F⁻ and the Job's plot from which the stoichiometry of the fluoride–**14b** interaction was determined to be 2:1 are shown in **Figure 33**.

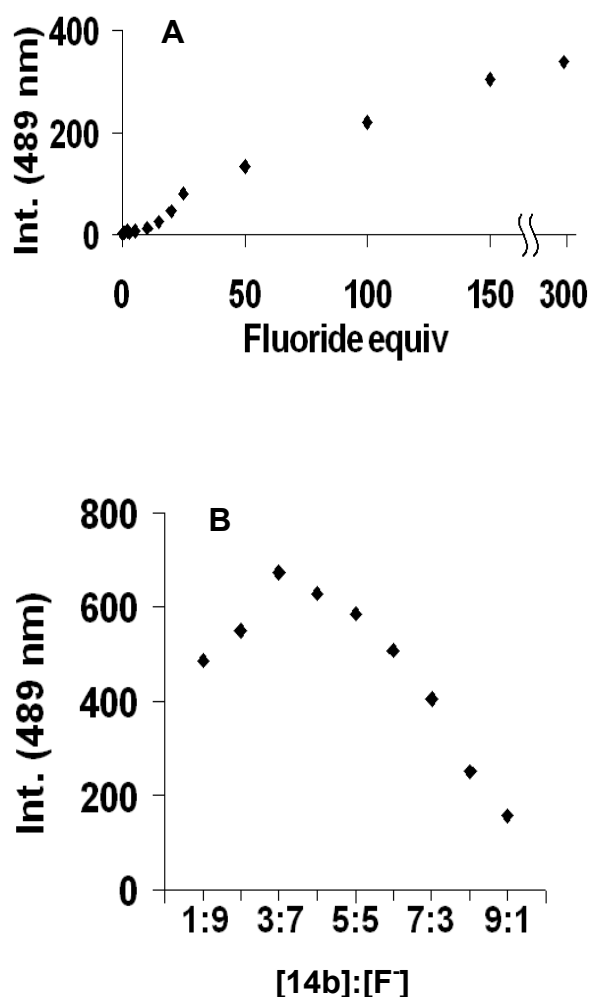


Figure 33. (A) Fluorescence intensity at 489 nm versus equiv of F⁻ and (B) Job's plot of **14b**–fluoride interaction in CH₃CN (total [**14b**]+[F⁻]=5×10⁻⁵ M)

In subsequent experiments, the effects of F⁻ binding on the parent 5,6-diacetoxyindole and the acetylated trimer **13b** were investigated. Trimer **13b** was a suitable model to identify the chromogenic and fluorogenic systems in **14b**, since it exhibited the diacetoxyindole and acetamido moieties placed at a comparable distance by a non-conjugating spacer chain replacing the rigid quinoline ring. Upon the addition of F⁻ neither diacetoxyindole nor **13b** developed significant fluorescence. This observation suggests that the quinoline ring is an essential constituent of the fluoride sensing fluorophore.

To gain a deeper insight into the mechanism of F⁻ coordination by **14b**, ¹H NMR titration experiments were carried out in DMSO-d₆. With 0.5 equiv F⁻, the indole NH proton signal at δ 11.6 (**Figure 34A**) disappeared (**Figure 34B**). A similar behavior has previously been reported for several systems containing NH protons, indicating interaction with F⁻ anions.^{86a,c,88a,89} Addition of further amounts of the anion caused disappearance of the amide NH proton signal at δ 9.81, accompanied by a slight upfield shift of the other proton signals (**Figure 34C**).^{88c,89,90} A visible fluorescence with concomitant color change was well apparent at this stage. No alteration of the signals due to the acetyl groups was observed, ruling out deacetylation during F⁻ coordination.

The ROESY spectrum of **14b** in the absence of F⁻ showed distinct cross peaks between: (a) the quinoline H-4 and the indole H-4 resonances; (b) the quinoline H-8 and the amide NH signals; and (c) the benzylic proton singlet and the indole H-2 proton doublet. These contacts suggested a preferential conformation with the indole NH group close to the benzylic methylene and the amide group facing the quinoline nitrogen, as previously described for related systems on the basis of X-ray analysis.⁸⁵ Interestingly, in the ROESY spectrum recorded after addition of 0.5 equiv of F⁻, at a stage when only the indole NH has disappeared, the cross peak between the amide NH and the quinoline H-8 signals was no longer detectable.

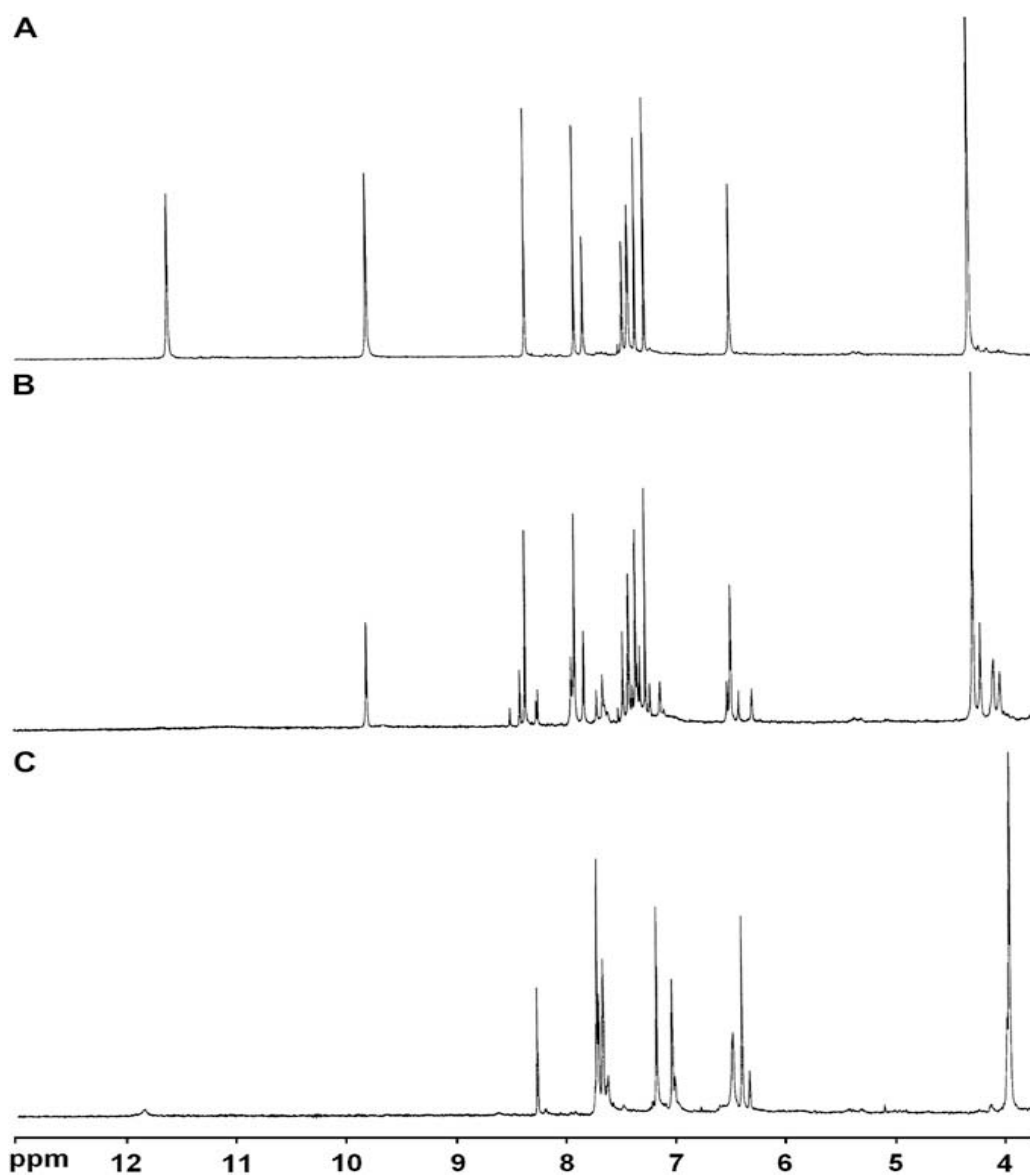
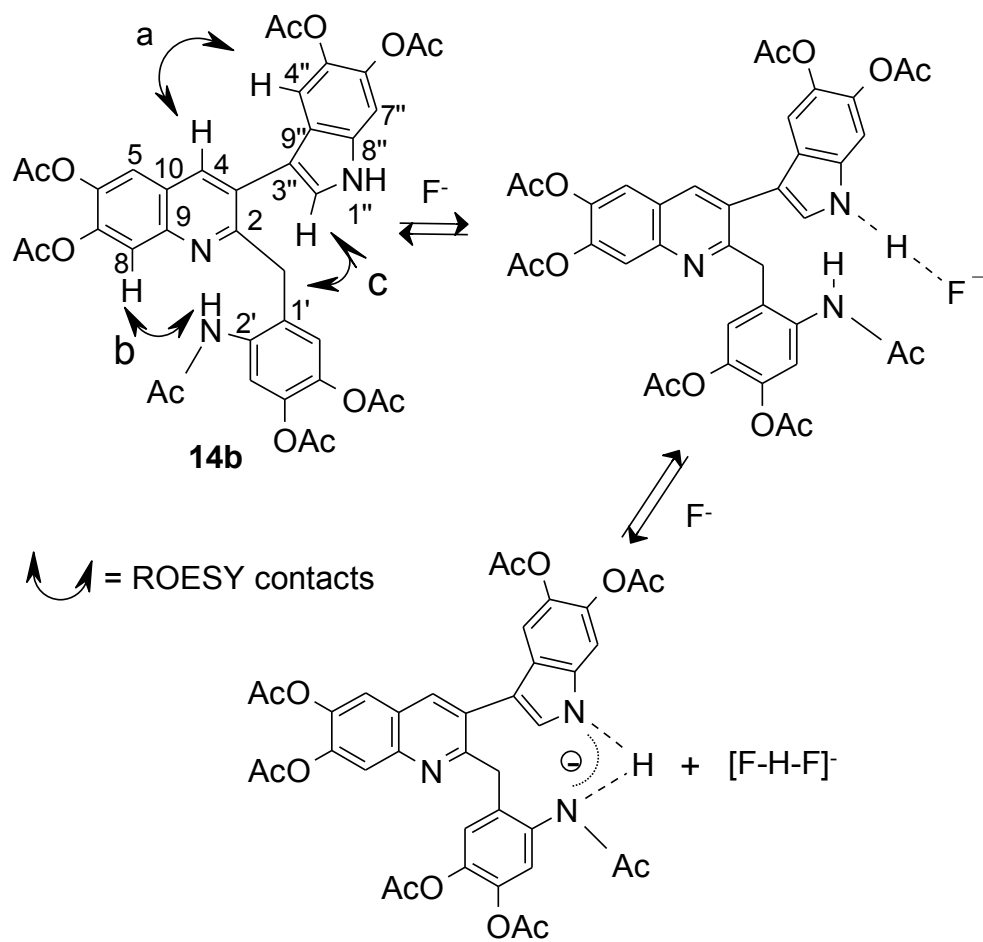


Figure 34. Partial ^1H NMR spectra of **14b** in DMSO-d_6 (A) in the absence or in the presence of (B) 0.5 or (C) 2.5 equiv of TBAF.

Based on the above NMR data and the 2:1 stoichiometry inferred from the titration experiments, it is suggested that the initial coordination of F⁻ to the indole NH hydrogen induces a rotation of 180° of the benzylic ring. Upon the addition of further aliquots of fluoride, significant deprotonation may occur,⁹¹ and the deprotonated indole can be stabilized by an intramolecular hydrogen bond with the amide NH group (**Scheme 7**).⁹² A locked coplanar disposition of the indole and quinoline rings would then ensue, with consequent fluorescence enhancement and UV bathochromic shift.^{88a,92b} Attempts to detect the HF₂⁻ signal in the ¹H NMR spectrum at ca. δ 16 were however unsuccessful. This has been attributed to fast proton exchange with the water impurity present in the DMSO solvent.^{88c}

Verification of the proposed Bronsted acid–base reaction by titration experiments with the strong base [(Bu)₄N]OH (TBAOH) was precluded by deacetylation of the catechol functions under such conditions.⁵⁹ Because of this deacetylation reaction and the lack of effect of acetate and hydrogen sulfate anions, **14b** should be regarded as a specific fluoride sensor and not a mere acid–base sensor.

The fluorescence titration profile apparently supported the two-step process depicted in **Scheme 7**. Quantitative measurements of the F⁻ affinity from the titration data by previously reported procedures⁹³ gave values of log*K* = 6.04 and 4.08, which are comparable with those of many known fluorescence based sensors.^{88c, 82,92b, 94}



Scheme 7. Mechanism of coordination of F^- to **14b**

CONCLUSIONS

Despite the vast literature that accumulated during the past few years, the quest for easily accessible and efficient fluoride-sensing molecular systems is still an active area of research⁶ because of the significant biological, medical, industrial, and environmental relevance of fluoride chemistry.

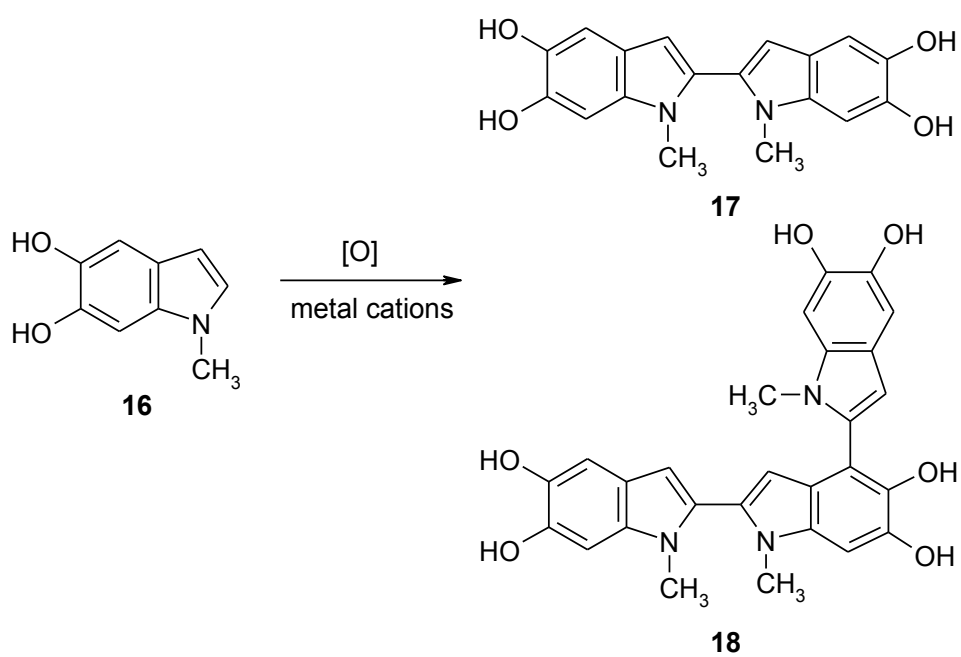
In this chapter I have reported a novel fluoride-sensing scaffold featuring an unusual 2-(2-amidobenzyl)-3-(indol-3-yl)quinoline skeleton, which was obtained from **1** by a mild one-pot variant of the classic acid-promoted trimerization of indoles followed by acetylation. Compound **14b** represents a chromogenic and fluorogenic fluoride sensing system⁹⁵ operating in the turn-on mode and its characterization may stimulate further studies on the potential fluoride sensing properties of related indolylquinoline systems.

CHAPTER IV

Oxidative chemistry of 5,6-dihydroxy-1-methylindole

INTRODUCTION

In the previous chapters I reported the results of studies directed to the preparation and characterization of higher oligomers with a 5,6-dihydroxyindole-based scaffolds^{58,96} by an oligomer coupling strategy. In particular, interesting results concerning new tetramer products were obtained by isolation of the main intermediates in the oxidative polymerization of a 2,4'-biindole and a 2,7'-biindole. Since 5,6-dihydroxyindole derivatives tend to dimerize via 2,2'-bonds under metal ion-assisted conditions, it was of considerable interest to extend the study to the oxidation behavior of the 2,2'-biindole system from **1**. Unfortunately, pursuit of this goal was frustrated by the marked difficulty to obtain sufficient amounts of the desired 2,2'-dimer by metal-assisted oxidation of **1**, the reaction leading invariably to side products and impurities difficult to remove. However, it was known that 5,6-dihydroxy-1-methyl-indole (**16**), a major oxidation product of adrenaline (epinephrine) undergoes metal ion-assisted oxidation, e.g. with Ni²⁺ or Zn²⁺ to give as main oligomer products dimer **17** and trimer **18**, which share the desired and little explored 2,2'-biindole system (**Scheme 8**). On this basis it was decided to investigate 5,6-dihydroxy-1-methylindole-derived oligomers as potential building blocks for novel oligomeric scaffolds. An additional advantage of using **16** as the starting substrate relates to the more favorable solubility and chromatographic properties of its oligomers with respect to those of most oligomers of **1**.^{97, 98}



Scheme 8: Oligomers obtained by oxidation of **16** in the presence of metal cations.

RESULTS AND DISCUSSION

Biomimetic oxidation of dimer **17** was carried out with peroxidase/H₂O₂ at pH 7.4. The dimer, stored as the acetyl derivative, was deprotected in MeOH with sodium *tert*-butoxide under an Ar atmosphere; after oxidation, the reaction mixture was acidified and reduced and the ethyl acetate extractable fraction was acetylated. TLC analysis (CHCl₃:AcOEt=4:6) of the resulting mixture indicated a principal product at R_f 0.53 and traces of a product at R_f 0.33, that were been isolated by repeated TLC. ESI-MS analysis of principal product showed pseudomolecular ion peaks [M +H]⁺ and [M+Na]⁺ at *m/z* 983 and 1005, indicating a tetramer of **16**. The ¹H NMR spectrum exhibited only 5 signals in the aromatic region (**Figure 35**), suggesting a symmetric structure.

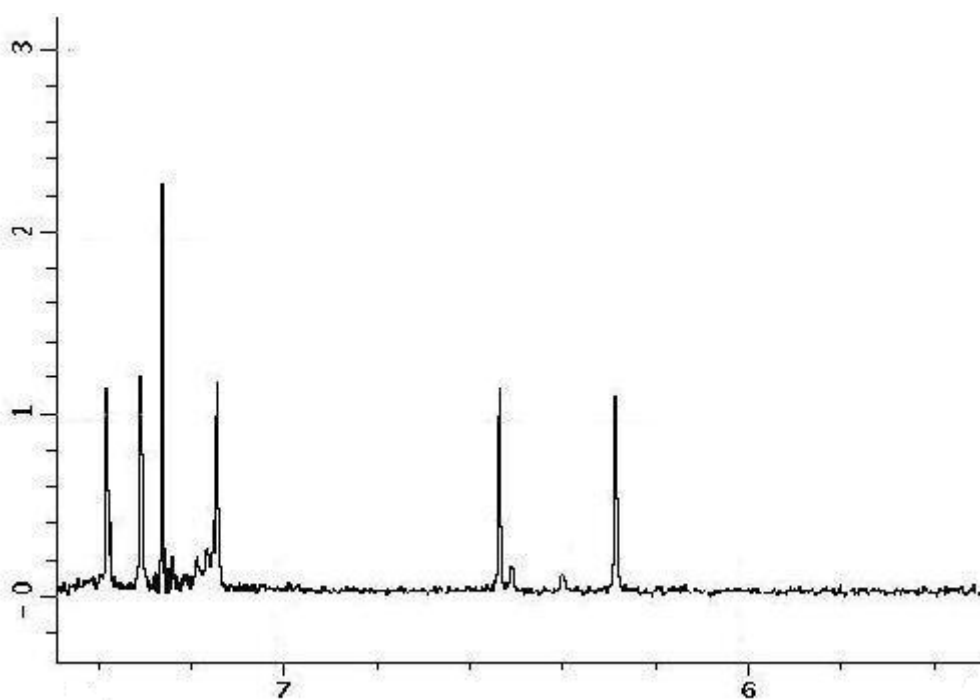


Figure 35. Selected region of the ¹H NMR spectrum of tetramer **19**-acetylated.

The presence of two resonances above δ 7.00 correlating with N-CH₃ protons in the ROESY spectrum (**Figure 36**) and only one correlating with a resonance typical of a

3-H allowed formulation of the compound as the acetylated symmetric tetramer **19**-acetylated, with a 4,4 link between the dimeric units.

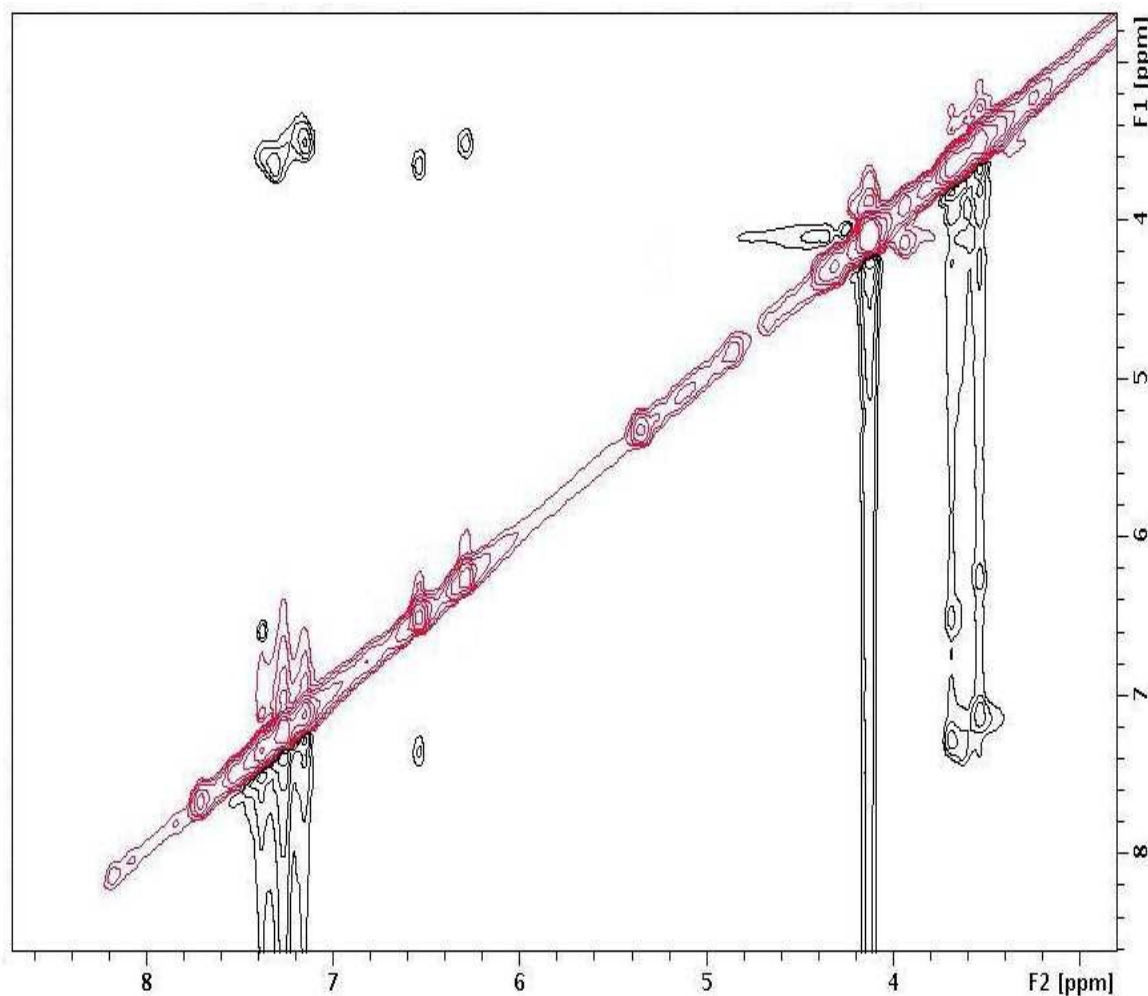
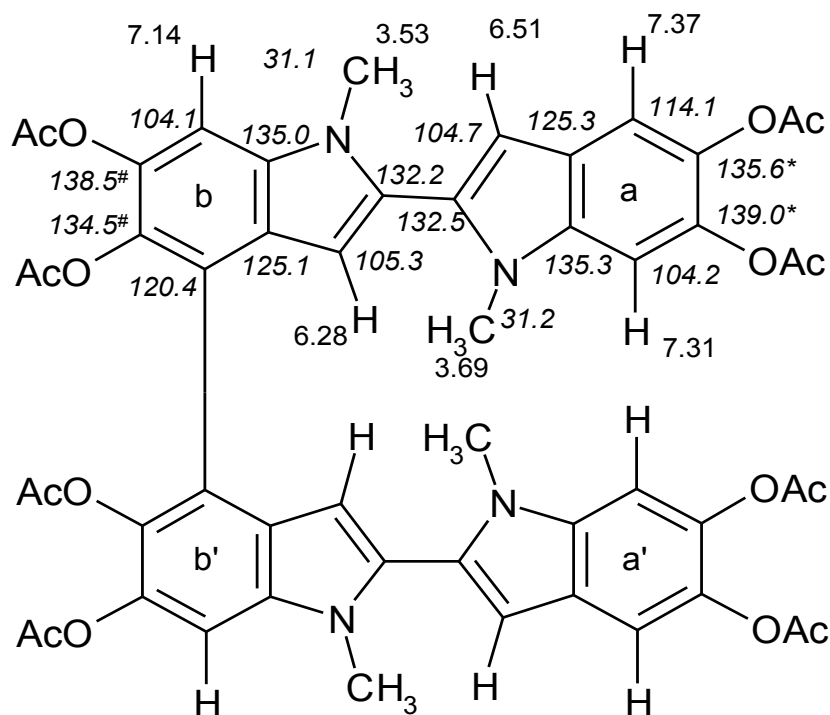


Figure 36. ROESY spectrum of tetramer **19**-acetylated.

Analysis of the ^1H , ^{13}C HSQC -DEPT and ^1H , ^{13}C HMBC spectra allowed the assignment of all proton and carbon resonances (**Figure 37**).

Preferential reactivity of **17** via the 4-position may be largely determined by steric factors, including the effect of the *N*-Me groups hindering the 7-position relative to the parent 5,6-dihydroxyindole.⁹⁷



*,# interchangeable

Figure 37. Structure of tetramer **19**-acetylated with proton (regular style) and carbon (italic style) resonances.

The product at R_f 0.33 could not be fully characterized, because of the small amount isolated. However ESI(+)-MS analysis showed pseudomolecular ion peaks $[M + H]^+$ and $[M + Na]^+$ at m/z 1473 and 1495, indicating a hexamer; however, the 1H -NMR spectrum displayed a smaller number of resonances than those expected for an asymmetric hexamer; in particular, only three resonances typical of protons at the indolic 3-position and only three signals for N - CH_3 groups were observed. Based on this, the structure of the acetylated symmetric hexamer **20-Ac** was hypothesized (**Figure 38**).

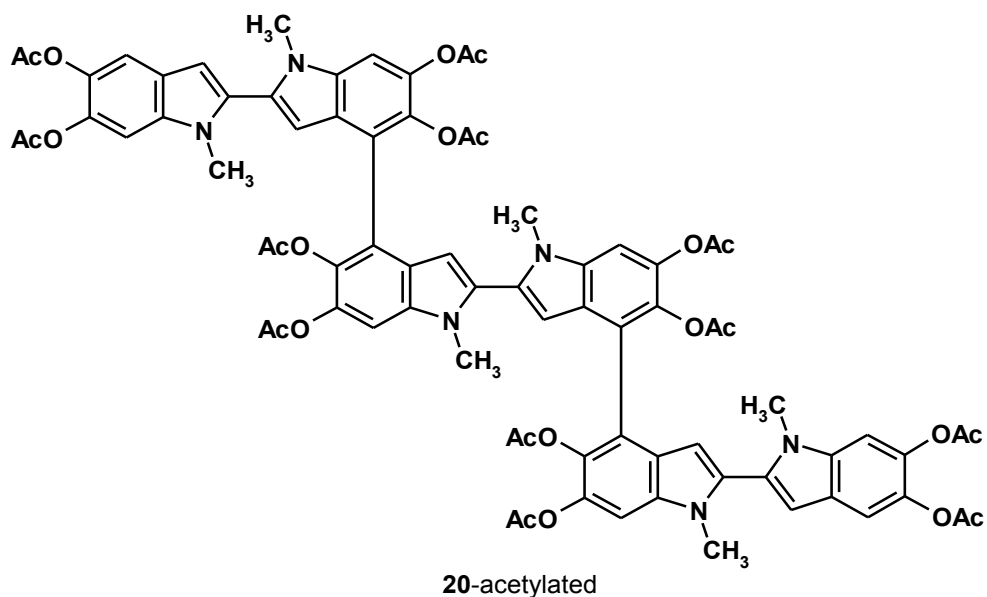


Figure 38. Proposed structure of the product at R_f 0.33 ($\text{CHCl}_3:\text{AcOEt}=4:6$).

Quite interestingly, biomimetic oxidation of an equimolar mixture of **17** and **18** with peroxidase/ H_2O_2 at pH 7.4 followed by reductive treatment and acetylation of the ethyl acetate extractable fraction led to the formation of a single isolable product, along with abundant eumelanin-like material. Repeated chromatographic steps eventually afforded small amounts of the product, which displayed pseudomolecular ion peaks ESI(+)-MS at m/z 1226 ($[\text{M}+\text{H}]^+$) and 1248 ($[\text{M}+\text{Na}]^+$), i.e., two mass units lower than those expected for a pentamer. The ^1H NMR spectrum (**Figure 39**) indicated only 10 singlets in the aromatic region, and the ^{13}C NMR spectrum displayed consistently 10 sp^2 C-H signals.

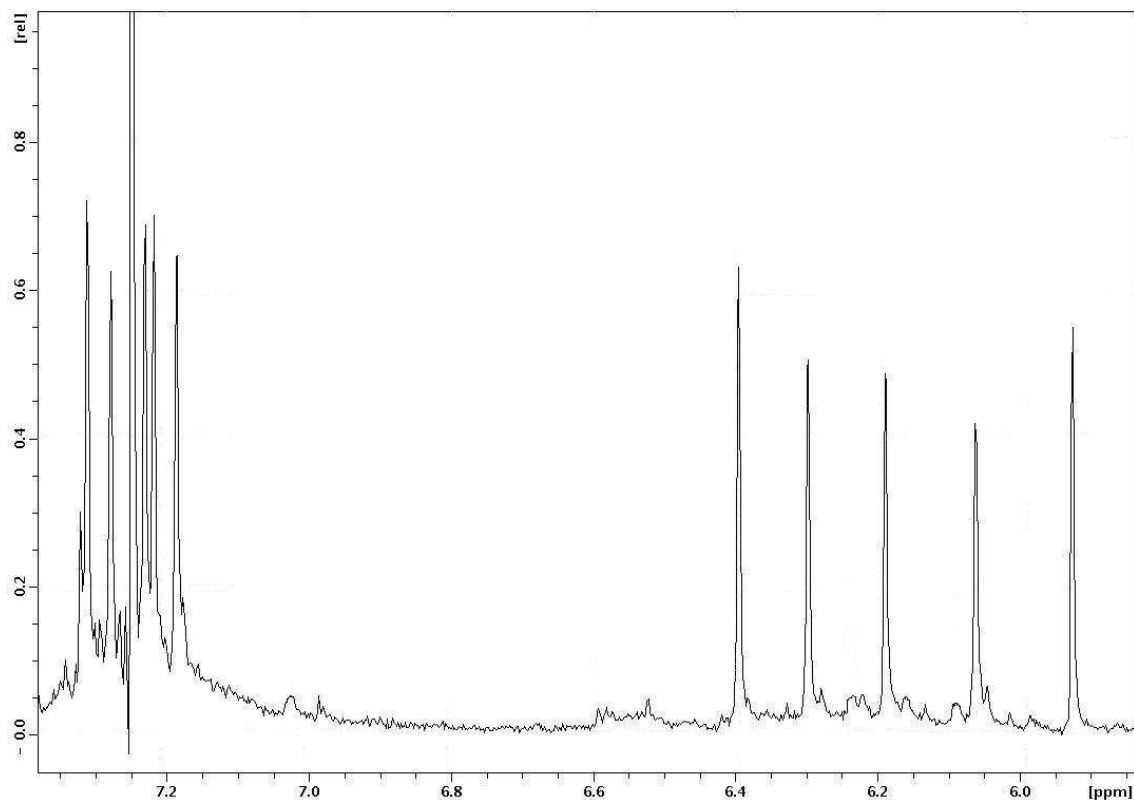


Figure 39. Selected region of ^1H NMR spectrum of pentamer **21**-acetylated.

These resonances were attributed to the presence of five H3-type protons and five H7-type protons on the basis of ^1H , ^{13}C HSQC -DEPT and ^1H , ^{13}C HMBC spectra and comparison with available NMR data for 5,6-dihydroxyindole oligomers.^{97,98}

The presence of five H7-type protons was confirmed since these correlated in the ROESY spectrum with *N*-CH₃-type protons (**Figure 40**).

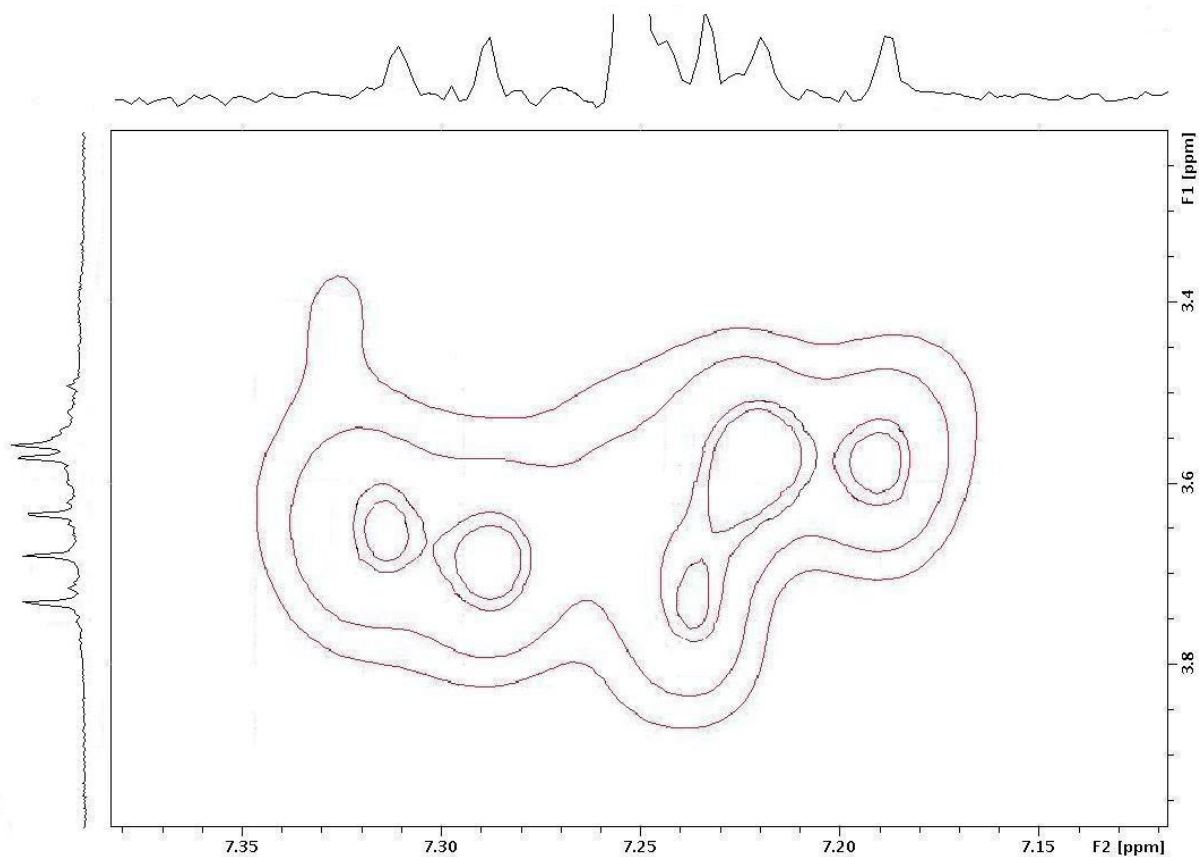


Figure 40. Selected region of the ROESY spectrum of **21**-acetylated.

Accordingly, the product was unambiguously identified as the cyclopentamer **21**-acetylated (**Figure 41**).

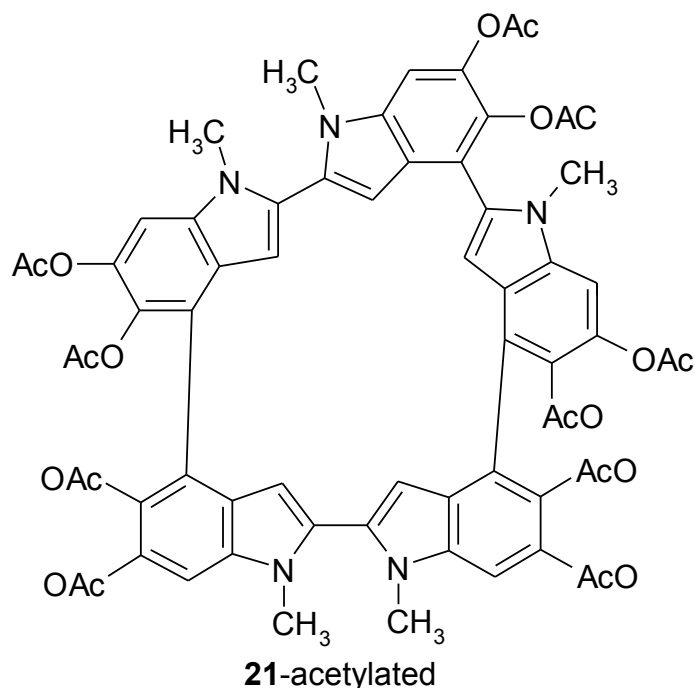


Figure 41. Structure of cyclopentamer **21**-acetylated.

Compound **21**-acetylated is the highest 5,6-dihydroxyindole oligomer so far isolated and the first macrocycle composed of five *N*-methyl-5,6-dihydroxyindole units. Its isolated yield (ca. 5%) is comparable to that of most 5,6-dihydroxyindole oligomers⁵⁸ and is significant considering that the building of cyclic structures, though entropically favored, has to compete against the distribution of the linear oligomers.

The structural features of **21** were explored at the DFT level of theory, using the hybrid PBE0 functional⁴² in conjunction with the 6-31+G(d,p) basis set.⁹⁹ All structural minima are of *C*₁ symmetry and therefore occur as pairs of conformational enantiomers. **Table 3** lists computed inter-ring dihedrals and relative energies of the main conformers of the *N*-Me-DHI cyclic pentamer **21**. For the sake of clarity, the five indole units have been dubbed as A (unprimed), B (primed), C (double primed), etc. only the one for which the first dihedral is positive is reported in the **Table 3**.

Table 3. Computed inter-ring dihedrals and relative energies of the main conformers of the *N*-Me-DHI cyclic pentamer **21**

Conformer	N(A)- C2(A)- C2(B)- N(B)/ deg	C8(B)- C4(B)- C4(C)- C8(C)/ deg	N(C)- C2(C)- C2(D)- N(D)/ deg	C8(D)- C4(D)- C2(E)- N(E)/ deg	C8(E)- C4(E)- C4(A)- C8(A)/ deg	<i>E</i> / kcal/mol
20a	109	-49	44	-132	-67	0.00 ¹
20b	114	-49	43	-132	-68	0.33
20c	35	-50	78	97	62	2.76
20d	34	48	-70	-112	-72	3.35
20e	33	48	-68	-112	-73	3.58
20f	36	-50	80	97	56	3.76
20g	35	-51	83	96	56	4.31
20h	109	-46	-17	-131	-64	10.82

¹ -2759.005272 hartree

Equilibration of the enantiomeric pairs would require a concerted inversion at the C4(A)-C4(E) and C2(E)-C4(D) interring dihedrals, which cannot be achieved without severe strain of the macrocyclic ring (as a matter of fact, steric interactions at the biphenyl-type 4,4'- bonds suffice to induce atropisomerism even in linear biindoles).¹⁰⁰

Within each series, two main conformational basins can be identified: in the first one, the A and B indole rings assume an almost perpendicular disposition (and the C and D units are much less skewed); the opposite holds in the second basin. Additional conformational complexity is connected to the details of the pattern of intramolecular O-H···O hydrogen bonds. Such a complex conformational behavior suggests an inherent difficulty to efficient supramolecular packing, which may well account for our failure to grow crystals suitable for X-ray analysis. **Figure 42** shows the most stable conformer identified.

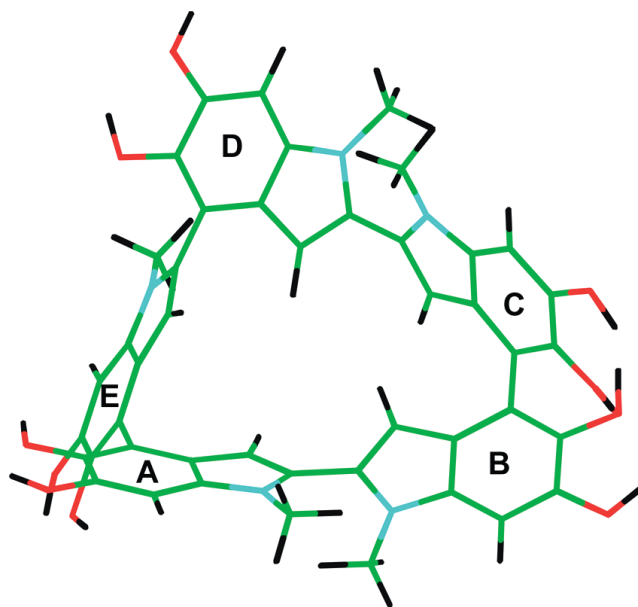


Figure 42. Most stable conformer of **21**.

Compound **21** conceivably arises by sequential crosscoupling-cyclization of **17** and **18** via catechol-quinone interactions.^{96,97}

A DFT investigation was therefore carried out on **17** and **18**, both in their reduced and oxidized (quinonoid) forms and computed inter-ring dihedrals and relative energies of the main conformers / tautomers are listed in **Tables 4** and **Table 5**.

Table 4. Computed inter-ring dihedrals and relative energies of the main conformers / tautomers of the fully reduced (QH_2) and quinonoid (Q) forms of dimer **17**.

2,2' N-Me-DHI	In vacuo		In water	
	Species	$\varphi_{N-C2-C2'-N'}/$ deg	$\Delta G[\text{vac}]/$ kcal/mol	$\varphi_{N-C2-C2'-N'}/$ deg
QH_2				
<i>anti</i> ; OH, OH' <i>anti</i> ¹	135	0.15	142	0.70
<i>syn</i> ; OH, OH' <i>anti</i>	62	0.00 ²	63	1.19 ³
<i>anti</i> ; OH <i>anti</i> , OH' <i>syn</i>	135	0.47	144	0.00 ⁴
<i>anti</i> ; OH, OH' <i>syn</i>	135	1.69	143	0.29
Q				
extended, <i>anti</i> ; OH, OH' closed ⁵	166	0.00 ⁶	165	0.00 ⁷
extended, <i>syn</i> ; OH, OH' closed	16	0.93	18	1.66
localized, <i>anti</i> ; OH' <i>anti</i>	149	8.04	157	1.61
localized, <i>syn</i> ; OH' <i>anti</i>	47	8.64	37	2.87

¹ OH *syn/anti*, OH' *syn/anti* designations refer to the orientation of the phenolic hydroxyl groups on each ring with respect to the indole nitrogen of the same ring

² -1104.519544 hartree

³Due to convergence difficulties when using the default value of 0.2 Å² for the average area of the PCM cavity surface elements (tesserae), these figures have been obtained by averaging the results of two distinct calculations with tesserae areas of 0.15 and 0.25 Å², respectively

⁴ -1104.595638 hartree

⁵ Cyclic H-bond between the phenolic hydroxyl group(s) and the adjacent quinonoid carbonyl group(s)

⁶-1103.303369 hartree

⁷ -1103.363872 hartree

Table 5. Computed inter-ring dihedrals and relative energies of the main conformers / tautomers of the fully reduced (QH_2) and quinonoid (Q) forms of trimer **18**.

2,2':4',2'' N-Me-DHI	In vacuo			In water		
	Species	$\varphi_{N-C2-C2'-N'}$ / deg	$\varphi_{C8'-C4'-C2''-N''}$ / deg	$\Delta G[vac]$ / kcal/mol	$\varphi_{N-C2-C2'-N'}$ / deg	$\varphi_{C8'-C4'-C2''-N''}$ / deg
QH_2						
+ <i>anti</i> , + <i>anti</i> ; OH, OH', OH'' <i>anti</i> ¹	138	123	1.21	142	117	0.00 ²
+ <i>anti</i> , + <i>anti</i> ; OH, OH'' <i>anti</i> , OH' <i>syn</i>	137	128	4.33			
+ <i>anti</i> , - <i>anti</i> ; OH, OH', OH'' <i>anti</i> ³						
+ <i>anti</i> , - <i>anti</i> ; OH, OH'' <i>anti</i> , OH' <i>syn</i>	138	-128	4.68			
+ <i>anti</i> , + <i>syn</i> ; OH, OH', OH'' <i>anti</i>	139	59	0.49	142	66	1.39
+ <i>anti</i> , - <i>syn</i> ; OH, OH', OH'' <i>anti</i>	136	-58	0.00 ⁴	141	-71	0.76
+ <i>anti</i> , - <i>syn</i> ; OH, OH'' <i>anti</i> , OH' <i>syn</i>	137	-55	4.92	138	-69	0.91
Q						
extended across 2,2', + <i>anti</i> , - <i>anti</i> ; OH, OH' closed, OH'' <i>anti</i> ⁵	167	-130	1.55	167	-125	0.45
extended across 2,2', + <i>anti</i> , + <i>anti</i> ; OH, OH' closed, OH'' <i>anti</i>	167	129	1.65	166	124	0.00 ⁶
extended across 2,2', + <i>anti</i> , - <i>syn</i> ; OH, OH' closed, OH'' <i>anti</i>	166	-60	2.18	166	-64	1.07

extended across 2',4", + <i>anti</i> , - <i>anti</i> ; OH <i>anti</i> ; OH', OH" closed	135	-156	0.57	143	-152	3.62
extended across 2',4", + <i>syn</i> , - <i>anti</i> ; OH <i>anti</i> ; OH', OH" closed	65	-156	0.00 ⁷	61	-152	3.08
extended across 2',4", + <i>anti</i> , + <i>anti</i> ; OH <i>anti</i> ; OH', OH" closed	133	156	0.43	141	153	2.82
extended across 2',4", + <i>syn</i> , + <i>anti</i> ; OH <i>anti</i> ; OH', OH" closed	66	156	0.22	62	153	2.94
extended across 2,2' and 2',4", + <i>anti</i> , - <i>anti</i> ; OH, OH" closed, OH' <i>syn</i>	159	-145	18.46			
extended across 2,2' and 2',4", + <i>anti</i> , - <i>syn</i> ; OH, OH" closed, OH' <i>syn</i>	158	-32	18.91			
extended across 2,2' and 2',4", + <i>syn</i> , + <i>syn</i> ; OH, OH" closed, OH' <i>syn</i>	42	36	26.20			
extended across 2,2' and 2',4", + <i>anti</i> , + <i>anti</i> ; OH, OH" closed, OH' <i>syn</i>	158	144	18.73	161	143	11.90
localized on the first unit, + <i>anti</i> , - <i>syn</i> ; OH closed, OH' OH" <i>anti</i>	149	-58	7.26	157	-71	3.65
localized on the second unit, + <i>anti</i> , - <i>syn</i> ; OH, OH" <i>anti</i> , OH' closed	148	-40	10.33	158	-54	2.24

localized on the third unit, <i>+anti</i> , <i>-syn</i> ; OH OH' <i>anti</i> , OH'' closed	137	-52	7.74	146	-53	5.06
localized on the first unit, <i>+anti</i> , <i>+anti</i> , OH closed, OH' OH'' <i>anti</i>	149	126	8.22	159	122	2.70
localized on the second unit, <i>+anti</i> , <i>+anti</i> ; OH, OH'' <i>anti</i> , OH' closed	149	139	8.81	158	127	1.46
localized on the third unit, <i>+anti</i> , <i>+anti</i> ; OH OH' <i>anti</i> , OH'' closed	138	139	9.30	146	134	4.17

¹ The OH *syn/anti*, OH' *syn/anti*, OH'' *syn/anti* designations refer to the orientation of the phenolic hydroxyl groups on each ring with respect to the indole nitrogen of the same ring

² -1656.294387 hartree

³ Evolves to *+anti*, *-syn*; OH, OH', OH'' *anti*

⁴ -1656.191433 hartree

⁵ The OH closed/OH' closed/OH'' closed designations indicate the presence of a cyclic H-bond between the phenolic hydroxyl group and the adjacent quinonoid carbonyl group on the same ring

⁶ -1655.062432 hartree

⁷ -1654.973367 hartree

The most stable conformation of 17-quinone (**17Q**) (**Figure 43**) features an interunit double bond with a N-C2-C2'-N' dihedral angle of 165°, consistent with previous results on the *N*-unsubstituted 2,2'-dimer.⁵⁹ On the other hand, the most stable tautomer of the quinone trimer (**18Q**) possesses only one inter-ring double bond on the 2,2'-biindole moiety (**Figure 43**).

The free energy change for the equation $17 + 18Q \rightleftharpoons 17Q + 18$ was estimated as -1.19 kcal/mol (in vacuo) and as -0.12 kcal/mol following introduction of solvent effects by means of the polarizable continuum model (PCM)^{52,53,76} in its united atom for Hartree-Fock (UAHF) parametrization.⁵¹

On this basis, it was suggested that formation of **21** involves generation of 17-quinone and its coupling with **18** via a 4,4'- type bonding (**Scheme 9**). The rigid 2,2'-biindole moieties in the resulting pentamer would bring the two termini into close proximity upon folding, thus favoring intramolecular cyclization after an additional oxidation step.

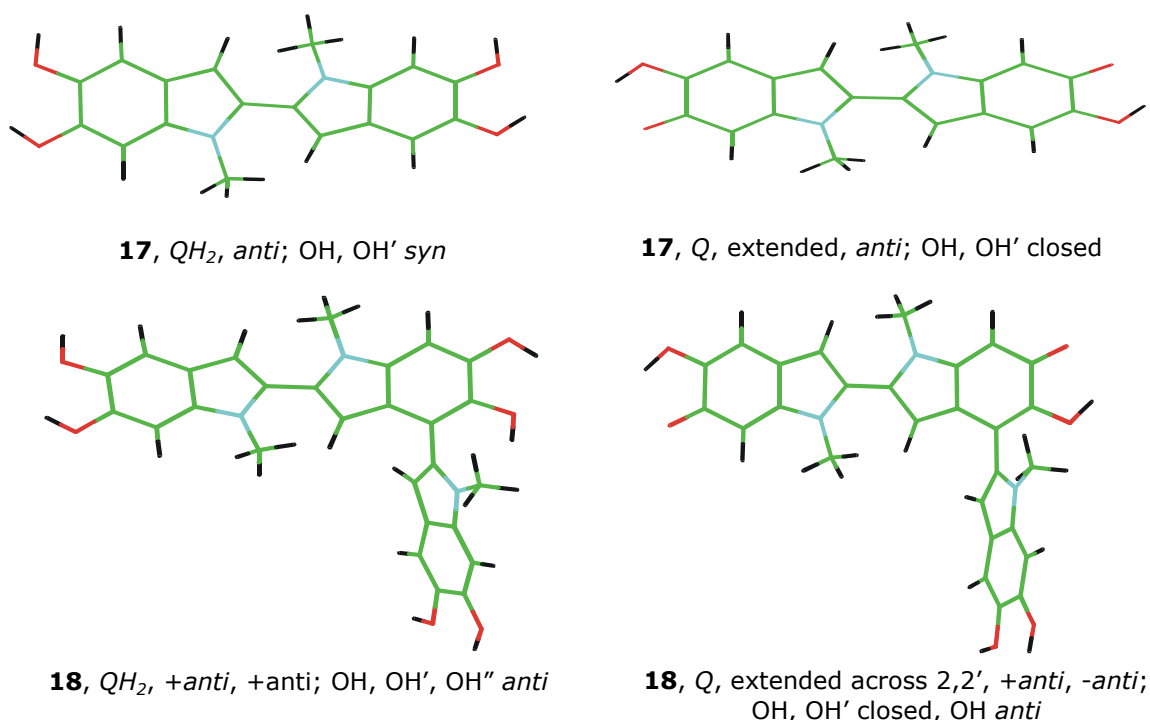
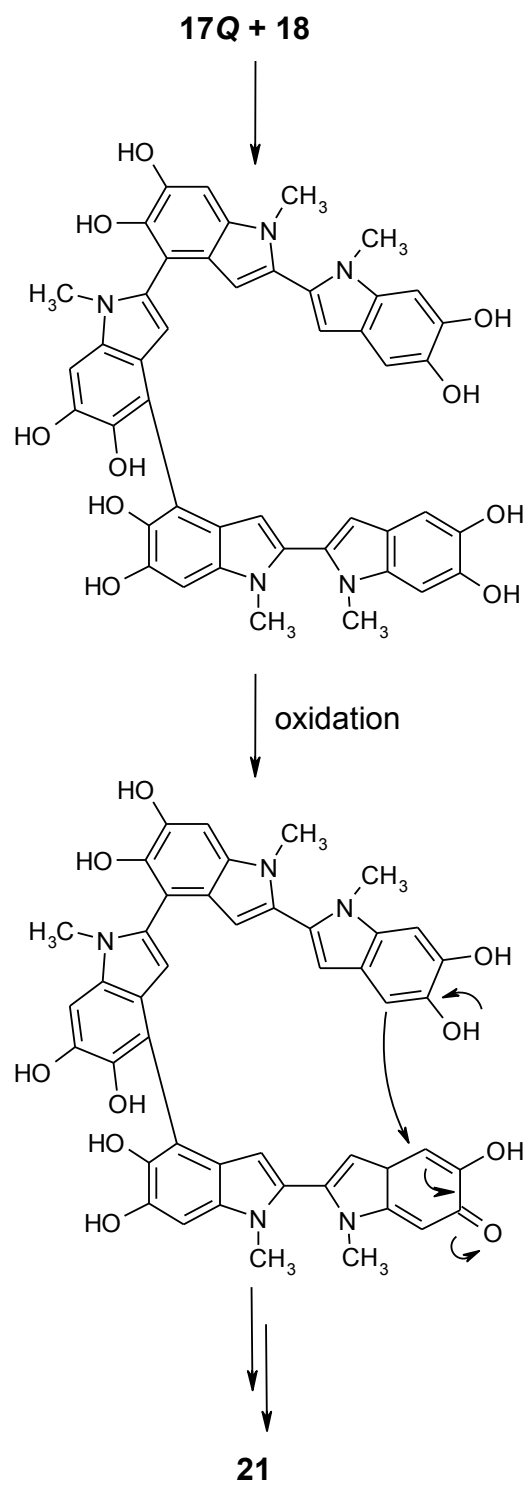


Figure 43. Optimized structures of the most stable (in water) reduced (QH_2) and quinonoid (Q) forms of dimer **17** and trimer **18**.



Scheme 9. Representative mechanism of formation of **21**.

Some insights into **17**-quinone was gained by pulse radiolytic oxidation of **17** (**Figure 44**), using the same methods as previously applied to the corresponding unmethylated 2,2' dimer.⁵⁹ The initial product formed 200 μs after the pulse was the semiquinone, with a maximum around 460 nm (for the reaction of **17** with $\text{Br}_2^{\cdot-}$, $k = 3.5 \times 10^8 \text{ M}^{-1} \text{ s}^{-1}$).

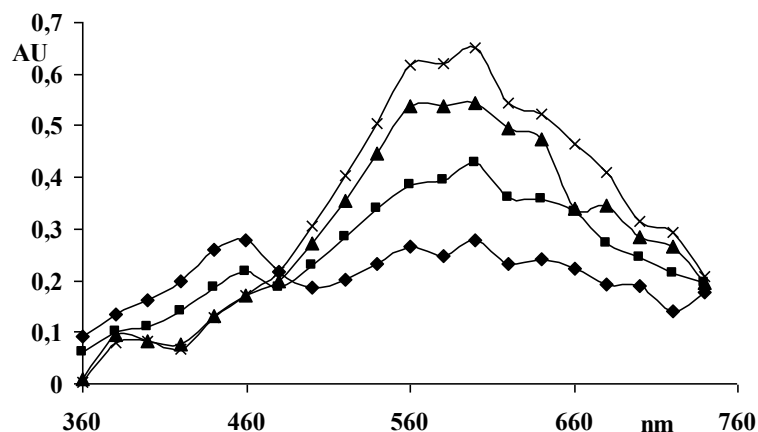


Figure 44. Changes in absorption at various times after pulse radiolysis of an N_2O -saturated aqueous solution of dimer **17**: (\blacklozenge) 200 μs , (\blacksquare) 1060 μs , (\blacktriangle) 4060 μs , (\times) 8980 μs .

The transient species decayed by second order kinetics ($2k = 3.6 \times 10^9 \text{ M}^{-1} \text{ s}^{-1}$) to a strongly absorbing chromophore ($\lambda_{\text{max}} = 600 \text{ nm}$, $\epsilon = 5.3 \times 10^4 \text{ M}^{-1} \text{ cm}^{-1}$) which was attributed to the quinone based also on the good agreement with the computed absorption maximum (584 nm) of the most stable conformer of **17Q** in water (**Figure 45**).

Quinone formation apparently involves disproportionation of the semiquinone, as suggested by the isosbestic point at 480 nm and second order kinetics (**Scheme 10**).

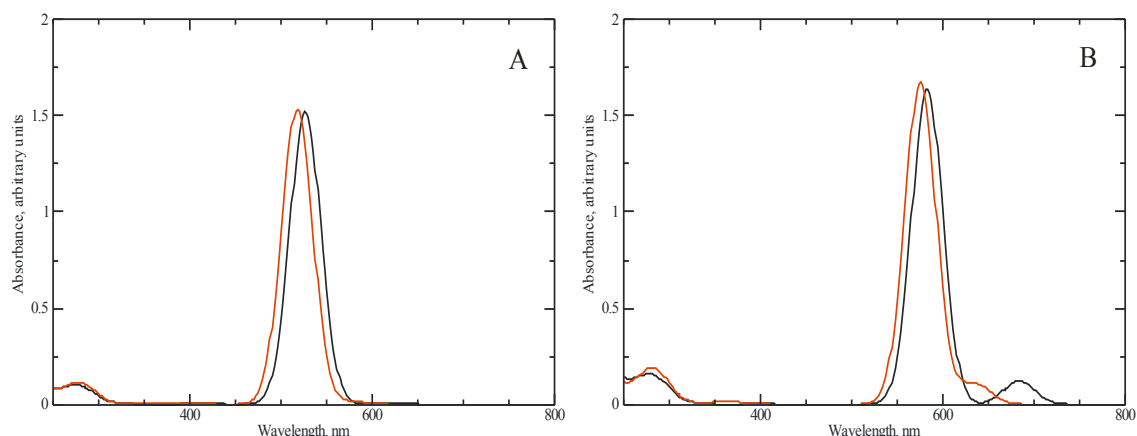
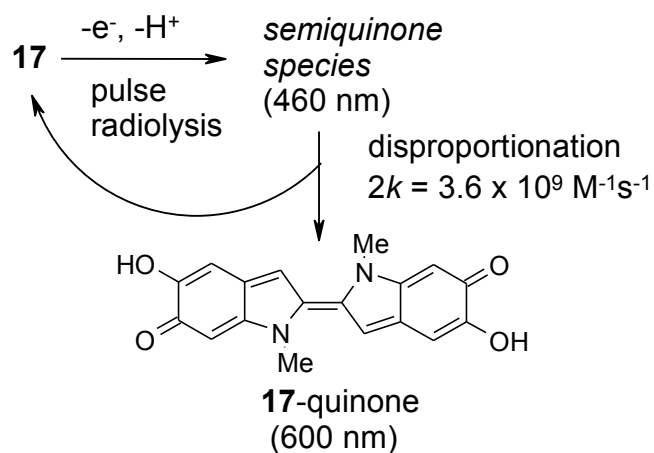


Figure 45. A: spectra computed in vacuo; B: spectra computed in water (PCM). Black line: **17Q**, extended, *anti*; OH, OH' closed; red line: **17Q**, extended, *syn*; OH, OH' closed (see **Table 4** for an explanation of the nomenclature adopted).

No detectable self-coupling products (e.g., **19** or hexamers) were formed by co-oxidation of equimolar amounts of **17** and **18**. This would point to prevalent cross-coupling pathways of **17** and **18**, with the necessary caution imposed by the poor mass balance and the abundant polymeric material interfering with product analysis.



Scheme 10. Generation of **17-quinone** by disproportionation of the semiquinone radical.

CONCLUSIONS

In this chapter I have disclosed the generation under biomimetic conditions of the first cyclic 5,6-dihydroxyindole oligomer. Indole-based macrocyclic systems attract increasing interest in relation to their conformational and self-association properties, stacking interactions, spectroscopic features, cavity shape, and performance as ligands or ion-sensing scaffolds.¹⁰¹ However, no macrocyclic structure built solely on indole units was described in the literature. In this connection, the cyclic 5,6-dihydroxyindole oligomer **22** (**Figure 46**), consisting of four units in an arrangement that contains an inner porphyrin ring,^{24,102} has recently been proposed on a theoretical basis as a fundamental building block accounting for the structural and spectral properties of eumelanins.

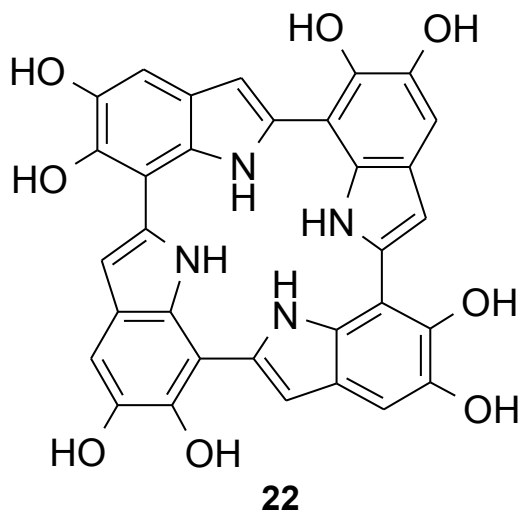


Figure 46. The cyclic 5,6-dihydroxyindole oligomer recently proposed on a theoretical basis to account for the structural and spectral properties of eumelanins.

Unfortunately, verification of this hypothesis has been hampered by the notorious difficulties in the investigation of the oxidative polymerization of 5,6-dihydroxyindoles, the key step in eumelanin synthesis.^{97,101} The characterization of cyclic 5,6-dihydroxyindole based oligomers has remained therefore a theoretical curiosity as well as an experimental challenge in an intriguing field of research at the crossroads of biology and materials science.^{97,103}

The importance of the results described in this chapter lies mainly in the discovery and characterization of an unprecedented indole-based structural motif of potential academic and practical interest. For example, the modular assembly of **21** by 2,2'-biindole-containing scaffolds highlights the bonding patterns and geometries required to construct a five-membered indole macrocycle. The spontaneous oligomer-oligomer coupling/cyclization pathway suggests, moreover, that macrocyclic structures like those recently hypothesized^{24,102} are not entirely devoid of foundation and may contribute to the patterns of structural diversity generated during 5,6-dihydroxyindole polymerization.^{14b,24} The great versatility of 5,6-dihydroxyindole in terms of positional reactivity would in principle allow for the formation of a diverse range of cyclic structures during eumelanin buildup.

On the other hand the isolation of symmetrical oligomers by oxidation of **17** suggests the possibility of realizing melanic polymers with higher structural order.

CHAPTER V
Oxidative polymerization of 5,6-dihydroxyindole
in phosphate buffer/polyvinyl alcohol (PVA)

INTRODUCTION

The elucidation of the structure and mechanism of buildup of eumelanin is a most challenging task because of the high molecular heterogeneity, the amorphous character and the lack of solubility in common solvents which makes it impossible even to draw a tentative description of the polymer at molecular level.

Recently, the importance of the structural organization of melanosomes, the melanin-containing organelles, in determining pigment roles and functions has also been emphasized.^{104,105} As a result of such investigations,¹⁰⁵ it has become increasingly clear that an understanding of the biological significance of melanin pigmentation is strictly dependent on a detailed elucidation of the molecular composition, architecture and surface properties of melanosomes. The latter is crucial to some of the key properties and supposed functions of melanins, *e.g.* as organic semiconductors and photoprotecting agents.^{103,106}

The absorbance in the ultraviolet and visible is monotonic and broad-band that is, it is featureless and fits a single exponential in wavelength space to a high degree of accuracy (**Figure 47**). The exponential shape can be fitted by a sum of Gaussians with full widths at half maxima characteristic of inhomogeneously broadened chromophores at room temperature.^{16b,17}

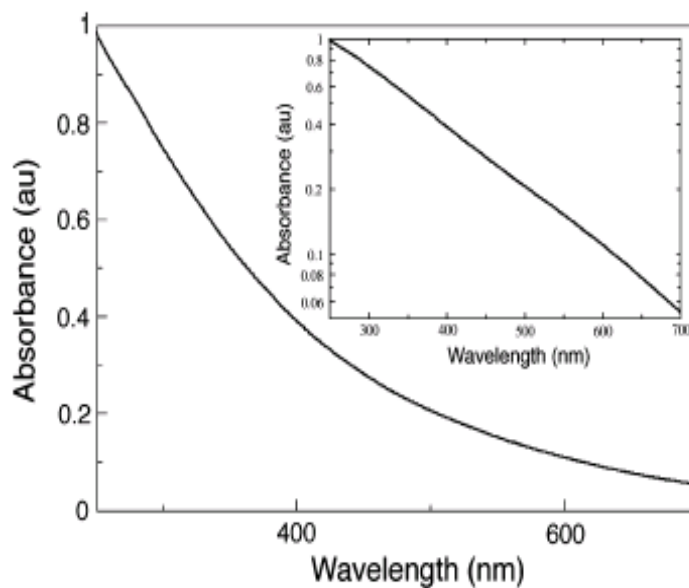


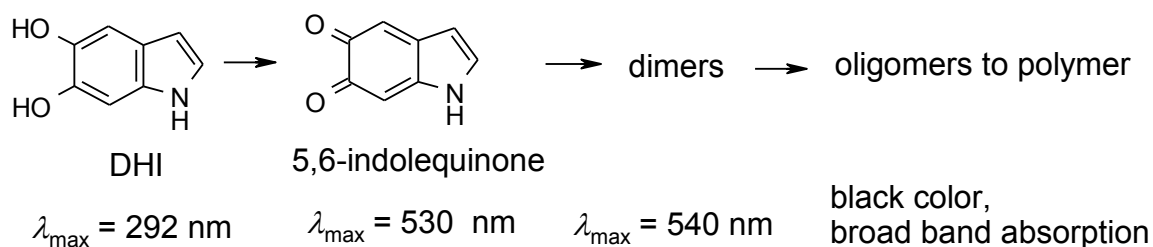
Figure 47. The broad-band absorption of eumelanin: the spectrum is monotonic and fits an exponential in wavelength space (insert shows the logarithmic-linear plot).

Dissecting the fundamental structural factors responsible for this absorption spectrum and black color remains therefore a central goal of eumelanin research. In fact it is an actively debated issue whether broad-band absorption is due to an extended conjugated polymeric backbone or rather reflects a highly disordered system made up of mixtures of π -stacked oligomers. Whether the black chromophore of DHI-derived synthetic eumelanins is due to the formation of a high molecular weight polymer with extended electron delocalization or of mixtures of oligomers remains also a subject of debate.

Although both scattering and molecular absorption effects have been reported to contribute to the optical properties of eumelanin,⁵ current evidence suggests that the black color of the pigment is mainly intimately associated with the multichromophoric heterogeneous mixtures of species of different structures that are produced by the oxidation of DHI and DHICA.

Early studies of DHI oxidation¹⁰⁷ revealed the initial generation of a distinct chromophoric species, termed melanochrome, with a maximum centered at 530 nm attributed initially to 5,6-indolequinone and later to an oxidized oligomer (**Scheme 11**).

In all these studies, however, the efforts toward chromophore characterization were thwarted by the exceedingly low solubility of the intermediate and final products, their instability and the marked scattering effects that hindered spectrophotometric investigations.



Scheme 11. Early hypothesis on the origin of spectral changes during DHI oxidation.¹⁰⁹

Some insight into the relationships between oxidation level, π -electron delocalization and HOMO-LUMO gaps in DHI oligomers has derived from integrated pulse radiolysis and computational investigations of the transient species generated by oxidation of DHI and related oligomers,^{59,73} as well as from studies of the chromophoric changes that occur along the oligomer sequence from the monomer to a tetramer. Other information has been obtained from characterization of organic-soluble eumelanin-like pigments from DHICA benzyl and octyl esters,¹⁰⁸ as well as from a study of DHI oxidation using a Cu(II) mimic of tyrosinase at low temperature.¹⁰⁹

More recently, the development and characterization of the first water-soluble DHI polymer¹¹⁰ obtained by oxidative polymerization of a thioglycosyl derivative of DHI has yielded unprecedented insights into the origin of eumelanin black chromophore. The results underscored the importance of the coexistence of reduced and oxidized moieties for the visible absorption properties and black chromophore. Finally, a reinvestigation of eumelanin supramolecular structure using low voltage-high resolution transmission electron microscopy has lent further support to the conclusions that the absorption spectra reflect more the intrinsic properties of the oligomers than effects due to their aggregation in the solid state.¹¹¹

Despite these and other advances, the characterization of visible light-absorbing intermediates in the oxidative polymerization of underivatized DHI in aqueous solution and in the absence of precipitation phenomena remains a most important goal for an understanding of the origin of eumelanin absorption spectrum and optical properties.

A novel approach to elucidating eumelanin chromophore is based on a systematic evaluation of the effect of various additives on the spectrophotometric course of DHI oxidation. In this chapter I report the results of a study aimed at developing conditions that could prevent oligomer and polymer precipitation in order to investigate intermediate and final chromophores in the absence of scattering effects.

RESULTS AND DISCUSSION

In searching for additives capable of preventing aggregation and precipitation of DHI oligomers/polymers in neutral aqueous solution, the attention was directed to polymers with hydrophilic properties and functional groups capable of establishing efficient interactions with the growing synthetic melanin. It was found that polyvinylalcohol (PVA) was a suitable candidate combining good water solubility with efficient emulsifying and surfactant properties.

Accordingly, the effects of PVA (27000 Da) on DHI oxidation in 0.1M phosphate buffer, pH 7.0, were investigated using peroxidase/H₂O₂ as the oxidizing system and the polymer up to 10% wt/wt. On visual inspection, oxidation led to the generation of dark brown species that persisted in solution over prolonged periods of time without apparent precipitation of solid material (**Figure 48**).

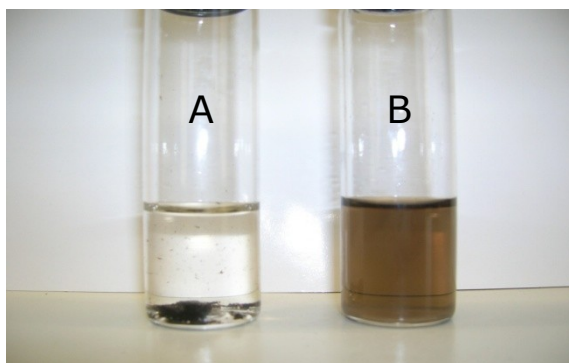


Figure 48. Synthetic eumelanin produced by peroxidase catalyzed oxidation of **1**: (A) in phosphate buffer pH 7.0, (B) 1% PVA w/w / phosphate buffer pH 7.0.

A systematic analysis showed that 1% wt/wt PVA was sufficient to prevent solid separation during the reaction (as checked by filtration on a Millipore membrane). Another test was carried out by centrifugation of solution at *ca.* 23000 g for 30 min at 4°C, as shown by the UV–Vis spectrum before and after centrifugation (**Figure 49**)

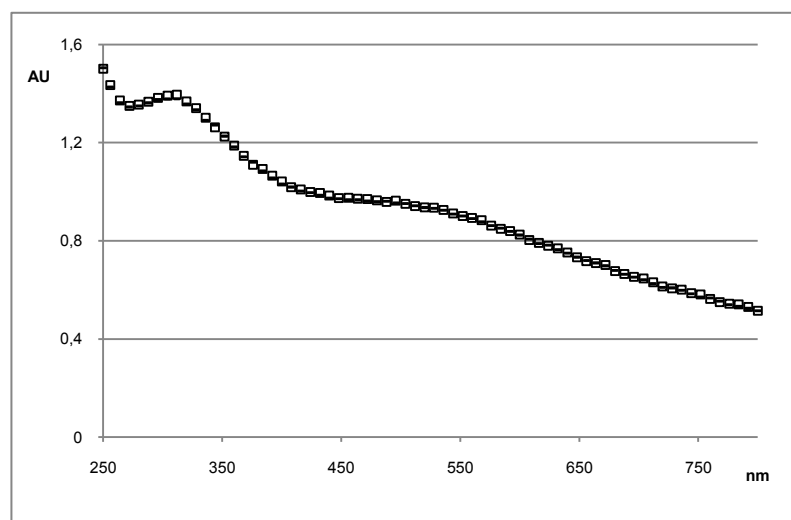


Figure 49. UV–Vis absorption of melanin solution in 0.1 M phosphate buffer, pH 7.4, containing 1% wt/wt of PVA at 24 h from the beginning of the DHI oxidation. (gray square, □) before centrifugation; (black line, —) after centrifugation.

Spectrophotometric monitoring of the oxidation course revealed the development of a broad band around 530 nm which remained virtually unchanged for 1 h or so and then decayed slowly to give after several hours an almost featureless trace in the visible region. This behavior was in marked contrast with that of a typical oxidation reaction carried out in the absence of PVA, which showed the almost immediate precipitation of a dark solid with marked scattering effects partly covering chromophoric features. Generation of the 530 nm band was apparently related to the chemical events underlying the transient chromophoric phase traditionally referred to as “melanochrome”.^{2,107} Treatment of the dark reaction mixture with a reducing agent, e.g. sodium borohydride or dithionite, led to the complete discoloration of the solution

(**Figure 50**) and a corresponding decrease in the visible absorption (**Figure 51**). No significant effect of dithionite was observed on the black solid obtained in the absence of PVA. It is noteworthy that a distinct absorption band was eventually apparent in the UV region around 320 nm, typical of reduced oligomers, which was not affected by the reductive treatment. This behavior supports previous observations¹¹⁰ suggesting the existence, along with oxidized quinonoid moieties, of reduced *o*-diphenolic units within the pigment polymer.

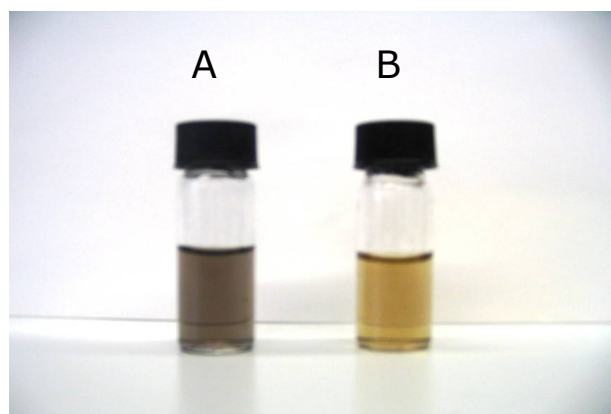


Figure 50. (A) Synthetic eumelanin produced by peroxidase catalyzed oxidation of **1** in phosphate buffer, pH 7.0, containing 1% PVA; (B) as (A), after reduction with NaBH₄.

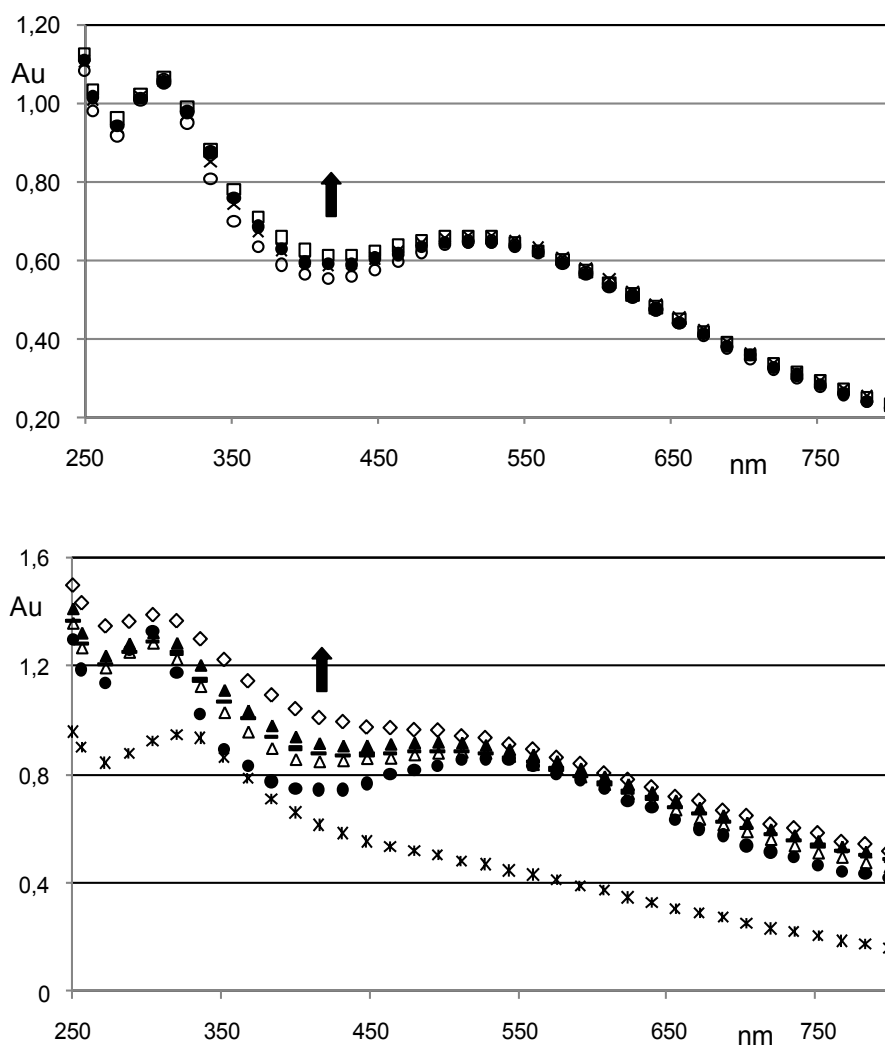


Figure 51 UV-Vis absorption profiles of H_2O_2 / peroxidase-promoted DHI oxidation in 0.1 M phosphate buffer pH 7.4 containing 1% wt / wt of PVA. Upper plot: (○) 1 min, (x) 5 min, (●) 15 min, (□) 30 min; lower plot: (●) 1 h, (Δ) 2 h, (—) 4 h, (▲) 6 h, (◇) 24 h (arrows denote the trend with time); the profile after reduction of the mixture (24 h) with sodium dithionite is also shown (*).

Virtually similar traces were obtained by increasing the PVA concentration up to 5% or using PVA of higher molecular weight (112000 Da) (data not shown).

The results in **Figure 51** are of structural interest and support the fundamental role of the redox state in the “black chromophore” of eumelanin-like pigments from DHI. In particular, it appears that the individual components of the synthetic eumelanin polymer possess intrinsic chromophoric features that depend on the oxidation state, and that these chromophores are relatively stable under conditions preventing collapse into separate particles.

In **Figure 52** are reported kinetic experiments aimed at measuring the rates of chromophore formation and decay in the presence of 1% PVA.

Data show that the visible absorption plateaus after *ca* 1 h and is not significantly modified during the subsequent 2 h. Very similar kinetic and spectrophotometric courses were observed with 5% PVA, suggesting that 1% additive is sufficient to stabilize oxidized DHI polymers and that higher PVA concentrations do not influence chromophore features and development.

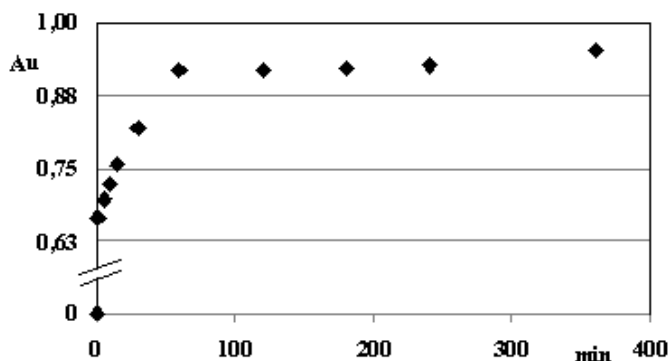
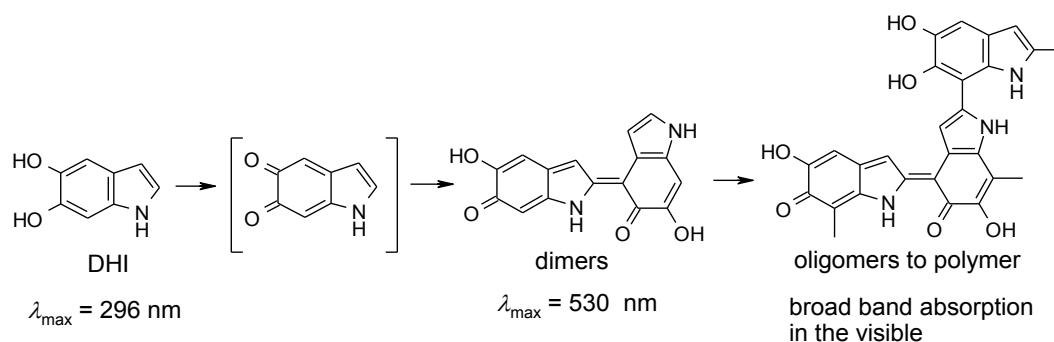


Figure 52. Kinetic course of DHI oxidation in 1 % PVA as measured at 530 nm.

Based on spectrophotometric results, it is concluded that DHI oxidation leads in the early stages to a transient quinone which is not detectable and is converted to mixtures of dimers and other oligomers of low molecular weights containing quinonoid moieties accounting for the 530 nm band⁵⁹ (**Scheme 12**).



Scheme 12. Proposed origin of spectral changes during DHI oxidation.

Persistence of this band over unexpectedly long periods of time reflects probably the presence in the growing oligomer chains of quinonoid chromophores spanning over dimeric and trimeric substructures and separated by stereochemically enforced breaks of inter-ring conjugation. This conclusion is supported by the following arguments: (1) intense absorption bands above 500 nm have been detected in the pulse radiolysis oxidation of DHI dimers;⁵⁹ (2) oxidation of DHI in the cold with a biomimetic copper-peroxo oxidant followed by warming at room temperature results in a broad and intense absorption band around 580 nm, suggesting mixtures of oligomers at various levels of oxidation or partially degraded, as indicated by mass spectrometric analysis;¹⁰⁹ (3) known oligomer structures from DHI feature inter-ring bondings that would hinder coplanar conformations and extended electron delocalization over a high number of units,⁵⁸ much like the case of DHICA.¹¹²

To inquire into the effects of PVA on the mechanism of DHI polymerization, oxidation mixtures were prepared by reacting 5 mM DHI and 20 mM H_2O_2 with 36 U mL^{-1} HRP in the presence and in the absence of added polymer. These mixtures were then analyzed at various intervals of time by an established protocol involving reduction with dithionite, acidification to pH 5, extraction with ethyl acetate and acetylation.⁹⁷ TLC analysis indicated in both cases a complex pattern of products corresponding to oligomers of variable molecular size. Product distribution, as apparent from TLC analysis, markedly changed with reaction time, reflecting the gradual conversion of the initial oligomers into more polar species of supposedly high molecular weight. The partial oxidative breakdown of indole units may also play a role in determining the complexity of reaction mixtures.^{2,109} A relatively abundant low

molecular weight fraction could be recovered when the oxidation reaction was halted and worked up in the early stages (*e.g.* 1 min). This fraction contained two main species which were isolated and identified on the basis of NMR and MS data as the 2,4'-biindole **3** and the 2,7'-biindole **4**, which appear to be obligatory intermediates in the oxidative polymerization of **1** in phosphate buffer at pH 7.0. Dimer **3** usually occurs in greater amounts than dimer **4**¹⁰⁶ so it was of interest to find that in the presence of 5% PVA a marked alteration in the dimer formation ratio occurred, with a significant prevalence for **4**, as observed from HPLC analysis. (**Figure 53**).

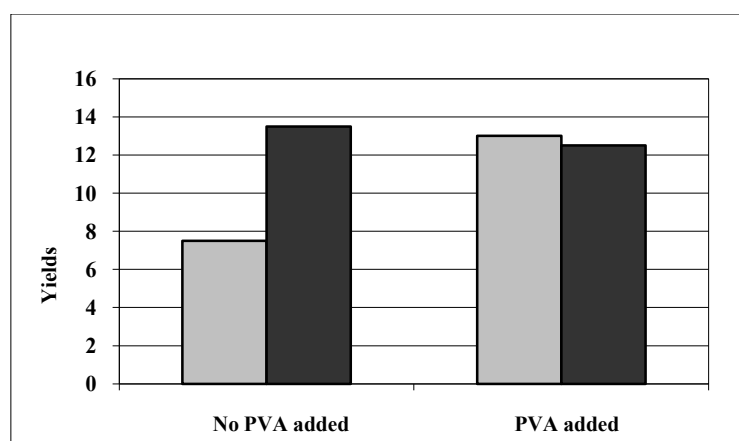


Figure 53. Percent molar yields (HPLC quantitation) of products **4** (gray) and **3** (black) obtained by DHI oxidation with peroxidase/H₂O₂ in phosphate buffer 0.1 M pH 7.0 and phosphate buffer/PVA.

A similar variation in product formation with medium was previously observed in the presence of organic solvents, such as methanol, ethanol, THF or acetone. For example, 75% acetone subverted the **3/4** product ratio from *ca* 1.6 to *ca* 0.3. Thus, the effect of PVA reported herein not only definitively supports the influence of the polarity of the medium on the chemical course of DHI polymerization and its coupling mode, but also provides an indirect demonstration of the active role of the polymer during DHI oxidation. Clearly, there is scope for further work to establish precisely the effects of PVA on the rate and mode of formation of higher oligomers.

Previous detailed investigations of solvent effects on the aggregation behavior of PVA¹¹³ have shown that water is a poor solvent for PVA molecules and the polymer chains would be largely unperturbed coils. Weak H-bonding is expected between PVA and water, whereby the polymer coils would be arranged midway between extended and collapsed conformations. They would therefore be capable of wrapping the growing indole chains thus affecting the oxidative polymerization process. Besides acting as a disaggregating agent, PVA may thus establish effective hydrophobic interactions driving the reactivity of quinonoid intermediates. Along these “hydrophobic tracks,” growing DHI oligomers might be somewhat shielded from both extensive water solvation and mutual interactions, thus exhibiting stable chromophoric features devoid of scattering effects. In this regard it is noteworthy that PVA concentrations as low as 1% serve to completely prevent synthetic eumelanin from precipitating, and higher PVA concentrations induce little or no further effect. We have established that PVA and other solvents exert regiocontrol over DHI coupling. One ponders whether it is possible in future work to tailor the properties of eumelanin by the fine modulation of pigment aggregation. The incorporation of stabilized eumelanin-type chromophores into PVA films or gels is another possible extension of this study for practical applications.

CONCLUSIONS

This chapter reports a novel experimental approach to the direct investigation of eumelanin-related chromophores which relies on the discovery of the efficient oligomer solubilizing properties of 1–10% PVA in phosphate buffer. By this approach I have shown that the initial chromophoric phases of DHI oxidation are due to absorbing species which persist in solution for a relatively long time indicating relatively stable mixtures of oligomers. This is the first spectrophotometric characterization of oxidized DHI oligomers as such (*i.e.* without derivatization) in the absence of precipitation and scattering. Interestingly, the addition of PVA, like other organic modifiers, has been found to significantly affect product distribution at the dimer stage, which may provide a new means of controlling the properties of the final polymer. Moreover, the absorption profile of the final polymer is similar to that of suspensions of synthetic DHI melanins except for the lack of scattering effects, suggesting that the latter are not the key determinant of the spectral features of eumelanin, in line also with recent conclusions by a different approach.¹¹¹ As a most relevant finding, I have finally shown that the polymer absorption spectrum can be significantly modified in the visible region, but not at the main UV band (320 nm), after a reductive treatment, corroborating the notion that the coexistence of reduced and oxidized components is critical for broad- band absorption and the dark chromophore.¹¹⁰

CHAPTER VI
Study of oxidative polymerization of 5,6-dihydroxyindole (1) by Dynamic
Light Scattering
(DLS) and Small-angle Neutron Scattering (SANS)

INTRODUCTION

As mentioned in previous chapters, eumelanin structure is still little understood.^{5,74, 103} Pending issues include the bonding modes of the base units, the basic three-dimensional structure of the pigment particle, and the average molecular weight.

In order to investigate the fundamental mechanism of eumelanin formation, Dynamic Light Scattering (DLS) and Small-angle Neutron Scattering (SANS) experiments were performed on the oxidation behavior of its precursor **1**. The reaction was studied in phosphate buffer without or with PVA that, as previously described, inhibits precipitation of the eumelanin polymer. In this chapter are reported the results of preliminary experiments carried out in collaboration with the group of Prof. L. Paduano of the University of Naples "Federico II".

DLS (also known as Photon Correlation Spectroscopy-PCS or Quasi-Elastic Light Scattering-QELS) is a technique which can be used to determine the size distribution profile of small particles in suspension or polymers in solution while SANS can give information about the size, shape and orientation of structures in a sample.

Details of the fundamental principles of these techniques are given in the following.

INTRODUCTION TO LIGHT SCATTERING

A light beam crossing a polarizable medium undergoes the phenomenon of light scattering in all directions due to local inhomogeneities. These are formed by the aggregates present in solution, that represent the scattering centers (*scatterers*) and, being larger than the particles of solvent, give a stronger signal than the background of scattered light from the solvent.¹¹⁴

In a microscopic description of the phenomenon, when light interacts with matter, the electric component of electromagnetic radiation induces an electronic polarization, and the resulting oscillating dipoles become secondary sources of light (scattered light). When the light source is a monochromatic incident laser beam, one can observe a fluctuation of scattering intensity (I_s) which depends on the time.

The scattered light is subject to phenomena of constructive and destructive interference, due to the presence of other particles nearby in the solution; therefore, variations observed in the scattered intensity can provide information concerning the reciprocal movement of the aggregates in solution.

A schematic representation of the scattering process is reported in **Figure 54**.

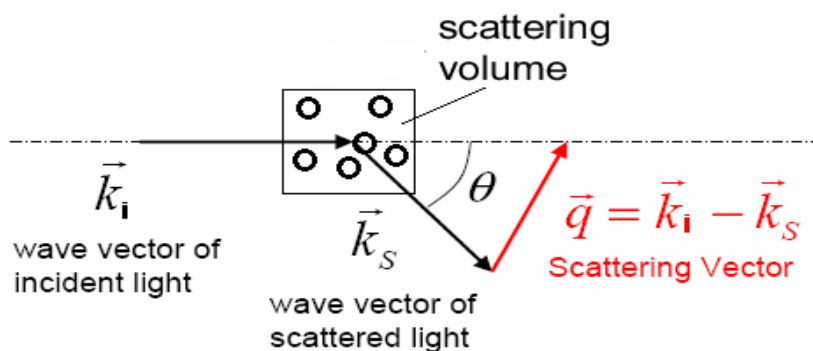


Figure 54. Schematic representation of scattering process.

An incident monochromatic laser beam of wavelength λ_i and wavevector \vec{k}_i irradiates the scattering volume V_s containing N particles. The scattered light, with wavevector \vec{k}_s , is observed at a scattering angle θ .

The scattering vector \vec{q} is defined as the vector difference between the two wavevectors (**Figure 54**).

In elastic scattering, which is predominant in the DLS experiments, the impact of photons occurs without changes in energy and then

$$|\vec{k}_i| = |\vec{k}_s| = \frac{2\pi}{(\lambda/n)}$$

$$q = |\vec{q}| = |\vec{k}_i - \vec{k}_s| = \frac{2\pi}{\lambda/n} (2 \sin(\theta/2))$$

where λ is the laser wavelength in vacuum and n is the refractive index of the solution.

Scattering light intensity (I_s) is a complex function that depends on many factors and can be described by the following relation

$$I_s \propto I_0 \frac{n_0^2}{\lambda^4} \left(\frac{\partial n}{\partial C} \right)^2 \cdot R^6 \cdot N \cdot P(Q) \cdot S(Q; \text{concentration})$$

where I_0 is incident light intensity, λ its wavelength in vacuum, n_0 and n are the refractive indexes of the solvent and solution respectively, $\partial n / \partial C$ is the refractive index increment, N is the number of scattering particles in the irradiated volume, R is the radius of the particles, $P(Q)$ and $S(Q; C)$ are the form factor and structure factor respectively.

$P(Q)$ provides useful information on the form and structure of macromolecules in solution while $S(Q; C)$ take into account the effects of interference between the particles, so it depends on concentration (for dilute solutions $S \approx 1$) and allows for an assessment of the structure of the solution.

In a diluted sample in which aggregates can act as *scatterers*, the scattered light intensity depends on several parameters:

- the optical contrast factor compared to the solvent (refractive index of the particles);
- the considered angle of measures;
- number, size and shape of particles;
- relative position of particles;

Specifically, the signal characteristic of the suspended particles can be detected experimentally only if their refractive index is sufficiently different from that of the solvent.

For this purpose often is introduced the relative index of refraction:

$$m = \frac{n_p}{n_s}$$

where subscripts p and s are related to particles and solvent respectively.

Particle/solvent systems with relative refractive index very close to 1 will be hardly visible in a light scattering experiment, since the aggregates will produce a weak signal compared to the background of light scattered by molecules of the solvent.

Assuming spherical particles, the concentration (N) and size (and hence polarizability, R^6) dependence shows the dependence of the scattered light from extensive properties such as the *scatterers* number and the volume of material that diffuses the light (Volume² or R^6).

In the case in which factors $S(Q,C)$ e $P(Q)$ are close to 1 (diluted solutions and particles that are small in comparison to the incident radiation wavelength), the scattered light varies with the sixth power of the radius of the involved particles.

Within the approximations made, in conditions of elastic *scattering* (*Rayleigh* regime), a particle with a radius of 50 nm diffuses light a million times more than a particle having a radius of 5 nm. Therefore the technique is more sensitive to the presence of large particles, rather than small.

Focusing on the dependence of scattering from scattering angle, we have:

$$I(Q) = P(Q) \cdot S(Q; C)$$

where $S(Q;C)$ takes into account interference between particles, providing information regarding the distribution of aggregates in space, while $P(Q)$ models the effect of the

shape of the particle, and is important only if particle size is comparable to the radiation wavelength λ .

Particles with sizes much smaller than λ can be considered point-like, so that $P \rightarrow 1$ and the diffused radiation is isotropic. In contrast, particles of a size comparable to the radiation wavelength λ , are characterized by an angular dependence of the scattered light, which can be predicted on the basis of the shape of such particles.

DYNAMIC LIGHT SCATTERING (DLS)

In a DLS experiment the fluctuations of the scattered light intensity, originated by Brownian motions of particles, are measured as a function of time at a constant scattering angle.

The temporal variation of the intensity is measured and represented usually through the so-called intensity autocorrelation function.

In practice, temporal fluctuations of the scattered light are recorded and analyzed through by estimating the time correlation function of the electric field

$$g^{(1)}(\tau) \propto \langle E_s(t) \cdot E_s(t + \tau) \rangle$$

where $E_s(t)$ and $E_s(t + \tau)$ represent the electrical field intensity of the scattered light at time t and $(t + \tau)$ and described the correlation level of a dynamic quantity in a delay time τ . This function is obtained by the intensity autocorrelation function:

$$g^{(2)}(\tau) \propto \langle I_s(t + \tau) \cdot I_s(t) \rangle$$

The two functions are correlated by Siegert relation¹¹⁵

$$g^{(2)}(\tau) = 1 + \beta |g^{(1)}(\tau)|^2$$

Where β is the coherence factor, which accounts for deviation from ideal correlation and depends on the experimental geometry.

For a monodisperse system, $g^{(1)}(\tau)$ will decay as a single exponential function with a characteristic relaxation time τ .¹¹⁶

$$g^{(1)}(q, \tau) = \exp(-q^2 D \tau)$$

whereas for a polydisperse system $g^{(1)}(\tau)$ will be multiexponential

$$g^{(1)}(q, \tau) = \sum_j W_j \exp(-q^2 D_j \tau)$$

where q is the scattering vector, D is the mutual diffusion coefficient, the subscript j indicate particles of different size present in solution and the weights W_j are related to particles concentration and their molecular weight.

Measuring the relaxation rate $G = 1/\tau$ from the first moment of the relaxation time distribution, from its value is possible to estimate the apparent translational diffusion coefficient D , through this relation:¹¹⁷

$$D = \lim_{q \rightarrow 0} \frac{\Gamma}{q^2}$$

D is, thus, obtained from the slope of G as a function of q^2 , where G is measured at different scattering angles.

Finally, using the Stokes–Einstein equation,^{118,119} the value of the hydrodynamic radius (R_h) of the equivalent sphere can be determined from

$$D = \frac{k_B T}{6\pi\eta R_h}$$

valid for infinite dilute dispersions, where η is the solvent viscosity, k_B the Boltzmann constant and T the absolute temperature.

In **Figure 55** is reported a schematic representation of a DLS experiment.

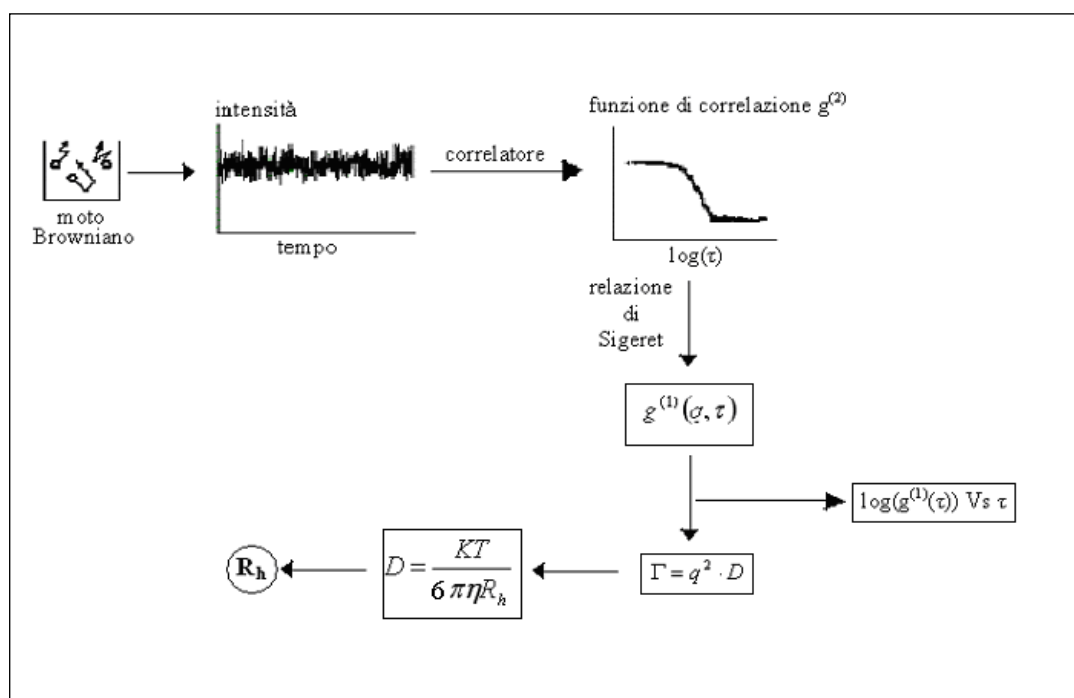


Figure 55. Schematic representation of a DLS experiment.

SMALL ANGLE NEUTRON SCATTERING (SANS)

SANS is a small angle scattering technique that exploits the wave-particle duality of the neutron and its unique nuclear properties to provide information about the size (length scale varies from 1 to 1000 nm) and shape of molecules and their assemblies.

In SANS, the scattering vector \vec{q} is used to describe the relationship between the incident and the scatter wavevectors. Its module, q , is the independent variable in a SANS experiment and has magnitude $q = 2\pi\sin(\theta/2)/\lambda$ and dimensions of $(\text{length})^{-1}$.

By combining q with the Bragg law of diffraction, one obtains the simple and useful relationship $d = 2\pi/q$, from which the molecular-level length scale (d) at any accessible q can be obtained. The dependent variable in a SANS experiment is the differential scattering cross-section, $d\Sigma/d\Omega$, improperly also called intensity of scattering $I(q)$. The scattering cross-section $d\Sigma/d\Omega$ contains information on interactions, size and shapes of aggregates present in the system, and can be expressed for a collection of monodisperse bodies as¹²⁰

$$\frac{d\Sigma}{d\Omega}(q) = n_p P(q) S(q) + \left(\frac{d\Sigma}{d\Omega}\right)_{\text{inch}}$$

where n_p represents the number density of the scattering object present in the system, $P(q)$ and $S(q)$ are respectively the form and the structure factor of the scattering particles, whereas $(d\Sigma/d\Omega)_{\text{inch}}$, takes into account for the incoherent contribution to the cross-section measured, mainly due to the presence of hydrogenated molecules, that has no angular dependence. The form factor contains information on the shape of the scattering objects, whereas the structure factor accounts for inter-particle correlations and is normally important for concentrated or charged systems. Provided that solutions are quite dilutes ($c < 10^{-3} \text{ mol kg}^{-1}$) the structure function $S(q)$ can be approximated to the unity, and the scattering cross-section is reduced to

$$\frac{d\Sigma}{d\Omega}(q) = n_p P(q) + \left(\frac{d\Sigma}{d\Omega}\right)_{inch}$$

By applying the appropriate model to experimental SANS data, chosen on the basis of the characteristics of the graph $I(q)$ vs. q , is possible to obtain the microstructural parameters of the aggregates.

The models used for fitting of graphs with a linear section of slope -2, as those obtained in the experiments reported in this thesis, consider analyzed objects as infinite planar sheets of thickness d , because in the characteristic SANS q range ($10^{-3}\text{\AA} \div 1\text{\AA}$) it is not possible detect the curve plateau.

The model adopted is therefore based on the following wording of the form factor:¹²¹

$$P(q) = 2\pi(\rho_v - \rho_0)^2 S \tau^2 \frac{1}{q^2} \frac{\sin^2\left(\frac{q\tau}{2}\right)}{\left(\frac{q\tau}{2}\right)^2}$$

where $(\rho_v - \rho_0)$ is the difference between the scattering density of particles and that of the solvent, τ is the thickness of the plane and S is the flat surface per volume unit.

RESULTS AND DISCUSSION

In a DLS experiment analysis of the intensity fluctuations allows determination of the distribution of diffusion coefficients of the particles which are converted then into a size distribution using established theories.^{118,122}

A solution of **1** in phosphate buffer exposed to an oxidizing atmosphere readily develops a brown coloration. However, DLS measurements require light-colored samples in order to prevent the decrease of the incident light intensity due to absorption. After several tests, an initial concentration of **1** 0.1 mM was selected as suitable for DLS measurements. A solution of **1** at this concentration in phosphate buffer was treated with peroxidase/H₂O₂ and, after filtration, the oxidation was followed by DLS. Data showed that the hydrodynamic radius R_h increased from an initial value of about 300 nm at 1 min from the addition of oxidant to reach ~ 1200 nm in about 1 hour (Figure 56).

This shows that the largest size that the eumelanin polymer can reach before precipitation corresponds to an R_h value of about 1200 nm.

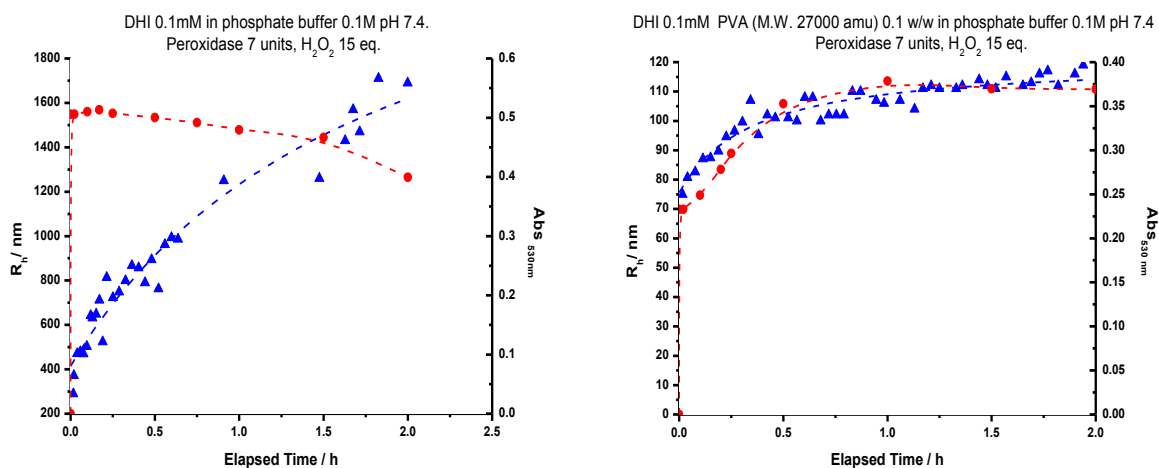


Figure 56. Hydrodynamic radii obtained by means of DLS technique (▲) and absorbance measured at 530 nm (●) for the oxidative process of **1** with peroxidase/H₂O₂ in phosphate buffer in the absence (left panel) and in the presence (right panel) of PVA 0.1 w/w.

Subsequently **1** was oxidized in phosphate buffer with 0.1% PVA (w/w), which is capable to inhibit precipitation at these concentrations of **1**. The eumelanin obtained by oxidation of **1** in PVA reached a smaller hydrodynamic radius (about 110 nm). Notably, the chromophoric variations that accompany oxidation were found to be independent of the value of the hydrodynamic radius, indicating a lack of direct correlation between molecular size and optical/absorption properties (**Figure 56**). A plausible interpretation of the effect of PVA is that it may prevent interactions among the polymeric chains, thus slowing down the growth rate and, at the same time, helping to maintain the polymer in solution.

In another series of experiments oxidation of **1** was carried out with tyrosinase; it is well known that tyrosinase-catalyzed oxidation is typically slower than the peroxidase-catalysis process,^{26,27} and such a slower rate was desirable to improve the quality of measurements. The results confirm this expectation. In the absence of PVA, the R_h value of incipient precipitation was reached after 6 h from the beginning of oxidation (**Figure 57**).

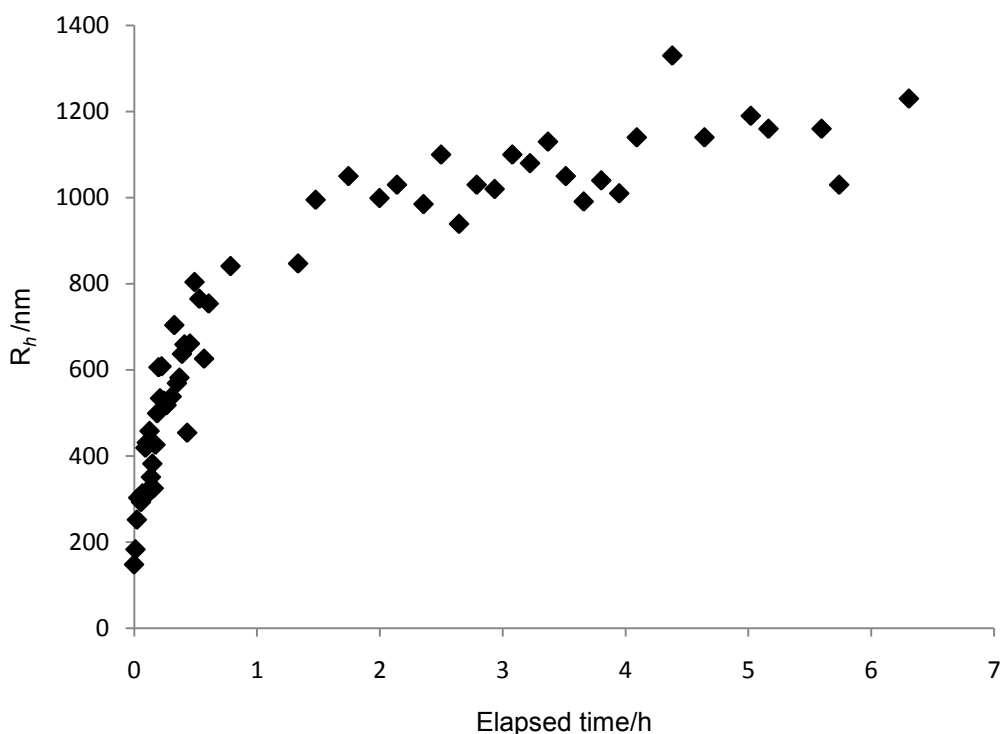


Figure 57. Hydrodynamic radii obtained by means of DLS technique for the oxidative process of **1** with tyrosinase in phosphate buffer.

In the presence of PVA (0.1%, w/w), the initially detected R_h value of ~ 30 nm gradually increased to about 100 nm over the time span of 5 hours. In subsequent experiments, it was noted that even lower concentrations of PVA (down to 0.01%, w/w) were able to inhibit the precipitation of polymer. A series of measurements at different PVA percentages was then carried out, and it was observed that the kinetics of growth of eumelanin slowed and the hydrodynamic radius of the aggregates decreased with increasing concentration of PVA. **Figure 58** shows data for the four PVA concentrations studied: 0.01%, 0.05%, 0.1% and 0.5%, w/w.

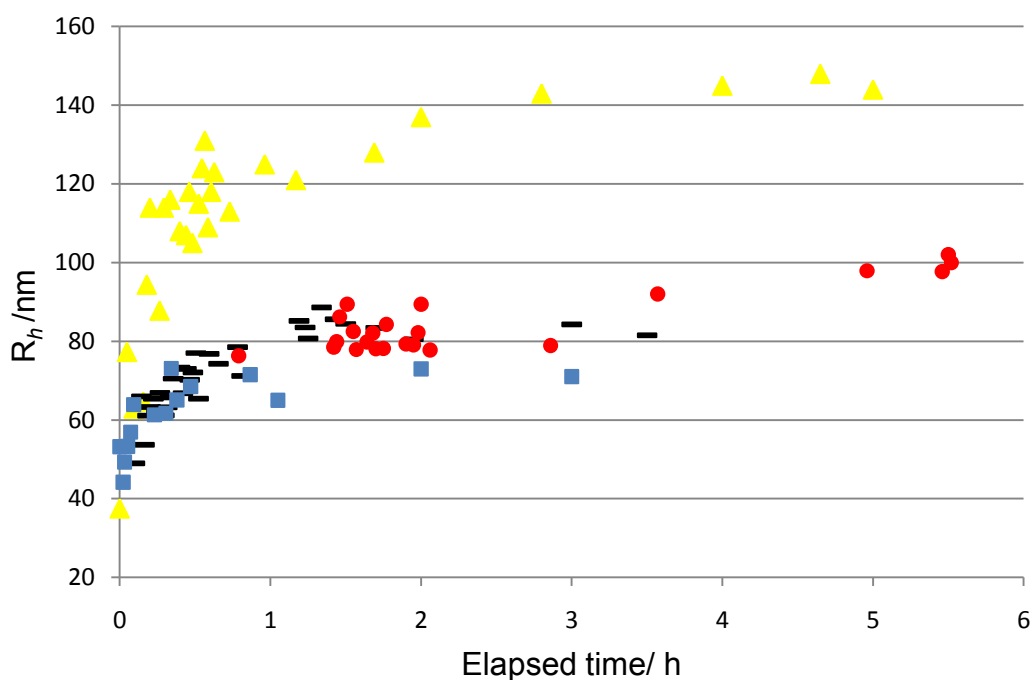


Figure 58. Hydrodynamic radii obtained by means of DLS technique for the oxidative process of **1** with tyrosinase in phosphate buffer with several PVA percentages w/w: (\blacktriangle) 0.01%, ($-$) 0.05%, (\bullet) 0.1%, (\blacksquare) 0.5%.

In all DLS experiments performed a single distribution of R_h shifted gradually to higher values (**Figure 59**). Failure to detect multiple hydrodynamic radii may indicate that growth of the polymer occurs sequentially.

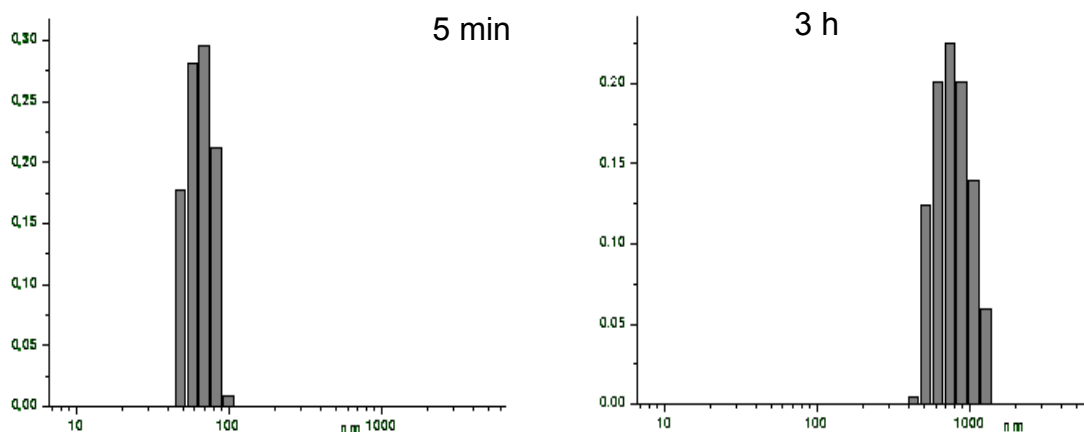


Figure 59. R_h distributions determined by means of DLS technique at two different times.

In order to gain more information on the polymerization process, SANS measurements were then performed.

The measurements were carried out in deuterated phosphate buffer in order to minimize the incoherent scattering contribution to the total cross section; substrate concentrations were larger than in DLS measurements, on account of instrumental sensitivity.

As shown by the DLS experiments, in the presence of PVA the eumelanin polymer grew to a certain size within a few hours and then remained “stable” for days. SANS measurements were performed at 24 hours from the beginning of the oxidation to make sure that the system was in a stable condition. A graph of scattering intensity $I(q)$ vs. scattering vector q shows a power law of -2 at low q : this hints that the final polymer is a two-dimensional object, such as a plane or a disk. Based on this model, a thickness of 44 ± 4 nm could be estimated. Furthermore, since $d = 2\pi/q$, the presence of small

oligomers (less than about 30 nm) was ruled out by the fact that no peaks were observed at values over 0.01 \AA^{-1} . Several different concentrations of PVA were tested, but all samples analyzed showed a rather uniform behavior (**Figure 60**). No further information concerning polymer size could be deduced from these measurements because of instrumental limitations.

SANS data obtained in the absence of PVA at 2 min after oxidant addition produced a graph of $I(q)$ vs. q similar to that recorded in the presence of PVA; in particular, a power law of -2 at low values of q , and the absence of peaks at high values ($0.01\text{-}0.1 \text{ \AA}^{-1}$) (**Figure 61**). The curvature of the graph obtained in the absence of PVA may be traced back to the fact that the measurement was performed at 2 min after the beginning of the oxidative polymerization process, when the largest objects in the mixture were still modest in size.

Overall, the SANS data are in agreement with a growth model of the polymer consisting in the consecutive addition of low molecular weight units; the observed lack of small objects is particularly significant in this respect.

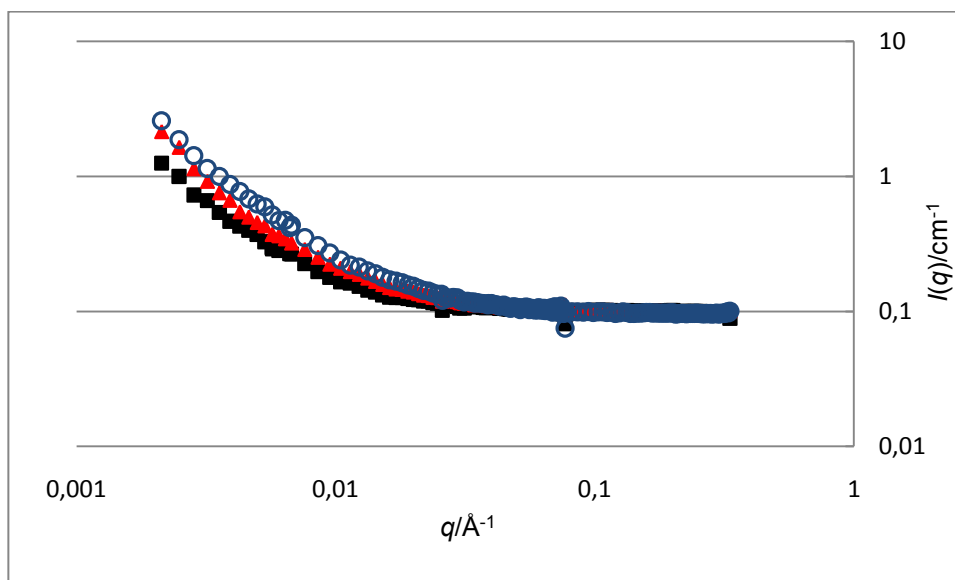


Figure 60. Scattering Intensity vs. scattering vector obtained by SANS technique for the oxidative process of **1** with tyrosinase at 24 hours in phosphate buffer with several PVA percentage w/w: (■) 0.05%, (▲) 0.1%, (○) 0.2%.

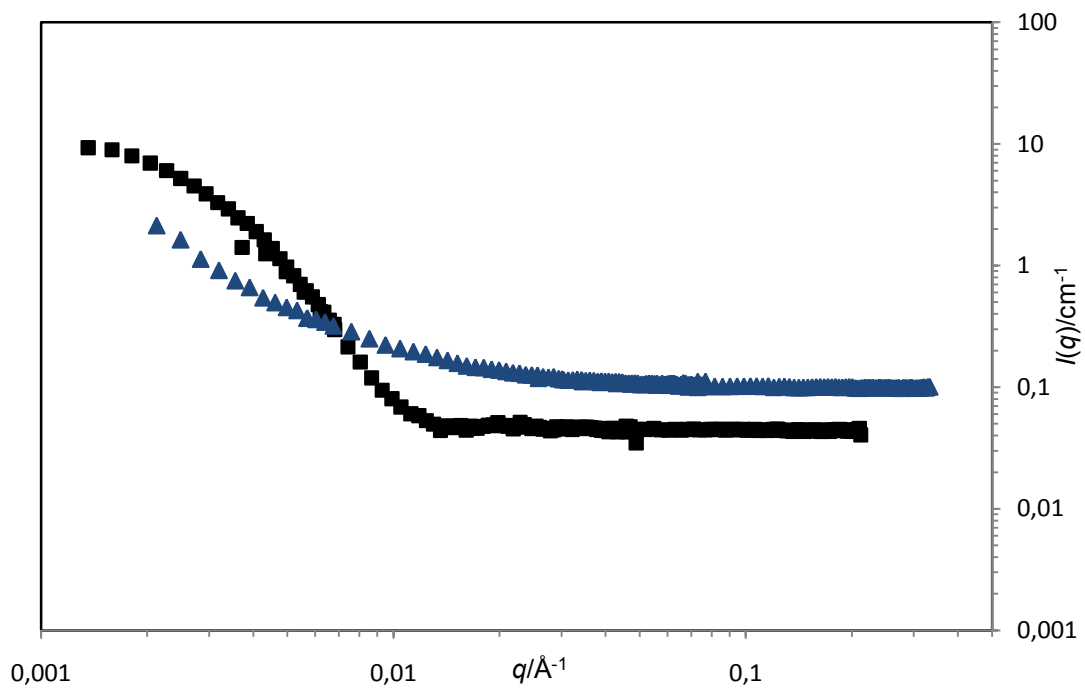


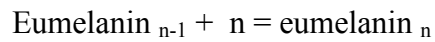
Figure 61. Scattering intensity vs. scattering vector obtained by SANS technique for the oxidative polymerization of **1** with tyrosinase in phosphate buffer without PVA at 2 min (■) and with PVA (0.01% w/w at 24 h (▲)).

CONCLUSIONS

From DLS experiments it was inferred that the eumelanin polymer grows sequentially until it reaches such a size that it can no longer remain in solution ($R_h \sim 1200$ nm), at which stage it precipitates out. Such precipitation is inhibited in the presence of PVA: in these conditions, smaller polymer sizes can be reached.

The SANS measurements showed that the polymer has a two-dimensional structure, such as a flat or a disk; it was not possible to detect oligomers consisting of a small number of monomers in the mixture.

In summary, the growth process of the polymer should be of the type:



where n is an oligomer consisting of 1 to 5 monomer units, that cannot be detected by the instrumentation adopted.

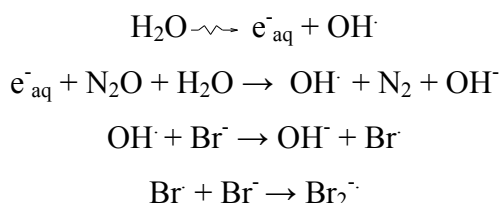
CHAPTER VII

Computational investigation of the stability of DHI-related catechols, radicals, and quinonoid forms

INTRODUCTION

Another topic addressed during the PhD study concerns the computational stability of the radical and quinone forms of DHI (**1**) and related catechols. The chemical and spectroscopic characterization of 5,6-indolequinones and their semiquinones, key transient intermediates in the oxidative conversion of 5,6-dihydroxyindoles to eumelanin biopolymers, is a most challenging task.

The unstable semiquinone and quinone species produced by oxidation of DHI and related compounds have been detected in previous studies by the pulse radiolysis,^{73,123} technique that allows the recording of UV-vis spectra in a time comparable to the lifetime of these species. In pulse radiolysis experiments, the oxidizing species $\text{Br}_2^{\cdot -}$ is generated by irradiating N_2O -saturated solutions of KBr. $\text{Br}_2^{\cdot -}$ radicals are formed within 0.1 μs after the radiation pulse according to the following equations



This technique allowed to record the first transient spectrum at such time that the buildup of initial radical absorption was complete and that subsequent decay had not proceeded to any significant extent.

DHI is converted by one-electron oxidation into an unstable semiquinone that decays with second order kinetics ($2k = 3.0 \times 10^9 \text{ M}^{-1} \text{ s}^{-1}$) to give a chromophore at 450 nm (**Figure 62**).¹²³

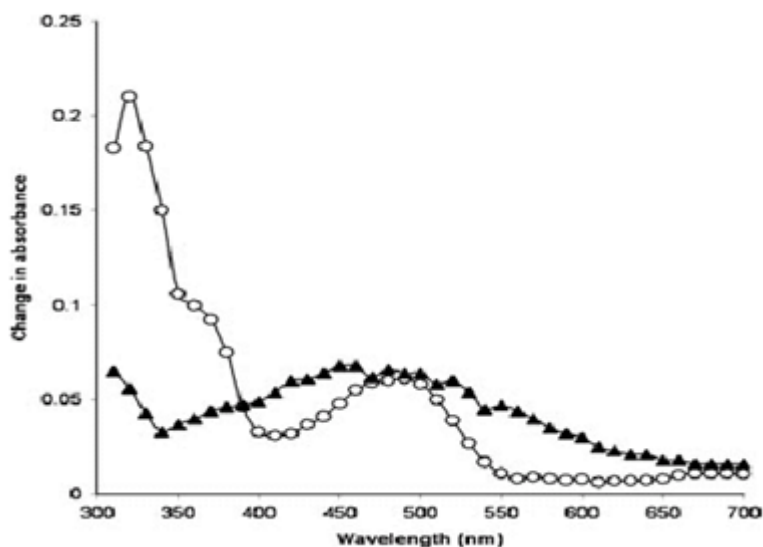
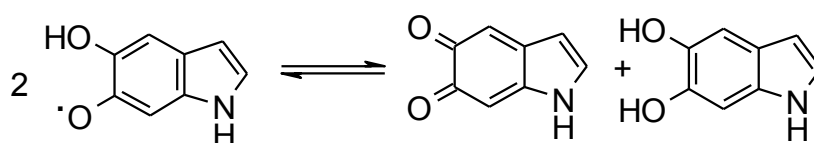


Figure 62. Absorption changes 14 μs (\circ) and 864 μs (\blacktriangle) after pulse radiolysis of an N_2O -saturated aqueous solution of 3.0×10^{-4} M DHI in the presence of 0.1 M KBr and 0.01 M phosphate buffer, pH 7.0.¹²³

Similarly, from 5,6-dihydroxy-3-iodoindole a semiquinone is obtained that decays with second-order kinetics ($2k = 1.1 \times 10^{10} \text{ M}^{-1} \text{ s}^{-1}$) to give a chromophore with broad absorption bands centered around 600 and 750 nm.⁷³

Commonly it is believed that the semiquinone decays with a disproportionation mechanism to give an *o*-quinone in equilibrium with its tautomeric quinonmetide and quinonimine forms (**Scheme 13**).



Scheme 13. Disproportionation mechanism of DHI radical.

However, the position of the absorption maximum computed for the 5,6-indolquinone⁷¹ (280 nm) does not seem to be compatible with the spectrophotometric course of the reaction under the conditions of pulse radiolysis experiments.

These results may be of relevance in connection with the interpretation of the chemical course of pulse radiolysis experiments involving oxidation of DHI and related catechols.

RESULTS AND DISCUSSION

The mechanism of bimolecular decay of semiquinones derived from dihydroxyindoles has been investigated by computational methods. The dihydroxyindoles considered are shown in **Figure 63**:

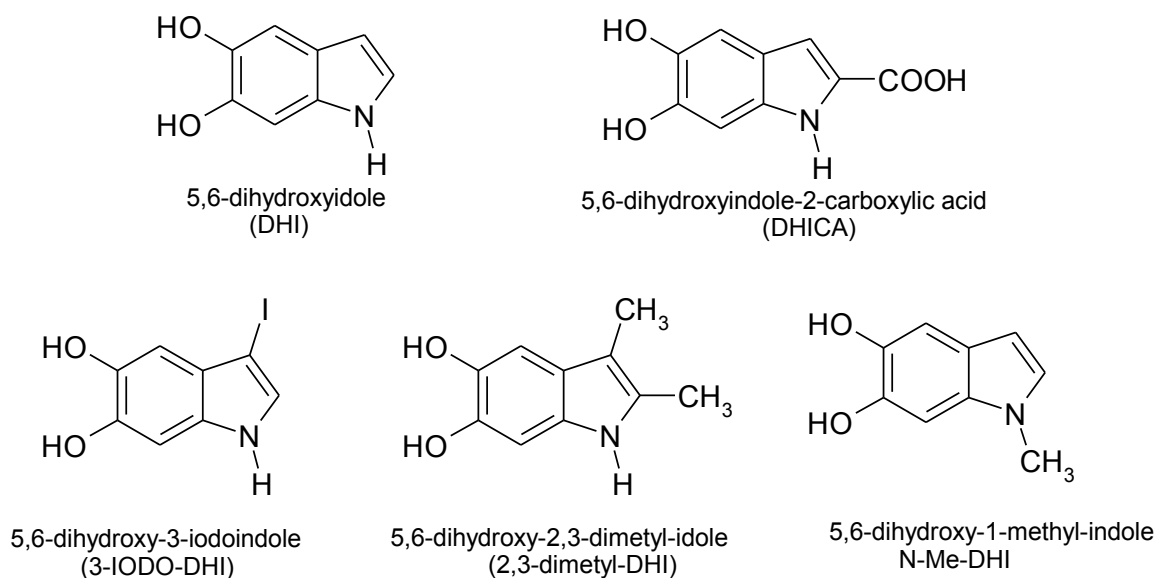
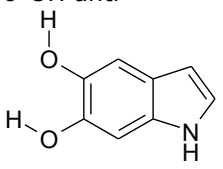
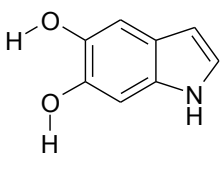
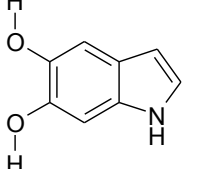
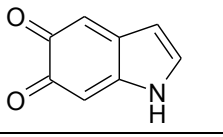
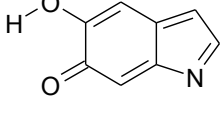
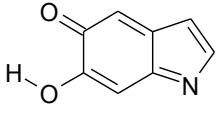
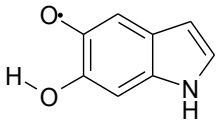
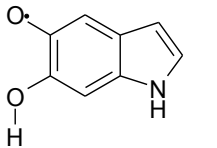
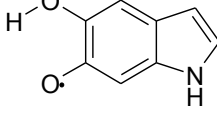
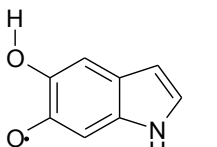


Figure 63. Structures of dihydroxyindoles investigated by computational methods

For each species examined different tautomers / conformers have been explored, whose geometries were optimized at the DFT level with the hybrid functional PBE0^{32b} and a reasonably large basis set [6-31+G(d,p)]⁹⁹; the unrestricted formulation was adopted to describe radical species. The calculations were performed both in vacuum and in aqueous environment, modeled by the polarizable continuum model (PCM).^{52,53,76} Selected single point energy evaluations were also performed at the PBE0/6-311++G(2d,2p) level. Energies and free energies calculated for each specie are reported in the following tables (**Table 6, 7, 8, 9, 10**).

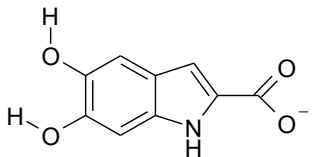
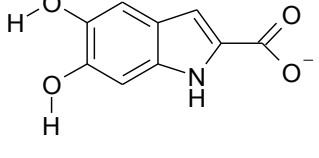
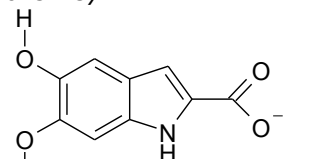
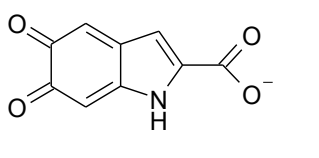
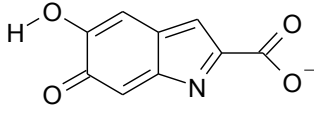
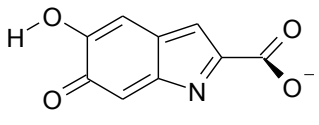
Table 6. Relative energies and free energies for several tautomers / conformers of DHI. Data are reported in kcal mol⁻¹

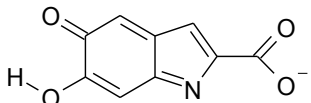
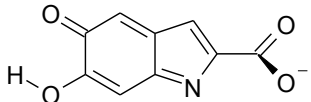
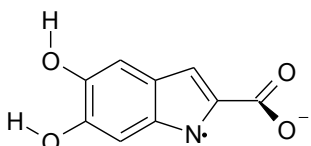
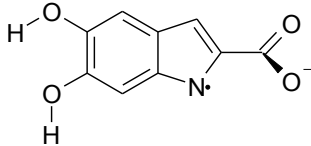
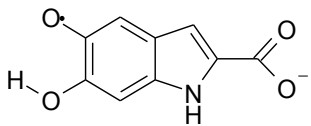
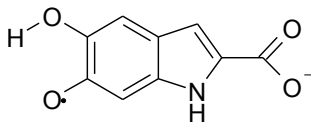
DHI	Energy [E_{vac}]	Free energy [$G_{vac,RRHO}$]	PCM free energy [G_{PCM}]	PCM free energy [$G_{PCM,RRHO}$]	Energy (large base) [E_{vac}]
<i>QH₂</i>					
5-OH anti, 6-OH anti 	0.0 ^a	0.0 ^b	0.0 ^c	0.0 ^d	0.0 ^e
5-OH syn, 6-OH syn 	1.0	0.8	0.2	0.4	
5-OH anti, 6-OH syn 	5.1	5.1	2.2	2.5	
<i>Q</i>					
quinone 	0.0 ^f	0.0 ^g	0.0 ^h	0.0 ⁱ	0.0 ^l
quinonemethide 	0.6	1.4	7.6	8.2	
quinonimine	4.9	5.4	12.4	12.7	

					
<i>QH</i>					
5-yl, 6-anti 	1.0	1.2	1.4	1.5	
5-yl, 6-syn 	11.6	11.1	6.5	6.2	
6-yl, 5-syn 	0.0 ^m	0.0 ⁿ	0.0 ^o	0.0 ^p	0.0 ^q
6-yl, 5-anti 	9.7	9.1	5.0	4.7	

^a -513.720071; ^b -513.614396; ^c -513.733427; ^d -513.628146; ^e -513.841828;
^f -512.464148; ^g -512.382885; ^h -512.485136; ⁱ -512.403820; ^l -512.583587, ^m -513.098166;
ⁿ -513.004531; ^o 513.112156; ^p 513.018637; ^q 513.219041 (data in hartree)

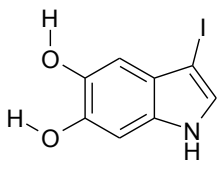
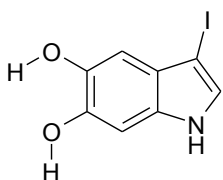
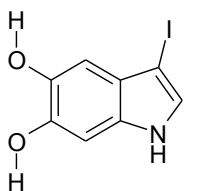
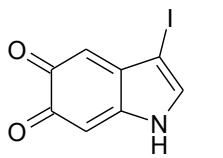
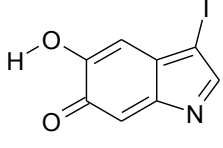
Table 7. Relative energies and free energies several tautomers / conformers of DHICA. Data are reported in kcal mol⁻¹

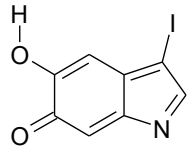
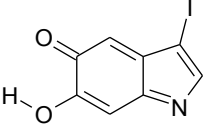
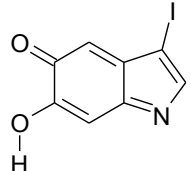
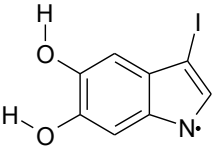
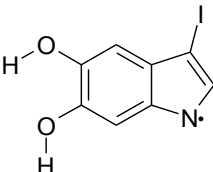
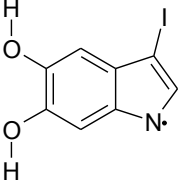
DHICA	PCM free energy [G _{PCM}]	PCM free energy [G _{PCM,RRHO}]	PCM free energy (large base) [G _{PCM}]
<i>QH₂</i>			
carboxylate, 5-OH <i>anti</i> , 6-OH <i>anti</i> 	0.0 ^a	0.0 ^b	0.0 ^c
carboxylate, 5-OH <i>syn</i> , 6-OH <i>syn</i> 	0.2	0.4	
carboxylate, 5-OH <i>anti</i> , 6-OH <i>syn</i> 	2.2	2.2	
<i>Q</i>			
carboxylate, quinone 	0.0 ^d	0.0 ^e	0.0 ^f
carboxylate, quinonemethide, planar 	10.8	Saddle point	
carboxylate, quinonemethide, staggered 	9.9	10.1	

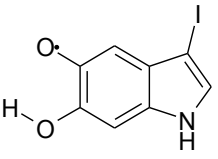
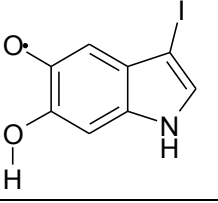
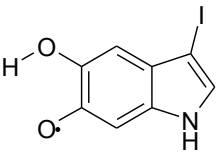
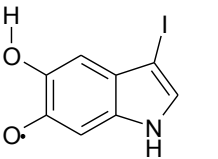
carboxylate, quinonimine, planar 	16.1	Saddle point	
carboxylate, quinonimine, staggered 	16.1	15.7	
<i>QH'</i>			
carboxylate, 1-yl, 5-OH <i>anti</i> , 6-OH <i>anti</i> 	22.2	20.7	
carboxylate, 1-yl, 5-OH <i>syn</i> , 6-OH <i>syn</i> 	22.9	21.7	
carboxylate, 5-yl, 6-OH <i>anti</i> 	1.5	1.7	
carboxylate, 6-yl, 5-OH <i>syn</i> 	0.0 ^g	0.0 ^h	0.0 ⁱ

^a -701.674280; ^b -701.571375; ^c -701.845821; ^d -700.427655; ^e -700.349140; ^f -700.597591
^g -701.054339; ^h -700.963458; ⁱ -701.225490 (data in hartree)

Table 8. Relative energies and free energies for several tautomers / conformers of 3-iodo-DHI. Data are reported in kcal mol⁻¹

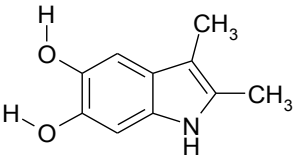
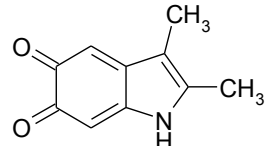
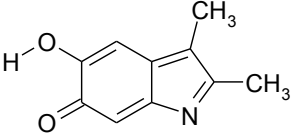
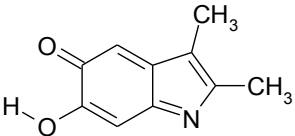
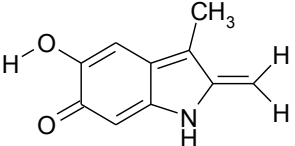
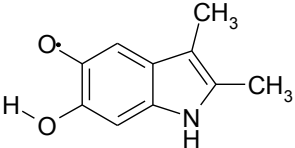
3-iodo-DHI	Energy [E_{vac}]	Free energy [$G_{\text{vac,RRHO}}$]	PCM free energy [G_{PCM}]	PCM free energy [$G_{\text{PCM,RRHO}}$]
QH_2				
5-OH <i>anti</i> , 6-OH <i>anti</i> 	0.0 ^a	0.0 ^b	0.0 ^c	0.0 ^d
5-OH <i>syn</i> , 6-OH <i>syn</i> 	1.4	1.2	0.2	0.3
5-OH <i>anti</i> , 6-OH <i>syn</i> 	5.2	5.2	2.2	2.4
Q				
Quinine 	2.8	2.0	0.0 ^e	0.0 ^f
quinonemethide, 5-OH <i>syn</i> 	0.0 ^g	0.0 ^h	4.8	5.3
quinonemethide,	7.4	7.0	8.3	8.6

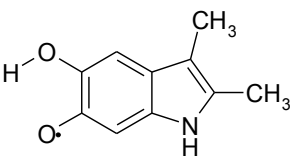
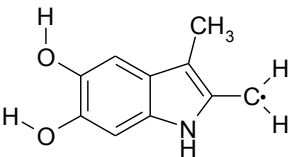
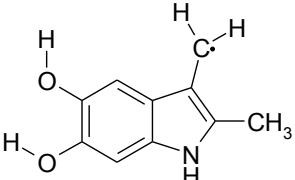
5-OH <i>anti</i> 				
quinonimine, 6-OH <i>anti</i> 	6.2	5.9	11.1	11.4
quinonimine, 6-OH <i>syn</i> 	12.6	11.9	14.2	14.2
<i>QH^a</i>				
1-yl, 5-OH <i>anti</i> , 6-OH <i>anti</i> 	13.9	12.8	15.0	13.8
1-yl, 5-OH <i>syn</i> , 6- OH <i>syn</i> 	14.6	13.5	15.6	14.6
1-yl, 5-OH <i>anti</i> , 6-OH <i>syn</i> 	18.5	17.4	17.3	16.2
5-yl, 6-OH <i>anti</i>	0.9	1.1	1.2	1.3

				
5-yl, 6-OH <i>syn</i> 	11.4	11.0	6.2	6.0
6-yl, 5-OH <i>syn</i> 	0.0 ⁱ	0.0 ^l	0.0 ^m	0.0 ⁿ
6-yl, 5-OH <i>anti</i> 	9.3	8.7	4.9	4.6

^a-524.532738; ^b524.441171; ^c-524.546393; ^d-524.454964; ^e-523.293643; ^f-523.226692;
^g-523.277158; ^h-523.209055; ⁱ-523.908182; ^l-523.828975; ^m-523.92244; ⁿ-523.843128
 (data in hartree)

Table 9. Relative energies and free energies for several tautomers / conformers of 2,3-dimethyl-DHI. Data are reported in kcal mol⁻¹

2,3-dimethyl-DHI	Energy [E_{vac}]	Free energy [$G_{vac,RRHO}$]	PCM free energy [G_{PCM}]	PCM free energy [$G_{PCM,RRHO}$]	Energy (large base) [E_{vac}]
QH_2					
5-OH <i>anti</i> , 6-OH <i>anti</i> 	0.0 ^a	0.0 ^b	0.0 ^c	0.0 ^d	0.0 ^e
Q					
quinone 	11.6	9.9	7.0 7.2 ^f	5.8 6.0 ^f	13.4
quinonemethide 	8.8	8.1	10.8 10.8 ^f	10.1 10.1 ^f	
quinonimine 	15.6	14.8	19.1 18.9 ^f	18.2 18.2 ^f	
extended quinonemethide 	0.0 ^g	0.0 ^h	0.0 ⁱ	0.0 ^l	0.0 ^m
QH'					
5-yl, 6-OH <i>anti</i> 	1.3	2.0	1.9	3.0	

6-yl, 5-OH <i>syn</i> 	0.0 ⁿ	0.0 ^o	0.0 ^p	0.0 ^q	0.0 ^r
2-benzylic, 5-OH <i>anti</i> , 6-OH <i>anti</i> 	13.8	13.1	15.2	14.7	
3-benzylic, 5-OH <i>anti</i> , 6-OH <i>anti</i> 	17.1	16.2	17.6	17.1	

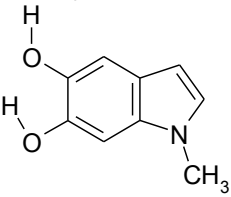
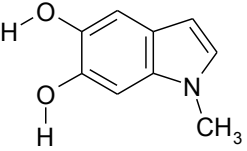
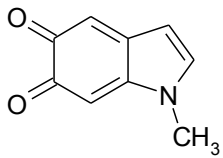
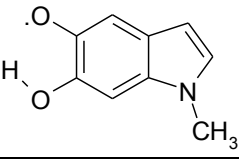
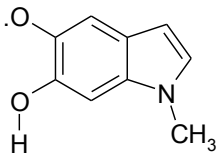
^a-592.266824; ^b-592.110863; ^c-592.279781; ^d-592.124149; ^e-592.404484;

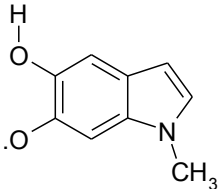
^f Values computed in methanol; ^g-591.034437; ^h-590.899891; ⁱ-591.048844, -591.048379^f;

^l-590.914726, -590.914298^f; ^m-591.172704; ⁿ-591.647585; ^o-591.504139; ^p-591.662237;

^q-591.519577; ^r-591.784297 (data in hartree)

Table 10. Relative energies and free energies for several tautomers / conformers of N-Me-DHI. Data are reported in kcal mol⁻¹

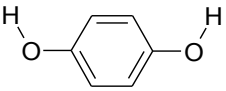
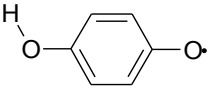
N-Me-DHI	Energy [E _{vac}]	Free energy [G _{vac,RRHO}]	PCM energy [EPCM]	PCM free energy [G _{PCM,RRHO}]
<i>QH₂</i>				
5-OH anti,6-OH anti 	0.0 ^a	0.0 ^b	0.0c	0.0 ^d
5-OH syn, 6-OH syn 	1.0	0.9	0.2	0.4
<i>Q</i>				
Quinone 	0.0 ^e	0.0 ^f	0.0g	0.0 ^h
<i>QH'</i>				
5-yl, 6-OH anti 	1.1	1.2	1.4	1.4
5-yl, 6-OH syn 	11.8	11.2	6.9	6.1

6-yl, 5-OH syn 	0.0 ⁱ	0.0 ^l	0.0 ^m	0.0 ⁿ
6-yl, 5-OH anti 	9.7	9.1	5.3	5.1

^a -552.982542; ^b -552.85143; ^c -552.979394; ^d -552.848342; ^e -551.727716427;
^f 551.620846; ^g -551.732013; ^h -551.625052; ⁱ -552.361363; ^l -552.242211; ^m -552.359077;
ⁿ -552.239798 (data in hartree)

As reference compound to validate the computational results and possibly to correct for systematic errors *p*-benzoquinone was considered (**Table 11**), for which experimental data are available in the literature.¹²⁵

Table 11. Relative energies and free energies for hydroquinone, *p*-benzoquinone and the related phenoxyl radical. Data are reported in kcal mol⁻¹

<i>p</i> -benzoquinone	Energy [E_{vac}]	Free energy [$G_{\text{vac,RRHO}}$]	PCM free energy [G_{PCM}]	PCM free energy [$G_{\text{PCM,RRHO}}$]	Energy (large base) [E_{vac}]
QH_2					
C_{2h} 	0.0 ^a	0.0 ^b	0.0	0.0	0.0 ^c
C_{2v} 	0.1	0.1	0.0 ^d	0.0 ^e	0.1
Q					
D_{2h} 	0.0 ^f	0.0 ^g	0.0 ^h	0.0 ⁱ	0.0 ^l
$QH\cdot$					
C_s 	0.0 ^m	0.0 ⁿ	0.0 ^o	0.0 ^p	0.0 ^q

^a-382.283145; ^b-382.203648; ^c-382.377467; ^d-382.294580; ^e-382.215177; ^f-381.041526; ^g-380.985144; ^h-381.050980; ⁱ-380.994688; ^l-381.133294; ^m-381.647944; ⁿ-381.582033; ^o-381.661873; ^p-381.595801; ^q-381.740244 (data in hartree)

Considering for simplicity only the most stable tautomers / conformers obtained, the energy parameters for the reaction of disproportionation of the semiquinone to quinone and catechol were then calculated (**Table 12**).

Table 12. The energy balances for the disproportionation reaction, referred to the most stable tautomers / conformers identified for each species. Data are reported in kcal mol⁻¹

Substrate	Reaction	ΔE_{vac}	$\Delta G_{\text{vac,RRHO}}$	ΔG_{PCM}	$\Delta G_{\text{PCM,RRHO}}$	ΔE_{vac} (large base)
DHI	2 QH [•] → QH ₂ + Q	7.6	7.4	3.6	3.3	7.9
DHICA	2 QH [•] → QH ₂ + Q			4.2	4.0	4.7 ^a
3-iodo-DHI	2 QH [•] → QH ₂ + Q (quinonemethide)	4.0	4.8	7.9	8.2	3.1
	2 QH [•] → QH ₂ + Q (quinone)	6.8	6.8	3.0	2.9	7.2
2,3-dimethyl-DHI	2 QH [•] → QH ₂ + Q (extended quinonemethide)	-3.8	-1.6	-2.6	0.2	-5.4
	2 QH [•] → QH ₂ + Q (quinone)	7.7	8.4	4.4	6.0	8.0
N-Me-DHI	2 QH [•] → QH ₂ + Q	7.8	7.6	3.9		
<i>p</i> -benzoquinone	2 QH [•] → QH ₂ + Q	-18.1	-15.5	-13.7	-11.5	-19.0

The experimental standard free energy change for the disproportionation reaction of *p*-benzosemiquinone radicals¹²⁴ in DMSO (-15.1 kcal mol⁻¹) compares quite well with the results computed in vacuo (-15.5 kcal mol⁻¹). Even in aqueous solution, the experimental value at low pH ($\Delta G = -14.4$ kcal mol⁻¹) is reasonably close to the value obtained by a PCM calculation (-11.5 kcal mol⁻¹). Overall, this preliminary comparison with experimental results hints that the computational levels adopted are capable of providing useful estimates of the reaction energetics in the cases at hand.

In DHI, DHICA, 3-iodo-DHI and N-Me-DHI the disproportionation of semiquinone radicals to quinones and catechol-like species is in general thermodynamically unfavorable.

In 2,3-dimethyl-DHI, conversion of the 2-methyl substituent into an exocyclic methylene provides a pathway for further stabilization of the quinonoid species; in this case, the overall thermodynamic balance for the disproportionation reaction becomes favorable.

CONCLUSIONS

The disproportionation reaction of radicals derived from DHI and related compounds appears to be thermodynamically unfavorable; in those situations in which 5,6-dihydroxyindole oxidation occurs by the initial formation of phenoxyl radicals, these will display little tendency to convert into indolequinones, and the concentration of indolequinones will remain small with respect to that of the radicals. On account of the high reactivity expected from radical species, it is conceivable that other reaction channels may prevail over the disproportionation reaction (e.g., radical coupling reactions).

Phenoxyl radicals are definitely involved in the initial stages of pulse-radiolysis oxidation of 5,6-dihydroxyindoles and their derivatives: however, the computational results presented above cast some doubt on the contention that the reaction proceeds in all cases through the intermediacy of indolequinones. Instead, different / concurrent reaction pathways may be involved, depending on the energetic balance of the specific disproportionation reaction.

In specific chemical or enzymatic oxidation conditions (e.g., periodate oxidation, or tyrosinase-catalyzed oxidation), two-electron oxidation products may be formed and released directly by mechanisms which do not imply the disproportionation of phenoxyl radicals: in these cases, kinetic considerations may favor indole / quinone couplings even at the expense of a thermodynamically favorable comproportionation reaction ($H_2Q + Q = 2 QH$). Thus, in principle, both reaction pathways remain available.

CHAPTER VIII

Other studies

INTRODUCTION

During the course of my PhD, I collaborated in the computational aspects of a project on the chemistry of nitrated lipids.

Nitrated derivatives of unsaturated fatty acids have emerged during the past decade as important products of lipid modification under (patho)physiological conditions associated with oxidative stress and elevated production of nitric oxide (NO).^{125,126} Although the detailed structural features of the nitrated fatty acids generated in vivo remain to be defined, a significant proportion of them appears to be present in the form of nitroalkene derivatives, such as the nitrooleic acids and the nitrolinoleic acids.^{127,128} These latter comprise four isomeric derivatives of (*Z,Z*)-9,12-octadecadienoic acid exhibiting a conjugated nitro group on the terminal (9- and 13-) or inner (10- and 12-) positions of the (*Z,Z*)-1,4-pentadienyl system. So far, 10-nitrolinoleic acid, (*9E,12Z*)-10-nitrooctadecadienoic acid (**24**), and the 12-nitro isomer have been detected in human plasma and urine by LC-MS techniques,¹²⁹⁻¹³¹ whereas 9-nitrolinoleic acid, (*9E,12Z*)-9-nitrooctadecadienoic acid (**23**), and its 13-nitro isomer have been described only as products of chemical nitration of linoleic acid in an organic solvent.^{132,133}

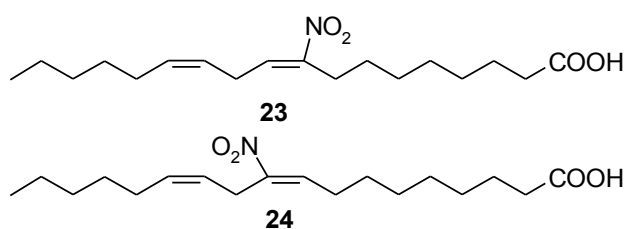


Figure 64. Structures of (*9E,12Z*)-9-nitrooctadecadienoic acid (**23**) and (*9E,12Z*)-10-nitrooctadecadienoic acid (**24**).

A substantial body of evidence indicates that nitrolinoleic acids behave as pluripotent signaling molecules that transduce the actions of NO via multiple mechanisms,^{131,134,135} which in part are receptor-mediated and in part reflect the

electrophilic and NO-releasing behavior of the nitropentadiene reactive moiety in a physiological milieu. The electrophilic nature of nitrolinoleates is deduced by their ability to cause post-translational modifications of protein residues^{133,136,137} and by the occurrence in vivo of a significant proportion of vicinal hydroxynitro derivatives,^{131,134} suggesting addition of water onto the double bond. The ability of nitrolinoleic acids to release NO is the focus of much interest. Experimental evidence derived from different experiments (EPR, chemiluminescence, deoxy- and oxymyoglobin assays)^{134,138-141} suggests the release of NO as well as nitrite,^{139,140} but the detailed pathways remain to be definitively assessed. In the presence of other lipids or amphiphiles at levels above the critical micellar concentration, nitrolinoleic acids are stabilized and become highly resistant to NO-release. This finding suggests that nitrolinoleic acids provide a hydrophobically stabilized NO reserve and, in view of their accumulation to detectable levels in lipophilic biological compartments, represent the single largest pool of bioactive oxides of nitrogen in the vasculature.¹³⁴ Apart from the above studies, current knowledge of the chemical behavior and fate of these nitroalkene fatty acid derivatives under physiologically relevant conditions is scanty and limited to the decomposition routes supposedly associated to their NO donor abilities. Surprising is also the lack of general information about the free radical oxidation pathways of the nitro-1,4-pentadienyl system, the reactive core of nitrated polyunsaturated fatty acids. A detailed elucidation of the chemical properties of nitrolinoleic acids under physiologically relevant conditions is therefore of paramount importance for further progress toward an understanding of the signaling capabilities of these bioactive lipids. To this aim, access to the individual isomers is essential to advancing structure-activity knowledge and to rationally design new more active structural variants for therapeutic purposes. Was thus developed the first convenient access route to pure **23** and **24** as free acids and a comparative investigation of their chemical behavior in aqueous phosphate buffer at pH 7.4. By integrating product analysis with mechanistic experiments, was provided a comparative description of the basic chemistry of nitrolinoleic acids under physiologically relevant conditions. The remarkable position-dependent influence of the nitro group on the oxidation behavior of the 1,4-pentadienyl moiety is also addressed with the aid of a density functional theory (DFT) investigation.

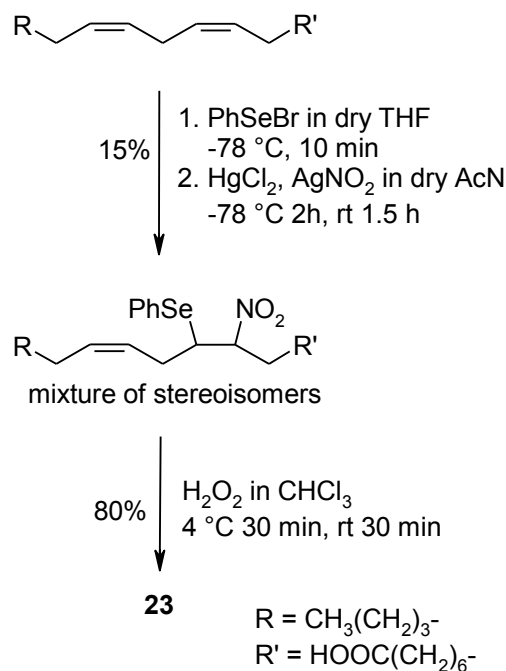
RESULTS AND DISCUSSION

Preparation, stability and product studies of 23 and 24 (this section reports work carried out mainly by Drs Luigia Capelli and Paola Manini)

Unlike nitrooleic acids, for which simple access routes based on standard Henry condensation chemistry are available,^{141,142} nitrolinoleic acids are difficult to synthesize. Their preparation currently relies on direct nitration of the parent fatty acid^{127,129,131,132,143,144} because of the lack of synthetic routes assembling the C-18 nitrated fatty acid chain. Early methods based on acidic nitrite or NO₂⁺-forming reagents led invariably to mixtures of regio- and stereoisomers in low yields, along with abundant side-products, and only small amounts of **24** and the 12-nitro isomer as carboxylate esters could be obtained. More recently, a nitrophenylselenenylation/oxidation protocol has been reported to produce a statistical distribution of the four regioisomeric nitrolinoleic acids in good overall yields,¹³³ but their separation as free acids remained a difficult task. To provide access to individual nitrolinoleic acid isomers needed for probing the structural basis of their biological activities and fate, to determine if certain isomers are more reactive than others in competing autoxidation/NO-release and water addition pathways, and to understand why unsaturated lipids with the nitro group on terminal positions of the polyene systems (e.g. **23**) have so far eluded identification *in vivo*, it was necessary to devise expedient methods for preparation of representative isomeric nitrolinoleates as pure free acids. Nitrolinoleates **23** and **24** were thus selected for the purposes of the present study because of their appropriate positional isomerism. After an extensive search of reaction conditions with a variety of nitrating systems, it was found that the target nitroalkenes **23** and **24** could be conveniently obtained by a modification of the reported nitrophenylselenenylation/oxidation procedure¹³³ through a judicious combination of experimental conditions and protection strategies.

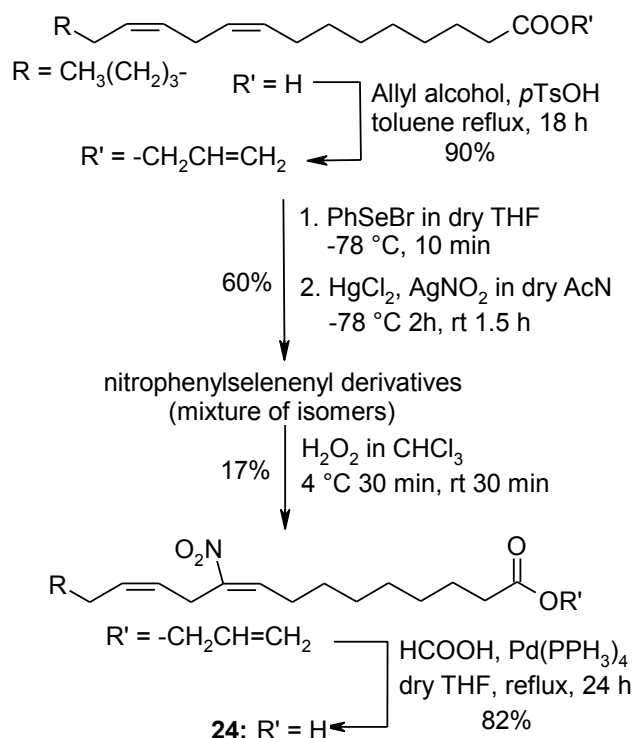
Compound **1** was prepared by a modified protocol in which linoleic acid was reacted with PhSeBr in THF at -78 °C and then with HgCl₂ and AgNO₂ in dry acetonitrile to produce regioisomeric nitrophenylselenenyl-adducts (**Scheme 14**).¹⁴⁵ Preparative HPLC then afforded a main fraction containing a mixture of the appropriate stereoisomeric nitrophenylselenenyl-adducts, which were treated with H₂O₂ to remove

phenylselenenic acid and give the desired **23** in 12% overall yield, characterized by a complete spectroscopic analysis.



Scheme 14. Preparation of **23**.

The same procedure was successfully extended to obtain ^{15}N -labeled **23** in 9% isolated yield using $\text{Na}^{15}\text{NO}_2$ in the place of AgNO_2 . Preparation of **24** as free acid could not be achieved by the same protocol because of difficulties in the separation of the appropriate nitrophenylselenenyl intermediates or the final nitrolinoleates. Accordingly, an alternate strategy was devised which involved the use of the allylic ester of linoleic acid as the substrate. This ester group was preferred over simple alkyl groups because of the facile removal by hydrogenolysis¹⁴² and the presence of an additional double bond expected to improve chromatographic separation over silver nitrate-impregnated silica gel.¹³² Indeed, nitrophenylselenenylation/oxidation of linoleic acid allylester as above followed by a chromatographic step gave pure **24**-allylester, from which **24** was eventually obtained in ca. 10% overall yield after a deprotection step (**Scheme 15**).



Scheme 15. Preparation of **24**.

Prior to product investigation, the relative stability of regioisomeric nitrolinoleic acids under physiologically relevant conditions was investigated. Accordingly, freshly prepared pure **23** and **24** were dissolved in phosphate buffer at pH 7.4 containing 20% ethanol, under the conditions used in previous and related studies^{134,146} and their rates of decomposition at 20 °C were monitored by HPLC. Data revealed a markedly faster decay of **23** relative to **24**: after 15 min nearly 80% **23** had decayed *versus* little or no **24**. Under the same conditions, linoleic acid remained virtually unchanged over more than 5 hours.

The faster decay of **23** relative to **24** was also apparent from NMR analyses of the crude ethyl acetate extracts of the reaction mixtures from the nitrolinoleic acids suspended in 0.1 M phosphate buffer, pH 7.4 and from NMR analysis of an equimolar mixture of **23** and **24**. Notably, even when stored dry in the cold, **23** was unstable compared to **24**: whereas pure samples of the former underwent extensive degradation after a month or so, the latter remained virtually unaffected during the same period. In separate experiments the NO-releasing abilities of **23** and **24** in phosphate buffer were investigated using the oxymyoglobin assay.^{134,128,139} The results indicated a faster decrease in the 580 and 543 nm maxima (characteristic of the visible α - and β -band

absorbance of oxymyoglobin) and a more rapid increase in the 630 and 503 nm maxima (characteristic of metmyoglobin) in the case of **23**, suggesting faster NO-release from this fatty acid.

Overall, these preliminary data highlighted a marked instability of **23** in phosphate buffer when compared to **24**, and a consistently higher tendency to release NO. With this information available, the main reaction products generated under the same conditions were then investigated.

Incubation of **23** in 0.1 M phosphate buffer, pH 7.4, resulted in the generation of a very complex mixture of products. After 2 h the mixture was worked up and chromatographed on silica gel plates to give three main UV visible bands, identified on the basis of ESI(+)/MS, ESI(-)/MS/MS, and NMR data as compounds **25**, **26** and **27** (**Figure 65**).

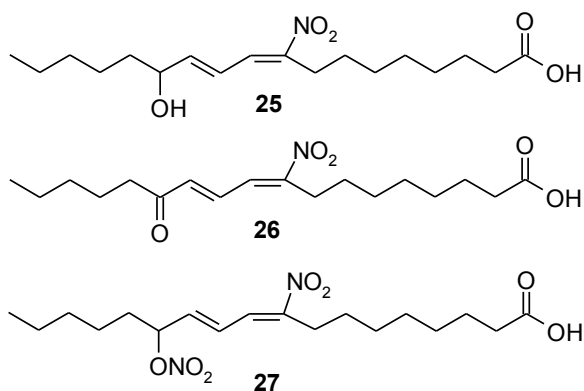


Figure 65. Structures of (9E,11E)-13-hydroxy-9-nitro-9,11-octadecadienoic acid (**25**), (9E,11E)-9-nitro-13-oxo-9,11-octadecadienoic acid (**26**), (9E,11E)-9-nitro-13-nitrate-9,11-octadecadienoic acid (**27**).

Formation of products **25-27** was independent of substrate concentration (HPLC evidences). In a subsequent set of control experiments it was found that: *a*) in unbuffered water (pH around 5) formation of peroxidation products of **23** was markedly slower with no detectable **27**; *b*) under an argon atmosphere formation of products **25-27** was inhibited; *c*) when **23** was left to decompose at room temperature as a dry film formation of **25** and **26** occurred but no detectable **27**.

To gain a deeper insight into the products resulting from aqueous decomposition of **23**, the crude reaction mixtures obtained from both the unlabeled and ^{15}N -labeled substrates were investigated by LC-MS. Besides **25**, **26** and **27** in the mixtures there were several additional species, including the 13-hydroperoxy derivative of **23** and a dienone in which the nitro group was evidently lost. Similar species generated by decomposition of nitrolinoleic acids had been reported previously.¹³⁴

In contrast to **23**, decay of **24** in aqueous phosphate buffer at pH 7.4 gave after 2 h a single isolable species which was obtained by preparative TLC and was identified as (12*Z*)-9-hydroxy-10-nitrooctadec-12-enoic acid (**28**) (9% isolated yield, **Figure 66**) by extensive spectral characterization.

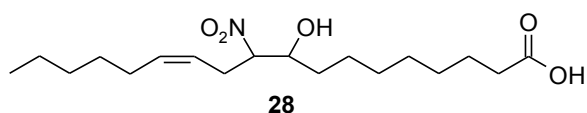
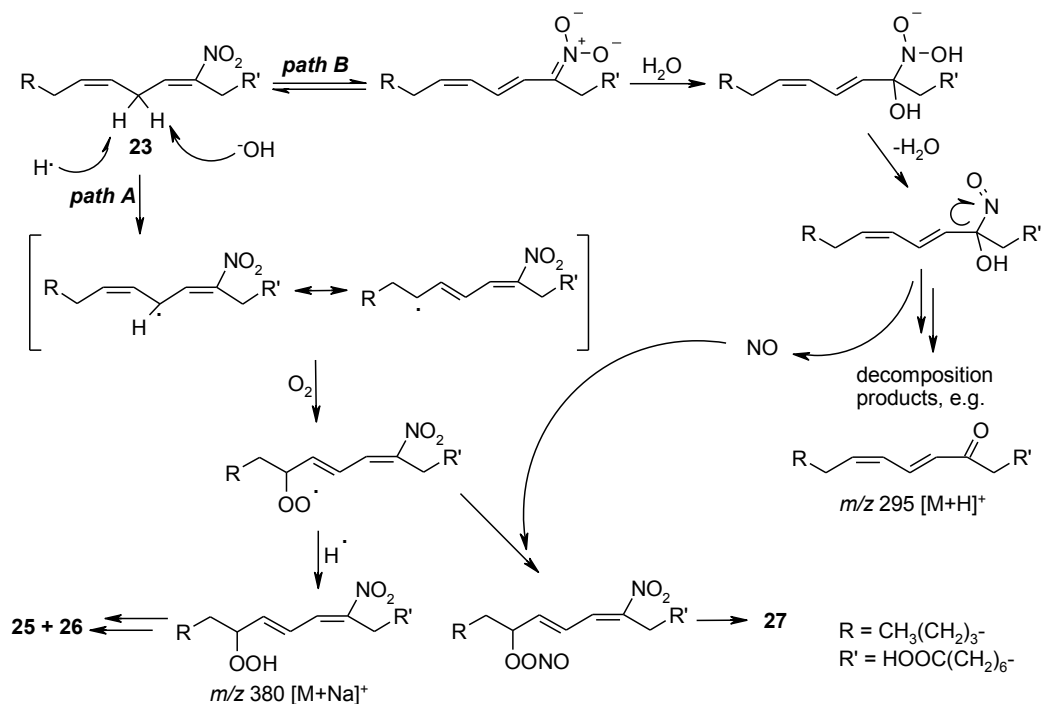


Figure 66. Structure of (12*Z*)-9-hydroxy-10-nitrooctadec-12-enoic acid (**28**).

Unreacted **24** accounted for some 80% of the mixture after 2 h reaction time. Although no other single product could be isolated from the mixture, NMR and LC-MS investigations indicated the formation, besides **28**, of several species all in minute amounts.

The product studies reported above revealed three main degradation channels of the nitropentadienyl system in neutral aqueous buffer, namely: *a*) H-atom abstraction from the bis-allylic methylene group triggering classic peroxidation chain reactions; *b*) NO-release; and *c*) nucleophilic addition of water onto the nitroalkene moiety. Whereas the latter path accounts for the observed formation of **28** by decay of **24**, the first two routes may lead to **25-27**, as outlined in **Scheme 16**.



Scheme 16. Mechanistic pathway proposed for the formation of compounds **25-27** from **23**.

H-Atom abstraction from the bis-allylic methylene group (**Scheme 16, path A**) would result in a stabilized nitropentadienyl radical which would undergo coupling with oxygen to give **25** and **26** via the classic lipid peroxidation steps. This path is supported by the mass spectrometric identification of the hydroperoxy derivative and the substantial inhibition of product formation in the absence of oxygen. NO-Release is apparently a pH-dependent route triggered by a deprotonation equilibrium, and is involved in the formation of **27** at pH 7.4. One viable mechanism for NO-release is based on the recently proposed modified Nef sequence¹³⁶ and is sketched in **Scheme 16, path B**.

Product analysis suggested a higher oxidizability of **23** relative to **24**. Since H-atom abstraction from the 1,4-pentadiene system (C-H bond dissociation enthalpy (BDE) = $76.4 \text{ kcal mol}^{-1}$)¹⁴⁷⁻¹⁴⁸ dictates the oxidizability of polyunsaturated fatty acids, at least a rough estimate of the relative abilities of nitrolinoleic acids to act as H-atom donors was desirable. Accordingly, the activity of **23** and **24** in the diphenylpicrylhydrazide (DPPH) radical quenching spectrophotometric test was determined against linoleic acid, as a reference fatty acid.¹⁵⁰ This test, which is run in

ethanol and is therefore independent of pH-related effects, enables to measure the radical scavenging properties of a given substance and is often used in the food industry to establish the rank order of antioxidants. The results in **Figure 67** indicated more effective H-atom transfer to the DPPH radical from **23** than from **24** or linoleic acid. This trend can be taken to suggest a larger radical-stabilizing effect of the nitro group on the terminal pentadienyl positions, making **23** more prone to H-atom loss and free radical formation.

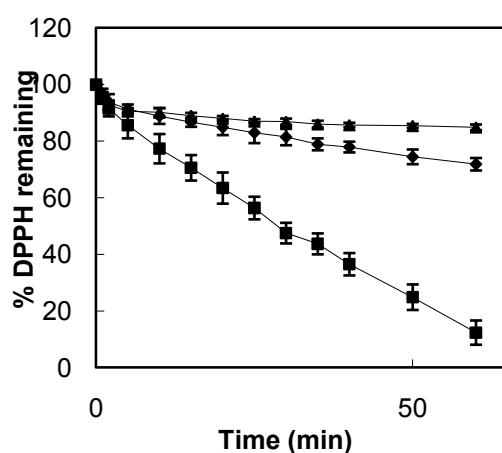


Figure 67. Absorbance decay at 515 nm of a 100 μ M solution of DPPH in ethanol after addition of: **23** (■), **24** (◆) and linoleic acid (▲). Final fatty acid concentration: 7.7 mM. All experiments have been carried out in triplicate. Data are expressed as average \pm S.D.

Computational studies

To support this conclusion and to investigate in some detail the position-dependent influence of the nitro group on radical stability, I performed a computational investigation at the DFT level of the isomeric nitro-1,4-pentadienyl systems. A theoretical description of the 1,4-pentadiene system and the corresponding radical, and a discussion of how theoretical methodologies perform in modeling these systems, including determination of bond dissociation enthalpies (BDEs), has appeared recently.¹⁴⁸ For the purposes of the present study two simplified truncated structures featuring the isomeric nitropentadiene moieties typical of **23** and **24** were investigated, namely **29** and **30**, respectively.

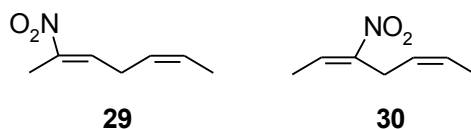


Figure 68. Truncated structures featuring the isomeric nitropentadiene moieties typical of **23** (**29**) and **24** (**30**).

Geometry optimizations were based on the “hybrid” PBE0 functional,^{32b} which has provided quite satisfactory energies and geometries for a wide range of organic and biological systems (including notably radical species) in combination with the 6-31+G(d,p) basis set.⁹⁸ The unrestricted formulation was used to describe radical species. The conformational spaces of **29** and **30**, as well as the corresponding bis-allylic radicals (dubbed **29R** and **30R**), were sampled by relaxed grid-searches of the C3-C4 and C4-C5 dihedrals (methyl rotations were not systematically explored). For both **29** and **30**, four minima were identified, arranged in enantiomeric pairs which, within each compound, are separated by 0.2 - 0.4 kcal mol⁻¹: the energy difference between the absolute minimum of **30** with respect to **29** is also rather small (0.5 kcal mol⁻¹). The bis-allylic radical **29R** gives rise to six minima (two enantiomeric pairs, and two structures of *C_s* symmetry), one of the planar conformers being definitely more stable than the others (by at least 3.9 kcal mol⁻¹). By contrast, planar conformers were not found among the stable conformers of **30R**, which features instead four pairs of enantiomeric minima:

even in those conformers in which the carbon skeleton is approximately planar, the nitro group is significantly distorted out of the molecular plane. A first indication of the relative stabilities of the two radicals can be gained by comparison of the energies of their most stable conformers: then, **29R** is favored by 9.0 kcal mol⁻¹ with respect to **30R**. Such a direct comparison is significant, since, as stated before, **29** and **30** are almost isoenergetic at this level. Moreover, the overall picture is confirmed when more refined treatments are adopted, including single point energy evaluations with the recently developed M05-2X density functional,¹⁵¹ which has shown remarkable performance for energetics involving radicals,¹⁵² use of a large basis set, and introduction of rotational/harmonic vibrational contributions: in terms of computed enthalpies at 298.15 K, **30** is more stable than **29** by 0.4 kcal mol⁻¹, while **30R** is less stable than **29R** by 8.4 kcal mol⁻¹. Selected geometric parameters (dihedrals in degrees) and relative energies of the main conformers of **29**, **30**, **29R** and **30R** are listed in **Table 13**, whereas thermal corrections to enthalpy are listed in **Table 14**.

Table 13. Selected geometric parameters (dihedrals in degrees) and relative energies (in kcal mol⁻¹) of the main conformers of **29** and **30**, and the corresponding bis-allylic radicals, computed at the PBE0/6-31+G(d,p) level. For radical species, the unrestricted formulation was adopted. Single point energies computed at the M05-2X/6-31+G(d,p) and M05-2X/6-311+G(2df,p) levels are also shown.

	C2-C3- C4-C5	C3-C4- C5-C6	O-N-C2- C3/ O-N-C3-C2^a	ΔE PBE0/6- 31+G(d,p)	ΔE M05-2X/6- 31+G(d,p)	ΔE M05-2X/6- 311+G(2df,p)
29						
Conformer 1	116.6	114.4	180.0	0.0 ^b	0.0 ^c	0.0 ^d
Conformer 2	128.0	-120.8	179.9	0.4	0.3	0.3
30						
Conformer 1	100.2	118.1	170.4	0.0 ^e	0.0 ^f	0.0 ^g
Conformer 2	99.1	-124.2	-176.8	0.2	0.4	0.4
29R						
Conformer 1	180.0	180.0	180.0	0.0 ^h	0.0 ⁱ	0.0 ^j
Conformer 2	180.0	0.0	180.0	3.9	3.7	3.9
Conformer 2	10.4	-178.7	176.1	4.8	-	-
Conformer 4	22.4	36.4	-173.7	10.1	-	-
30R						
Conformer 1	11.7	-178.9	171.1	0.0 ^k	0.0 ^l	0.0 ^m
Conformer 2	176.8	-176.9	147.3	0.3	0.3	0.2
Conformer 3	38.6	24.2	170.9	5.8	-	-
Conformer 4	-157.0	17.7	-144.7	6.3	-	-

[a] For **29/29R**, and **30/30R**, respectively. [b] -477.920670 hartrees.

[c] -478.388108 hartrees. [d] -478.522353 hartrees. [e] -477.919887 hartrees.

[f]-478.388567 hartrees. [g] -478.522986 hartrees. [h] -477.305368 hartrees.

[i] -477.768374 hartrees. [j] -477.902367 hartrees. [k] -477.291091 hartrees.

[l] -477.754970 hartrees. [m] -477.888747 hartrees.

Table 14. Thermal corrections to enthalpy (at 298.15 K, in kcal mol⁻¹) of the main conformers of **29** and **30**, and the corresponding bis-allylic radicals, computed at the PBE0/6-31+G(d,p) level. For radical species, the unrestricted formulation was adopted. The predominant conformers of each species (see **Table 6**) are highlighted in italic.

	<i>H_{corr}</i>
29	
<i>Conformer 1</i>	117.00
<i>Conformer 2</i>	116.94
30	
<i>Conformer 1</i>	116.94
<i>Conformer 2</i>	116.94

	<i>H_{corr}</i>
29R	
<i>Conformer 1</i>	108.58
Conformer 2	108.72
Conformer 3	108.73
Conformer 4	108.57
30R	
<i>Conformer 1</i>	108.42
<i>Conformer 2</i>	108.33
Conformer 3	108.24
Conformer 4	-

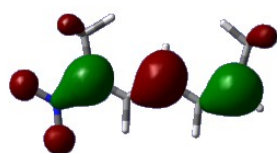
In view of the relatively apolar nature of the models, it is not surprising that introduction of the aqueous environment by means of an implicit model (namely the PCM)^{49,52,53,76} involves only minor changes in computed geometries and relative stabilities (**Table 15**).

Table 15. Selected geometric parameters (dihedrals in degrees) and relative energies (in kcal mol⁻¹) of the main conformers of **29** and **30**, and the corresponding bis-allylic radicals, computed at the PBE0/6-31+G(d,p) level by inclusion of the polarizable continuum model to account for the aqueous solvent. For radical species, the unrestricted formulation was adopted.

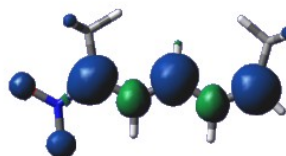
	C2-C3-C4-C5	C3-C4-C5-C6	O-N-C2-C3/ O-N-C3-C2^a	ΔE PBE0/ 631+G(d,p)/PCM
29				
Conformer 1	114.5	111.3	-179.2	0.0
Conformer 2	128.7	-119.1	-179.3	0.3
30				
Conformer 1	100.2	123.6	173.4	0.0
Conformer 2	100.2	-125.8	-177.7	0.2
29R				
Conformer 1	180.0	180.0	180.0	0.0
Conformer 2	180.0	0.0	180.0	4.2
Conformer 3	11.8	-178.7	177.4	4.4
Conformer 4	22.1	36.4	-173.4	10.1
30R				
Conformer 1	12.8	-179.0	167.4	0.0
Conformer 2	174.5	-177.0	143.7	0.3
Conformer 3	43.2	21.0	-177.7	5.6
Conformer 4	-154.0	16.5	-145.5	6.1

[a] For **29** (and its radical), and **30** (and its radical), respectively.

Figure 69 depicts the SOMO and the total spin density for the main conformer of **29R**: the 2, 4 and 6 positions appear almost equivalent, with significant involvement of the nitro group.



SOMO



Spin density

Figure 69. Isodensity surfaces of the singly occupied molecular orbital and total spin density of the main conformer of **29R**, computed at the UPBE0/6-31+G(d,p) level.

A more quantitative comparison (**Table 16**) based on SOMO localization and on use of a larger basis set shows a slightly lower relative weight at position C-6 with respect to C-2 and C-4.

Table 16. SOMO localization¹⁵³ for the bis-allylic radicals **29R** and **30R**, computed at the UPBE0/6-31+G(d,p) and UPBE0/6-311+G(2df,p)//UPBE0/6-31+G(d,p) levels, with the VModes program (Nemykin, V. N., and Basu, P. VModes, Revision A 7.1; Department of Chemistry, Duquesne University: Pittsburgh, PA, 2001, 2003). The predominant conformers of each species (see **Table 6**) are highlighted in italic

	UPBE0/6-31+G(d,p)					
	C-2	C-3	C-4	C-5	C-6	NO ₂
29R						
<i>Conformer 1</i>	0.267	0.009	0.264	0.010	0.254	0.117
Conformer 2	0.261	0.008	0.266	0.010	0.256	0.118
Conformer 3	0.178	0.041	0.234	0.161	0.266	0.065
Conformer 4	0.221	0.067	0.228	0.050	0.137	0.076
30R						
<i>Conformer 1</i>	0.296	0.055	0.250	0.097	0.233	0.008
Conformer 2	0.305	0.205	0.190	0.022	0.168	0.045
Conformer 3	0.140	0.155	0.309	0.052	0.182	0.027
Conformer 4	0.267	0.444	0.102	0.100	0.051	0.009

	UPBE0/6-311+G(2df,p)					
	C-2	C-3	C-4	C-5	C-6	NO ₂
29R						
<i>Conformer 1</i>	0.263	0.010	0.264	0.013	0.247	0.124
Conformer 2	0.256	0.008	0.266	0.012	0.252	0.121
Conformer 3	0.263	0.020	0.267	0.017	0.236	0.114
Conformer 4	0.228	0.037	0.222	0.045	0.151	0.088
30R						
<i>Conformer 1</i>	0.249	0.066	0.302	0.012	0.260	0.010
Conformer 2	0.279	0.170	0.235	0.015	0.210	0.009
Conformer 3	0.174	0.170	0.267	0.052	0.208	0.027
Conformer 4	0.247	0.340	0.188	0.039	0.131	0.008

A note of caution here is in order concerning the validity of the truncated structure to model lipid peroxidation. In particular, steric interactions between the long tails of the real lipids are evidently ill reproduced by the small methyl groups of the models. However, for both **29** and **30**, the most stable conformer is characterized by a skew arrangement of the terminal C-CH₃ units, which should be compatible even with the complete chains. The chain termini are almost cooriented in the secondary conformers identified, but again this holds for both **29** and **30**. The situation is slightly more involved for the radical species: in the most stable conformer of **29R**, the C-CH₃ units are coplanar and point in the same direction; in the conformer which comes next, the backbone is still planar, but the methyl groups are now on opposite sides (however, as hinted above, this conformer is significantly less stable). The most stable conformer identified for **30R** corresponds, with minor distortions, to this latter chain fold; conversely, the second conformer of **30R** resembles the geometry of the absolute minimum of **29R** (but is much closer in energy to its own minimum). While the relative orientation of the terminal C-CH₃ groups can admittedly provide only a rough indication as to the stability of the untruncated compounds, overall it would appear that longer terminal tails could be better accommodated in the floppier **30R** than in **29R**; in turn, this would imply a smaller energy separation between the two radicals, and would to some extent qualify the rather drastic reactivity differences predicted by use of the heptadiene models.

CONCLUSIONS

The preparation of two isomeric nitrolinoleic acids in pure form is reported for the first time (only the ester derivative of **24** was obtained previously),¹³² and their markedly different chemical behavior is disclosed. Compound **23**, bearing a nitro group on a terminal position of the pentadiene moiety, is markedly unstable when exposed to phosphate buffer at pH 7.4, and partitions mainly between two concurrent degradation pathways, one resulting in NO-release presumably via a base-dependent Nef-type reaction, and the other involving a typical peroxidation process. A remarkable outcome is formation of the nitronitrate ester **27** involving probably trapping of NO by transient peroxy radicals. Compound **24** decays at slower rate and gives mainly the stereoisomeric hydroxynitro derivatives **28** by nucleophilic addition of water. The differential behavior of **23** and **24** can be rationalized on the basis of DPPH radical quenching experiments and DFT calculations, indicating a higher H-atom donating ability and a larger radical stabilization when the nitro group is located on the terminal rather than inner positions of the 1,4-pentadienyl core. These results provide an underpinning for ongoing investigations of the physiological properties of nitrolinoleic acids, and may orient the design of new pharmacologically active nitrated lipids. They also offer a plausible explanation as to why **23** and the isomeric 13-nitrolinoleic acid have so far eluded detection in biological systems.

EXPERIMENTAL AND COMPUTATIONAL METHODS

1. Oxidative chemistry of the 2,7'-biindolyl (4)

1.1 Materials and instrumentation

L-Dopa, sodium dithionite, hydrogen peroxide (30% solution in water), horseradish peroxidase (HRP) (donor: H₂O₂ oxidoreductase, EC 1.11.1.7) type II were commercially available and were used as obtained. All the solvents were of analytical grade quality.

ESI+/MS(HR) and ESI+/MS spectra were with the cone and the fragmentator voltages set at 4 kV and 80 V respectively and obtained in 1% TFA-methanol. UV spectra were obtained on a diode array spectrophotometer equipped with a thermostated sample cell holder.

¹H NMR spectra were recorded at 600, 400 or 300 MHz, ¹³C NMR spectra at 75 MHz. ¹H,¹H COSY and ¹H,¹H ROESY experiments were run using standard pulse programs. ¹H, ¹³C DEPT HSQC, and ¹H, ¹³C HMBC experiments were run at 600 and 400 MHz respectively on instruments equipped with a 5 mm ¹H/broadband gradient probe with inverse geometry using standard pulse programs. The HMBC experiments used a 100 ms long-range coupling delay. Chemical shifts are reported in δ values (ppm) downfield from TMS.

Analytical and preparative TLC were carried out on silica gel plates (0.25 and 0.50 mm, respectively) using CHCl₃/MeOH (98:2) as the eluant. TLC plates were visualised using a UV lamp ($\lambda = 254$ nm). Liquid chromatography—was performed on silica gel (60-230 mesh).

HPLC analysis of the reaction mixtures was carried out on an apparatus equipped with a UV detector set at 280 nm using a Spherclone ODS (5 micron, 4.6 × 250 mm) column; 1% v/v acetic acid/acetonitrile 95:5 (v/v) (eluant A) , aceto nitrile (eluant B) gradients were used as follows: from 0-5 min 30% eluant B, 5-40 min 30-80% eluant B, 40-50 min 80% eluant B. Flow rate of 1 mL/min was used. Purity of isolated compounds was estimated by ¹H NMR analysis.

5,6-dihydroxyindole (1)¹⁵⁴ and 5,5',6,6'-tetraacetoxy-2,7-biindolyl (4)⁵⁹ were synthesized as previously reported.

1.2 Oxidation of 4: Isolation of tetramers 9-11

A solution of **4** (280 mg, 0.60 mmol) in acetone (5 mL) was taken under a flux of argon and treated with 0.1 M phosphate buffer pH 12 (0.5 L) which had been prior thoroughly purged with argon. After 2 min the pH of the solution was taken to 8 by addition of 3 M HCl and peroxidase (4.9 U/mL) and 30% H₂O₂ (135 μ L, 1.3 mmol) were added sequentially. The reaction mixture turned immediately from pale yellow to deep violet. After 20 s the oxidation was halted by addition of 5% w/w aqueous solution of sodium dithionite and acidified to pH 4 with 3 M HCl. The reaction mixture was extracted repeatedly with ethyl acetate (3 x 250 mL) and the combined organic layers were dried over sodium sulphate and taken to dryness. The residue was acetylated with acetic anhydride-pyridine 95:5 (v/v) and fractionated by preparative TLC (CHCl₃/MeOH 98:2) to give besides residual **4** (*R_f* 0.70, 50 mg), acetylated **9** (*R_f* 0.42; *R_t* 24.5 min; 8 mg, 3% yield, >95% pure by ¹H NMR analysis) and acetylated **10** (*R_f* 0.27, *R_t* 26.7 min; 10 mg, 4% yield, >95% pure by ¹H NMR analysis). In other experiments the oxidation reaction was carried out in the presence of zinc sulfate (534 mg, 1.8 mmol) in 0.5 M TRIS buffer at pH 8.0 as the reaction medium. Workup and fractionation as above afforded besides unreacted **4** (60 mg), acetylated **9** (*R_f* 0.42; 6 mg, 2% yield) and acetylated **11** (*R_f* 0.20; *R_t* 23.8 min; 15 mg, 5% yield, >95% pure by ¹H NMR analysis) as colorless oils.

9-acetylated:

HR ESI+-MS m/z 949.2186 $[M + Na]^+$, calcd for C₄₈H₃₈N₄O₁₆Na 949.2180;

UV λ_{max} (EtOH) 301, 320 (s) nm;

¹H-NMR (CD₃COCD₃): δ (ppm) 2.12 (3H×2, s, -COCH₃), 2.28 (3H×3, s, -COCH₃), 2.32 (3H×3, s, -COCH₃), 6.02 (1H×2, s, H-3, H-3'''), 6.94 (1H×2, s, H-4', H-4''), 6.95 (1H×2, s, H-2, H-2'''), 7.34 (1H×2, s, H-7', H-7''), 7.49 (1H×2, s, H-4, H-4'''), 9.02 (1H×2, s, -NH, -NH'''), 10.54 (1H×2, s, -NH', -NH'').

¹³C-NMR (CD₃COCD₃): δ (ppm) 20.2 (COCH₃), 169.5 (COCH₃), 101.6 (C-3, C-3'''), 106.7 (C-7', C-7''), 110.1 (C-7, C-7'''), 110.1 (C-3', C-3''), 114.1 (C-4', C-4''), 114.9 (C-4, C-4'''), 125.1 (C-9, C-9'''), 125.6 (C-9'-C-9''), 128.5 (C-2, C-2'''), 133.8 (C-2', C-2''), 133.8 (C-8, C-8'''), 133.8 (C-8', C-8''), 135.1 (C-5, C-5'''), 136.1 (C-6, C-6'''), 137.5 (C-5', C-5''), 139.6 (C-6', C-6'')

10-acetylated:

HR ESI+-MS m/z 949.2175 [M + Na]⁺, calcd for C₄₈H₃₈N₄O₁₆Na 949.2180;

UV λ_{\max} (EtOH) 313, 337 nm;

¹H-NMR (CD₃COCD₃): δ (ppm) 2.04 (3H×2, s, -COCH₃), 2.21 (3H×2, s, -COCH₃), 2.31 (3H×2, s, -COCH₃), 2.32 (3H×2, s, -COCH₃); 6.16 (1H×2, s, H-3', H-3''), 6.84 (1H×2, s, H-3, H-3'''), 7.39 (1H×2, s, H-2', H-2''), 7.40 (1H×2, s, H-7, H-7'''), 7.44 (1H×2, s, H-4, H-4'''), 10.71 (1H×2, s, -NH', -NH''), 10.78 (1H×2, s, -NH, -NH''').

¹³C-NMR (CD₃COCD₃): δ (ppm) 20.1 (COCH₃), 168.3 (COCH₃), 103.8 (C-3, C-3''), 103.9 (C-3', C-3'''), 106.5 (C-7, C-7'''), 111.8 (C-7', C-7''), 114.3 (C-4, C-4''), 121.4 (C-4', C-4'''), 126.7 (-C9, C-9'''), 126.8 (C-9', C-9''), 127.0 (C-2', C-2''), 132.4 (C-2, C-2'''), 134.9 (C-8, C-8'''), 134.9 (C-8', C-8''), 137.7 (C-5, -C5'''), 138.0 (C-5', C-5''), 139.5 (C-6', C-6''), 139.9 (C-6, C-6''')

11-acetylated:

HR ESI+-MS m/z 949.2178 $[M + Na]^+$, calcd for $C_{48}H_{38}N_4O_{16}Na$ 949.2180;

UV λ_{max} (EtOH) 313 nm;

1H -NMR (CD_3COCD_3): δ (ppm) 2.17 (3H, s, $COCH_3$), 2.27(3H, s, $COCH_3$), 2.30 (3H \times 2, s, $COCH_3$), 2.31 (3H, s, $COCH_3$), 2.32 (3H, s, $COCH_3$), 2.33 (3H, s, $COCH_3$), 2.34 (3H, s, $COCH_3$), 5.96 (1H, m, H-3), 6.47, (1H, m, H-3'''), 6.84 (1H, m, H-3'), 7.18 (1H, d, H-2'''), 7.30 (1H, s, H-7), 7.35 (1H, s, H-4''), 7.43 (1H, s, H-7''), 7.44 (1H, s, H-4), 7.64 (1H, s, H-4''), 7.81 (1H, s, H-4'), 9.26 (1H, s, -NH'), 10.18 (1H, s, -NH), 10.39 (1H, s, -NH'''), 10.97 (1H, s, -NH'').

^{13}C -NMR (CD_3COCD_3): δ (ppm) 20.1 ($COCH_3$), 169.9 ($COCH_3$), 100.5 (C-3'), 102.6 (C-3'''), 102.8 (C-3), 105.8 (C-7'), 106.1 (C-7), 106.6 (C-7''), 107.4 (C-7'''), 108.4 (C-3''), 113.4 (C-4''), 113.9 (C-4'), 114.2 (C-4), 116.0 (C-4'''), 124.6 (C-9''), 126.3 (C-9), 127.0 (C-9'), 127.7 (C-2'''), 127.7 (C-9'''), 133.3 (C-2'')^a, 134.5 (C-2')^a, 134.7 (C-8), 134.7 (C-8'), 134.7 (C-8''), 134.7 (C-8'''), 135.2 (C-2)^a, 137.3 (C-5), 137.3 (C-5'), 137.3 (C-5''), 137.3 (C-5'''), 137.8 (C-6'''), 139.2 (C-6), 139.6 (C-6''), 139.9 (C-6')

2. Structural effect on the electronic absorption properties of oligomers of 5,6-dihydroxyindole (1)

2.1 Materials and instrumentation

5,6-dihydroxyindole (1)¹⁵⁴ and acetylated oligomers 3-8^{26,58,59} were synthesized as previously reported. All the solvents were of analytical grade quality.

UV spectra were made with a diode array spectrophotometer.

2.2 Absorption measurements

Deacetylation of oligomers was carried out as follows⁷³: a solution of oligomer (ca. 5 mg) in methanol (1.0 mL) was slowly added under vigorous stirring to a 0.025 M trisodium phosphate solution (2.5 mL) that had previously been purged with argon. The reaction mixture was stirred under an argon atmosphere and after 10 min acidified to pH 7.0 with 2 M HCl. The solutions thus obtained were immediately used for spectrophotometric determinations following appropriate dilution in 0.05 M phosphate buffer, pH 7.0, up to 1 mL. A minimal time of exposure of the deacetylated oligomers to air was critical for limiting melanin formation. Deacetylated oligomers were markedly unstable to air and were therefore unsuitable for standard procedures of molar extinction coefficient determination using crystallized samples. Residual acetate in the mixture was at a concentration up to eight-fold that of the oligomer and was judged not to affect the spectrophotometric measurements because it absorbs below 240 nm, i.e. a region where the oligomers do not exhibit diagnostic absorption bands and which is therefore out of the range of interest for the purposes of the present paper. Absorption measurements were carried out on a single beam spectrophotometer using phosphate buffer at pH 7.0 as the blank.

2.3 Computational methods

Computational studies were carried out at the DFT level, using the “hybrid” PBE0 functional.^{32b} Geometry optimizations were performed with the 6–31 + G(d,p) basis set,⁹⁹ using the most recent implementation⁵² of the polarizable continuum model (PCM)^{52,53,76} to simulate the aqueous environment. The effective cavities occupied by the solute in the solvent were built using UA0 atomic radii⁵² during optimizations, while the final evaluations of PCM energies were performed with the UAHF radii⁵¹, as these latter provide more reliable estimates for solvation free energies. The thresholds for the maximum and the root mean square (RMS) forces and the maximum and the RMS atomic displacements (in a.u.) were set to 0.00045, 0.00030 and 0.00180, 0.00120, respectively. Absorption spectra of all the energetically relevant species were computed using the TD-DFT approach,^{47,74,75,77} and the large 6–311 + +G(2d,2p) basis set. As the absorption process presents a short characteristic time, only the electronic distribution of the solvent can adapt to the excited state electronic structure: therefore, the appropriate nonequilibrium formulation of the PCM⁵⁵ was employed. All quantum mechanical computations were performed with the Gaussian 03 suite.¹⁵⁵

3. Reaction behavior of 5,6-dihydroxyindole (1) in acidic medium

3.1 Materials and instrumentation

L-Dopa, potassium ferricyanide, 5-hydroxyindole, 6-hydroxyindole, cerium ammonium nitrate and tetrabutylammonium salts were commercially available and were used as obtained. All the solvents were of analytical grade quality.

5,6-Dihydroxyindole was prepared as reported.¹⁵⁴ TBAF 1.0 M solution in THF was used as obtained.

UV spectra were made with a diode array spectrophotometer. The fluorimetric measurements were performed with a spectrofluorimeter Jasco.

¹H and ¹³C NMR spectra were recorded at 400 or 100 MHz, respectively. ¹H, ¹H COSY, ¹H, ¹³C HMBC, ¹H, ¹³C HSQC-DEPT, and ROESY spectra were run at 400 MHz using standard pulse programs. Chemical shifts are reported in δ values (ppm) downfield from TMS.

ESI+/MS(HR) mass spectra were registered with the cone and the fragmentator voltages set at 4 kV and 80 V, respectively.

LC/MS analysis was carried out on an instrument equipped with an ESI ion source; an octadecylsilane-coated column, 150 mm \times 4.6 mm, 3.5 mm particle size, at 0.4 mL/min was used. The eluant system was 0.2% formic acid, solvent A; acetonitrile, solvent B; 5% B, 0–10 min; from 5 to 30% B, 10–25 min; from 30 to 70% B, 25–50 min.

Analytical and preparative TLC were carried out on silica gel plates (0.25 and 0.50 mm, respectively). TLC plates were visualised using a UV lamp ($\lambda = 254$ nm).

The liquid chromatography was performed on silica gel (60-230 mesh).

3.2 Reaction of **1** in acidic medium. General procedure

A solution of **1** (10 mg) in MeOH (200 μL) was added to 2 mL of 0.1 M phosphate buffer (pH 2) in Argon atmosphere. Mixture was kept under vigorous stirring and periodically analyzed by LC/MS or freeze-dried, treated with acetic anhydride (500 μL) and pyridine (20 μL) for 16 h at room temperature and analyzed by TLC.

In other experiments the reaction was carried out: 1) at **1** concentration of 60 mM, 2) in the presence of $(\text{NH}_4)_2\text{Ce}(\text{NO}_3)_6$ (2 molar equivalent), 3) in 0.1 M phosphate buffer at pH 1 or 3, 4) in 0.1 M phosphate buffer at pH 2 and after 2 h the mixture was adjusted to pH 8 by addition of NaHCO_3 ; 5) in 0.1 M phosphate buffer at pH 2 to air; 6) in methanol containing 1 M HCl or 6 M at 10% in the air.

3.3 Isolation of pentaacetyl derivative of 5,6-dihydroxy-2-(5,6-dihydroxyindol-3-yl) indoline (12) and heptaacetyl derivative of 2-(2-amino-4,5-dihydroxyphenyl)-1,1-bis(5,6-dihydroxyindol-3-yl) ethane (13)

Reaction was carried out under Argon atmosphere in 0.1 M phosphate buffer at pH 2, as described in the general procedure on 200 mg of **1**. After 2h mixture was freeze-dried, treated with acetic anhydride (2 mL) and pyridine (80 μ L) for 16 h at room temperature and fractionated by TLC to give the acetylated derivative of **12** (R_f = 0.39, 17 mg, yield 5%) and **13** (R_f = 0.15, 12 mg, yield 4%).

12 acetyl derivative:

ESI+/MS: m/z 509 $[M+H]^+$.

^1H NMR CDCl_3 : δ (ppm) 2.02-2.33 (COCH_3), 2.58 (1H, d, J = 16.0 Hz, H-3), 3.53 (1H, dd, J = 16.0, 9.6 Hz, H-3), 5.53 (1H, d, J = 9.6 Hz, H-2), 6.53 (1H, s, H-2'), 6.78 (1H, s, H-4), 7.15 (1H, s, H-4'), 7.18 (1H, s, H-7'), 8.13 (1H, s, H-7), 8.39 (1H, s, NH).

^{13}C NMR CDCl_3 : δ (ppm) 20.6-20.7 (COCH_3), 23.5 (NCOCH_3), 36.9 (C-3), 57.8 (C-2), 106.1 (C-7'), 111.9 (C-4'), 112.2 (C-7), 117.2 (C-3'), 119.6 (C-4), 120.7 (C-9'), 122.8 (C-2'), 128.4 (C-9), 133.9 (C-8'), 136.2 (C-5'), 138.3 (C-5), 138.4 (C-6'), 140.5 (C-6), 140.9 (C-8), 168.6-169.5 (COCH_3).

13 acetyl derivative:

ESI+/MS: m/z 742 $[M+H]^+$, 764 $[M+Na]^+$.

^1H NMR CDCl_3 : δ (ppm) 2.04-2.29 (COCH_3), 3.15 (2H, d, J = 6.0 Hz), 4.35 (1H, m), 6.16 (2H, bs), 6.89 (1H, s), 7.12 (4H, s), 7.48 (1H, s), 8.44 (2H, bs).

3.4 Isolation of 2-(2-Acetamido-4,5-diacetoxybenzyl)-6,7-diacetoxy-3-(5,6-diacetoxyindol-3-yl)quinoline (14b)

To a solution of 5,6-dihydroxyindole (200 mg) in methanol (4 mL) 0.1 M phosphate buffer (pH 2.0) (40 mL) was added and the reaction mixture was taken under stirring. After 24 h, when LC/MS analysis showed the formation of a product at t_R 24 min with a pseudomolecular ion peak $[M+H]^+$ at m/z 446 as a major constituent, the mixture was taken to dryness. The residue was treated with acetic anhydride (2 mL) and pyridine (80 mL) for 16 h at room temperature and fractionated by silica gel column chromatography (2 cm×36 cm) using chloroform–ethyl acetate as the eluant (9:1 to 4:6 gradient mixtures). Fractions eluted with chloroform–ethyl acetate 7:3 were collected and taken to dryness to give **14b** (33 mg, 10% yield, >97% purity estimated by 1H NMR analysis) as a pale yellow oil.

HR ESI⁺/MS: m/z 740.2089 $[M+H]^+$, calcd for C₃₈H₃₄N₃O₁₃ m/z 740.2092;

UV (CH₃CN): λ_{max} 276, 330 nm;

IR (CHCl₃): ν_{max} 3468, 1767, 1691, 1611, 1550, 1497, 1417, 1365, 1326, 1197, 1117, 1012, 903 cm⁻¹;

1H NMR (CDCl₃): δ (ppm) 2.18–2.39 (21H, COCH₃), 4.14 (2H, s, –CH₂), 6.28 (1H, s, H-6), 7.04 (1H, br s, H-2''), 7.09 (1H, s, H-4''), 7.32 (1H, s, H-7''), 7.59 (1H, s, H-5), 7.87 (1H, s, H-8), 7.96 (1H, s, H-3'), 8.02 (1H, s, H-4), 8.99 (1H, br s, NH), 10.82 (1H, br s, NHCOCH₃);

^{13}C NMR (CDCl₃): δ (ppm) 20.5–20.8 (COCH₃), 24.9 (NHCOCH₃), 39.1 (–CH₂), 106.2 (C-7''), 112.3 (C-4''), 112.8 (C-3''), 117.3 (C-3'), 120.4 (C-5), 120.9 (C-8), 124.8 (C-6', C-9''), 125.3 (C-10), 127.1 (C-1', C-2''), 128.6 (C-3), 133.1 (C-8''), 135.9 (C-2'), 136.9 (C-5''), 137.5 (C-5'), 138.6 (C-6''), 139.0 (C-4), 140.5 (C-4'), 141.7 (C-6), 144.0 (C-9), 144.4 (C-7), 161.5 (C-2), 167.9–169.1 (COCH₃).

3.5 Reactions of **14b** with anions

A 5×10^{-5} M solution of **14b** in acetonitrile was treated with 25 molar equivalents of the appropriate anion in the form of tetrabutylammonium salt (F^- , HSO_4^- , IO_4^- , I^- , Br^- , NO_2^-). The mixtures obtained were subjected to UV-vis and fluorescence analysis.

In other experiments, the UV-vis spectra and fluorescence were recorded after addition of increasing amounts of F^- (0.5-300 molar equivalent) at a 1×10^{-5} or 5×10^{-7} M solution of **14b** in acetonitrile.

4. Oxidative chemistry of 5,6-dihydroxy-1-methyl-indoles

4.1 Materials and instrumentation

16, 17 and **18** were synthesized as previously reported.^{97,98}

Sodium dithionite, sodium tert-butoxide, hydrogen peroxide (30% solution in water), horseradish peroxidase (HRP) (donor: H₂O₂ oxidoreductase, EC 1.11.1.7) type II were commercially available. All the solvents were of analytical grade quality.

ESI+/MS(HR) and ESI+/MS spectra were registered with the cone and the fragmentator voltages set at 4 kV and 80 V, respectively and obtained in 1% TFA-methanol.

¹H NMR spectra were recorded at 400 or 300 MHz, ¹³C NMR spectra at 75 MHz. ¹H, ¹³C DEPT HSQC, and ¹H, ¹³C HMBC experiments were run at 400 MHz, respectively on instruments equipped with a 5 mm ¹H/broadband gradient probe with inverse geometry using standard pulse programs. The HMBC experiments used a 100 ms long-range coupling delay. Chemical shifts are reported in δ values (ppm) downfield from TMS.

Analytical and preparative TLC were carried out on silica gel plates (0.25 and 0.50 mm, respectively) using CHCl₃/AcOEt (7:3) or (1:1) as the eluant. TLC plates were visualised using a UV lamp (λ = 254 nm). The liquid chromatography was performed on silica gel (60-230 mesh).

Purity of isolated compounds was estimated by ¹H NMR analysis.

4.2 Isolation of 19 and 20 acetylated

MeOH (80 mL) was taken under a flux of argon and, after 10 min, sodium tert-butoxide (60 mg) and **17**-acetylated (50 mg) dissolved in the smallest amount of chloroform were added sequentially. Mixture was left to react for 5 min and was treated with 0.1 M phosphate buffer pH 7.4 (250 mL) and then peroxidase (3u/mL) and 30% H₂O₂ (28 μ L, 2.8 eq) were added sequentially. After 60 s the oxidation was stopped by addition of a 5% w/w aqueous solution of sodium dithionite, acidified to pH 4 with 3 M HCl. The reaction mixture was extracted with ethyl acetate (3 x 250 mL) and the united organic layers were dried over sodium sulfate and taken to dryness. The residue was acetylated with acetic anhydride-pyridine 95:5 v/v and fractionated by preparative TLC (CHCl₃/AcOEt 4:6) to give **19**-acetylated (R_f 0.53; 2.5 mg, 5% yield) and **20**-acetylated (R_f 0.53 in traces).

19 acetylated:

ESI(+) /HRMS *m/z* 983.3105 [M+H]⁺, calc for C₅₂H₄₇N₄O₁₆ 983.2987; *m/z* 1005.2765 [M+Na]⁺ calc for C₅₂H₄₆N₄O₁₆Na, 1005.2806;

¹H-NMR (CDCl₃): δ (ppm) 2.2-2.4 (3H x4,s, -COCH₃), 3.53 (3Hx2, s, N-CH₃', N-CH₃''), 3.69 (3Hx2, s, N-CH₃, N-CH₃''), 6.28 (1Hx2, s, H-3', H-3''), 6.51 (1Hx2, s, H-3, H-3''), 7.14 (1Hx2, s, H-7', H-7''), 7.31 (1Hx2, s, H-7, H-7''), 7.37 (1Hx2, s, H-4, H-4'').

¹³C-NMR (CDCl₃): δ (ppm) 20.3-20.9 (COCH₃), 31.1 (N-CH₃', N-CH₃''), 31.2 (N-CH₃, N-CH₃''), (167-169 (COCH₃), 104.1 (C-7', C-7''), 104.2 (C-7, C-7''), 104.7 (C-3, C-3''), 105.3 (C-3', C-3''), 114.1 (C-4, C-4''), 120.4 (C-4', C-4''), 125.1 (C-9', C-9''), 125.3 (C-9, C-9''), 132.2 (C-2', C-2''), 132.5 (C-2, C-2''), 134.5 (C-5', C-5''), 135.0 (C-8', C-8''), 135.3 (C-8, C-8''), 135.6 (C-5, C-5''), 138.5 (C-6', C-6''), 139.0 (C-6, C-6'').

4.3 Isolation of 21-acetylated

Sodium tert-butoxide (80 mg) was added to MeOH (80 mL) taken under a flux of argon for 10 min and then **17**-acetylated (40 mg, 0.056 mmol) and **18**-acetylated (28 mg, 0.056 mmol) dissolved in the smallest amount of chloroform were added too. Mixture was left to react for 5 min and was treated with 0.1 M phosphate buffer pH 7.4 (240 mL) and then peroxidase (5u/mL) and 30% H₂O₂ (48 μ L, 4.3 eq) were added sequentially. Oxidation was stopped by addition of a 5% w/w aqueous solution of sodium dithionite and acidified to pH 4 with 3 M HCl. The reaction mixture was extracted with ethyl acetate (3 x 250 mL) and the united organic layers were dried over sodium sulfate and taken to dryness. The residue was acetylated with acetic anhydride-pyridine 95:5 v/v and fractionated by preparative TLC (CHCl₃/AcOEt 1:1) to give **21**-acetylated (R_f 0.36; 3.5 mg, 5% yield):

ESI(+)/HRMS *m/z* 1226.3551 [M+H]⁺, calc for C₆₅H₅₆N₅O₂₀ 1226.3519; *m/z* 1248.3380 [M+Na]⁺ calc for C₆₅H₅₅N₅O₂₀Na, 1248.3338;

¹H NMR (CDCl₃): δ (ppm) 3.55 (3H, N-CH₃); 3.58 (3H, N-CH₃); 3.61 (3H, N-CH₃); 3.68 (3H, N-CH₃); 3.73 (3H, N-CH₃); 5.92 (1H, H-3); 6.07 (1H, H-3); 6.19 (1H, H-3); 6.31 (1H, H-3); 6.42 (1H, H-3); 7.19 (1H, H-7); 7.22 (1H, H-7); 7.24 (1H, H-7); 7.29 (1H, H-7); 7.31 (1H, H-7); 2.25-2.45 (10 x COOCH₃);

¹³C NMR (CDCl₃): δ (ppm) 30.8 (N-CH₃); 30.9 (N-CH₃); 31.2 (N-CH₃); 32.2 (N-CH₃); 32.4 (N-CH₃); 104.0 (C-7); 104.1 (C-7); 104.4 (C-7); 104.5 (C-7); 104.6 (C-7); 103.6 (C-3); 105.3 (C-3); 105.8 (C-3); 107.7 (C-3); 107.9 (C-3); 120.5; 120.6; 120.7; 120.8; 120.9; 125.4; 125.8; 125.9; 126.2; 126.4; 131.5; 131.9; 133.6; 134.0; 134.2; 134.4; 134.5; 134.5; 134.7; 135.2; 135.5; 135.7; 136.4; 136.5; 138.2; 138.6; 138.6; 138.8; 139.0; 139.1; 20.2-21.0/168-170 (COOCH)

4.4. Computational methods

All optimizations and frequency calculations were carried out at the DFT level, using the “hybrid” PBE0 functional^{32b} and the 6–31 + G(d,p) basis set.⁹⁹

All quantum mechanical computations were performed with the Gaussian 03 suite.¹⁵⁵

In the calculations labelled “PCM” the influence of the aqueous medium was accounted for by the polarizable continuum model (PCM)^{52,53,76} in its UAHF parametrization;⁵¹ dispersion, repulsion¹⁵⁶ and cavitation¹⁵⁷ contributions are included.

Electronic absorption spectra of significant tautomers/conformers of **17Q** were estimated on the basis of excitation energy calculations using the time-dependent DFT (TD-DFT) approach.^{32b,47,74,75} The PBE0 functional with the large 6-311++G(2d,2p) basis set was employed for TD-DFT computations. Spectra in solution were computed with the non-equilibrium formulation of the PCM method.¹⁵⁸ To produce graphs of computed UV-Vis spectra, transitions above 190 nm were selected, and an arbitrary Gaussian linewidth of 20 nm was imposed.

5. Oxidative polymerization of 5,6-dihydroxyindole (1) in phosphate buffer/polyvinyl alcohol (PVA)

5.1 Materials and instrumentation

L-Dopa, sodium dithionite, hydrogen peroxide (30% solution in water), horseradish peroxidase (HRP) (donor: H₂O₂ oxidoreductase, EC 1.11.1.7) type II, PVA (F.W. 27000 Da) were commercially available and were used as obtained. All the solvents were of analytical grade quality.

1 was synthesized as reported previously¹⁵⁴

Absorption spectra were taken on a spectrophotometer having the cell compartment thermostated at 25 + 0.2°C. Mass spectra were registered in ESI+ mode with the cone and the fragmentator voltage set at 4 kV and 80 V, respectively and obtained in 1% TFA-methanol.

¹H and ¹³C NMR spectra were recorded at 400 or 300 MHz, respectively. Analytical and preparative TLC was carried out on silica gel plates (0.25 and 0.50 mm, respectively) from Merck. TLC plates were visualised using a UV lamp ($\lambda = 254$ nm).

HPLC analysis of the reaction mixtures was carried out on a Gilson apparatus equipped with a UV detector set at 280 nm using a Sphercclone ODS (5 μ m, 4.6 \times 250 mm) column; 1% v/v acetic acid/acetonitrile 95:5 (v/v) (eluant A), acetonitrile (eluant B) gradients were used as follows: from 0-5 min 30% eluant B, 5-40 min 30-80% eluant B, 40-50 min 80% eluant B. Flow rate of 1 mL/min was used.

Centrifugations were performed with a Beckman Avant J-25 centrifuge.

5.2 Oxidation of **1** for recording absorption spectra

Oxidation of **1** (8 mM) in 0.1 M phosphate buffer pH 7.0 was carried out with horseradish peroxidase (HRP; 36 U mL⁻¹) and H₂O₂ (20 mM) in the absence or in the presence of several percentage of PVA; at different times solution was diluted 25 fold with 0.1 M phosphate buffer pH 7.4 and spectra were recorded. When necessary the mixture was treated with a solution of NaBH₄ in water (20 mM). In PVA-added medium the buffers used was prepared by dissolving PVA in the appropriate weight ratio and warming to prevent cluster formation.

5.3 Oxidation of **1** for products analysis

To a 8 mM solution of **1** in 0.1 M phosphate buffer at pH 7.4 with or without 5% PVA were added horseradish peroxidase (HRP; 36 U mL⁻¹) and H₂O₂ (20 mM). Mixture was analyzed at different times by TLC after being subjected to the following procedures: reduction with sodium dithionite, acidification to pH 5, extraction with ethyl acetate and acetylation with acetic anhydride-pyridine 95:5 (v/v). In other experiments mixture was analyzed by HPLC with 1% vol/vol acetic acid/acetonitrile 95:5 (vol/vol) (eluant A), acetonitrile (eluant B) gradients: 0–5 min 30% eluant B, 5–40 min 30–80% eluant B, 40–50 min 80% eluant B, flow rate of 1 mL min⁻¹.

6. Study of oxidative polymerization of 5,6-dihydroxyindole (1) by Dynamic Light Scattering (DLS) and Small-angle Neutron Scattering (SANS)

6.1 Materials and instrumentation

Sodium dithionite, hydrogen peroxide (30% solution in water), horseradish peroxidase (HRP) (donor: H₂O₂ oxidoreductase, EC 1.11.1.7) type II, tyrosinase (monophenol monooxygenase, EC 1.14.18.1), PVA (F.W. 27000 Da) were commercially available and were used as obtained. All the solvents were of analytical grade quality.

1 was obtained as described above.¹⁵⁴

The light scattering setup was an ALV/CGS-3 based compact goniometer system from ALV-GmbH (Langen, Germany).

The light source was constituted by a He–Ne laser operating at 632.8 nm with a fixed output power of 22 mW.

Laplace transform for the parameter $g^{(1)}(t)$ was performed using the RILT algorithm incorporated in the commercial ALV/CGS-3 software.¹⁵⁹

SANS measurements were performed at 25 °C with the KWS2 instrument located at the Heinz Meier Leibnitz Source, Garching Forschungszentrum (Germany). Neutrons with a wavelength spread $\Delta\lambda/\lambda \leq 0.2$ were used. A two-dimensional array detector at three different wavelengths (W)/collimation (C)/sample-to-detector(D) distance combinations ($W_{7\text{\AA}}C_{8m}D_{2m}$, $W_{7\text{\AA}}C_{8m}D_{8m}$ and $W_{19\text{\AA}}C_{8m}D_{8m}$), measured neutrons scattered from the samples. These configurations allowed collecting data in a range of the scattering vector modulus between 0.0019 and 0.179 \AA^{-1} . The investigated samples were contained in a closed quartz cell, in order to prevent the solvent evaporation, and kept under measurements for a period such as to have ~ 2 million counts of neutrons. The obtained raw data were then corrected for background and empty cell scattering. Detector efficiency corrections, radial average and transformation to absolute scattering cross sections $d\Sigma/d\Omega$ were made with a secondary plexiglass standard.^{160,161}

6.2. Preparation of the samples

For DLS measurements 500 μL of a solution of **1** (2 mg, 0.01 mmol) in MeOH (5 mL) were added to 0.1 M phosphate buffer pH 7.4 (10 mL) without or with several percentage of PVA (0.05, 0.1, 0.5 mM), in order to obtain a concentration of 0.1 mM. 2 mL of this solution were taken and filtrated on MILLEXHA 0.45 μm filter in a test tube and peroxidase/ H_2O_2 (7 units and 15 molar equivalents respectively) or tyrosinase (161 units) were added . DLS measurements were performed at time intervals from 1min to several hours.

For SANS measurements was used deuterated phosphate buffer as solvent in order to minimize the incoherent scattering contribution to the total cross section. To a solution 2 mM of **1** in 0.1 M deuterated phosphate buffer pH 7.4 without or with several percentage of PVA, was added tyrosinase (161 units) and in some tests sodium dithionite as reductive agent.

7. Computational investigation of the stability of DHI-related catechols, radicals, and quinonoid forms

7.1 Computational methods

All calculations were performed with the Gaussian package of programs.¹⁵⁵

All structures were geometry optimized at the DFT level, with a hybrid functional (PBE0)^{32b} and basis set [6-31+G(d,p)]⁹⁹; the unrestricted formulation was adopted to describe radical species. For the iodine atom, a valence basis with pseudopotentials was employed, augmented with one d function.

Computations were performed in aqueous ambient with adoption of a polarizable continuum medium (PCM)^{52,53,76} to account for the influence of the aqueous environment.

Vibrational-rotational contributions to the free energy were also computed. Selected single point energy evaluations were also performed at the PBE0 / 6-311++G(2d,2p) level in vacuo.

8. Other studies: Study of the chemistry of nitrated lipids

8.1 Experimental methods

Sections regarding material, instrumentation and synthesis procedures and characterization of the various nitro-linoleic acids can be found in the publication on this study (Manini P., Capelli L., Reale S., Arzillo M., Crescenzi O., Napolitano A., Barone V., d'Ischia M. *J. Org. Chem* **2008**, *73*, 7517-7525)

8.2 Computational methods

All calculations were performed with the Gaussian package of programs.¹⁵⁵ Geometries were optimized at the DFT level of theory using the PBE0 functional with the 6-31+G(d,p) basis set.⁹⁹ The PBE0 (also referred to as PBE1PBE) is a hybrid functional obtained by combining a predetermined amount of exact exchange with the Perdew-Burke-Ernzerhof exchange and correlation functionals.^{32b} In control calculations, the polarizable continuum model (PCM)^{52,53,76} was used to simulate the aqueous environment. In view of the faster convergence, a scaled Van der Waals cavity based on universal force field (UFF) radii¹⁶² was used, and surface elements were modeled by spherical Gaussian functions.^{163,164} All minima were checked by computing the harmonic vibrational frequencies. Single-point energy evaluations were also performed with the recently developed M05-2X density functional¹⁵¹ and the large 6-311+G(2df,p) basis set.

REFERENCES

1. Nordlund, J. J.; Boissy, R. E.; Hearing, V. J.; King, R. A.; Ortonne, J., Eds., *The pigmentary system. Physiology and pathophysiology*. **1998**, Oxford University Press, New York
2. Prota, G. *Melanins and Melanogenesis*, **1992**, Academic Press, San Diego CA
3. Prota, G. "The chemistry of melanins and melanogenesis", in "*Fortschritte der chemie organischer Naturstoffe*", Hertz, W.; Kirby, G. W.; Moore, R. E.; Steglich, W.; Tamm, Ch., Eds., **1995**, vol. 64, Springer-Verlag, Wien, p. 93
4. Prota, G.; d'Ischia, M.; Napolitano, A. In *The Pigmentary System: Its Physiology and Pathophysiology*; Nordlund, J. J.; Boissy, R. E.; Hearing, V. J.; King, R. A.; Ortonne, J. P. Eds.; Oxford University Press: New York, **1998**; chap. 24, pp. 307-332
5. Meredith, P.; Sarna, T. *Pigment Cell Res.* **2006**, *19*, 572-594
6. Nighswander-Rempel, S. P.; Riesz, J.; Gilmore, J.; Bothma, J.P.; Meredith, P. *J. Phys. Chem. B* **2005**, *109*, 20629-20635
7. Seagle, B.L.; Rezai, K. A.; Gasyna, E. M.; Kobori, Y.; Rezaei, K.A.; Norris, J.R. Jr. *J Am Chem Soc.* **2005**, *127*, 11220-11221
8. Bridelli, M. G.; Ciati, A.; Crippa, P. R.; *Biophys. Chem.* **2006**, *119*, 137-145
9. Hong, L.; Liu, Y.; Simon, J. D. *Photochem Photobiol.* **2004**, *80*, 477-481.
10. Samokhvalov, A.; Liu, Y.; Simon, J. D. *Photochem Photobiol.* **2004**, *80*, 84-88
11. Ye, T., Hong, L., Garguilo, J., Pawlak, A., Edwards, G. S.; Nemanich, R. J.; Sarna, T.; Simon, J. D. *Photochem Photobiol.* **2006**, *82*, 733-777
12. Meredith, P.; Riesz, J. *Photochem Photobiol.* **2004**, *79*, 211-216
13. McGinness, J.; Corry, P.; Proctor, P. *Science.* **1974**, *183*, 853-855
14. (a) de Albuquerque, J. E.; Giacomantonio, C.; White, A. G.; Meredith, P. *Eur. Biophys. J.* **2006**, *35*, 190-195. (b) Meredith, P.; Powell, B. J.; Riesz, J.; Nighswander-Rempel, S. P.; Pederson, M. R.; Moore, E. G. *Soft Matter* **2006**, *2*, 37-44. (c) Meredith, P.; Powell, B. J.; Riesz, J.; Vogel, R.; Blake, D.; Kartini, I.; Will, G.; Subianto, S. In: *Broadband photon-harvesting biomolecules for photovoltaics*. Collings, A. F.; Critchley, C. Eds **2005**, 37-65
15. Cheng, J.; Moss, S. C.; Eisner, M. *Pigment Cell Res.* **1994**, *7*, 263-273
16. (a) Simon, J D.; Ito, S. *Pigment Cell Res.* **2004**, *17*, 423-424. (b) Clancy, C. M. R.; Simon, J. D. *Biochemistry* **2001**, *40*, 13353-13360. (c) Cheng, J; Moss, S.C.; Eisner, M. *Pigment Cell Res.* **1994**, *7*, 263-273. (d) Zajac, G.W.; Gallas, J.M.; Alvarada-Swaisgood, A.E. *J. Vac. Sci. Technol. B.* **1994**, *12*, 1512
17. (a) Liu Y., Simon J. D., *Pigm. Cell Res.* **2003**, *16*, 606 – 618. (b) Liu Y., Simon J. D., *Pigm. Cell Res.* **2005**, *18*, 42 – 48
18. Adhyaru B. B., Akhmedov N. G., Katritzky A. R. , Bowers C. R., *Magn. Reson. Chem.* **2003**, *41*, 466 – 474

19. Lorite G. S., Coluci V. R., da Silva M. I. N., Deziderio S. N., Graeff C. F. O., Galvao D. S., Cotta M. A. *J. Appl. Phys.* **2006**, *99*, 113511
20. Capozzi V., Perna G., Carmone P., Gallone A., Lastella M., Mezzenga E., Quartucci G., Ambrico M., Augelli V., Biagi P. F, Ligonzo T., Minafra A., Schiavulli L., Pallara M., Cicero R., *Thin Solid Films* **2006**, 511–512, 362 – 366
21. Pezzella A., Napolitano A., d'Ischia M., Prota G., Seraglia R., Traldi P., *Rapid Commun. Mass Spectrom.* **1997**, *11*, 368 – 372
22. Ghiani S., Baroni S., Burgio D., Digilio G., Fukuhara M., Martino P., Monda K., Nervi C., Kiyomine A., Aime S., *Magn. Reson. Chem.* **2008**, *46*, 471 – 479.
23. Stark, K. B.; M. Gallas, J.; Zajac, G. W.; Golab, J. T.; Gidanian, S.; McIntire, T.; Farmer P. J. *J. Phys. Chem. B* **2005**, *109*, 1970-1977
24. Kaxiras E., Tsolakidis A., Zonios G., Meng S., *Phys. Rev. Lett.* **2006**, *97*, 218102.
25. Meng S., Kaxiras E. *Biophys. J.* **2007**, *94*, 2095 – 2105
26. d'Ischia, M.; Napolitano, A.; Tsiakas, K. Prota, G. *Tetrahedron* **1990**, *46*, 5789-5796
27. Napolitano, A.; Corradini, M.G.; Prota, G. *Tetrahedron Lett.* **1985**, *26*, 2805-2808.
28. Szabo A., Ostlund N. S. *Modern Quantum Chemistry* McGraw-Hill Inc., New York (1989)
29. (a) Hohenberg P., Kohn W. *Phys. Rev.* **136**, B864 (1964); (b) Kohn W., Sham L.J. *Phys. Rev.* **140**, A1133 (1965)
30. Ceperley D. M., Alder B. J. *Phys. Rev. Lett.* **1980**, *45*, 566 (1980)
31. (a) Becke A. D., *Phys. Rev. A* **1988**, *38*, 3098; (b) Murray C. W, Laming G. J., Handy N. C, Adams R. D. *Chem. Phys. Lett.* **1992**, *199*, 551; (c) Perdew J. P., Zunger A. *Phys. Rev. B* 1981, *23*, 5048
32. (a) Becke A. *J. Chem. Phys.* **1993**, *98*, 648 b) Adamo C., Barone V *J. Chem. Phys.* **1999** *110*, 6158
33. Improta, R.; Barone, V. *J. Am. Chem. Soc.* **2004**, *126*, 14320–14321.
34. Benzi, C.; Improta, R.; Scalmani, G.; Barone, V. *J. Comp. Chem.* **2002**, *23*, 341–350
35. Langella, E.; Rega, N.; Improta, R.; Crescenzi, O.; Barone, V. *J. Comp. Chem.* **2002**, *23*, 650–661
36. Improta, R.; Mele, F.; Crescenzi, O.; Benzi, C.; Barone, V. *J. Am. Chem. Soc.* **2002**, *124*, 7857–7865
37. Jacquemin, D.; Wathelet V.; Perpète, E. A. *J. Phys. Chem. A* **2006**, *110*, 9145–9152
38. Preat, J.; Jacquemin, D.; Wathelet, V.; Andre, J.M.; Perpète, E. A. *J. Phys. Chem. A* **2006**, *110*, 8144–8150
39. Jacquemin, D.; Preat, J.; Wathelet, V.; Fontaine, M.; Perpète E. A. *J. Am. Chem. Soc.* **2006**, *128*, 2072–2083

40. Crescenzi, O.; Pavone, M.; De Angelis, F.; Barone V. *J. Phys. Chem. B* **2005**, *109*, 445–453
41. Aquilante, F.; Cossi, M.; Crescenzi, O.; Scalmani G.; Barone, V. *Mol. Phys.* **2003**, *101*, 1945–1953
42. Adamo, C; Barone, V. *Chem. Phys. Lett.* **2000**, *330*, 152–160
43. Adamo C., Cossi M., Rega N., Barone V. *Processes and Properties of Biological Systems*, L.Eriksson, Ed., Elsevier, 467 (**2001**)
44. Runge E, Gross E.K.U. *Phys. Rev. Lett* **1984**, *52*:997
45. Galli G., Pasquarello A., in *Computer Simulation in Chemical Physics*, eds. M.P. Allen, D. J. Tildesley, p. 261, Kluwer: Dordrecht, 1994
46. Pavone M., Barone V., Ciofini I., Adamo C. *J. Chem. Phys.* **2004**, *120*, 9167
47. Stratmann R. E., Scuseria G. E, Frish M. J. *J. Chem. Phys.* **1998**, *109*, 8218
48. Tomasi J., Persico M. *Chemical Reviews* **1994**, *94*, 2027
49. Tomasi J., Mennucci B., Cammi R. **2005**, *105*, 2999
50. Cramer C. J., Truhlar D. G. *Chemical Reviews* **1999**, *99*, 2161
51. Barone, V.; Cossi, M.; Tomasi, J. *J. Chem. Phys.* **1997**, *107*, 3210–3221.
52. Cossi, M.; Scalmani, N.; Rega, N.; Barone, V. *J. Chem. Phys.* **2002**, *117*, 43-54
53. Scalmani, G.; Barone, V.; Kudin, K. N.; Pomelli, C. S.; Scuseria, G. E.; Frisch, M. J. *Theor. Chem. Acc.* **2004**, *111*, 90-100
54. Cossi, M.; Barone, V. *J. Chem. Phys.* **1998**, *109*, 6246
55. Cossi, M.; Barone, V. *J. Chem. Phys.* **2001**, *115*, 4708-4717
56. Ciofini I., Adamo C., Barone V. *J. Chem. Phys.* **2004**, *121*, 6710
57. Benzi C., Crescenzi O., Pavone M., Barone V. *Magnetic Resonance In Chemistry* **2004**, *42*, S57
58. Panzella, L.; Pezzella, A.; Napolitano, A.; d’Ischia, M. *Org. Lett.* **2007**, *9*, 1411-1414
59. Pezzella, A.; Panzella, L.; Crescenzi, O.; Napolitano, A.; Navaratnam, S.; Edge, R.; Land, E. J.; Barone, V.; d’Ischia, M. *J. Am. Chem. Soc.* **2006**, *128*, 15490-15498
60. Pezzella, A.; Vogna, D.; Prota, G. *Tetrahedron: Asymmetry* **2003**, *14*, 1133-1140
61. Tran, M. L.; Powell, B. J.; Meredith, P. *Biophys. J.* **2006**, *90*, 743-752
62. Manini, P.; d’Ischia, M.; Milosa, M.; Prota, G. *J. Org. Chem.* **1998**, *63*, 7002-7008
63. (a) Stark, K. B.; Gallas, J. M.; Zajac, G. W.; Eisner, M.; Golab J. T. *J. Phys. Chem.* **2003**, *107*, 3061-3067. (b) Stark, K. B.; Gallas, J. M.; Zajac, G. W.; Eisner, M.; Golab J. T. *J. Phys. Chem.* **2003**, *107*, 11558-11562
64. Ito, S. *Pigment Cell Res.* **2003**, *16*, 230-236
65. Alaluf, S.; Heath, A.; Carter, N.; Atkins, D.; Mahalingam, H.; Barrett, K.; Kolb, R.; Smit, N. *Pigment Cell Res.* **2001**, *14*, 337-347

66. Powell, B. J.; Baruah, T.; Bernstein, N.; Brake, K.; McKenzie, R. H.; Meredith, P.; Pederson, M. R. *J. Chem. Phys.* **2004**, *120*, 8608-8615
67. Powell, B. J. *Chem. Phys. Lett.* **2005**, *402*, 111-115
68. Sobolewski, A. L.; Domcke, W. *ChemPhysChem* **2007**, *8*, 756-762
69. Olsen, S.; Riesz, J.; Mahadevan, I.; Coutts, A.; Bothma, J. P.; Powell, B. J.; McKenzie, R. H.; Smith S. C.; Meredith P. *J. Am. Chem. Soc.* **2007**, *129*, 6672-6673
70. Okuda, H.; Nakamura, A.; Wakamatsu, K.; Ito, S.; Sota, T. *Chem. Phys. Lett.* **2007**, *433*, 355-359
71. Il'ichev, Y. V.; Simon, J. D. *J. Phys. Chem. B* **2003**, *107*, 7162-7171
72. Bochenek, K.; Gudowska-Nowak E. *Acta Phys. Pol. B* **2003**, *34*, 2775-2790
73. Pezzella A., Crescenzi O., Natangelo A., Panzella L., Napolitano A., Navaratnam S., Edge R., Land E.J., Barone V., d'Ischia M. *J. Org. Chem.* **2007**, *72*, 1595-1603
74. Bauernschmitt, R.; Ahlrichs, R. *Chem. Phys. Lett.* **1996**, *256*, 454-464
75. Casida, M. E.; Jamorski, C.; Casida, K. C.; Salahub, D. R. *J. Chem. Phys.* **1998**, *108*, 4439-4449
76. Miertus, S.; Scrocco, E.; Tomasi, J. *Chem Phys.* **1981**, *55*, 117-129
77. Adamo, C.; Scuseria, G. E.; Barone, V. *J. Chem. Phys.* **1999**, *111*, 2889-2899
78. O'Neill, L.; Byrne, H. J. *J. Phys. Chem.* **2005**, *109*, 12685-12690
79. Santoro, F.; Improta, R.; Lami, A.; Bloino, J.; Barone, V. *J. Chem. Phys.* **2007**, *126*(8), 084509
80. Improta, R.; Barone, V.; Santoro, F. *Angew. Chem. Int. Edit.* **2007**, *46*, 405-408
81. Wahlström, N.; Slätt, J.; Stensland, B.; Ertan, A.; Bergman, J.; Janosik, T. *J. Org. Chem.* **2007**, *72*, 5886-5889
82. Wu, Y. H.; Lobeck, W. G. Jr.; Ryan, R. P. *J. Med. Chem.* **1972**, *15*, 529-534
83. Manini, P.; Pezzella, A.; Panzella, L.; Napolitano, A.; d'Ischia, M. *Tetrahedron* **2005**, *61*, 4075-4080
84. Ishii, H.; Sakurada, E.; Murakami, K.; Takase, S.; Tanaka, H. *J. Chem. Soc., PerkinTrans. 1* **1988**, 2387-2395.
85. Mahato, S. B.; Mandal, N. B.; Chattopadhyay, S.; Nandi, G.; Luger, P.; M. *Tetrahedron* **1994**, *50*, 10803-10812.
86. (a) Liu, B.; Tian, H. *J. Mater. Chem.* **2005**, *15*, 2681-2686; (b) Vasquez, M.; Fabbrizzi, L.; Taglietti, A.; Pedrido, R. M.; Gonza' lez-Noya, A. M.; Bermejo, M. R. *Angew. Chem., Int. Ed.* **2004**, *43*, 1962-1965; (c) Wu, Y.; Peng, X.; Fan, J.; Gao, S.; Tian, M.; Zhao, J.; Sun, S. *J. Org. Chem.* **2007**, *72*, 62-70; (d) Kim, S. K.; Bok, J. H.; Bartsch, R. A.; Lee, J. Y.; Kim, J. S. *Org. Lett.* **2005**, *7*, 4839-4842; (e) Gale, P. A. *Chem. Commun.* **2005**, 3761-3772; (f) Winstanley, K. J.; Sayer, A. M.; Smith, D. K. *Org. Biomol. Chem.* **2006**, *4*, 1760-1767

87. (a) Xu, Z.; Kim, S.; Kim, H. N.; Han, S. J.; Lee, C.; Kim, J. S.; Qian, X.; Yoon, J. *Tetrahedron Lett.* **2007**, *48*, 9151–9154; (b) Duke, R. M.; Gunnlaugsson, T. *Tetrahedron Lett.* **2007**, *48*, 8043–8047; (c) Wu, C.-Y.; Chen, M.-S.; Lin, C.-A.; Lin, S.-C.; Sun, S.-S. *Chem. Eur. J.* **2006**, *12*, 2263–2269; (d) Gunnlaugsson, T.; Davis, A. P.; Hussey, G. M.; Tierney, J.; Glynn, M. *Org. Biomol. Chem.* **2004**, *2*, 1856–1863; (e) Miao, R.; Zheng, Q.-Y.; Chen, C.-F.; Huang, Z.-T. *Tetrahedron Lett.* **2004**, *45*, 4959–4962; (f) Black, C. B.; Andrioletti, B.; Try, A. C.; Ruiperez, C.; Sessler, J. L. *J. Am. Chem. Soc.* **1999**, *121*, 10438–10439
88. (a) Xu, G.; Tarr, M. A. *Chem. Commun.* **2004**, 1050–1051; (b) Chu, Q.; Medvetz, D.A.; Pang, Y. *Chem. Mater.* **2007**, *19*, 6421–6429; (c) Peng, X.; Wu, Y.; Fan, J.; Tian, M.; Han, K. *J. Org. Chem.* **2005**, *70*, 10524–10531
89. (a) Jose, D. A.; Kumar, D. K.; Ganguly, B.; Das, A. *Org. Lett.* **2004**, *6*, 3445–3448; (b) Boiocchi, M.; Del Boca, L.; Esteban-Go´mez, D.; Fabbrizzi, L.; Licchelli, M.; Monzani, E. *J. Am. Chem. Soc.* **2004**, *126*, 16507–16514
90. He, X.; Hu, S.; Liu, K.; Guo, Y.; Xu, J.; Shao, S. *Org. Lett.* **2006**, *8*, 333–336
91. See for example: (a) Pfeffer, F. M.; Lim, K. F.; Sedgwick, K. *J. Org. Biomol. Chem.* **2007**, *5*, 1795–1799; (b) Suresh, M.; Jose, D. A.; Das, A. *Org. Lett.* **2007**, *9*, 441–444; (c) Bonizzoni, M.; Fabbrizzi, L.; Taglietti, A.; Tiengo, F. *Eur. J. Org. Chem.* **2006**, 3567–3574; (d) Amendola, V.; Bonizzoni, M.; Esteban-Go´mez, D.; Fabbrizzi, L.; Licchelli, M.; Sanceno´n, F.; Taglietti, A. *Coord. Chem. Rev.* **2006**, *250*, 1451–1470; (e) Evans, L. S.; Gale, P. A.; Light, M. E.; Quesada, R. *Chem. Commun.* **2006**, 965–967; (f) Quinlan, E.; Matthews, S. E.; Gunnlaugsson, T. *Tetrahedron Lett.* **2006**, *47*, 9333–9338
92. (a) Caltagirone, C.; Bates, G. W.; Gale, P. A.; Light, M. E. *Chem. Commun.* **2008**, 61–63; (b) Lin, C.-I.; Selvi, S.; Fang, J.-M.; Chou, P.-T.; Lai, C.-H.; Cheng, Y.-M. *J. Org. Chem.* **2007**, *72*, 3537–3542
93. (a) Connors, K. A. Binding Constants. *The Measurement of Molecular Complex*; Wiley: New York, NY, **1987**; (b) Benesi, H. A.; Hildebrand, J. H. *J. Am. Chem. Soc.* **1949**, *71*, 2703–2707
94. (a) Ghosh, T.; Maiya, B. G.; Wong, M. W. *J. Phys. Chem. A* **2004**, *108*, 11249–11259; (b) Anzenbacher, P., Jr.; Palacios, M. A.; Jursi´kova´, K.; Marquez, M. *Org. Lett.* **2005**, *7*, 5027–5030; (c) Jose, D. A.; Kar, P.; Koley, D.; Ganguly, B.; Thiel, W.; Ghosh, H. N.; Das, A. *Inorg. Chem.* **2007**, *46*, 5576–5584; (d) Quinlan, E.; Matthews, S. E.; Gunnlaugsson, T. *J. Org. Chem.* **2007**, *72*, 7497–7503
95. Lin, Z. H.; Zhao, Y. G.; Duan, C. Y.; Zhang, B. G.; Bai, Z. P. *Dalton Trans.* **2006**, 3678–3684
96. Okuda, H.; Wakamatsu, K.; Ito, S.; Sota, T. *J. Phys. Chem. A* **2008**, *112*, 11213–11222
97. d’Ischia M., Napolitano A., Pezzella A., Land E. J., Ramsden C. A., Riley P. A. *Adv. Heterocycl. Chem.* **2005**, *89*, 1–63
98. Corradini, M. G.; Napolitano, A.; Protta, G. *Tetrahedron* **1985**, *42*, 2083–2088
99. Francl, M. M.; Pietro, W. J.; Hehre, W. J.; Binkley, J. S.; Gordon, M. S.; DeFrees, D. J.; Pople, J. A. *J. Chem. Phys.* **1982**, *77*, 3654–3665

100. Pezzella A., Iadonisi A., Valerio S., Panzella L., Napolitano A., Adinolfi M., d'Ischia M. *J. Am. Chem. Soc.* **2009**, *131*, 15270-15275
101. For examples of indole macrocycles and their applications, see: (a) Black, D.St.C.; Craig, D.; Kumar, N. *Tetrahedron Lett.* **1995**, *36*, 8075–8078. (b) Bowyer, P. K.; Black, D.St. C.; Craig, D. C. *Tetrahedron* **2005**, *61*, 10781–10792. (c) Chang, K.-J.; Moon, D.; Lah, M. S.; Jeong, K.-S. *Angew. Chem., Int. Ed.* **2005**, *44*, 7926–7929. (d) Hiyoshi, H.; Sonoda, T.; Mataka, S. *Heterocycles* **2006**, *68*, 763–769. (e) Suk, J.-M.; Chae, M. K.; Kim, N.-K.; Kim, U.-I.; Jeong, K.-S. *Pure Appl. Chem.* **2008**, *80*, 599–608. (f) Santoso, M.; Somphol, K.; Kumar, N.; Black, D.St. C. *Tetrahedron* **2009**, *65*, 5977–5983
102. Meng, S.; Kaxiras, E. *Biophys. J.* **2008**, *94*, 2095–2105
103. d'Ischia M., Napolitano A., Pezzella A., Meredith and Sarna T. *Angew. Chem. Int. Ed. Engl.* **2009**, *48*, 3914-3921. S3914/1-S3914/40
104. Liu, Y., L. Hong, K. Wakamatsu, S. Ito, B. Adhyaru, C. Y. Cheng, C. R. Bowers and J. D. Simon *Photochem. Photobiol.* **2005** *81*, 135–144
105. Simon, J. D., L. Hong and D. N. Peles *J. Phys. Chem. B* **2008**, *112*, 13201–13217
106. Nighswander-Rempel, S. P., I. Mahadevan, H. R. Rubinsztein-Dunlop and P. Meredith *Photochem. Photobiol.* **2007**, *83*, 1449–1454
107. Bu'Lock, J. D. & Harley-Mason, J. (1960). *Arch.Biochem. Biophys.* **91**, 189-193
108. Lawrie, K. J., P. Meredith and R. P. McGeary *Photochem. Photobiol.* **2008**, *84*, 632–638
109. Hatcher, L. Q. and J. D. Simon *Photochem. Photobiol.* **2008**, *84*, 608–612
110. Pezzella, A., A. Iadonisi, S. Valerio, L. Panzella, A. Napolitano, M. Adinolfi and M. d'Ischia *J. Am. Chem. Soc.* **2009**, *131*, 15270–15275
111. Watt, A. A. R., J. Bothma and P. Meredit *Soft Matter* **2009**, *5*, 3754–3760
112. Pezzella, A., L. Panzella, O. Crescenzi, A. Napolitano, S. Navaratnam, R. Edge, E. J. Land, V. Barone and M. d'Ischia *J. Org. Chem.* **2009**, *74*, 3727–3734
113. Tacx, J. C. J. F., H. M. Schoffeleers, A. G. Brands and L. Teuwen *Polymer* **2000**, *41*, 947–957
114. Fennell Evans, D.; Wennerström, H.; *The Colloidal Domain (1994)*, Wiley VCH
115. Pusey, P.N. In *Neutrons, X-Ray and Light: Scattering Methods Applied to SoftCondensed Matter*; Lindener, P.; Zemb, T.; Eds. Elsevier: Amsterdam, **2002**, pp 203-220
116. Brown, W. *Scattering Methods: A brief Introduction. Lecture notes*; **1994**, Uppsala University, Sweden
117. Brehm G. A. and Bloomfield V. A. *Macromolecules*, **1975**, *8(5)*, 663–665
118. Berne, B.J.; Pecora, R. *Dynamic Light Scattering: with Applications to Chemistry, Biology, and Physics*, 2nd **2000**, ed. Dover publications, Inc.: New York
119. Cussler, E.L. *Diffusion Mass Transfer in Fluid Systems*, 2 **1997**, ed. Cambridge University Press: Cambridge, UK

120. Kotlarchyk, M.; Chen, S. H. *Journal of Chemical Physics* **1983**, *79*, 2461
121. Morel, S.; Terreno, E.; Ugazio, E.; Aime, S.; Gasco, M. R., *European Journal of Pharmaceutics and Biopharmaceutics* **1998**, *45*, 157
122. Pusey, P.N.; Lindener, P.; Zemb T. ,*In Neutrons, X-Ray and Light Scattering* Eds. Elsevier: Amsterdam, **2002**, pp 203
123. Lambert, C.; Chacon, J. N.; Chedekel, M. R.; Land, E. J.; Riley, P. A.; Thompson, A.; Truscott, T. G. *Biochim. Biophys. Acta* **1989**, *993*, 12-20
124. Hale,J.M.; Parson,R. *Transaction of the Faraday Society* **1963**, *59*,1429-1437
125. Freeman, B.A.; Baker, P.R.S.; Schopfer, F.J.; Woodcock, S.R.; Napolitano, A.; d'Ischia, M. *J. Biol. Chem.* **2008**, *283*, 15515-15519
126. a) Trostchansky, A.; Rubbo, H. *Free Radic. Biol. Med.* **2008**, *44*, 1887-1896; b) Trostchansky, A.; Souza, J.M.; Ferreira, A.; Ferrari, M.; Blanco, F.; Trujillo, M.; Castro, D.; Cerecetto, H.; Baker, P.R.S.; O'Donnell, V.B.; Rubbo, H. *Biochemistry* **2007**, *46*, 4645-4653
127. Cui, T.; Schopfer, F.J.; Zhang, J.; Chen, K.; Ichikawa, T.; Baker, P.R.S.; Batthyany, C.; Chacko, B.K.; Feng, X.; Patel, R.P.; Agarwal, A.; Freeman, B.A.; Chen, Y.E. *J. Biol. Chem.* **2006**, *281*, 35686-35698
128. Lim, D.G.; Sweeney, S.; Bloodsworth, A.; White, C.R.; Chumley, P.H.; Krishna, N.R.; Schopfer, F.; O'Donnell, V.B.; Eiserich, J.P.; Freeman, B.A. *Proc. Natl. Acad. Sci. USA* **2002**, *99*, 15941-15946
129. Lima, E.S.; Di Mascio, P.; Rubbo, H.; Abballa, D.S.P. *Biochemistry* **2002**, *41*, 10717-10722
130. Baker, P.R.S.; Schopfer, F.J.; Sweeney, S.; Freeman, B.A. *Proc. Natl. Acad. Sci. USA* **2004**, *101*, 11577-11582
131. Baker, P.R.S.; Lin, Y.; J. Schopfer, F.J.; R. Woodcock, S.R.; Groeger, A.L.; Batthyany, C.; Sweeney, S.; Long, M.H.; Iles, K.E.; Baker, L.M.S.; Branchaud, B.P.; Chen, Y.E.; Freeman, B.A. *J. Biol. Chem.* **2005**, *280*, 42464-42475
132. (a) Napolitano, A.; Camera, E.; Picardo, M.; d'Ischia, M. *J. Org. Chem.* **2000**, *65*, 4853-4860; (b) d'Ischia, M. *Tetrahedron Lett.* **1996**, *37*, 5773-5774; (c) d'Ischia, M.; Rega, N.; Barone V. *Tetrahedron* **1999**, *55*, 9297-9308
133. Alexander, R.L.; Bates, D.J.P.; Wright, M.W.; King, S.B.; Morrow, C.S. *Biochemistry* **2006**, *45*, 7889-7896
134. Schopfer, F.J.; Baker, P.R.S.; Giles, G.; Chumley, P.; Batthyany, C.; Crawford, J.; Patel, R.P.; Hogg, N.; Branchaud, B.P.; Lancaster, J.R. Jr.; Freeman, B.A. *J. Biol. Chem.* **2005**, *280*, 19289-19297
135. Wright, M.M.; Schopfer, F.J.; Baker, P.R.S.; Vidyasagar, V.; Powell, P.; Chumley, P. Iles, K.E.; Freeman, B.A.; Agarwal, A. *Proc. Natl. Acad. Sci. USA* **2006**, *103*, 4299-4304
136. Batthyany, C.; Schopfer, F.J.; Baker, P.R.S.; Duran, R.; Baker, L.M.S.; Huang, Y.; Cervenansky, C.; Branchaud, B.P.; Freeman, B.A. *J. Biol. Chem.* **2006**, *281*, 20450-20463

137. Baker, L.M.S.; Baker, P.R.S.; Golin-Bisello, F.; Schopfer, F.J.; Fink, M.; Woodcock, S.R.; Branchaud, B.P.; Radi, R.; Freeman, B.A. *J. Biol. Chem.* **2007**, *282*, 31085-31093
138. Gorczynski, M.J.; Huang, J.; Lee, H.; King, S.B. *Bioorg. Med. Chem. Lett.* **2007**, *17*, 2013-2017
139. Chakrapani, H.; Gorczynski, M.J.; King, S.B. *J. Am. Chem. Soc.* **2006**, *128*, 16332-16337
140. Gorczynski, M.J.; Huang, J.; King, S.B. *Org. Lett.* **2006**, *8*, 2305-2308
141. Lima, E.S.; Bonini, M.G.; Augusto, O.; Barbeiro, H.V.; Souza, H.P.; Abballa, D.S.P. *Free Radic. Biol. Med.* **2005**, *39*, 532-539
142. Woodcock, S.R.; Marwitz, A.J.V.; Bruno, P.; Branchaud, B.P. *Org. Lett.* **2006**, *8*, 3931-3934
143. O'Donnell, V.B.; Eiserich, J.P.; Chumley, F.H.; Jablonsky, M.J.; Krishna, N.R.; Kirk, M.; Barnes, S.; Darley-USmar, V.M.; Freeman, B.A. *Chem Res. Toxicol.* **1999**, *12*, 83-92
144. O'Donnell, V.B.; Eiserich, J.P.; Bloodsworth, A.; Chumley, F.H.; Kirk, M.; Barnes, S.; Darley-USmar, V.M.; Freeman, B.A. *Methods Enzymol.* **1999**, *301*, 454-470
145. Hayama, Y.; Tomoda, S.; Takeuchi, Y.; Nomura, Y. *Tetrahedron Lett.* **1982**, *23*, 4733-4734
146. Lin, D.; Zhang, J.; Sayre, L.M. *J. Org. Chem.* **2007**, *72*, 9471-9480
147. Trenwith, A.B. *J. Chem. Soc. Faraday Trans. 1* **1982**, *78*, 3131-3136
148. Pratt, D.A.; Mills, J.H.; Porter, N.A. *J. Am. Chem. Soc.* **2003**, *125*, 5801-5810
149. Tallman, K.A.; Pratt, D.A.; Porter, N.A. *J. Am. Chem. Soc.* **2001**, *123*, 11827-11828
150. Yu, L.; Adams, D.; Gabel, M. *J. Agric. Food Chem.* **2002**, *50*, 4135-4140
151. Zhao, Y.; Schultz, N.E.; Truhlar, D.G. *J. Chem. Theory Comput.* **2006**, *2*, 364-382
152. Zhao, Y.; Truhlar, D.G. *J. Phys. Chem. A* **2008**, *112*, 1095-1099
153. Ros, P.; Schuit, G.C.A. *Theor. Chim. Acta* **1966**, *4*, 1-12
154. Edge, R.; d'Ischia, M.; Land, E. J.; Napolitano, A.; Navaratnam, S.; Panzella, L.; Pezzella, A.; Ramsden, C.A.; Riley, P. A. *Pigment Cell Res.* **2006**, *19*, 443-450
155. Frisch, M. J.; Trucks, G. W.; Schlegel, H. B.; Scuseria, G. E.; Robb, M. A.; Cheeseman, J. R.; Montgomery Jr., J. A.; Vreven, T.; Kudin, K. N.; Burant, J. C.; Millam, J. M.; Iyengar, S. S.; Tomasi, J.; Barone, V.; Mennucci, B.; Cossi, M.; Scalmani, G.; Rega, N.; Petersson, G. A.; Nakatsuji, H.; Hada, M.; Ehara, M.; Toyota, K.; Fukuda, R.; Hasegawa, J.; Ishida, M.; Nakajima, T.; Honda, Y.; Kitao, O.; Nakai, H.; Klene, M.; Li, X.; Knox, J. E.; Hratchian, H. P.; Cross, J. B.; Bakken, V.; Adamo, C.; Jaramillo, J.; Gomperts, R.; Stratmann, R. E.; Yazyev, O.; Austin, A. J.; Cammi, R.; Pomelli, C.; Ochterski, J. W.; Ayala, P. Y.; Morokuma, K.; Voth, G. A.; Salvador, P.; Dannenberg, J. J.; Zakrzewski, V. G.;

- Dapprich, S.; Daniels, A. D. ; Strain, M. C.; Farkas, O.; Malick, D. K.; Rabuck, A. D.; Raghavachari, K.; Foresman, J. B.; Ortiz, J. V.; Cui, Q.; Baboul, A. G. ; Clifford, S.; Cioslowski, J. ; Stefanov, B. B.; Liu, G.; Liashenko, A.; Piskorz, P.; Komaromi, I.; Martin, R. L.; Fox, D. J.; Keith, T.; Al-Laham, M. A.; Peng, C. Y.; Nanayakkara, A.; Challacombe, M.; W. Gill, P. M.; Johnson, B.; Chen, W.; Wong, M. W.; Gonzalez C.; Pople J.A. *Gaussian 03* (Revision D.02). Gaussian, Inc., **2004**, Wallingford, CT
156. (a) Floris, F.; Tomasi, J. *J. Comp. Chem.* **1989**, *10*, 616-627. (b) Floris, F.; Tomasi, J.; Pascual-Ahuir, J. L. *J. Comp. Chem.* **1991**, *12*, 784-791
157. Pierotti, R. A. *Chem. Rev.* **1976**, *76*, 717-726
158. Cossi, M.; Barone, V. *J. Phys. Chem. A* **2000**, *104*, 10614-10622
159. Peters R., ALV-5000/E/EPP%ALV-60X0 for WINDOWS-95/NT 4.0 Software, 3.0.1.12, **2003**
160. Wignall G. D. and Bates F. S. *Journal of Applied Crystallography*, **1987**, *20*(1), 28-40
161. Russell T. P., Lin J. S., Spooner S. and Wignall G. D. *Journal of Applied Crystallography*, **1988**, *21*(6), 629-38
162. Rappé, A.K.; Casewit, C.J.; Colwell, K.S.; Goddard III, W.A.; Skiff, W.M. *J. Am. Chem. Soc.* **1992**, *114*, 10024-10035
163. York, D.A.; Karplus, M. *J. Phys. Chem. A* **1999**, *103*, 11060-11079
164. Caricato, M.; Scalmani, G.; Frisch, M.J. In: *Continuum Solvation Models in Chemical Physics*; Mennucci, B., Cammi, R. Eds.; John Wiley & Sons: Chichester, **2007**; pp. 64-81

LIST OF PUBLICATIONS

PEZZELLA ALESSANDRO, PANZELLA LUCIA, NATANGELO ANNA, ARZILLO M., NAPOLITANO ALESSANDRA, D'ISCHIA MARCO. (2007). 5,6-dihydroxyindole tetramers with "anomalous" interunit bonding patterns by oxidative coupling of 5,5',6,6'-tetrahydroxy-2,7'-biindolyl: emerging complexities on the way toward an improved model of eumelanin buildup. *JOURNAL OF ORGANIC CHEMISTRY* vol. 72, pp. 9225-9230 ISSN: 0022-3263.

D'ISCHIA MARCO, CRESCENZI ORLANDO, PEZZELLA ALESSANDRO, ARZILLO M., PANZELLA LUCIA, NAPOLITANO ALESSANDRA, BARONE VINCENZO. (2008). Structural effect on the electronic absorption properties of 5,6-dihydroxyindole oligomers: the potential of an integrated experimental and DFT approach to model eumelanin optical properties. *PHOTOCHEMISTRY AND PHOTOBIOLOGY* vol. 84, pp. 600-607 ISSN: 0031-8655.

MANINI PAOLA, CAPELLI LUIGIA, REALE SAMANTHA, ARZILLO M., CRESCENZI ORLANDO, NAPOLITANO ALESSANDRA, BARONE VINCENZO, D'ISCHIA MARCO. (2008). Chemistry of nitrated Lipids: remarkable instability of 9-nitrolinoleic acid in neutral aqueous medium and a novel nitronitrate ester product by concurrent autoxidation/nitric oxide-release pathways. *JOURNAL OF ORGANIC CHEMISTRY* vol. 73, pp. 7517-7525 ISSN: 0022-3263.

PANZELLA LUCIA, PEZZELLA ALESSANDRO, ARZILLO M., MANINI PAOLA, NAPOLITANO ALESSANDRA, D'ISCHIA MARCO. (2009). A novel fluoride-sensing scaffold by a peculiar acid-promoted trimerization of 5,6-dihydroxyindole. *TETRAHEDRON* vol. 65, pp 2032-2036.

ALESSANDRO PEZZELLA, VERONICA AMBROGI, MARIANNA ARZILLO, ALESSANDRA NAPOLITANO, COSIMO CARFAGNA, MARCO D'ISCHIA. (2010). 5,6-dihydroxyindole oxidation in buffer/polyvinyl alcohol: a new model system for studies of visible chromophore development in synthetic eumelanin polymers. *PHOTOCHEMISTRY AND PHOTOBIOLOGY* vol. 86, pp 533-537.

MARIANNA ARZILLO, ALESSANDRO PEZZELLA, ORLANDO CRESCENZI, ALESSANDRA NAPOLITANO, EDWARD J. LAND, VINCENZO BARONE, MARCO D'ISCHIA. (2010). Cyclic Structural motifs in 5,6-dihydroxyindole polymerization uncovered: biomimetic modular buildup of a unique five-membered macrocycle. *ORGANIC LETTERS* vol.12, pp 3250-3253.